

DISS. ETH NO. 25554

MULTIPHASE CHEMICAL REACTIVITY IN COLD REGIONS

A thesis submitted to attain the degree of
DOCTOR OF SCIENCES of ETH ZURICH
(Dr. sc. ETH Zurich)

presented by
JACINTA EDEBELI

MSc., ETH in Umweltnaturwissenschaften

born on *03.08.1987*
citizen of Nigeria

accepted on the recommendation of
Prof. Markus Ammann
Dr. Hans-Werner Jacobi
Prof. Konrad Steffen

2018

Contents

| | |
|---|------------|
| ABSTRACT | iv |
| ZUSAMMENFASSUNG..... | vii |
| 1. Towards understanding chemistry in cold regions | 1 |
| 1.1 Introduction | 1 |
| 1.2 Thesis mission | 7 |
| 1.3 Thesis outline | 10 |
| 2. Probing the interfacial process of bromide oxidation by ozone in aqueous salt solutions | 20 |
| 2.1 A surface–stabilized ozonide triggers bromide oxidation at the aqueous solution–vapor interface..... | 20 |
| 2.2 Supplementary information: Details of the different methods..... | 35 |
| 3. Interplay of microphysics and kinetics in bromide oxidation by ozone | 64 |
| 3.1 Microphysics of the aqueous bulk counter water activity driven rate acceleration in bromide oxidation by ozone from 289 – 245 K | 64 |
| 3.2 Supplementary information..... | 86 |
| 4. Urban wintertime atmospheric composition: gas phase – PM_{2.5} partitioning, snow cover, and meteorology..... | 100 |
| 4.2 Supplementary Information..... | 120 |
| 5. Snow metamorphism and chemistry in snow: reactive assessment of ion redistribution in snow grains | 128 |
| 5.2 Supplementary information..... | 141 |
| 6. Summary and Outlook | 147 |
| Acknowledgements | 154 |

ABSTRACT

The cryosphere plays an important role in Earth's energy balance and in the cycling of compounds in the environment. The cryosphere also serves as an important archive of the Earth's past climate and atmospheric composition. In addition, the cryosphere is a reactive matrix, and multiphase chemical reactions in these cold regions of Earth impact the atmospheric composition. When reactive losses lead to significant loss of compounds trapped in snow, interpretation of ice core records of these compounds become challenging. From a chemical perspective, the cryospheric matrices such as surface snow, sea ice, and ice clouds are complex matrices, where the reactions can proceed in a number of distinct compartments. To understand cryospheric chemistry in full complexity, reaction rates of key reactants have to be known in their compartments. These compartments include the air-ice interface, aerosol deposits, and brine in micropockets. This thesis investigated chemistry with relevance to cold regions in the world, especially the polar regions, using bromide oxidation by ozone in well-defined laboratory experiments.

Given the importance of halogens in Polar boundary layer chemistry, their reactions at the air-ice interface and in aerosol have been investigated in great detail. Therefore, this system was chosen here as a model system to investigate chemistry in the snow compartments with a major focus on increasing complexity in laboratory samples to mimic conditions in the environment better. The general interest in halogen chemistry stems from its impact on the oxidative capacity of the polar atmosphere and the role of halide on the fate of compounds in the atmosphere due to formation of reactive halogen species (RHS). Of particular importance is the reaction of RHS with gas phase mercury, which increases the deposition of mercury with implications for ecosystem and human health.

Sea spray aerosols are omnipresent in coastal polar environments. In this work, we have tackled the effects of temperature on reactivity especially below 0 °C to -25 °C, temperatures relevant for polar regions, using a coated wall flow tube. To increase relevance to the polar environment, mixtures of an organic species with sea spray aerosol proxies were used in this study. It was found that with decrease in water activity and increase in solute activity due to decrease in temperature, the Henry's law solubility constant of the reactive gas (ozone, in this case) decreased; in the presence of organics, the viscosity significantly increased, which resulted in significant decrease in diffusivity.

ABSTRACT

Decreased solubility of ozone and decreased diffusivity of the reactive species resulted in decreased reactivity despite increase in the activity of bromide at lower temperatures. This is an important, and somewhat surprising finding as the viscosity of organics is usually discussed at much lower relative humidity and temperatures in aerosol science. This work illustrates the role of organics already at moderate temperature and relatively high humidity as typically found in surface snow and arctic boundary layer aerosol.

Focusing more on the molecular mechanism of this reaction, an interfacial intermediate (BrOOO^-) was identified for the first time. Its presence at the air–water interface gives a clear explanation of the long–standing question about the relative importance of the interfacial chemistry of this reaction compared to bulk chemistry. The parameters relevant for the interfacial reaction were determined; the temperature dependence of the partition coefficient of BrOOO^- to the surface (K) was parameterized and the maximum surface coverage of the interfacial species was quantified (10^{12} molecules per cm^2). This study led to the conclusion that this interfacial process is very significant for bromide oxidation on sea–spray aerosols at environmentally relevant ozone concentrations.

The above experiment shares a crucial limitation with most, if not all, studies of cryospheric chemistry. The ice phase is in thermodynamic equilibrium. In nature, however, this is seldom the case and ice or snow are frequently growing or shrinking. Therefore, this thesis investigated the effect of snow metamorphism on the redistribution of bromide ions in snow and the implications for the reactivity in collaboration with snow physicists. Preliminary assessment of the results from this study showed that, with 12 days of metamorphism at temperature gradient typically found in polar snow, there was a significant decrease in the reactivity. These results indicate that bromide may have been incorporated in the ice grains with the movement of water vapor during metamorphism. This finding demonstrates that exchange between the individual snow compartments are frequent and have severe impact on reactivity. To summarize, in these laboratory experiments the complexity of the studied samples and processes was significantly increased revealing new details on cryospheric chemistry. However, to take full advantage of laboratory experiments, the experiments were still well defined.

To increase complexity even further, an urban wintertime atmospheric composition field campaign was conducted during this study from January 12 to February 23, 2018 at Kalamazoo, Michigan, USA. Gas phase concentrations of ammonia (NH_3), sulfur dioxide (SO_2), and nitric acid (HNO_3), and $\text{PM}_{2.5}$ concentrations of ammonium (NH_4^+), sulfate (SO_4^{2-}), and nitrate (NO_3^-) were measured. Observations showed that $\text{PM}_{2.5}$ episodes were stronger during periods with snow cover, which were related to stable boundary layer height and high relative humidity especially as temperatures increased. This implies that snow may be contributing to the water vapor available for particle formation and growth. There was a strong deposition of ammonia with snowfall, which resulted in high concentrations of ammonia and high pH in surface snow sampled during this study. This study also observed

ABSTRACT

high temperature dependence of ammonia concentrations. From this temperature dependence, we estimated the enthalpy of ammonia volatilization to be 50 ± 6 kJ/mol. This temperature dependence was stronger on days with snow cover, which indicates that snow may be a temperature dependent source of ammonia in the winter. This campaign also contributes to the database of urban wintertime atmospheric composition for which there have been only a few studies conducted.

Therefore, this thesis contributes to the better understanding of chemistry in snow and cold aerosol, and in particular, to the reaction of ozone with bromide: the interfacial process and the temperature dependence of this reaction, and the partitioning of bromide between the surface and the bulk of the ice during snow metamorphism.

ZUSAMMENFASSUNG

Die Energiebilanz der Erde sowie globale Stoffkreisläufe werden durch die Kryosphäre, die gefrorenen Wasservorkommen der Erde, beeinflusst und die Kryosphäre bildet zudem ein wichtiges Archiv des vergangenen Klimas und Zusammensetzung der Atmosphäre. Die Kryosphäre ist zudem ein Hort für chemische Reaktionen welche die Zusammensetzung der Atmosphäre beeinflussen können. Wenn diese Reaktionen beispielsweise zu einem Verlust der im Schnee enthaltenden Verbindungen führen, wird die Interpretation von Eisbohrkernen schwierig. Aus chemischer Sicht stellen die einzelnen Gebiete der Kryosphäre, wie der Oberflächenschnee, das Meereis und die Eiswolken komplexe Gemische da, in denen die Reaktionen in einer Reihe von verschiedenen Kompartiments ablaufen können. Um die Chemie der Kryosphäre in ihrer ganzen Komplexität zu verstehen, müssen Reaktionsraten von Schlüsselprozessen in den jeweiligen Kompartimenten bekannt sein. Zu diesen gehören die Luft–Eis–Grenzfläche, Aerosolablagerungen und wässrige Lösungen in mikro–Tropfen. Diese Dissertation untersuchte die Chemie in diesen Kompartimenten auf Grund der Relevanz für die kalte Regionen der Erde, insbesondere die polaren Regionen, anhand der Oxidation von Bromid mit Ozon in wohldefinierten Laborexperimenten.

Angesichts der Bedeutung von Halogenen in der polaren Chemie wurden diese Reaktionen bereits sehr detailliert untersucht, auch an der Luft–Eis–Oberfläche und in Aerosolen. Daher wurde dieses System hier als Modellsystem ausgewählt, um die Chemie in den Schneekompartimenten besser zu verstehen. Dabei wurde der Schwerpunkt darauf gelegt die Bedingungen in der Umwelt im Labor besser nachzuahmen indem die Komplexität der verwendeten Laborproben erhöht wurde. Das allgemeine Interesse an der Halogenchemie beruht auf ihrer wesentlichen Auswirkung auf die oxidative Kapazität polarer Atmosphären und auf der Rolle von Halogenen auf das Schicksal einer Reihe von Verbindungen in der Atmosphäre aufgrund der Bildung von reaktiven Halogenspezies (RHS). Von besonderer Bedeutung sind die Auswirkungen auf Quecksilber in der Gasphase, das durch RHS oxidiert wird was zu einer erhöhten Ablagerung von Quecksilber im Schnee mit Auswirkungen auf das Ökosystem und die menschliche Gesundheit führt.

Meerwassersprühnebel sind in polaren Küstenumgebungen allgegenwärtig. In dieser Arbeit wurde die Auswirkung der Temperatur auf deren Reaktivität, insbesondere in dem für die

ZUSAMMENFASSUNG

polaren Gebiete relevanten Temperaturbereich von 0 °C bis –25 °C, mit einem beschichteten Flussreaktor untersucht. Um die Relevanz für die polare Umgebung zu erhöhen, wurden in dieser Studie Mischungen organischer Spezies mit Meersalz–Proxies verwendet. Die Ergebnisse lassen sich wie folgt zusammenfassen. Mit Abnahme der Wasseraktivität und mit der Erhöhung der Aktivität des gelösten Stoffes, beides aufgrund der Temperaturabnahme, wurde eine verminderte Löslichkeit des reaktiven Gases (in diesem Fall Ozon) gefunden; zudem nahm in Gegenwart von organischen Stoffen die Viskosität signifikant zu, was zu einer starken Abnahme der Diffusion führte. Die verringerte Löslichkeit von Ozon und die verringerte Diffusionsfähigkeit der reaktiven Spezies führten zu einer verminderten Reaktivität, und dies trotz der Erhöhung der Aktivität von Bromid bei niedrigeren Temperaturen. Dies ist ein wichtiger und etwas überraschender Befund, da die Viskosität von organischen Stoffen üblicherweise bei viel niedrigeren relativen Feuchten und Temperaturen in den Atmosphärenwissenschaften diskutiert wird. Diese Arbeit veranschaulicht die Rolle von organischen Stoffen bereits bei moderaten Temperaturen und relativ hoher Luftfeuchtigkeit, wie sie typischerweise in Oberflächenschnee und arktischem Aerosol vorkommen. Desweiteren wurde der molekulare Mechanismus dieser Reaktion untersucht und erstmals ein Oberflächen–Intermediat (BrOOO^-) identifiziert. Dessen Anwesenheit an der Luft–Wasser–Oberfläche klärt die seit langem offene Frage, warum die Oberflächenchemie dieser Reaktion so schnell abläuft. Die für die Oberflächenreaktion relevanten Parameter wurden bestimmt; die Temperaturabhängigkeit des Verteilungskoeffizienten von BrOOO^- und der Oberfläche (K) wurde parametrisiert und die maximale Oberflächenbedeckung der Grenzflächenspezies wurde quantifiziert (10^{12} Moleküle/cm²). Diese Studie führte zu der Schlussfolgerung, dass dieser Oberflächenprozess für die Bromidoxidation in Aerosolen aus Meerwassersprühnebel bei umweltrelevanten Ozonkonzentrationen von großer Bedeutung ist.

Die obigen Experimente teilt eine entscheidende Einschränkung mit den meisten – wenn nicht allen – Studien an Eis und Schnee: Die gefrorene Phase befindet sich im thermodynamischen Gleichgewicht. In der Natur ist dies jedoch selten der Fall und Eis oder Schnee wachsen oder verdampfen häufig. Daher wurde in dieser Arbeit der Effekt der Schneemetamorphose auf die Umverteilung von Bromidionen im Schnee und die auf die Reaktivität in Zusammenarbeit mit Schneephysikern untersucht. Die vorläufige Bewertung der Ergebnisse dieser Studie zeigte, dass nach 12 Tagen Metamorphose mit einem Temperaturgradienten, der typischerweise im polaren Schnee auftritt, die Reaktivität signifikant abnahm. Dieses Ergebnis zeigt, dass Bromid möglicherweise in die Eiskörner während der Metamorphose eingebaut wurde und dass der Austausch zwischen den einzelnen Schneekompartimenten häufig ist und grosse Auswirkungen auf die Reaktivität hat.

Zusammenfassend war in diesen Laborexperimenten die Komplexität der untersuchten Proben und Prozesse signifikant erhöht worden. Um die Vorteile von Laborexperimente voll

ZUSAMMENFASSUNG

auszunutzen, waren die experimentellen Bedingungen jedoch immer noch gut definiert. In einer Feldstudie vom 12. Januar bis zum 23. Februar 2018 in Kalamazoo, Michigan, USA, wurde die Chemie im Schnee in seiner vollen Komplexität untersucht. Die Gasphasenkonzentrationen von Ammoniak (NH_3), Schwefeldioxid (SO_2), und Salpetersäure (HNO_3) sowie die $\text{PM}_{2.5}$ -Konzentrationen von Ammonium (NH_4^+), Sulfat (SO_4^{2-}) und Nitrat (NO_3^-) wurden gemessen. Beobachtungen zeigten, dass $\text{PM}_{2.5}$ -Episoden während schneebedeckten Perioden stärker waren. Als Grund wurden eine stabilere atmosphärische Grenzschicht und eine hohe relative Feuchte identifiziert. Offenbar ist Schnee eine signifikante Quelle von Wasserdampf für die Partikelbildung und das Partikelwachstum. Es gab eine starke Auswaschung von atmosphärischem Ammoniak während Schneefallepisoden, was zu hohen Konzentrationen von Ammoniak und zu einem hohen pH-Wert in Oberflächenschnee führte, der während dieser Studie entnommen wurde. Diese Studie zeigte auch eine hohe Temperaturabhängigkeit der Ammoniakkonzentrationen im Schnee. Aus dieser Temperaturabhängigkeit schätzen wir die Enthalpie der Ammoniakverflüchtigung auf 50 ± 6 kJ/mol. An schneebedeckten Tagen wurde eine stärkere Temperaturabhängigkeit gefunden, was darauf hindeutet, dass Oberflächenschnee eine – temperaturabhängige– Quelle von Ammoniak im Winter sein könnte. Die Ergebnisse dieser Kampagne erweitern den Datensatz über die Zusammensetzung der Atmosphäre im städtischen Winter, für die bisher nur wenige Studien durchgeführt wurden.

Diese Arbeit trägt daher zum besseren Verständnis der Chemie in Schnee– und kaltem Aerosol und insbesondere zur Ozonreaktion mit Bromid bei: der Oberflächenprozess und die Temperaturabhängigkeit dieser Reaktion sowie die Verteilung von Bromid zwischen der Oberfläche und dem Inneren des Eises während der Schneemetamorphose.

Towards understanding chemistry in cold regions

1.1 Introduction

The Earth's cryosphere includes all of the Earth's environmental ice compartments. Some of these are snow covered regions of the world including seasonal snow coverage, sea ice, stratospheric ice clouds, frozen lakes and rivers, glaciers, and geologic ice (Robinson *et al.*, 1993; Grannas *et al.*, 2013). The cryosphere plays a significant role in the Earth's energy balance, global atmospheric circulation, and climate, including that through the albedo effect (Domine and Shepson, 2002; Grannas *et al.*, 2013). In addition, the cryosphere is a large reservoir of Earth's water holding about 75% of the Earth's freshwater (Grannas *et al.*, 2013); this indicates significant roles in the water cycle, and in biological, chemical, and geological processes (Robinson *et al.*, 1993).

In addition to the cryosphere's role in the Earth's function, the cryosphere serves as a reliable archive of the Earth's historical atmospheric composition and climate (Alley, 2010). In persistently cold places, compounds in the atmosphere, deposited on and trapped in snow, may be preserved. The concentrations of the compounds in the snow are related to the concentrations in the air mass over the snow field containing compounds, which may be produced locally and/or brought in by long-range transport (Alley, 2010). These compounds get trapped in the snow and are isolated from most post-depositional losses as the snow gets converted to firn and to ice with compaction and densification over time (Bartels-Rausch *et al.*, 2012). During this conversion from snow to firn and ice, atmospheric gases in pore spaces may also be trapped in gas bubbles in the ice (Bartels-Rausch *et al.*, 2012). These compounds in the ice and in the entrapped gas bubbles such as CO₂, N₂O, methane,

Chapter 1 Towards understanding chemistry in cold regions

and isotopic signatures of hydrogen and oxygen *via* enrichment in ^{18}O and deuterium provide useful information of historical climate and atmospheric pollution (Alley, 2010).

Compounds, whose concentrations in snow are strongly affected by post-depositional processes, will not give true representation of their past atmospheric concentrations in ice archives (Röthlisberger *et al.*, 2000). For instance, nitrates are subject to both evaporative (thermal) and reactive post-depositional losses (photochemistry) with implications on the concentrations observed in ice archives (Röthlisberger *et al.*, 2000; Blunier, 2005; Erbland *et al.*, 2013). To address challenges with reactive compounds, stable isotopes and fractionation of isotopes with processing of these compounds may be useful (Blunier, 2005; Erbland *et al.*, 2015). In the case of nitrate photochemistry, studies have provided model parameterizations that may be able to predict isotope ratios of nitrogen and oxygen, which may indicate the extent of photochemical processing of nitrate deposited on snow and improve estimates of past concentrations (Blunier, 2005; Erbland *et al.*, 2015).

1.1.1 The cryosphere and the fate of contaminants

The interaction between the cryosphere and the atmosphere begins in the atmosphere with uptake of compounds in the atmosphere during cloud and ice formation. Contaminants emitted into the atmosphere as gases or aerosols and atmospheric trace gases undergo reactions in the atmosphere. These compounds and the products of reactions in the atmosphere may be scavenged during atmospheric ice formation as cloud droplet condensation nuclei or ice nuclei or taken up during riming or adsorbed on existing ice surfaces, and deposited with snow (Barrie, 1985; Mitchell and Lamb, 1989; Bergin *et al.*, 1995; Domine and Shepson, 2002; Grannas *et al.*, 2013). Note that reactions may also occur on ice in the atmosphere (Barrie, 1985). There is also the occurrence of dry deposition of gases and particles on and into a snowpack driven by impaction, adsorption, diffusion and wind pumping (Barrie, 1985; Mitchell and Lamb, 1989; Bergin *et al.*, 1995; Domine and Shepson, 2002; Grannas *et al.*, 2013).

The scavenging of compounds by snowfall and the concentration of compounds deposited with snowfall depend on the concentration of these compounds present in the atmosphere (Barrie, 1985; Grannas *et al.*, 2013). Scavenging also depends on the partitioning properties of the trace gases between the gas phase and the snow (Barrie, 1985; Grannas *et al.*, 2013). For aerosols, scavenging depends on the scavenging efficiency, the cloud condensation potential and ice nucleation potential of aerosol particles in the atmosphere (Barrie, 1985; Grannas *et al.*, 2013). Importantly also, the amount of snowfall (or precipitation) influences the concentration of both gases and aerosols deposited on the ground; high amount of snowfall dilutes the concentration deposited (Barrie, 1985; Grannas *et al.*, 2013).

Snow on sea ice and over other frozen water bodies may also receive contaminant input from the water bodies. For instance, sea spray aerosol and sea spray may deposit salts on snow over sea ice (Abbatt *et al.*, 2012). In addition, during freezing of sea ice, salt and organics are excluded as high concentration and high salinity brine cells in the ice (Lake and Lewis, 1970). With ice growth, strain is induced within the ice structure from differential thermal expansion between the ice and brine cells (Lake and Lewis, 1970; Ehn *et al.*, 2007). This strain leads to the formation of channels within the ice through which brine drains downward into the underlying ice or upward to the surface depending on the porosity of the surface ice (Lake and Lewis, 1970; Ehn *et al.*, 2007). Young sea ice is also mushy at the air–ice interface with mixtures of ice and pools of sea water or brine (Ehn *et al.*, 2007; Worster and Rees Jones, 2015) and may be a source of salinity to snow deposited on the surface (Abbatt *et al.*, 2012).

Compounds in the snowpack may undergo post–depositional processes and release to the atmosphere with impacts on atmospheric composition (Domine and Shepson, 2002; Bartels–Rausch *et al.*, 2012; Grannas *et al.*, 2013). Post depositional processes could be desorption and volatilization from the snow, incorporation in the snow grains with ice growth and movement of water vapor in the snowpack, reactions in the snow and release by diffusion and wind pumping back into the atmosphere, transport with meltwater (Grannas *et al.*, 2013). Reactions in the snow may occur on the surface of the snow grains, in the grain boundaries, in pore spaces and brine (Domine and Shepson, 2002). These post–depositional loss processes indicate that snow is not a permanent sink for some environmental contaminants. Loss processes lead to changes in the concentrations in the snow and in the atmosphere.

With focus on interaction with the atmosphere, Domine and Shepson (2002) provided an overview of impacts of the cryosphere on atmospheric composition showing that for some compounds, the concentrations measured over snow covered areas differed significantly from that predicted from gas phase chemistry alone. For instance, nitrate photochemistry in snow leads to higher concentration of NO_x than predicted from gas phase chemistry (Röthlisberger *et al.*, 2000; Domine and Shepson, 2002). Another important reaction especially in polar regions close to sea ice is halide oxidation initiated in halide containing snow, sea–spray aerosol, and brine. This halide oxidation leads to higher concentrations of reactive halogen species, lower concentrations of ozone, and lower concentrations of gas phase mercury (Barrie *et al.*, 1988; Domine and Shepson, 2002; Nerentorp Mastromonaco *et al.*, 2016).

The location of contaminants in the snowpack plays a key role on their availability for reaction or exchange with the atmosphere. Snow is a porous medium with low density (Domine *et al.*, 2002) comprising of solid, liquid, and gas phases. In snow, compounds may be adsorbed on the surface of snow grains and then incorporated into the ice forming a solid solution with the ice (Thibert and Domine, 1998; Hullar and Anastasio, 2016). Such

Chapter 1 Towards understanding chemistry in cold regions

incorporation depends on the solubility limit of the compounds in crystalline ice and the concentration present (Thibert and Domine, 1998; He *et al.*, 2016; Wu *et al.*, 2017). At higher concentrations, compounds may be adsorbed on the surface or dissolved in the disordered interface, which forms on the ice surface (Abbatt, 2003) or incorporated in micropockets in the ice (Hullar and Anastasio, 2016). Some compounds with low solubility limit in ice would be predominantly present in the grain boundaries and/or adsorbed on the surface such as sulfate (Mulvaney *et al.*, 1988). In the pore spaces, which may contain interstitial air or liquid water depending on temperature, compounds may also be present depending on the partitioning properties of the compounds to ice (Bartels–Rausch *et al.*, 2012; Grannas *et al.*, 2013). Compounds on the surface or near the surface and in pore spaces are more likely to be exposed to reactive gases and to loss processes such as diffusion and wind pumping and to exchanges with the atmosphere.

In addition, the release of compounds to the atmosphere depends on the properties of the snow such as the specific surface area (SSA), the density and porosity of the snowpack, the permeability of the snow to fluids. The SSA is the surface area relevant for adsorption, evaporative loss and reactivity of contaminants located on the surface of snow grains in the snowpack. SSA is often measured as surface area per gram of snow (cm^2/g). Snow generally has high SSA ranging from about $1500 \text{ cm}^2/\text{g}$ for dendritic snow to about $125 \text{ cm}^2/\text{g}$ for depth hoar (Domine *et al.*, 2002). The density of snow provides information on the packing of the snow. Snow generally has low density ranging from about $0.01 \text{ g}/\text{cm}^3$ for fresh dendritic snow to $0.35 \text{ g}/\text{cm}^3$ for wind packed snow (Domine *et al.*, 2002). The porosity of snow is the fraction of the snowpack that is air or pore space. The low density of snow implies that snow also has relatively high porosity. Permeability provides an indication of how freely gases and liquids move through the snowpack, that is, the connectivity of the pores (Domine *et al.*, 2008).

The transport of gases through a snowpack and exchange with the atmosphere depend on the amount of pore spaces and pore size and shape (tortuosity), and the air permeability of the snowpack (Domine *et al.*, 2008). If the pores are poorly connected (having low permeability), interruptions in the flow of gases by diffusion or advection through the snow column will not permit compounds produced *via* reactions in the snow pack or desorption to be released to the atmosphere (Domine *et al.*, 2008). Transport from the atmosphere to the snow may also be hampered.

With knowledge of the transformation of snow to firn and ice with time, one can deduce that the properties of snow are not stagnant. The process of change in the physical structure of snow over time is referred to as metamorphism. This process is driven by the movement of water molecules resulting in the restructuring of snow grains (Colbeck, 1983). Metamorphism could be wet metamorphism, involving the movement of liquid water, or

dry metamorphism without the movement of liquid water. For the purpose of the thesis, the discussion on metamorphism will focus on dry metamorphism.

Colbeck (1983) presented the theory behind snow metamorphism in detail. In summary (for dry metamorphism), dry metamorphism could be isothermal (also known as equi-temperature metamorphism, ET) or temperature gradient induced metamorphism (TGM). TGM involves an external temperature gradient resulting in a large water vapor gradient with higher vapor pressure at the region of higher temperature. This gradient drives the flux of water vapor from the high temperature region to the lower temperature region. TGM results in the formation of faceted snow grains. ET does not involve an external temperature gradient, but there are small temperature gradients in the snowpack due to the curvature of the grains. These small temperature gradients induce water vapor pressure gradients leading to the flux of water vapor. ET results in the formation of more rounded and uniform grains. Alternating temperature gradients often observed in the field, though TGM, also result in more rounded grains (Pinzer and Schneebeli, 2009)

The changes in snow structure due to metamorphism have been well investigated (Sommerfeld and LaChapelle, 1970; Colbeck, 1983; Pinzer *et al.*, 2012). This information is of importance due to relevance for avalanche prediction (Schweizer, 2014). As snow metamorphism changes the physical structure of the snow grains, it also changes the aforementioned properties of the snowpack. Studies show that both TGM and ET significantly reduces the SSA of snow with faster reductions at warmer temperatures (Domine *et al.*, 2002; Domine *et al.*, 2008). Pinzer *et al.* (2012) showed that at a temperature gradient of 50 K/m, a column of snow could have a complete turnover of the snow grains within 48 to 72 hours.

To a much lower extent, some studies have considered the effect of metamorphism on the chemical composition of the snowpack and reactivity in the snowpack. Studies have investigated the effect of ice growth on the partitioning of trace gases and their uptake on snow and ice (Thibert and Domine, 1997; Ullerstam and Abbatt, 2005; Hoog *et al.*, 2007). Hoog *et al.* (2007) and Ullerstam and Abbatt (2005), for instance, observed higher uptake of ammonia and nitric acid, respectively, in growing ice than in static ice. This may be due to incorporation in the growing crystals as with scavenging of atmospheric trace gases with riming (Hoog *et al.*, 2007). However, due to poorly defined growth rates or too little range of growth rates, one cannot ascertain the dependence of the uptake of these gases on ice growth rate. Recent advances in snow physics, which accurately establish the growth rate of snow crystals (e. g., Pinzer *et al.*, 2012), in combination with the sensitive analytical methods established in ice core research (e. g., Osterberg *et al.*, 2006) may be able to answer this key question in atmospheric research.

In addition to effect on uptake of contaminants, the changes in the surface area and density with ageing of snow also impact the release of compounds to the atmosphere. Domine *et al.*, in their laboratory studies on the adsorption of phenanthrene in natural snow with different

Chapter 1 Towards understanding chemistry in cold regions

SSAs showed that higher adsorption in samples with higher SSA than on samples with lower SSA. Laboratory study of the release of scavenged mercury from snow also showed a strong relationship between ageing and the release of gas phase mercury (GEM) with higher GEM release from aged snow (Mann *et al.*, 2011). This was attributed to effects of reduced surface area on the partitioning to the gas phase (Mann *et al.*, 2011). Field studies have made similar observations with higher density snow having lower concentrations of polychlorinated biphenyls (PCBs) than low density snow. These studies indicate that the ageing of snow may reduce the storage capacity of compounds in snow (Domine *et al.*, 2007; Grannas *et al.*, 2013). Laboratory studies also show that the surface area and density evolution of snow with metamorphism impacts the effective diffusion of gases such as HONO, which interact with the ice surface in snow (Pinzer *et al.*, 2010).

Metamorphism involves the movement of water vapor, which leads to turnover and recrystallization of ice (Pinzer and Schneebeli, 2009; Pinzer *et al.*, 2012). This redistribution of water molecules may also be coupled with the redistribution of ions and molecules adsorbed or trapped in snow (Cragin *et al.*, 1996). There is limited research investigating the redistribution of ions with ageing.

Elution studies on inorganic ions in the field and in laboratories give an indication of the distribution of ions in the snowpack. One should note that samples in the field may have also undergone wet metamorphism, and natural elution with melt water may also induce wet metamorphism. In elution studies, ions which are exposed in the grain boundaries, pore spaces, and on the surface of snow grains would be eluted first. The redistribution of ions in snow exposed to metamorphism is dependent on the solubility limit of the ions in ice (Cragin *et al.*, 1996). For example sulfate, which has low solubility in ice, redistributed to the surface and eluted first (Brimblecombe *et al.*, 1985; Brimblecombe *et al.*, 1988; Mulvaney *et al.*, 1988; Davis *et al.*, 1995). Ions which are more soluble such as ammonium, bromide, chloride would be incorporated in the bulk of the ice, may form solid solutions with the ice (Thibert and Domine, 1998; Wu *et al.*, 2017), or be incorporated in micropockets and bubbles in the ice (Hullar and Anastasio, 2016). As with elution, the more exposed ions are also more likely to be available for reactions than those buried.

The rate of snow metamorphism in the field depends on meteorological factors such as temperature and wind speed (Colbeck, 1983). Metamorphism is faster at warmer temperatures than at lower temperatures (Domine *et al.*, 2008). In addition to effects on the metamorphism on snow, meteorology also plays an important role in atmospheric chemistry in cold environments. High elevation or alpine regions often have high winds which reduce the accumulation rate of snow. High wind velocities also mean stronger wind pumping and increased exchange with the atmosphere (Baltensperger *et al.*, 1993). At high elevation, concentration of deposited compounds is strongly related to in-cloud scavenging (Baltensperger *et al.*, 1993).

Wintertime meteorology in temperate regions is marked by low temperatures and low boundary layer height, and low winds (Stanier *et al.*, 2012). The stable and low boundary layer height in these regions during this period leads to accumulation of contaminants emitted into the atmosphere. In polar regions, strong winds may be present though low winds persist for most of the year (Domine *et al.*, 2002). With polar sunrise, photochemistry contributes significantly to the atmospheric composition. As a result, the accumulation of contaminants persists into the polar spring and early summer (Barrie and Hoff, 1985). Also, due to low temperatures in the arctic, metamorphism is slower with overall high SSA including at depth hoar level; densification is mostly driven by wind compaction (Domine *et al.*, 2007). As a result, arctic snow has a higher potential for adsorption of compounds as well as higher SSA, for reactivity, than subarctic snow (Domine *et al.*, 2007).

Snow also plays an important role in wintertime urban atmospheric composition. There are a few field campaigns investigating wintertime atmospheric composition in urban areas (e. g., Stanier *et al.*, 2012; Green *et al.*, 2015). Some of these studies have observed strong relationships between the presence of snow cover and concentrations of particles with aerodynamic diameter less than or equal to 2.5 μm (Stanier *et al.*, 2012; Green *et al.*, 2015). While snow scavenges contaminants from the atmosphere, these contaminant may be re-emitted with sublimation and evaporation (Stanier *et al.*, 2012). This release to the atmosphere has significant implications for human health as studies have observed concentrations of atmospheric contaminants higher than air quality standards during wintertime in some urban areas (Chen *et al.*, 2012).

Pooling the above discussion together, one realizes that snow is a reactive and dynamic environmental system with impacts on atmospheric composition. This also has potential implications for human and environmental health. The properties of snow, which affect its potential to impact the atmosphere, are constantly changing with snow metamorphism. There have been studies investigating various aspects of snow properties, reactivity in snow, and implications on atmospheric composition. However, the connection between changing snow properties due to metamorphism, changes in the distribution of compounds trapped in snow due to vapor flux during metamorphism, and the effects on reactivity of these compounds is not well established. This leads me to the thesis mission below.

1.2 Thesis mission

The mission of this thesis was to investigate an environmental reaction process relevant to cold regions while probing the role of snow in atmospheric composition and the effects of metamorphism on the redistribution of ions and observed chemistry in snow. This thesis is part of a larger project investigating the effects of metamorphism on the fate of impurities in snow and ice with relevance to glacier ice and sea ice, and ice core research.

Work on this thesis acted on the above mission *via* the following subprojects:

- I. Investigation of a reaction known to occur in snow and ice (bromide oxidation by ozone);
 - a. the kinetics of this reaction, and
 - b. the effects of the properties of the reactant environment on the observed reaction kinetics
- II. Investigation of wintertime atmospheric composition in an urban setting, and the role of snow
- III. Investigation of the role of metamorphism on bromide distribution and the reactivity in snow

Below, I will briefly discuss the proxy reaction, potential effects of the reactive medium on reactivity, and the outline of the thesis.

1.2.1 The Reaction: Halogen activation in the lower atmosphere

My reaction of focus for investigating chemical reactivity in snow is the reaction of ozone (O_3) with bromide (Br^-). This is one of the initiating reactions in halogen activation. Halogen activation and its involvement in ozone depletion was initially investigated with relevance to the stratospheric O_3 ozone depletion and ozone hole (Simpson *et al.*, 2007). But the focus of this thesis is on ozone depletion in the lower atmosphere, that is, with relevance to tropospheric or marine boundary layer ozone concentrations. In the lower atmosphere, the sources of halides, the propagation of this reaction, the wavelength for the photocatalytic ozone depletion, the lifetime of reactive species are different from stratospheric halogen activation (Abbatt *et al.*, 2012).

First observation of this tropospheric ozone driven halogen activation was *via* observations of high concentrations of reactive bromine species during the Polar Spring in the Arctic which coincided with lows in ozone concentration (Barrie *et al.*, 1988). These events of low ozone concentration with high reactive halogen concentration (bromine concentration) are referred to as bromine explosion or ozone depletion events (ODEs). Observations of such ODEs often coincided with polar sunrise, an indication of a photocatalytic process (Simpson *et al.*, 2007, and references therein). However, there is also the occurrence of ozone reaction with halides in the dark producing photo-labile reactive species (Oum *et al.*, 1998; Nerentorp Mastromonaco *et al.*, 2016). These photo-labile species then propagate a photocatalytic process with sunrise leading to ODEs (Nerentorp Mastromonaco *et al.*, 2016).

Observation of ODEs and bromine explosions were made in areas close to sea ice especially in areas with young sea ice, with availability of high salt concentrations in brine (Simpson *et al.*, 2007; Abbatt *et al.*, 2012; Bartels–Rausch *et al.*, 2014). Other important sources of halides in the lower atmosphere include sea spray aerosols, salty snow, and brine pools around salt lakes (Hebestreit *et al.*, 1999; Simpson *et al.*, 2007; Abbatt *et al.*, 2012). Snow on

sea ice may also obtain salinity through seepage of salty seawater through the ice and through deposition of sea spray aerosol (Simpson *et al.*, 2007; Abbatt *et al.*, 2012).

This reaction between ozone and halides is a multiphase process consisting of several reaction steps and involving ozone in the gas phase reacting with halides in the condensed phase. The mechanism of this reaction system in the dark is presented along with the kinetics studies in Chapter 2 and Chapter 3. In the case of bromide, Br₂, which is photo-labile, is the product of these dark phase reactions.

Tropospheric ODEs and halogen activation gained a lot of attention because of the impacts on the oxidation capacity of the atmosphere. Ozone is one of the main oxidants in the lower atmosphere with impact on atmospheric composition, health, and climate (Simpson *et al.*, 2007). Halogen activation leads to an increase in concentration of reactive halogen species (RHS), which participate in O₃ destroying chemical cycles. Recent improvement in global atmospheric chemistry models indicate that halogen chemistry is responsible for about 14% of the global tropospheric O₃ reduction (Schmidt *et al.*, 2016). In addition, RHS are also potent oxidants (Simpson *et al.*, 2007). These RHS oxidize other compounds in the atmosphere such as organics and, of particular interest, gas phase mercury, Hg⁰ (Simpson *et al.*, 2007; Simpson *et al.*, 2015). Oxidized mercury partitions more readily into condensed phases; this may lead to increased deposition of mercury in snow and water bodies (Nerentorp Mastro Monaco *et al.*, 2016). As a result, halogen activation may have implications for human and environmental health.

1.2.2 The reactive medium and effects on reactivity

The aforementioned environmental halide sources (sea-spray aerosol, sea-ice, and salty snow, and the ocean, salt lakes) are composed of more than just salts and water. These compartments may have significant amounts of organics. Sea-spray aerosol has been shown to contain high concentrations of organics depending on the biological activity of their origin, sometimes more than 30% of the mass fraction of aerosol (O'Dowd *et al.*, 2004; Bertram *et al.*, 2018). Sea ice brine also contains significant amount of organics, also dependent on biological activity in the vicinity (Papadimitriou *et al.*, 2007), so also, other environmental ices (Antony *et al.*, 2011; McNeill *et al.*, 2012; Legrand *et al.*, 2013). In other words, halide sources contain mixtures of salts and organics.

Studies investigating halogen activation often work with simple binary or ternary solutions of inorganic salts and water. This reduces the complexity in interpreting kinetic observations, and allows for better control of experimental conditions. In inorganic salt mixtures, the concentrations and ratio of halides present, and the pH play important roles on the products formed in halogen activation (Behnke *et al.*, 1999; Fickert *et al.*, 1999). For instance, in a mixture of bromide and chloride, at higher ratios of bromide to chloride

Chapter 1 Towards understanding chemistry in cold regions

(1/600), Behnke et al observed the production of Br₂ only, while at 1/1000 bromide to chloride, they observed production of BrCl (Behnke *et al.*, 1999).

Studies have shown that the presence of organics may significantly affect reactivity in the bulk of a condensed phase. Organics affect the hygroscopic properties of aerosol particles including particle growth and water uptake (Reid *et al.*, 2011; Lienhard *et al.*, 2012; Reid *et al.*, 2018). Organics tend to be more viscous and form glassy solids at low relative humidity and temperature (Murray, 2008; Marshall *et al.*, 2016). Such high viscosity in systems with organics results in lower diffusivity compared to systems without the organic species with implications on reactivity (Steimer *et al.*, 2015; Marshall *et al.*, 2016). While these facts have been elaborated already for atmospheric aerosols, the implications of these microphysical changes for the high relative humidity but low temperature environments of liquid phases in equilibrium with ice have not been addressed so far.

There have been studies investigating the chemical aspects of how organics affect halide oxidation in organic/inorganic mixtures (Behnke *et al.*, 1999; Hayase *et al.*, 2011; Lee *et al.*, 2015). In their study of iodide oxidation by ozone in solutions containing organic acids, Hayase *et al.* (2011) observed an enhancement of interfacial oxidation of iodide in the presence of surface active organic acids. As the reaction of halides with ozone is enhanced at low pH, Hayase *et al.* (2011) attributed this increased reactivity to an increase in H⁺ concentration at the interface due to the surfactant behavior of the organic acids. Lee *et al.* (2016) also observed enhanced bromide oxidation in the presence of citric acid. Behnke *et al.* (1999) observed the oxidation of hydrocarbons by products of halogen activation (Br and Cl radicals), which resulted in the formation of organic acids. These produced organic acids decreased the pH of their reactive medium, accelerating the formation of halogen radicals. Some organic acids were also a sink to the halogen radicals formed, slowing down the catalytic reactions in the halogen activation process (Behnke *et al.*, 1999).

Studies investigating halogen activation in organic/inorganic mixtures have often not considered the physical properties (viscosity, for instance) of their reaction matrix. We know that organics are involved in the reactivity. We also know that the presence of organics has implications on the physicochemical properties of the reactive medium. What we do not fully understand is how these bidirectional feedbacks between microphysical and chemical properties affect the extent of halogen activation. Another factor often missing in these studies is the role of temperature, which may be important especially due to the relevance of halogen activation in colder climates.

1.3 Thesis outline

The mission of this thesis has been outlined above. Below, I present a summary of the following chapters, highlighting the outcomes.

Chapter 2 presents investigations of the kinetics of bromide reaction with ozone in a bromide–water binary system at about 1 °C. The focus of this study was to understand the interfacial processes involved in the bromide oxidation reaction. Such interfacial processes are important for high surface area systems such as sea spray aerosol. This was a joint project involving three different research methods. One method included liquid jet x–ray photon spectroscopy measurements probing the interface. Through this method, the interfacial species relevant for the surface process was identified, BrOOO[−]. The second research method was theoretical calculations, which provided information on the energetics of the reaction. And the third method, a laboratory kinetics study, linked information from the other experimental methods with observations. The coherence of the three research methods allowed for more convincing conclusions on the importance of the interfacial process.

Chapter 3 builds up on the work presented in Chapter 2 by increasing the complexity of the reactive medium. In Chapter 3, we extend the parameterization developed in Chapter 2 to include an organic species and extended the conditions to a wider temperature range (16 °C to −25 °C). We paid particular attention to changes in the reactive medium with temperature and the effects on the observed kinetics. This study extends the relevance of the kinetics study in Chapter 2 to sea spray aerosol exposed to different temperatures in long range transport and to brine on snow and ice.

Leaving the laboratory, in Chapter 4, we present observations of how snow interacts with atmospheric composition in an urban area. This chapter presents a field campaign at Kalamazoo, Michigan during the winter of 2018. Atmospheric concentrations of trace gases, NH₃, SO₂, and HNO₃, and PM_{2.5} concentrations of NH₄⁺, SO₄^{2−}, and NO₃[−] were measured. We observed a temperature dependent release of NH₃ related to the presence of snow cover. This is a notable observation that is presently not considered in ammonia emissions inventory. Further investigations are however needed to confirm this observation.

Chapter 5 presents ongoing research on the role of snow metamorphism on reactivity in snow. This work investigates the already characterized bromide reaction with ozone (Chapter 2 and 3) in doped artificial snow that has been exposed to a temperature dependent gradient (temperature gradient metamorphism). This chapter includes computer tomography (CT) measurements of the snow properties (specific surface area and density) and preliminary analysis of kinetics observations. Preliminary results indicate that bromide may be buried with the movement of water vapor due to temperature induced metamorphism. Conclusions from this work could aid understanding of the reactivity and release of trace gases and contaminants from snow, that is, the source and sink qualities of snow.

Bibliography

Abbatt, J. P.: Interaction of Atmospheric trace gases with ice surfaces: Adsorption and reaction, *Chemical Review*, 103, 4783 – 4800, 2003.

Abbatt, J. P. D., Thomas, J. L., Abrahamsson, K., Boxe, C., Granfors, A., Jones, A. E., King, M. D., Saiz-Lopez, A., Shepson, P. B., Sodeau, J., Toohey, D. W., Toubin, C., von Glasow, R., Wren, S. N., and Yang, X.: Halogen activation *via* interactions with environmental ice and snow in the polar lower troposphere and other regions, *Atmos Chem Phys*, 12, 6237–6271, 10.5194/acp-12-6237-2012, 2012.

Alley, R. B.: Reliability of ice-core science: historical insights, *Journal of Glaciology*, 56, 1095–1103, 2010.

Antony, R., Mahalinganathan, K., Thamban, M., and Nair, S.: Organic carbon in Antarctic snow: spatial trends and possible sources, *Environ Sci Technol*, 45, 9944–9950, 10.1021/es203512t, 2011.

Baltensperger, U., Schwikowski, M., Gäggeler, H. W., Jost, D. T., Beer, J., Siegenthaler, U., Wagenbach, D., Hofmann, H. J., and Synal, A.: Transfer of atmospheric constituents into an alpine snow field, *Atmospheric Environment*, 27A, 1881–1890, 1993.

Barrie, L. A.: Scavenging ratios, wet deposition, and in-cloud oxidation: An application to the oxides of sulphur and nitrogen, *Journal of Geophysical Research*, 90, 5789–5799, 1985.

Barrie, L. A., and Hoff, R. M.: Five years of air chemistry observations in the Canadian Arctic, *Atmospheric Environment*, 19, 1995–2010, 1985.

Barrie, L. A., Bottenheim, J. W., Schnell, R. C., Crutzen, P. J., and Rasmussen, R. A.: Ozone destruction and photochemical reactions at polar sunrise in the lower Arctic atmosphere, *Nature*, 334, 138 – 141, 1988.

Bartels-Rausch, T., Bergeron, V., Cartwright, J. H. E., Escribano, R., Finney, J. L., Grothe, H., Gutierrez, P. J., Haapala, J., Kuhs, W. F., Pettersson, J. B. C., D., P. S., Sainz-Diaz, C. I., Stokes,

Bibliography

D. J., Strazzulla, G., Thomson, E. S., Trinks, H., and Uras–Aytemiz, N.: Ice structures, patterns, and processes: A view across the icefields, *Rev. Mod. Phys.*, **84**, 885–944, 2012.

Bartels–Rausch, T., Jacobi, H. W., Kahan, T. F., Thomas, J. L., Thomson, E. S., Abbatt, J. P. D., Ammann, M., Blackford, J. R., Bluhm, H., Boxe, C., Domine, F., Frey, M. M., Gladich, I., Guzmán, M. I., Heger, D., Huthwelker, T., Klán, P., Kuhs, W. F., Kuo, M. H., Maus, S., Moussa, S. G., McNeill, V. F., Newberg, J. T., Pettersson, J. B. C., Roeselová, M., and Sodeau, J. R.: A review of air–ice chemical and physical interactions (AICI): liquids, quasi–liquids, and solids in snow, *Atmos Chem Phys*, **14**, 1587–1633, 10.5194/acp–14–1587–2014, 2014.

Behnke, W., Elend, M., Krüger, U., and Zetzsch, C.: The influence of NaBr/NaCl ratio on the Br⁻ catalysed production of halogenated radicals, *Journal of Atmospheric Chemistry*, **34**, 87–99, 1999.

Bergin, M. H., Jaffrezo, J. L., Davidson, C. I., Dibb, J. E., Pandis, S. N., Hillamo, R., Maenhaut, W., Kuhns, H. D., and Makela, T.: The contributions of snow, fog, and dry deposition to the summer flux of anions and cations at Summit, Greenland, *Journal of Geophysical Research*, **100**, 16,275–216,288, 1995.

Bertram, T. H., Cochran, R. E., Grassian, V. H., and Stone, E. A.: Sea spray aerosol chemical composition: elemental and molecular mimics for laboratory studies of heterogeneous and multiphase reactions, *Chem Soc Rev*, **47**, 2374–2400, 10.1039/c7cs00008a, 2018.

Blunier, T.: Isotopic view on nitrate loss in Antarctic surface snow, *Geophysical Research Letters*, **32**, 10.1029/2005gl023011, 2005.

Brimblecombe, P., Tranter, M., Abrahams, P. W., Blackwood, I., Davies, T. D., and Vincent, C. E.: Relocation and preferential elution of acidic solute through the snowpack of a small, remote, high–altitude Scottish catchment, *Annals of Glaciology*, **7**, 141–147, 1985.

Brimblecombe, P., Clegg, S. L., Davies, T. D., Shooter, D., and Tranter, M.: The loss of halide and sulphate ions from melting ice, *Water Resources*, **22**, 693–700, 1988.

Chen, L. W. A., Watson, J. G., Chow, J. C., Green, M. C., Inouye, D., and Dick, K.: Wintertime particulate pollution episodes in an urban valley of the Western US: a case study, *Atmos Chem Phys*, **12**, 10051–10064, 10.5194/acp–12–10051–2012, 2012.

Colbeck, S. C.: Theory of metamorphism of dry snow, *Journal of Geophysical Research*, **88**, 5475 – 5482, 10.1029/JC088iC09p05475, 1983.

Bibliography

Cragin, J. H., Hewitt, A. D., and Colbeck, S. C.: Grain-scale mechanisms influencing the elution of ions from snow, *Atmos. Environ.*, 30, 171 – 208, 1996.

Davis, E. R., Petersen, C. E., and Bales, R. C.: Ion flux through a shallow snowpack: effects of initial conditions and melt sequences, *Biogeochemistry of seasonally snow-covered catchments (proceedings of a Boulder Symposium)*, 228, 115–126, 1995.

Domine, F., Cabanes, A., and Legagneux, L.: Structure, microphysics and surface area of the Arctic snowpack near Alert during ALERT 2000 campaign, *Atmospheric Environment*, 36, 2753–2765, 2002.

Domine, F., and Shepson, P. B.: Air-snow interactions and atmospheric chemistry, *Science*, 297, 1506–1510, 10.1126/science.1074610, 2002.

Domine, F., Cincinelli, A., Bonnaud, E., Martellini, T., and Picaud, S.: Adsorption of phenanthrene on natural snow, *Environ. Sci. Technol.*, 41, 6033 – 6038, 2007.

Domine, F., Albert, M., Huthwelker, T., Jacobi, H. W., Kokhanovsky, A. A., Lehning, M., Picard, G., and Simpson, W. R.: Snow physics as relevant to snow photochemistry, *Atmospheric Chemistry and Physics*, 8, 171–208, 2008.

Ehn, J. K., Hwang, B. J., Galley, R., and Barber, D. G.: Investigations of newly formed sea ice in the Cape Bathurst polynya: 1. Structural, physical, and optical properties, *Journal of Geophysical Research*, 112, 10.1029/2006jc003702, 2007.

Erbland, J., Vicars, W. C., Savarino, J., Morin, S., Frey, M. M., Frosini, D., Vince, E., and Martins, J. M. F.: Air-snow transfer of nitrate on the East Antarctic Plateau – Part 1: Isotopic evidence for a photolytically driven dynamic equilibrium in summer, *Atmospheric Chemistry and Physics*, 13, 6403–6419, 10.5194/acp-13-6403-2013, 2013.

Erbland, J., Savarino, J., Morin, S., France, J. L., Frey, M. M., and King, M. D.: Air-snow transfer of nitrate on the East Antarctic Plateau – Part 2: An isotopic model for the interpretation of deep ice-core records, *Atmospheric Chemistry and Physics*, 15, 12079–12113, 10.5194/acp-15-12079-2015, 2015.

Fickert, S., Adams, J. W., and Crowley, J. N.: Activation of Br₂ and BrCl *via* uptake of HOBr onto aqueous salt solutions, *Journal of Geophysical Research*, 104, 23719, 10.1029/1999jd900359, 1999.

Bibliography

Grannas, A. M., Bogdal, C., Hageman, K. J., Halsall, C., Harner, T., Hung, H., Kallenborn, R., Klán, P., Klánová, J., Macdonald, R. W., Meyer, T., and Wania, F.: The role of the global cryosphere in the fate of organic contaminants, *Atmos Chem Phys*, 13, 3271–3305, 10.5194/acp-13-3271-2013, 2013.

Green, M. C., Chow, J. C., Watson, J. G., Dick, K., and Inouye, D.: Effects of Snow Cover and Atmospheric Stability on Winter PM_{2.5} Concentrations in Western U.S. Valleys, *Journal of Applied Meteorology and Climatology*, 54, 1191–1201, 10.1175/jamc-d-14-0191.1, 2015.

Hayase, S., Yabushita, A., Kawasaki, M., Enami, S., Hoffmann, M. R., and Colussi, A. J.: Weak acids enhance halogen activation on atmospheric water's surfaces, *J Phys Chem A*, 115, 4935–4940, 10.1021/jp2021775, 2011.

He, Z., Xie, W. J., Liu, Z., Liu, G., Wang, Z., Gao, Y. Q., and Wang, J.: Tuning ice nucleation with counterions on polyelectrolyte brush surfaces, *Sci. Adv*, 2, 1–7, DOI: 10.1126/sciadv.1600345, 2016.

Hebestreit, K., Stutz, J., Rosen, D., Matveiv, V., Peleg, M., Luria, M., and Platt: DOAS measurements of tropospheric bromine oxide in mid-latitudes, *Science*, 283, 55–57, 1999.

Hoog, I., Mitra, S. K., Diehl, K., and Borrmann, S.: Laboratory studies about the interaction of ammonia with ice crystals at temperatures between 0 and –20 °C, *Journal of Atmospheric Chemistry*, 57, 73–84, 10.1007/s10874-007-9063-0, 2007.

Hullar, T., and Anastasio, C.: Direct visualization of solute locations in laboratory ice samples, *The Cryosphere*, 10, 2057–2068, 10.5194/tc-10-2057-2016, 2016.

Lake, R. A., and Lewis, E. L.: Salt rejection by sea ice during growth, *Journal of Geophysical Research*, 75, 583–597, 10.1029/JC075i003p00583, 1970.

Lee, M. T., Brown, M. A., Kato, S., Kleibert, A., Turler, A., and Ammann, M.: Competition between organics and bromide at the aqueous solution–air interface as seen from ozone uptake kinetics and X-ray photoelectron spectroscopy, *J Phys Chem A*, 119, 4600–4608, 10.1021/jp510707s, 2015.

Legrand, M., Preunkert, S., Jourdain, B., Guilhermet, J., Fan, X., Alekhina, I., and Petit, J. R.: Water-soluble organic carbon in snow and ice deposited at Alpine, Greenland, and Antarctic sites: a critical review of available data and their atmospheric relevance, *Climate of the Past*, 9, 2195–2211, 10.5194/cp-9-2195-2013, 2013.

Bibliography

Lienhard, D. M., Bones, D. L., Zuend, A., Krieger, U. K., Reid, J. P., and Peter, T.: Measurements of thermodynamic and optical properties of selected aqueous organic and organic–inorganic mixtures of atmospheric relevance, *J Phys Chem A*, 116, 9954–9968, 10.1021/jp3055872, 2012.

Mann, E., Meyer, T., Mitchell, C. P., and Wania, F.: Mercury fate in ageing and melting snow: development and testing of a controlled laboratory system, *J Environ Monit*, 13, 2695–2702, 10.1039/c1em10297d, 2011.

Marshall, F. H., Miles, R. E. H., Song, Y. C., Ohm, P. B., Power, R. M., Reid, J. P., and Dutcher, C. S.: Diffusion and reactivity in ultraviscous aerosol and the correlation with particle viscosity, *Chem Sci*, 7, 1298–1308, 10.1039/c5sc03223g, 2016.

McNeill, V. F., Grannas, A. M., Abbatt, J. P. D., Ammann, M., Ariya, P., Bartels–Rausch, T., Domine, F., Donaldson, D. J., Guzman, M. I., Heger, D., Kahan, T. F., Klán, P., Masclin, S., Toubin, C., and Voisin, D.: Organics in environmental ices: sources, chemistry, and impacts, *Atmos Chem Phys*, 12, 9653–9678, 10.5194/acp–12–9653–2012, 2012.

Mitchell, D. L., and Lamb, D.: Influence of riming on the chemical composition of snow in winter orographic storms, *Journal of Geophysical Research*, 94, 14831–14840, 1989.

Mulvaney, R., Wolff, E. W., and Oates, K.: Sulphuric acid at grain boundaries in Antarctic ice, *Nature*, 331, 247–249, 1988.

Murray, B. J.: Inhibition of ice crystallisation in highly viscous aqueous organic acid droplets, *Atmos. Chem. Phys*, 8, 5423 – 5433, 2008.

Nerentorp Mastromonaco, M., Gårdfeldt, K., Jourdain, B., Abrahamsson, K., Granfors, A., Ahnoff, M., Dommergue, A., Méjean, G., and Jacobi, H. W.: Antarctic winter mercury and ozone depletion events over sea ice, *Atmospheric Environment*, 129, 125–132, 10.1016/j.atmosenv.2016.01.023, 2016.

O'Dowd, C. D., Facchini, M. C., Cavalli, F., Cebrunis, D., Mircea, M., Decesari, S., Fuzzi, S., Yoon, Y. J., and Putaud, J.–P.: Biogenically driven organic contribution to marine aerosol, *Nature*, 431, 672–676, 10.1038/nature02970, 2004.

Osterberg, E. C., Handley, M. J., Sneed, S. B., Mayewski, P. A., and Kreutz, K. J.: Continuous ice core melter system with discrete sampling for major ion, trace element, and stable isotope analyses, *Environ. Sci. Technol.*, 40, 3344–3361, 10.1021/es052536w, 2006.

Bibliography

Oum, K. W., Lakin, M. J., and Finlayson–Pitts, B. J.: Bromine activation in the troposphere by the dark reaction of O₃ with seawater ice, *Geophys Res Lett*, 25, 3923–3926, 10.1029/1998gl900078, 1998.

Papadimitriou, S., Thomas, D. N., Kennedy, H., Haas, C., Kuosa, H., Krell, A., and Dieckmann, G. S.: Biogeochemical composition of natural sea ice brines from the Weddell Sea during early austral summer, *Limnol. Oceanogr.*, 52, 1809–1823, 2007.

Pinzer, B. R., and Schneebeli, M.: Snow metamorphism under alternating temperature gradients: Morphology and recrystallization in surface snow, *Geophysical Research Letters*, 36, 10.1029/2009gl039618, 2009.

Pinzer, B. R., Kerbrat, M., Huthwelker, T., Gäggeler, H. W., Schneebeli, M., and Ammann, M.: Diffusion of NO_x and HONO in snow: A laboratory study, *Journal of Geophysical Research*, 115, 10.1029/2009jd012459, 2010.

Pinzer, B. R., Schneebeli, M., and Kaempfer, T. U.: Vapor flux and recrystallization during dry snow metamorphism under a steady temperature gradient as observed by time–lapse micro–tomography, *The Cryosphere*, 6, 1141–1155, 10.5194/tc-6-1141-2012, 2012.

Reid, J. P., Dennis–Smither, B. J., Kwamena, N. O., Miles, R. E., Hanford, K. L., and Homer, C. J.: The morphology of aerosol particles consisting of hydrophobic and hydrophilic phases: hydrocarbons, alcohols and fatty acids as the hydrophobic component, *Phys Chem Chem Phys*, 13, 15559–15572, 10.1039/c1cp21510h, 2011.

Reid, J. P., Bertram, A. K., Topping, D. O., Laskin, A., Martin, S. T., Petters, M. D., Pope, F. D., and Rovelli, G.: The viscosity of atmospherically relevant organic particles, *Nat Commun*, 9, 956, 10.1038/s41467-018-03027-z, 2018.

Robinson, D. A., Dewey, K. F., and Richard R. Heim, J.: Global snow cover monitoring: An update, *Bulletin of the American Meteorological Society*, 74, 1689 – 1696, 1993.

Röthlisberger, R., Hutterli, M. A., Sommer, S., Wolff, E. W., and Mulvaney, R.: Factors controlling nitrate in ice cores: Evidence from the Dome C deep ice core, *Journal of Geophysical Research: Atmospheres*, 105, 20565–20572, 10.1029/2000jd900264, 2000.

Schmidt, J. A., Jacob, D. J., Horowitz, H. M., Hu, L., Sherwen, T., Evans, M. J., Liang, Q., Suleiman, R. M., Oram, D. E., Le Breton, M., Percival, C. J., Wang, S., Dix, B., and Volkamer, R.: Modeling the observed tropospheric BrO background: Importance of multiphase chemistry and implications for ozone, OH, and mercury, *Journal of Geophysical Research: Atmospheres*, 121, 8118–8118, 10.1002/2015jd024229, 2016.

Bibliography

Schweizer, J.: On recent advances in applied snow and avalanche research, *Cold Regions Science and Technology*, 97, 57–59, 10.1016/j.coldregions.2013.10.005, 2014.

Simpson, W. R., von Glasow, R., Riedel, K., Anderson, P., Ariya, P., Bottenheim, J., Burrows, J., Carpenter, L. J., Friess, U., Goodsite, M. E., Heard, D., Hutterli, M., Jacobi, H. W., Kaleschke, L., Neff, B., Plane, J., Platt, U., Richter, A., Roscoe, H., Sander, R., Shepson, P. B., Sodeau, J., Steffen, A., Wanger, T., and Wolff, E.: Halogens and their role in polar boundary-layer ozone depletion, *Atmos Chem Phys*, 7, 4375 – 4418, 2007.

Simpson, W. R., Brown, S. S., Saiz-Lopez, A., Thornton, J. A., and Glasow, R.: Tropospheric halogen chemistry: sources, cycling, and impacts, *Chem Rev*, 115, 4035–4062, 10.1021/cr5006638, 2015.

Sommerfeld, R. A., and LaChapelle, E.: The classification of snow metamorphism, *Journal of Glaciology*, 9, 1–17, 1970.

Stanier, C., Singh, A., Adamski, W., Baek, J., Caughey, M., Carmichael, G., Edgerton, E., Kenski, D., Koerber, M., Oleson, J., Rohlf, T., Lee, S. R., Riemer, N., Shaw, S., Sousan, S., and Spak, S. N.: Overview of the LADCO winter nitrate study: hourly ammonia, nitric acid and PM_{2.5}; composition at an urban and rural site pair during PM_{2.5} episodes in the US Great Lakes region, *Atmos Chem Phys*, 12, 11037–11056, 10.5194/acp-12-11037-2012, 2012.

Steimer, S. S., Berkemeier, T., Gilgen, A., Krieger, U. K., Peter, T., Shiraiwa, M., and Ammann, M.: Shikimic acid ozonolysis kinetics of the transition from liquid aqueous solution to highly viscous glass, *Phys Chem Chem Phys*, 17, 31101–31109, 10.1039/c5cp04544d, 2015.

Thibert, E., and Domine, F.: Thermodynamics and kinetics of solid solution of HCl in ice, *J. phys. Chem. B*, 101, 3554–3565, 1997.

Thibert, E., and Domine, F.: Thermodynamisc and kinetics of solid solution of HNO₃ in ice, *J. Phys. Chem. B*, 102, 4432–4439, 1998.

Ullerstam, M., and Abbatt, J. P.: Burial of gas-phase HNO₃ by growing ice surfaces under tropospheric conditions, *Phys Chem Chem Phys*, 7, 3596–3600, 10.1039/b507797d, 2005.

Worster, M. G., and Rees Jones, D. W.: Sea-ice thermodynamics and brine drainage, *Philos Trans A Math Phys Eng Sci*, 373, 10.1098/rsta.2014.0166, 2015.

Bibliography

Wu, S., Zhu, C., He, Z., Xue, H., Fan, Q., Song, Y., Francisco, J. S., Zeng, X. C., and Wang, J.: Ion-specific ice recrystallization provides a facile approach for the fabrication of porous materials, *Nat Commun*, 8, 15154, 10.1038/ncomms15154, 2017.

Probing the interfacial process of bromide oxidation by ozone in aqueous salt solutions

Published as: Artiglia, L., J. Edebeli, F. Orlando, S. Chen, M. Lee, P. Corral Arroyo, A. Gilgen, T. Bartels–Rausch, A. Kleibert, M. Vazdar, M. A. Carignano, J. S. Francisco, P. B. Shepson, I. Gladich & M. Ammann. A surface–stabilized ozonide triggers bromide oxidation at the aqueous solution–vapor interface. *Nat. Commun.*, **8**, 700, 1–8, 2017.

2.1 A surface–stabilized ozonide triggers bromide oxidation at the aqueous solution–vapor interface

I conducted a large part of the kinetics experiments and analysis. I developed the parameterization of the kinetics study discussed in the paper. I wrote the kinetics section (paper and supplementary information) and prepared figures 1 and 5 in the paper.

2.1.1 Abstract

Oxidation of bromide in aqueous environments initiates the formation of molecular halogen compounds, which is important for the global tropospheric ozone budget. In the aqueous bulk, oxidation of bromide by ozone involves a $[\text{Br}\bullet\text{OOO-}]$ complex as intermediate. Here, we report liquid jet X–ray photoelectron spectroscopy measurements that provide direct experimental evidence for the ozonide and establish its propensity for the solution–vapor

Chapter 2 Probing the interfacial process of bromide oxidation by ozone in aqueous salt solutions

interface. Theoretical calculations support these findings, showing that water stabilizes the ozonide and lowers the energy of the transition state at neutral pH. Kinetic experiments confirm the dominance of the heterogeneous oxidation route established by this precursor at low, atmospherically relevant ozone concentrations. Taken together, our results provide a strong case of different reaction kinetics and mechanisms of reactions occurring at the aqueous phase – vapor interface as compared to the bulk aqueous phase.

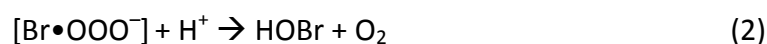
2.1.2 Introduction

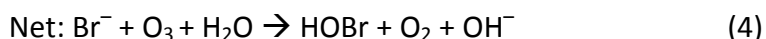
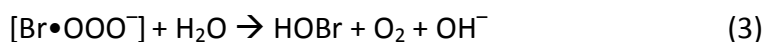
In atmospheric chemistry, halogen atoms resulting from photolysis of both organic and inorganic halogen compounds (Oum *et al.*, 1998; De Haan *et al.*, 1999) are important catalysts for ozone depletion both in the stratosphere and in the troposphere. with varying relative roles of chlorine, bromine and iodine in these compartments (Raso *et al.*, 2017). Halogen atoms are also oxidants themselves towards organic compounds and are implicated in the deposition of mercury (Parrella *et al.*, 2012; Schmidt *et al.*, 2016). Furthermore, halogen atoms are intermediates in waste water treatment, where halogenated organic secondary products are of concern (Heeb *et al.*, 2014).

For tropospheric chemistry, the main inorganic route is initiated by the oxidation of aqueous phase bromide to either bromine atom or to hypobromous acid (HOBr), which combines with other halide ions to form molecular halogen compounds that are released to the gas phase. Bromide is abundant and sometimes enriched (Sander *et al.*, 2003) in sea water and thus at the ocean surface, in sea spray particles, in brines associated with sea ice, frost flowers or snow, in artificial or natural salt pans, and in volcanic emissions.

Many radical oxidants such as $\cdot\text{OH}$ or excited triplets of organic chromophores require UV or at least near UV light to drive bromide oxidation. Therefore, both in the (dark) polar marine boundary layer and the upper troposphere, ozone (O_3) is one of the most important oxidants (Cao *et al.*, 2016; Schmidt *et al.*, 2016). The product HOBr ($\text{pK}_a=8.65$) reacts further in an acid-catalyzed mechanism with chloride, bromide or iodide to form bromine (Br_2), BrCl or BrI. The initial formation of HOBr limits the release of halogens to the gas phase, while a complex suite of gas phase and multiphase processes controls the halogen chemistry and the O_3 budget later on.

The bulk aqueous phase, acid catalyzed oxidation of bromide by O_3 to HOBr has been studied for a long time due to its relevance in debromination of waste water. (Haruta and Takeyama, 1981; Haag and Hoigne, 1983; Haag *et al.*, 1984; Liu *et al.*, 2001; Gunten, 2003; Heeb *et al.*, 2014; Gladich *et al.*, 2015).





To explain discrepancies in apparent kinetics among different experimental observations, Liu *et al.* proposed that there must be an ozone adduct (a steady-state intermediate formed in (1)) with the nucleophile, bromide, prior to oxygen atom transfer with release of molecular oxygen (Liu *et al.*, 2001) (2,3). The structure of the $[\text{Br}\bullet\text{OOO}^-]$ adduct (which we refer to as an “ozonide”), involves a weak bond between the bromide and the oxygen of ozone (Liu *et al.*, 2001). The aqueous solvation sphere has a large effect on the stability and reactivity of $[\text{Br}\bullet\text{OOO}^-]$. The kinetic data indicated formation of $[\text{Br}\bullet\text{OOO}^-]$ as a steady-state intermediate with an acid-assisted step to form HOBr and molecular oxygen (Liu *et al.*, 2001). Further calculations, performed for the gas phase, confirmed the stability of the $[\text{Br}\bullet\text{OOO}^-]$ intermediate, showing intricate details of its reactivity during the oxygen atom transfer process (Gladich *et al.*, 2015).

It is often assumed that $[\text{Br}\bullet\text{OOO}^-]$ is stabilized by solvation, and that the reaction occurs in the bulk. Further, the rate coefficient for the overall reaction (Liu *et al.*, 2001) and the low solubility of ozone (0.025 M atm^{-1} at 273 K) (Chameides and Davis, 1982) suggest that the formation of HOBr through the bulk aqueous phase route is rather inefficient and would not seem important as a source of gas phase bromine in the environment. In turn, heterogeneous oxidation experiments have consistently shown that oxidation at the aqueous solution–air interface may dominate in environments with high aqueous surface to volume ratio (Oum *et al.*, 1998; Hunt *et al.*, 2004; Clifford and Donaldson, 2007; Abbatt *et al.*, 2010; Wren *et al.*, 2010; Oldridge and Abbatt, 2011; Nissenson *et al.*, 2014; Lee *et al.*, 2015). Oldridge and Abbatt (Oldridge and Abbatt, 2011) used the inverse ozone concentration dependence of the uptake coefficient, γ , to suggest a Langmuir–Hinshelwood type process occurring on the surface in parallel to the bulk aqueous phase oxidation (see Supplementary Note 1 for a detailed description of the concept of heterogeneous kinetics of this system) (Oldridge and Abbatt, 2011). γ is the oxidation rate normalized by the gas collision rate of ozone with the surface.

Linked to a single composition and single temperature, the nature of the surface reaction, the identity of the potential precursor and its preference for the surface have never been tracked down. Similar behavior of other heterogeneous oxidation processes suggest a general type of ozone intermediate formed on electron rich surfaces of widely differing chemical composition and phase (McCabe and Abbatt, 2009; Shiraiwa *et al.*, 2011; Lampimaki *et al.*, 2013; Berkemeier *et al.*, 2016).

Finally, the idea of efficient surface oxidation of bromide had originally been related to the preference of the larger, more polarizable halide ions for the aqueous solution – vapor interface, as observed in molecular dynamics (MD) simulations (Jungwirth and Tobias, 2001; Hofft *et al.*, 2006) and X-ray photoelectron spectroscopy (XPS) experiments on static

Chapter 2 Probing the interfacial process of bromide oxidation by ozone in aqueous salt solutions

deliquesced crystals (Ghosal *et al.*, 2000). Recent MD simulations predicting the photoemission signal intensity by means of photoelectron scattering calculations and liquid jet XPS data indicate a less pronounced surface enhancement, which is in better agreement with the overall positive surface tension change (and thus negative surface excess) of bromide solutions (Weber *et al.*, 2004; Olivieri *et al.*, 2016). Therefore, the surface precursor limited bromide oxidation is likely unrelated to the amount of bromide ions directly at the interface of a neat salt solution.

In this work we use liquid jet XPS, a powerful tool to directly assess the structure of the interfacial region with high chemical selectivity and high selectivity for the interface due to the probe (or information) depth of just a few nanometers (Winter and Faubel, 2006). The continuously renewed surface of the flowing liquid jet avoids radiation damage effects but still allows probing a surface that is locally in equilibrium with the first few tens of nanometer of bulk aqueous phase (Thurmer *et al.*, 2013; Slavicek *et al.*, 2016) (as explained further in Supplementary Note 4). We combine classical heterogeneous kinetics experiments, which reconfirm the characteristics of the surface reaction, with theoretical investigations (including both the *ab-initio* electronic structure and MD method) and with liquid jet XPS. The results provide strong evidence for the $[\text{Br}\bullet\text{OOO}^-]$ intermediate, its preference for the liquid–vapor interface, the effect of water on its stabilization, and the reaction path to products.

2.1.3 Results

Kinetic results

Figure 2.1 shows the measured ozone uptake coefficients (γ_{obs}) at 274 K and pH 1 as a function of the square root of the bromide activity (plot a) and as a function of the ozone concentration (plot b). This data set confirms that γ decreases with increasing ozone concentration, which cannot be explained by aqueous phase bulk kinetics (more data available in Supplementary Figure 1). Reactivity in the bulk depends on the solubility of ozone, ionic strength of the solution, and diffusivity of ozone (see Supplementary Note 1). Figure 2.1 is in line with the involvement of a precursor on the surface, whose surface coverage saturates at higher ozone concentrations in the gas phase. These data confirm the findings of Oldridge and Abbatt (2011). At high ozone concentrations, the reactivity is dominated by the bulk aqueous phase reaction, which scales with the square root of bromide activity (see Supplementary Note 1, equation 4). At lower gas phase ozone concentrations, the surface component becomes relatively higher. Figure 2.1 also contains fits to the measured uptake coefficients that take into account both components (as explained in Supplementary Note 1 and further below). Notably, the data indicate that this

surface component is relatively higher also at lower bromide concentration, which will be discussed further below.

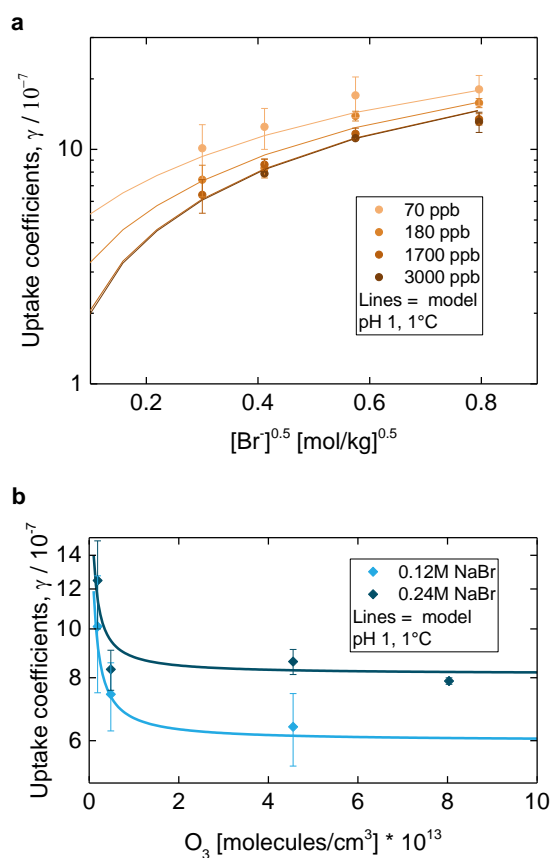


Figure 2.1 Heterogeneous kinetics results

Measured uptake coefficients of ozone, γ_{obs} , at different ozone concentrations (symbols) on aqueous bromide solutions, along with calculated uptake coefficients (lines) from a parameterized fit to several measured datasets, explained in Supplementary Note 1 and 2. The uptake coefficient is the loss rate of gas phase ozone to the aqueous solution normalized to the gas kinetic collision rate with the aqueous solution surface. In plot (a), data from experiments performed with solutions of varying bromide content are shown for four different ozone concentrations in the gas phase, while in plot (b), data result from experiments, in which the ozone concentration was varied, for two different bromide concentrations in the aqueous phase. Error bars represent standard deviations of measured values.

Ab-initio calculations of $[\text{Br}\bullet\text{OOO}^-]$ stability in water

Previous electronic structure calculations for the oxidation of bromide by ozone in the gas phase showed that the reaction is activated by the formation of a stable $^1[\text{Br}\bullet\text{OOO}^-]$ pre-complex likely followed by a spin crossing to the triplet potential energy surface due to the different spin state of the products (Gladich *et al.*, 2015). Herein, additional electronic structure calculations were performed to address the influence of water on the stability of the $^1[\text{Br}\bullet\text{OOO}^-]$ pre-complex. Water can profoundly affect the reaction rates and the nature of different atmospheric (and non-) reactions by coordinating (hydrogen) bonds to the

Chapter 2 Probing the interfacial process of bromide oxidation by ozone in aqueous salt solutions

reagents, products, and the different reaction pre-complexes (Vaida, 2011). Reaction profiles in solvated environment are often remarkably different from the ones obtained in the gas phase (Li *et al.*, 2016; Zhu *et al.*, 2016). Water cluster approach has been successfully used to model reactions in aqueous solutions and at the surface of water, ice, and aerosols (Hammerich and Buch, 2008; Bertram *et al.*, 2009; Miller *et al.*, 2009; Xantheas and Voth, 2009; Krepelova *et al.*, 2010; Li *et al.*, 2016; Zhu *et al.*, 2016). If sufficient number of water molecules are included in the electronic structure calculations, water cluster has been proven to describe reasonably the solvation environment of different reaction systems (Inaba, 2014; Gerber *et al.*, 2015; Inaba and Sameera, 2016). In our case, Supplementary Figure 5 shows how the energy difference between reaction complexes converge within the chemical accuracy of the method (Ramabhadran and Raghavachari, 2013) for cluster of four water molecules. The water cluster approach has the advantage of keeping the system size small, allowing the use of high-level theory electronic structure calculations. Figure 2.2 shows the reaction profile with four water molecules, using the singlet ground state of the reactants as an initial and reference level for the energetics. Comparing this reaction profile with previous gas phase results, we conclude that water further stabilizes the pre-complex with respect to the reactants and the other reaction complexes.

This stabilization effect is also visible in the optimized geometries of $^1[\text{Br}\cdot\text{OOO}^-]$ with water (see the Supplementary Note 3). The larger the number of water molecules, the closer the distance between bromine and the nearest oxygen atom. Moreover, the energy differences between $^1[\text{Br}\cdot\text{OOO}^-]$ and the transition states on the singlet and triplet surfaces are remarkably high. Conventional transition state theory provides a qualitative estimation of the rate constant along the singlet surface of the order of 10^{-28} s^{-1} . In conclusion, water stabilizes the $^1[\text{Br}\cdot\text{OOO}^-]$ pre-complex, while the heights of the transition barriers and the spin-crossing nature of the reaction suggest a slow kinetics, favoring a longer lifetime of the $^1[\text{Br}\cdot\text{OOO}^-]$ complex at the liquid water surface than in the gas phase. Next we address the extent to which we can detect this species experimentally.

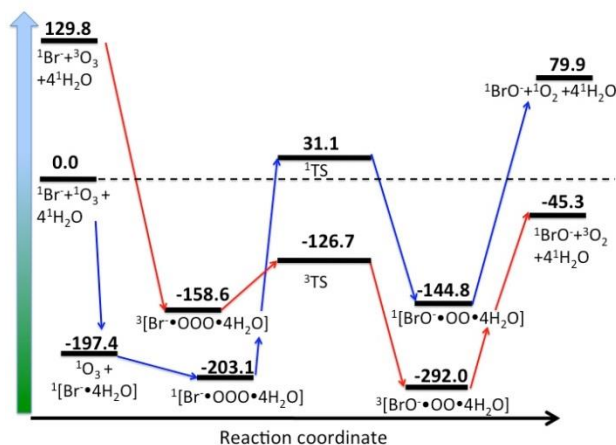


Figure 2.2 Energetic profile for the bromide–ozone reaction with water molecules obtained by electronic structure calculations

The figure reports the energetic profile for the reaction of bromide with ozone in 4 water cluster along the singlet (blue) and triplet (red) surface. Electronic structure calculations were performed at CCSD(T)/6–311++G(df,p)//MP2/6–311++G(df,p) level. All energies, which include the Zero Point Energy (ZPE) correction, are relative to the singlet reactants and are reported in kJ/mol. The spin crossing between the two potential energy surface is highlighted by the intersection of the red and blue arrows between the pre–reaction complexes and the transition states.

Liquid jet XPS experiments

Figure 2.3 shows the photoemission signal of the Br 3d core level region, a double–peak structure due to the spin orbit splitting. After normalization to the maximum, the spectra acquired before and during in–situ dosing of oxygen at a pressure of 0.25 mbar are identical. The signal collected while dosing a mixture of oxygen and ozone (approx. 1.0 % ozone, same pressure) displays clear changes both in the 3d_{5/2} and 3d_{3/2} region. This suggests the presence of a second doublet, which is highlighted in purple in Figure 2.3c, positively shifted by 0.7 eV with respect to the main peaks assigned to bromide (72.10 and 73.15 eV).

To identify the new spectral feature, we acquired the Br 3d spectra of two reference aqueous solutions of possible oxidation products, i.e. 0.08 M hypobromite and 0.125 M bromate (Figure 2.3d). As expected, the higher the oxidation state of bromine, the larger the positive shift of the binding energy. A chemical shift of +2.1 eV is observed for hypobromite, and of +7.0 eV for bromate. None of them corresponds to that of the new doublet. It is well known that x–rays can induce the radiolysis of water (George *et al.*, 2012), leading to the production of reactive hydroxyl radicals that may react with bromide ions. All the Br 3d spectra were recorded under the same experimental conditions (excitation energy, photon flux), and the high speed of the liquid filament ensures that the concentration of photo–generated hydroxyl radicals remains below 1.0·10^{–6} mol/L. Therefore, beam damage can be excluded. In parallel to the XPS data, we calculated the

Chapter 2 Probing the interfacial process of bromide oxidation by ozone in aqueous salt solutions

core electron binding energy (CEBE) at MP2/aug-cc-pvtz theory level of both the structure obtained at MP2/6-311++(df,p) geometric optimization and from first-principle MD (Table 2.1). It is important to highlight that the CEBEs are calculated for the species solvated in small water clusters. This reproduces quite well an interfacial environment but may not reproduce well species that are fully solvated in the bulk. As compared to the CEBEs of gas phase species the Δ between the bromide and the $[\text{Br}\cdot\text{OOO}^-]$ decreases when water is added, whereas that between the $[\text{Br}\cdot\text{OOO}^-]$ and the hypobromite increases. This suggests that the solvation sphere has a fundamental role. At the same time, theoretical calculations reproduce the same sequence of CEBE showed by XPS, i.e. $\text{CEBE}(\text{Br}^-) < \text{CEBE}([\text{Br}\cdot\text{OOO}^-]) < \text{CEBE}(\text{BrO}^-)$. In summary, the combination of in-situ XPS and theoretical calculations provides strong indications for the formation of an ozonide complex.

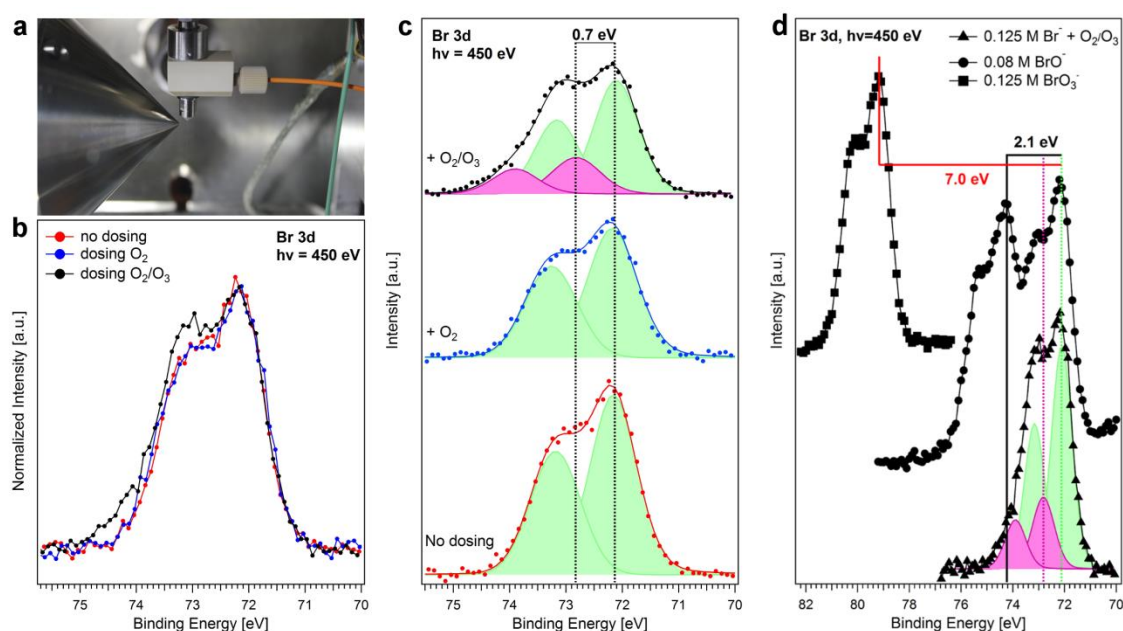


Figure 2.3 Photoemission spectra of the Br 3d peak acquired in-situ.

a, Picture of the liquid microjet assembly, equipped with the gas dosing system, during operation; **b**, Superimposition of the Br 3d photoemission spectra, normalized to the maximum, acquired before dosing (red), while dosing oxygen (blue), and while dosing a mixture of 1% ozone in oxygen; **c**, deconvolution of the raw spectra in plot b, performed using Gaussian peaks after subtraction of a Shirley background; **d**, comparison of the Br 3d photoemission spectra acquired while dosing a mixture of 1% ozone in oxygen with two reference spectra of hypobromite and bromate.

Table 2.1 Theoretical evaluation of the core electron binding energies (CEBE) of the bromide ions, the $[\text{Br}\bullet\text{OOO}^-]$ complex, the hypobromite ion in the gas phase, and all ions with three and five water molecules.

| | CEBE(Br^-_{3d}), eV | Δ (CEB–CEBE $_{\text{Br}^-}$), eV |
|---|--------------------------------|---|
| $^1\text{Br}^-$ | 70.01 ^(a) | 0.00 |
| $^1[\text{Br}\bullet\text{OOO}^-]$ | 72.79 ^(a) | 2.78 |
| $^1\text{BrO}^-$ | 73.10 ^(a) | 3.09 |
| <hr/> | | |
| $^1\text{Br}^- + 3 \text{H}_2\text{O}$ | 71.73 ^(a) | 0.00 |
| $^1[\text{Br}\bullet\text{OOO}^-] + 3 \text{H}_2\text{O}$ | 74.33 ^(a) | 2.60 |
| $^1\text{BrO}^- + 3 \text{H}_2\text{O}$ | 75.33 ^(a) | 3.60 |
| <hr/> | | |
| $^1\text{Br}^- + 5 \text{H}_2\text{O}^{(b)}$ | 72.02 ^(b) | 0.00 |
| $^1[\text{Br}\bullet\text{OOO}^-] + 5 \text{H}_2\text{O}^{(b)}$ | 73.83 ^(b) | 1.81 |
| $^1\text{BrO}^- + 5 \text{H}_2\text{O}^{(b)}$ | 74.69 ^(b) | 2.67 |

$\Delta(\text{CEBE} - \text{CEBE}_{\text{Br}^-})$ is the energy difference (in eV) between the species and the bromide, taken as a reference. CEBE marked with (a) are calculated on the top of MP2 optimized geometries. CEBE marked with (b) are averaged over the values obtained from five different snapshots extracted from the first-principle MD trajectory.

Surface propensity of the intermediate

First-principle MD simulations, which are a particularly suitable tool to study the dynamics and stability of non-standard compounds, were used to address the bulk vs. surface propensity of the different reaction intermediates (Marx and Hutter, 2009). Figure 2.4a shows a snapshot (corresponding to 8.5 ps) of the MD trajectory of the pre-complex on the surface of a water slab at 300 K. The inset shows the distance between bromine and each of the oxygen atoms of $^1[\text{Br}\bullet\text{OOO}^-]$ along the MD trajectory. This distance fluctuates around the average value of 2.7 Å, which is consistent with that obtained for the optimized geometries by electronic structure calculations (see ref. 9 and Supplementary Note 3). This further supports the scenario of a pre-complex stabilized on the surface of liquid water. Moreover, Figure 2.4b shows the density profile of the Br and OOO groups in the $^1[\text{Br}\bullet\text{OOO}^-]$ intermediate position along the coordinate perpendicular to the water interface, confirming that $^1[\text{Br}\bullet\text{OOO}^-]$ remains at the interface during the whole trajectory, with the Br group close to the OOO group.

Chapter 2 Probing the interfacial process of bromide oxidation by ozone in aqueous salt solutions

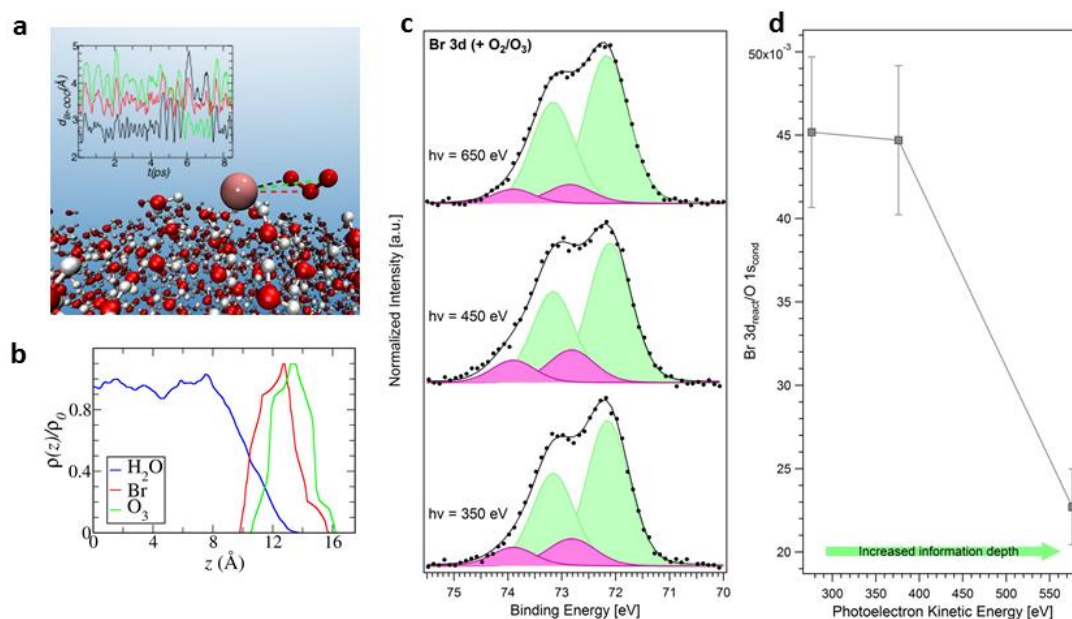


Figure 2.4 Surface propensity of [Br•OOO⁻]: experiment and theory

a) Snapshot from the first-principle MD trajectory demonstrating the stability of [Br•OOO⁻] on the surface of liquid water. The inset shows the distances between the bromine and each of the oxygen atoms in the ozone molecule recorded during the 8.5 ps MD trajectory. **b)** From the same trajectory, the bromide and ozone density profile showing the position of the center of mass of these two groups along the coordinate perpendicular to the interface. In blue, the water profile as reference in arbitrary units. **c)** Deconvolution of the Br 3d photoemission spectra (performed using Gaussian peaks after subtraction of a Shirley background), normalized to the area, acquired at $h\nu=350$, 450, and 650 eV, and corresponding to photoelectron kinetic energies of 276, 376 and 575 eV (Br 3d region centroid). **d)** Plot of the intensity of the Br 3d peaks associated to the [Br•OOO⁻] complex normalized to the O 1s (peak acquired with second order light) from the condensed phase (see Supplementary Note 4), as a function of the photoelectron kinetic energy. The error bars were calculated by propagating the errors associated with each peak area of three independent measurements.

In parallel to the MD simulations, we acquired the Br 3d photoemission peak at increasing excitation energies, hence, at increasing photoelectron kinetic energy or information depth, as shown in Figure 2.4c. A decrease of the relative intensity of the peaks associated to the [Br•OOO⁻] complex is observed at the highest excitation energy. We acquired the O 1s signal at the same photoelectron kinetic energies (Supplementary Figure 6a) and used the area of the peak corresponding to the condensed phase to normalize the area of the [Br•OOO⁻] doublet. Figure 4d shows that this ratio, normalized to the cross sections of the elements, decreases considerably at a kinetic energy of 576 eV, i.e. with greater depth sampled. This indicates that the [Br•OOO⁻] complex has a propensity for the surface, in

good agreement with the theoretical calculations discussed above. The photoemission intensity ratio between the complex and the bromide in the bulk ($I_{\text{BrOOO}^-}/I_{\text{Br}^-}$) shows a similar behavior as a function of the photoelectron kinetic energy (Supplementary Figure 7). An estimate of the surface coverage of the $[\text{Br}\bullet\text{OOO}^-]$ complex at the ozone concentration used in this study ($2.5\cdot 10^{-8}$ mol L^{-1}), obtained employing different models, yields approx. $2.0\cdot 10^{12}$ complexes cm^{-2} (see Supplementary Note 4 and Supplementary Figure 7 for more details). In conclusion, both MD results and XPS data confirm that $[\text{Br}\bullet\text{OOO}^-]$ resides at the interface, where it is stabilized by interfacial water molecules.

2.1.4 Discussion

As previously mentioned, the reaction of ozone with bromide in the bulk aqueous phase is fairly slow, with a rate coefficient of around $163 \text{ M}^{-1} \text{ s}^{-1}$ at 293 K and neutral pH (Haruta and Takeyama, 1981), and $38 \text{ M}^{-1} \text{ s}^{-1}$ at 273 K and neutral pH (Liu *et al.*, 2001). Therefore, when ozone is dosed, we would not expect the formation of HOBr or hypobromite within the ~ 100 μs exposure between the gas dosing system and the detection point of XPS. In turn, the actual collision rate of ozone molecules with the surface at about $6.0\cdot 10^{17}$ molecules $\text{cm}^{-2} \text{ s}^{-1}$ is sufficient to build up a high surface coverage of the complex with bromide, if the association kinetics is fast (see Supplementary Note 4). This of course also requires that the availability of bromide at the surface is sufficient. In the absence of any pre-existing enhanced concentration on the surface, formation of an even maximum conceivable complex surface coverage of around 10^{12} molecules cm^{-2} (as estimated from the XPS data) would deplete roughly the topmost few nanometers of a 0.1 M solution. Replenishing this by diffusion from the deeper bulk requires a few microseconds (see Supplementary Note 4) (Winter and Faubel, 2006; Lee *et al.*, 2015), fast enough to ensure equilibration between the surface and the bulk under the present experimental conditions. Due to the substantial transition state barrier towards products, the steady state surface coverage establishes quickly, and is determined by the rapid association and dissociation of ozone and bromide.

Combining the theoretical and spectroscopic results, we have extended the bulk phase kinetic mechanism by adding a simple scheme for the surface reaction. The $[\text{Br}\bullet\text{OOO}^-]$ replaces the adsorbed precursor of the Langmuir–Hinshelwood mechanism (see Supplementary Note 1), which remains in equilibrium with the gas phase. The temperature dependence of the equilibrium constant is driven by the energy difference, as in Figure 2.2. Furthermore, we assumed that the energy difference to the transition state on the triplet energy surface (and thus including spin–crossing, which is more likely to occur with heavy elements as bromine) would determine the decomposition kinetics on the surface and the temperature dependence for the formation of products.

As Figure 2.1 and Supplementary Figure 2 show, this parameterization allows reconciling the data presented in this study and those of Oldridge and Abbatt (Oldridge and Abbatt, 2011)

Chapter 2 Probing the interfacial process of bromide oxidation by ozone in aqueous salt solutions

within less than a factor of two, both with respect to the absolute value of the uptake coefficient and the concentration range where the surface reaction dominates. The $[\text{Br}\bullet\text{OOO}^-]$ complex is in fast equilibrium with gas phase ozone. Its surface coverage is saturated above 10^{11} molecule cm^{-3} , thus both at the lowest ozone concentration of the present study and at all atmospheric levels, and depends very weakly on the temperature. As apparent from Figure 2.1, the extent of the surface reaction, manifesting itself in the positive deviation from the bulk phase reactivity with decreasing gas phase concentration, gets relatively larger at lower bromide concentration. This is nicely reproduced by the surface reaction model constructed here. The measured kinetic data do not allow constraining the magnitude of the saturating surface coverage (to compare with that derived from XPS), since no data are available at low enough ozone concentrations to escape the saturating regime. For the present data, the rate of the surface reaction is only constrained by the product of the coverage and the surface reaction rate coefficient. The first order rate coefficient for the decomposition of the complex into hypobromite on the surface as derived from the kinetic data is about 10^{-3} s^{-1} .

Under atmospheric conditions, the relative importance of bulk and surface reactivity needs a more careful analysis. In the environment, salt brine may occur in various forms and spanning a large size range in snow, on sea-ice, on frost flowers, in salt pans, or as sea spray aerosol particles. Figure 5 shows the bulk reactivity (in absence of surface reaction) and the surface reactivity according to the mechanism in this study, for a hypothetical spherical sea salt brine droplet or aerosol particle as a function of the diameter, for both a bromide concentration as in sea water and a tenfold enhanced bromide concentration. Based on the data in Figure 2.1 and the surface coverage estimated from the XPS data, a constant ozonide complex coverage on the surface of 10^{12} complexes cm^{-2} is assumed, so that the surface reactivity is the same for both scenarios. The size dependence of the bulk reactivity comes from the fact that the oxidation rate scales with the volume of the particle for smaller particles, whereas the uptake coefficient is the oxidation rate normalized to the surface area (see Supplementary Note 1, equation 4a). Therefore, for environmental conditions, the surface reactivity may largely dominate over the bulk reactivity by two orders of magnitude, especially for brine pockets of smaller dimensions or aerosol particles. Since the global distribution of BrO responds notably to the oxidation of bromide by ozone (Schmidt *et al.*, 2016), and since our new results provide a significantly larger contribution by the surface reaction than the previously recommended parameterization (Lampimaki *et al.*, 2013), we expect notable changes to the relative importance of this reaction among the multiphase halogen chemical cycling reactions.

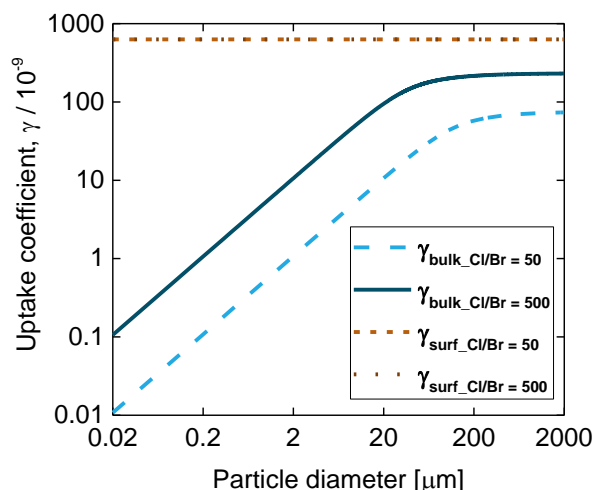


Figure 2.5 Implications for ozone uptake under atmospheric conditions

Predicted uptake coefficient for bulk reaction only (blue lines) and uptake coefficient due to surface reaction only (brown lines) for deliquesced sea salt solution equilibrated at 80% relative humidity (4.0 M Cl⁻) and a chloride to bromide ratio of 50 (light blue and light brown lines) and 500 (dark blue and dark brown)), as a function of the diameter of a spherical brine droplet or aerosol particle. The brown lines overlap, because the surface coverage of the bromide ozonide complex, and thus also the surface reaction rate, does not depend on the bromide concentration in the aqueous phase within the relevant range. This plot emphasizes the predominance of a surface process, especially for smaller particle sizes.

In summary, by combining kinetic studies with theoretical calculations and spectroscopy, we have demonstrated that the reactivity at the interface between bromide aqueous solutions and ozone from the gas phase is higher than in the bulk. While the kinetic experiments indirectly reconfirm and refine the picture of a precursor mediated process at the surface of aqueous solutions, the XPS results provide a clear spectroscopic evidence of this intermediate, the [Br•OOO⁻] pre-complex. Furthermore, a rough estimate of the surface coverage from the photoemission spectra of the Br 3d at increasing information depths shows that the new species has a preference for the interface, in good agreement with first-principle MD simulations. This multi-method approach investigates an elusive reaction intermediate that has been predicted from theory and interpretation of kinetic data but never directly observed in experiments. In addition, this work shows its preference for the liquid-gas interface, and sheds light on mechanistic and structural aspects of the reaction. The results provide evidence for a stronger contribution of the surface oxidation of bromide than previously thought, which will require re-assessment of the impacts on the global ozone budget and mercury deposition (Schmidt *et al.*, 2016). In turn, the formation of ozonides on surfaces may be a widespread phenomenon and a key step of important oxidation processes relevant not only for atmospheric chemistry but also for the effects of atmospheric particles on human health (Shiraiwa *et al.*, 2011; Berkemeier *et al.*, 2016; Lakey *et al.*, 2016).

2.1.5 Methods

Kinetic experiments

Kinetic experiments were conducted in a flow reactor setup previously described by Lee *et al.* (2015). Briefly, the setup comprises of a temperature regulated Teflon trough (surface area = 102 cm²) on which 10 mL – 45 mL of the reactive solution (NaBr (Sigma Aldrich) in deionized water) is loaded uniformly. Ozone is generated by UV light at different intensities from a mixture of 400 ml min⁻¹ O₂ and 600 ml min⁻¹ N₂. This gas flow is cooled and humidified to the water vapor pressure in the trough at the set temperature before delivery to the trough. Gas flow is alternated between a bypass to measure the maximum (initial) O₃ concentration and the trough to measure the O₃ left after reactive uptake by the solution. O₃ concentration was measured using a commercial ozone monitor (Teledyne API model 400).

Theory

Geometric optimization of the reaction intermediates were performed at MP2/6–311++g(df,p) level (Moller and Plesset, 1934) while, to improve the energetic, single point energy calculations were employed at CCSD(T)/6–311++g(df,p) level (Raghavachari *et al.*, 1989) on the top of the optimized structures obtained with MP2. Electronic structure calculations were performed using Gaussian09 (Frisch *et al.*, 2009).

First–Principle MD simulations were done as implemented in the CP2K code to study the stability and dynamics of the ¹[Br•OOO⁻] on the surface of liquid water (Hutter *et al.*, 2014). The optimized geometry for ¹[Br•OOO⁻] obtained at MP2 level was placed on the top of an equilibrated water slab of 216 water molecules. The simulation was done under NVT conditions, at 300 K, using BLYP (Becke, 1988; Lee *et al.*, 1988) and Grimme dispersion correction (Grimme *et al.*, 2010), Goedecker–Teter–Hutter pseudopotentials (Goedecker *et al.*, 1996) and DZVP basis set was employed in combination with plane wave representation for the valence electrons.

CEBE were calculated on top of MP2/6–311++g(df,p) geometries using GAMESS suite of codes (Schmidt *et al.*, 1993). For the CEBE in 5 water molecules cluster (Table 1), configurations were extracted from first–principle MD simulations. The core–hole state geometries were assumed to be identical to the corresponding ground states. The effect of relaxation was described by the ΔMP2 approach (Holme *et al.*, 2011; Shim *et al.*, 2011) with the electron correlation described at MP2/aug–cc–pVTZ level of theory. The CEBE was defined as the difference between the ground state energy and the cation core–hole state formed by ejection of a 3d electron from the Br⁻. Freezing the molecular orbitals during the SCF procedure prevented the collapse of the core–hole state to the more stable energetic state.

Liquid jet XPS

In-situ XPS was acquired at the near-ambient pressure photoemission endstation (NAPP), equipped with the liquid microjet setup. Measurements were performed at the Surfaces/Interfaces: Microscopy (SIM) beamline of the Swiss Light Source (SLS) at the Paul Scherrer Institute (PSI). The electron analyzer uses a three-stage differentially pumped electrostatic lens system and a hemispherical analyzer to collect photoelectrons from samples in chamber pressures up to the mbar range (Brown *et al.*, 2013). For the present experiments, a quartz nozzle, forming a liquid microjet with a diameter of 24 μm , was used to deliver a 0.125 M aqueous solution of Br^- into the chamber at a flow rate of 0.35 mL/min. The liquid was cooled to 277 K in a pre-cooling coil located immediately before entry into the experimental chamber. Based on these parameters, and considering the working distance of the quartz nozzle with respect to the detection point, a 100 μs time can be estimated between the injection of the liquid and the detection point. Further technical details about the procedures adopted during the experiments can be found in the Supplementary Note 4.

During the experiment we made use of linearly polarized light at 0° , and set the photon energy for the detection of Br 3d to 350, 450 and 650 eV, resulting in photoelectron kinetic energies of 276, 376 and 576 eV, respectively. The binding energy scale of the spectra was calibrated using the O 1s gas phase peak of water (539.9 eV) as a reference (Winter and Faubel, 2006). The streaming potential of a 0.125 mol/L bromide aqueous solution should be between 0.1 and 0.2 eV (Kurahashi *et al.*, 2014). The binding energy of the O 1s peak corresponding to the condensed phase is in good agreement with the values reported in literature (Winter and Faubel, 2006; Winter *et al.*, 2007) and did not change during the whole measurements. Other technical details about the experimental setup and the processing of the photoemission spectra can be found in the Supplementary Note 4.

2.1.6 Acknowledgements

For computer time, this research used the resources of the Supercomputing Laboratory at King Abdullah University of Science & Technology (KAUST) in Thuwal, Saudi Arabia. The engineering work and technical support by Mario Birrer is greatly acknowledged. J. E. acknowledges the Swiss National Science Foundation (SNF), grant 155999. M.A., F. O. and S.C. acknowledge funding by the Swiss National Science Foundation (grants no 149492 and 169176). We thank Michel Rossi for providing the ozone generator.

2.2 Supplementary information: Details of the different methods

Supplementary Note 1. Heterogeneous kinetics

Determining the uptake coefficient, γ

We follow the general method of describing the heterogeneous kinetics in terms of the uptake coefficient, γ , which is the overall loss rate from the gas phase normalized to the gas kinetic collision rate with the surface in a system, following the concepts outlined in the relevant literature (Poschl *et al.*, 2007; Kolb *et al.*, 2010; Berkemeier *et al.*, 2013). As evident from this definition, γ is not representing an elementary chemical process, but lumps together the multitude of processes involved in the transfer of a molecule from the gas phase to the surface, reactions thereon, transfer into the bulk, diffusion and reaction therein, as discussed further below. However, γ can be obtained experimentally from the measured loss rate of the gas phase reactant, ozone in the present case, assuming first-order kinetic conditions, which has been assured for the setup used in this work (Lee *et al.*, 2015). The relevant ozone concentration for uptake is the gaseous ozone concentration near the liquid surface, which is not necessarily the same as the average concentration measured after the trough, due to diffusional gradients. However, for the small uptake coefficients as in this study, limitation of gas diffusion can be neglected (Lee *et al.*, 2015). We calculated γ_{obs} as:

$$\gamma_{\text{obs}} = \frac{4 \cdot Q}{\omega_{\text{O}_3} \cdot SA_{\text{reactor}}} \times \ln \left(\frac{O_{3,\text{bypass}}}{O_{3,\text{reactor}}} \right) \quad (1)$$

$O_{3,\text{bypass}}$ is the measured ozone concentration delivered to the reactor. $O_{3,\text{reactor}}$ is the ozone concentration after the reaction has taken place. Q is the flow rate of the gas passing through the reactor ($\text{cm}^3 \text{s}^{-1}$). SA is the total surface area of the solution (cm^2) (Lee *et al.*, 2015).

Predicting the total uptake, γ_{calc}

Within the resistor model concept of heterogeneous kinetics, the general expression derived for a combination of reactive processes on the surface and in the bulk condensed phase is given by (Berkemeier *et al.*, 2013):

$$\frac{1}{\gamma} = \frac{1}{\alpha_s} + \frac{1}{\Gamma_s + \left(\frac{1}{\Gamma_{sb}} + \frac{1}{\Gamma_b} \right)^{-1}} \quad (2)$$

Where Γ_b denotes the limiting uptake coefficient contributed by the reaction in the bulk, Γ_s is the limiting uptake coefficient contributed by the reaction on the surface, Γ_{sb} is the limiting uptake coefficient contributed by the surface to bulk transfer of ozone, and α_s is the surface accommodation coefficient. As mentioned in the main text, γ_{calc} was calculated as direct addition of the bulk and surface reaction contribution (Oldridge and Abbatt, 2011; Berkemeier *et al.*, 2013; Lee *et al.*, 2015), because it is assumed that neither adsorption to the surface, nor transfer from the surface to the bulk aqueous phase is rate limiting, so that under steady state conditions,

$$\gamma_{\text{calc}} = \Gamma_b + \Gamma_s \quad (3)$$

We calculated Γ_b using the following equation (Hanson *et al.*, 1994; Poschl *et al.*, 2007):

$$\Gamma_b = \frac{4 \cdot R \cdot T \cdot H}{\omega_{O_3}} \times \sqrt{D_{\text{liq}} \cdot k_b^I}, \quad (4)$$

where R is the gas constant (0.08206 L atm K⁻¹ mol⁻¹), T is the temperature (K), H is the Henry constant (M atm⁻¹), D_{liq} is the diffusivity of ozone in the liquid phase (cm² s⁻¹), ω_{O_3} is the velocity of the ozone molecules in the gas phase (cm s⁻¹), and $k_b^I = k_b^{II} \cdot a_{\text{Br}^-,b}$ is the pseudo-first order reaction rate coefficient, the product of the second order reaction rate coefficient k_b^{II} (L mol⁻¹ s⁻¹) and the Br⁻ activity in the bulk, $a_{\text{Br}^-,bulk}$ (mol L⁻¹). It is assumed that $a_{\text{Br}^-,bulk}$ is not significantly depleted during the experiment. Equation 4 is valid as long as the reacto-diffusive length, $l_{rd} = \text{sqrt}(D_{\text{liq}}/k_b^I)$, is smaller than the thickness of the solution (d_{solution}), which is the case for our experiments ($l_{rd} \leq 10 \mu\text{m}$; $d_{\text{solution}} < 4\text{mm}$).

For spherical particles, the interplay between diffusion and reaction can be taken into account with a size dependent correction factor, where r_p is the radius of the particle:

$$\Gamma_b = \frac{4 \cdot R \cdot T \cdot H}{\omega_{O_3}} \times \sqrt{D_{\text{liq}} \cdot k_b^I} \times [\text{coth}(r_p/l_{rd}) - (l_{rd}/r_p)] \quad (4a)$$

We described Γ_s as a reaction of the Langmuir–Hinshelwood type (Γ_{LH}). Using the resistance model, the contribution of a Langmuir–Hinshelwood surface reaction can be described by (Ammann *et al.*, 2003; Berkemeier *et al.*, 2013):

Chapter 2 Probing the interfacial process of bromide oxidation by ozone in aqueous salt solutions

$$\Gamma_{\text{LH}} = \frac{4 \cdot k_s \cdot K_{\text{Lang}} \cdot N_{\text{max}}}{\omega_{\text{O}_3} \cdot (1 + K_{\text{Lang}} \cdot [\text{O}_3]_{\text{g}})} \quad (5)$$

Where k_s is the apparent second order surface reaction rate coefficient of the adsorbed ozone precursor with bromide, K_{Lang} is the Langmuir constant, N_{max} is the maximum surface coverage (corresponding to about 1×10^{12} molecules cm^{-2} , as obtained from the XPS data of this study, lower than for typical small molecules competing for area on the surface in the adsorbed state (Berkemeier *et al.*, 2013)), ω_{O_3} is the mean thermal velocity of ozone.

Equations 4 and 5 contain parameters that depend on several other variables. For example, H , which describes the solubility of ozone in the solution, depends on T , pH, and the composition of the solution. We parameterized some of these dependencies when calculating the Γ_b and Γ_{LH} .

Parameterizing Γ_b and Γ_{LH}

The uptake coefficient describes combinations of physical and/or chemical processes, which depend on the composition of the solution, temperature, and pH. The following describes the parameterization of some of the relevant variables as availability of data permits.

Estimating Γ_b

To predict the Γ_b using the model presented in equation (4), we accounted for the following dependences:

- a) The activity of the solutes in solution;
- b) The influence of pH, temperature, and the solution composition on the ozone solubility;
- c) The influence of the pH and temperature on the reaction rate coefficient;
- d) The effect of the viscosity of the solutions on diffusivity.

a) Activity of Br^-

The reactivity between Br^- and O_3 depends on the activity of the Br^- ions in the solution. The activity is given by

$$a_{\text{Br}^-} = C_{\text{Br}^-} \cdot \gamma_{\text{Br}^-} \quad (6)$$

Where c is the concentration and γ is the activity coefficient. At ionic strengths larger than $0.005 \text{ mol kg}^{-1}$, ion–ion interactions become important and the activity coefficient deviates from 1. We calculated the activities of solutes in solutions using the thermodynamic model AIOMFAC (Zuend *et al.*, 2008; Zuend *et al.*, 2011).

b) Effect of solution composition on ozone solubility

The solubility of ozone in the solution depends on the temperature, on the pH, and on the composition of the solution. The lower the temperature and the pH, the higher is the solubility of ozone in the solution (Battino *et al.*, 1983).

Studies have shown that salts like NaBr tend to decrease the solubility of ozone ("salting-out") in solution (Weisenberger and Schumpe, 1996; Bin, 2006). To account for this salting effect, the Henry's law constant (H ; $\text{molL}^{-1}\text{atm}^{-1}$) or the solubility of ozone in the solution was calculated using the Sechenov relationship (Setschenow, 1889; Bin, 2006):

$$\log\left(\frac{H_{\text{soln}}}{H_0}\right) = KC_s = \sum(h_i + h_G)C_i, \quad (7)$$

H_{soln} is the Henry's law constant of ozone in the solution of interest, H_0 is the Henry's law constant of ozone in pure water; K is the Sechenov coefficient; C_i is the concentration of ion, i , (in mol/L), h_i is the ion factor (h_{H^+} , h_{Na^+} , and h_{Br^-} were obtained from reference (Weisenberger and Schumpe, 1996), h_G is the gas coefficient, which is temperature-dependent for h_{O_3}) (Rischbieter *et al.*, 2000).

We described the temperature dependency of the solubility of ozone in water, H_0 , with the empirical function from the National Bureau of Standards (Chameides, 1986):

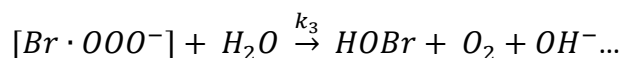
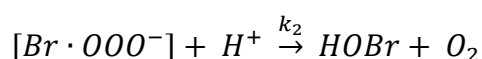
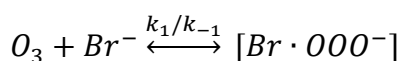
$$H_0 = 1.15 \times 10^{-2} \cdot \exp\left(2560 \cdot \left(\frac{1}{T} - \frac{1}{298}\right)\right) \quad (8)$$

Chapter 2 Probing the interfacial process of bromide oxidation by ozone in aqueous salt solutions

Activities in molal concentrations obtained from AIOMFAC were converted to molar concentration using a parameterization of Isono's temperature- and molality-dependent density of NaBr solutions (Tamamushi and Isono, 1984).

c) Temperature and pH-dependent rate coefficients, k_b^{II}

IUPAC has proposed a temperature-dependent rate coefficient for the reaction of O_3 and Br^- in the bulk (Haag *et al.*, 1984; Berkemeier *et al.*, 2013). However, studies have shown an enhancement of this reaction at low pH (Liu *et al.*, 2001). Liu *et al.* have proposed a pH-dependent k_b^{II} parameterization at three different temperatures for the scheme below (equation 9), providing values for k_1 , k_2/k_{-1} , k_3/k_{-1} , but not for the individual rate coefficients, k_2 , k_3 , or k_{-1} (Liu *et al.*, 2001).



$$k_b^{II} = \frac{k_1 \left(\frac{k_2}{k_{-1}} [H^+] + \frac{k_3}{k_{-1}} \right)}{1 + \frac{k_2}{k_{-1}} [H^+] + \frac{k_3}{k_{-1}}} \quad (9)$$

We have re-parameterized the Liu *et al.*'s rate coefficients from their k_{obs} measured at different pHs and temperatures to obtain temperature-dependent rate equations (Arrhenius expressions) for each k , which we applied to Liu *et al.*'s equation for k_{obs} . With this parameterization we obtained 53.9 kJ mol⁻¹ as the Arrhenius energy for k_1 , which agrees with Liu *et al.*'s (50 ± 10 kJ mol⁻¹).

$$k_1 = 2.07 \times 10^{13} \exp(-6480/T);$$

$$k_2 = 1.50 \times 10^{39} \exp(-25200/T);$$

$$k_3 = 1.62 \times 10^{36} \exp(-24100/T);$$

$$k_{-1} = 4.17 \times 10^{41} \exp(-26600/T);$$

d) Diffusion coefficient of ozone

The diffusion coefficient of ozone in the liquid phase (D_{O_3l}) was calculated using the Stokes–Einstein relation, for which the diffusivity is dependent on the viscosity of the solution (equation 10)(Lee *et al.*, 2015). The viscosity depends on the composition of the solution and the temperature (Tamamushi and Isono, 1984). We obtained a temperature and composition fit to Isono’s viscosity measurements on NaBr solutions, with which we extrapolated to the relevant temperatures.

$$D_{O_3l} = \frac{k_B T}{6\pi\eta(T)r_{O_3}} \quad (10)$$

For NaBr–HCl mixtures (acidified solution), we used the same viscosity as for the NaBr non–acidified solutions. At pH 1, which corresponds to 0.36 wt%, the effect of HCl on the viscosity of a water–HCl mixture is smaller than 0.5% (estimated from the fitting curves by Nishikata *et al.*) (Nishikata *et al.*, 1981).

Estimating Γ_{LH} (Γ_s)

In equation 5, for estimating the surface reactivity, the two parameters of concern are K_{Lang} and the k_s .

To our knowledge, the only available estimations for K_{Lang} in a bromide–ozone system was presented by Oldridge and Abbatt (Oldridge and Abbatt, 2011) and in the IUPAC evaluation (based on the same data)(Berkemeier *et al.*, 2013). As described in the theory results sections (and confirmed by the photoemission experiments) the pre–transition state species $[Br\bullet OOO^-]$ is stabilized by water and has a strong preference for the aqueous solution surface. We have adopted the energy difference between Br^- /water cluster $^1[Br^- \bullet 4H_2O]$ and the ozonide at the interface, 5.7 kJ/mol, from the energy diagram as the relevant energy for determining the negative temperature dependence of K_{Lang} (which controls the surface coverage of $[Br\bullet OOO^-]$).

Using this energy, we parameterized a temperature–dependent K_{Lang} in an Arrhenius expression with K_{Lang} observed by Oldridge and Abbatt at 0 °C as a fixed reference:

$$K_{Lang} = 6.0 \times 10^{-13} \cdot \exp\left(\frac{5.7 \text{ kJ mol}^{-1}}{RT}\right), \quad (10)$$

Where R is the gas constant (8.314 J mol⁻¹K⁻¹).

The removal of the surface species depends on k_s , the rate of the formation of BrO^- , which is limited by the energy difference to the transition state assuming a spin crossing. We therefore adopted the energy difference between the surface species and transition state

Chapter 2 Probing the interfacial process of bromide oxidation by ozone in aqueous salt solutions

species assuming spin crossing, 76.4kJ mol^{-1} , for parameterizing k_s . We have assumed that k_s is independent of the bromide concentration. This assumption is based on the stability of the surface species. Due to this stability, we expect that the surface is mostly saturated with respect to $[\text{Br}\cdot(\text{O}_3)]^-$ and effectively replenished from the excess in the bulk.

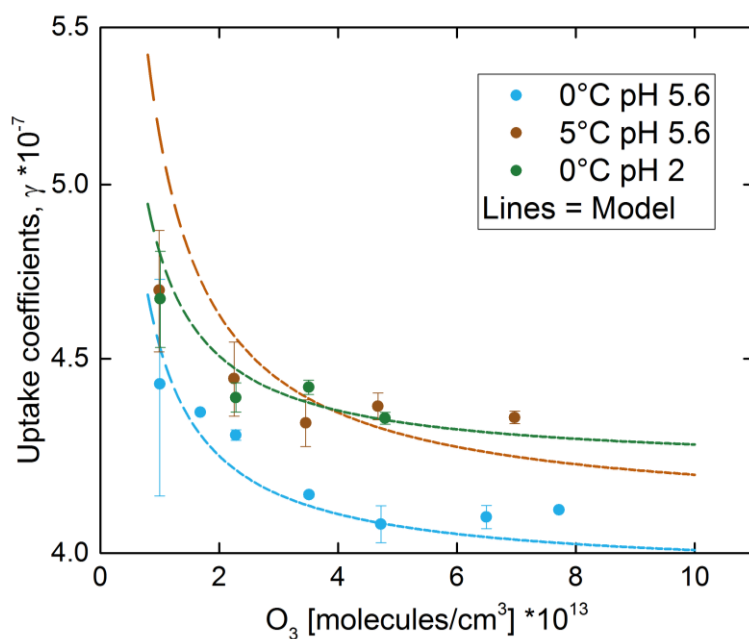
$$k_s = 2.1 \times 10^{12} \cdot \exp\left(\frac{-76.4\text{kJ mol}^{-1}}{RT}\right) \quad (11)$$

The measured data of γ_{obs} at the two different temperatures and pH values, and at different bromide concentrations, were fitted simultaneously by equations (2) to (4), with the rate coefficients and K_{Lang} as free variables. We note that several of the parameters are not well constrained by our data alone, since the surface reactivity is likely limited by the product of N_{max} , k_s^{II} , K_{Lang} . However, using available information with respect to the bulk solution properties, in combination with evidence from the present and past kinetic experiments, and taking into account the present spectroscopy and theory results, the kinetic model is able to rationalize the data obtained. The strong stability of the $[\text{Br}\cdot\text{OOO}^-]$ complex at the aqueous solution – vapor interface leads to saturating surface coverage as a function of both gas phase ozone concentration and bulk aqueous phase bromide concentration. This is the only way the surface component of the reactivity can become independent of the bromide concentration, as indicated by the experiment.

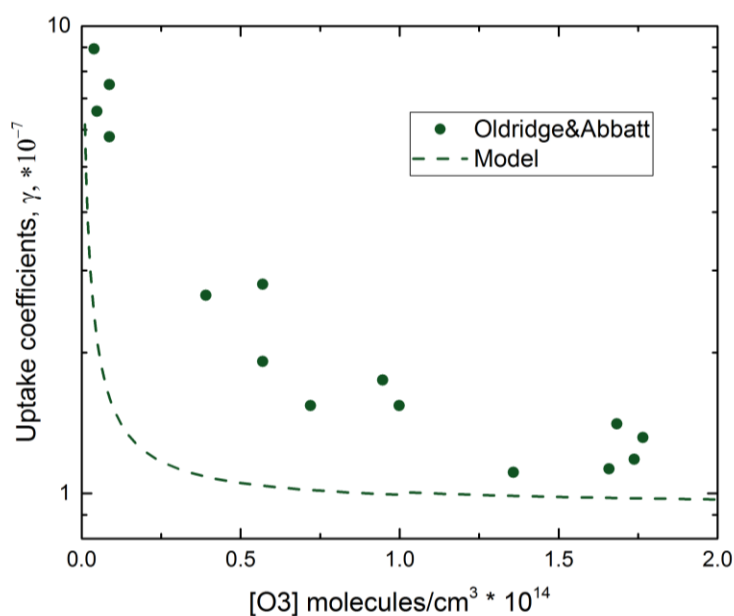
Supplementary Note 2. Comparison of measured kinetic data with model fits

Supplementary Figure 1 shows the data measured at 0 °C and 5 °C used together with the data in the main paper for fitting the model. In this case, the O_3 concentration was measured and used to obtain the measured ozone uptake coefficients.

To further assess the performance of the model, we compared it with Oldridge and Abbatt's measurement at 0 °C, and pH 1.97 (Supplementary Figure 2) (Oldridge and Abbatt, 2011). The model seems to underestimate these significantly, especially at intermediate ozone concentrations. However, the disagreement remains within less than a factor of two, and the increase of the uptake coefficient still occurs within the same ozone concentration range. Also, we caution that Oldridge and Abbatt measured the production of $\text{Br}_{2(\text{g})}$, which may include further steps in the activation reaction, not accounted for in the model, which treats O_3 loss only. Secondary halogen chemistry both in the boat containing the solution and along the surfaces in their flow system downstream of the boat could have enhanced the Br_2 yields.



Supplementary Figure 1. Assessment of the model (equation (3)) used to fit the experimental data at different temperatures and pH; all measurements were conducted with 0.125 M NaBr. Error bars represent the standard deviations of measured values.



Supplementary Figure 2. Model established by equation (3) compared to the measured data from Oldridge and Abbatt's study (Oldridge and Abbatt, 2011) at 0 °C, pH 1.97, [KBr⁻] = 8.6 mM, and [NaCl] = 0.55 M.

Supplementary Note 3. Computational set-up and benchmark

Chapter 2 Probing the interfacial process of bromide oxidation by ozone in aqueous salt solutions

Electronic structure calculations

Electronic structure calculations were performed using the Gaussian09 package (Frisch *et al.*, 2009)

The geometries for the bromide ozone reaction in water were optimized at MP2 level with 6–311++g(df,p) basis set (Moller and Plesset, 1934). Harmonic vibrational frequency analysis was used to verify the nature of the optimized structures (minima and saddle points) and to provide the zero-point vibrational energy (ZPE) correction. Supplementary Table 1 reports the Cartesian coordinate for $^1[\text{Br}\bullet\text{OOO}^-]$ optimized geometries, which are shown in the Supplementary Figure 3 with 1, 2, 3 and 4 water molecules.

Supplementary Table 1: Cartesian coordinates in Å for the $^1[\text{Br}\bullet\text{OOO}^-]$ structures, optimized at MP2 level.

Pre complex on singlet – 1 water

| | | | |
|----|-----------|-----------|-----------|
| O | -2.028302 | 0.138733 | 0.726193 |
| O | -1.331408 | 1.123714 | 0.087647 |
| O | -2.390859 | -0.830960 | -0.008698 |
| Br | 1.049010 | 0.055399 | -0.201898 |
| O | -1.069093 | -0.696775 | -2.809647 |
| H | -2.324401 | -0.449547 | -2.324401 |
| H | -1.701216 | -0.694276 | -2.084569 |

Pre complex on singlet – 2 water

| | | | |
|----|-----------|-----------|-----------|
| O | -1.829179 | 0.336954 | 0.567548 |
| O | -1.053554 | 1.228328 | -0.121675 |
| O | -1.842055 | -0.849271 | 0.092971 |
| Br | 1.334460 | 0.409987 | 0.530750 |
| O | -1.625829 | -1.627553 | -2.895359 |
| H | -0.940646 | -0.961359 | -3.046483 |
| H | -1.734378 | -1.554131 | -1.942769 |
| O | 0.199782 | 0.578217 | -2.632505 |
| H | 1.002157 | 0.377054 | -2.138821 |
| H | -0.361737 | 0.864582 | -1.896434 |

Pre complex on singlet – 3 water

| | | | |
|----|-----------|-----------|-----------|
| O | 0.570676 | 0.890872 | -0.034786 |
| O | -0.098421 | 2.065054 | -0.211318 |
| O | 0.048454 | 2.921100 | 0.720605 |
| Br | -0.838934 | -0.330286 | 1.782212 |
| O | 1.074274 | 1.956665 | 1.074274 |
| H | 0.505113 | 1.192273 | 3.232861 |
| H | 0.947062 | 2.446327 | 2.581750 |

| | | | |
|---|----------|-----------|----------|
| O | 1.406903 | -0.758554 | 1.406903 |
| H | 2.285485 | -0.003269 | 0.855335 |
| H | 1.628665 | -1.033053 | 1.681871 |
| O | 3.732763 | 0.777858 | 3.615718 |
| H | 3.503776 | 0.144443 | 2.924617 |
| H | 2.906484 | 1.274392 | 3.686174 |

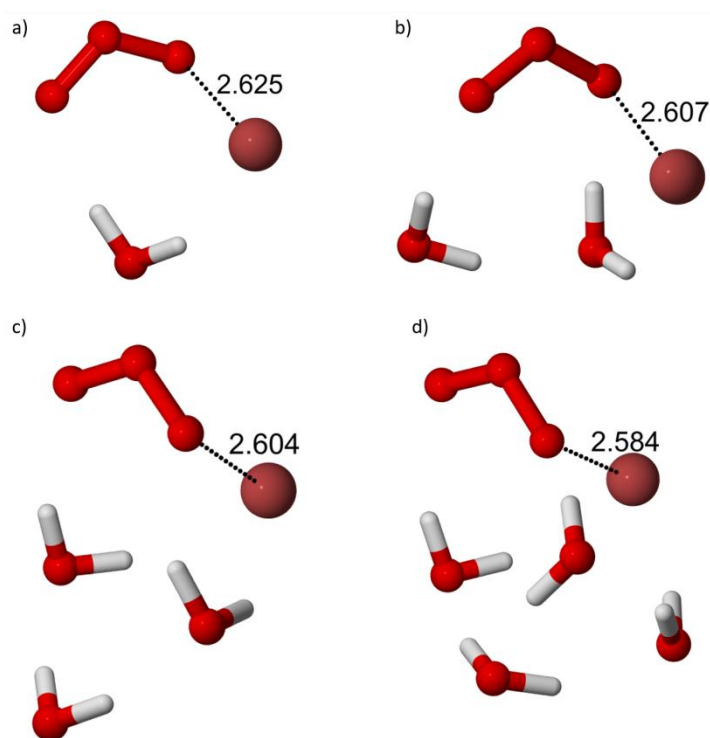
Pre complex on singlet – 4 water

| | | | |
|----|-----------|-----------|-----------|
| O | 0.114819 | 2.017727 | -1.781213 |
| O | -0.087542 | 1.323295 | -0.629811 |
| O | -0.351804 | 1.455881 | -2.825809 |
| Br | 1.616914 | -0.614865 | -0.752859 |
| O | -1.642114 | 1.297322 | 1.790612 |
| H | -1.084111 | 1.573737 | 1.056675 |
| H | -2.224534 | 0.638899 | 1.378187 |
| O | -0.211715 | -1.273567 | 2.087916 |
| H | -0.458498 | -0.355742 | 2.261192 |
| H | 0.427101 | -1.185151 | 1.366838 |
| O | -2.755410 | -1.102994 | 0.694493 |
| H | -2.011572 | -1.482342 | 1.182887 |
| H | -2.461076 | -1.182559 | -0.227129 |
| O | -1.487014 | -1.248374 | -1.862975 |
| H | -0.577567 | -1.371597 | -1.552270 |
| H | -1.410255 | -0.365879 | -2.242040 |

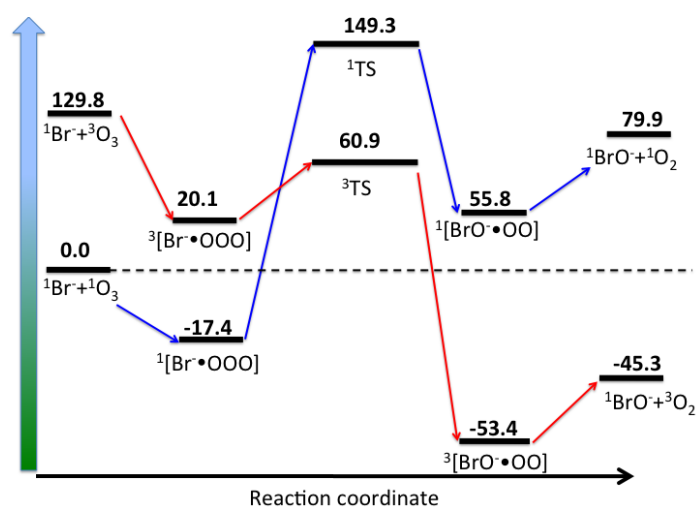
In order to improve the energetic, single point energy calculations were performed at CCSD(T)/6-311++g(df,p) level, on top of the previously optimized structures at the MP2 level (Raghavachari *et al.*, 1989). Possible multi-reference character for this reaction was already addressed in our previous publication showing negligible effects on the structures and reaction profile (Gladich *et al.*, 2015).

Previous results by Gladich *et al.* at the CCSD(T)/6-311++g(df,p)//CCSD/6-311++g(df,p) levels in the gas phase reaction were used as benchmark (Gladich *et al.*, 2015). Supplementary Figure 4 shows the gas phase reaction profile at CCSD(T)//MP2 level. Comparison with Ref. (Gladich *et al.*, 2015) shows that the key features and order of the reaction intermediates are preserved and also the relative energies are reasonable close to the benchmark ones.

Chapter 2 Probing the interfacial process of bromide oxidation by ozone in aqueous salt solutions

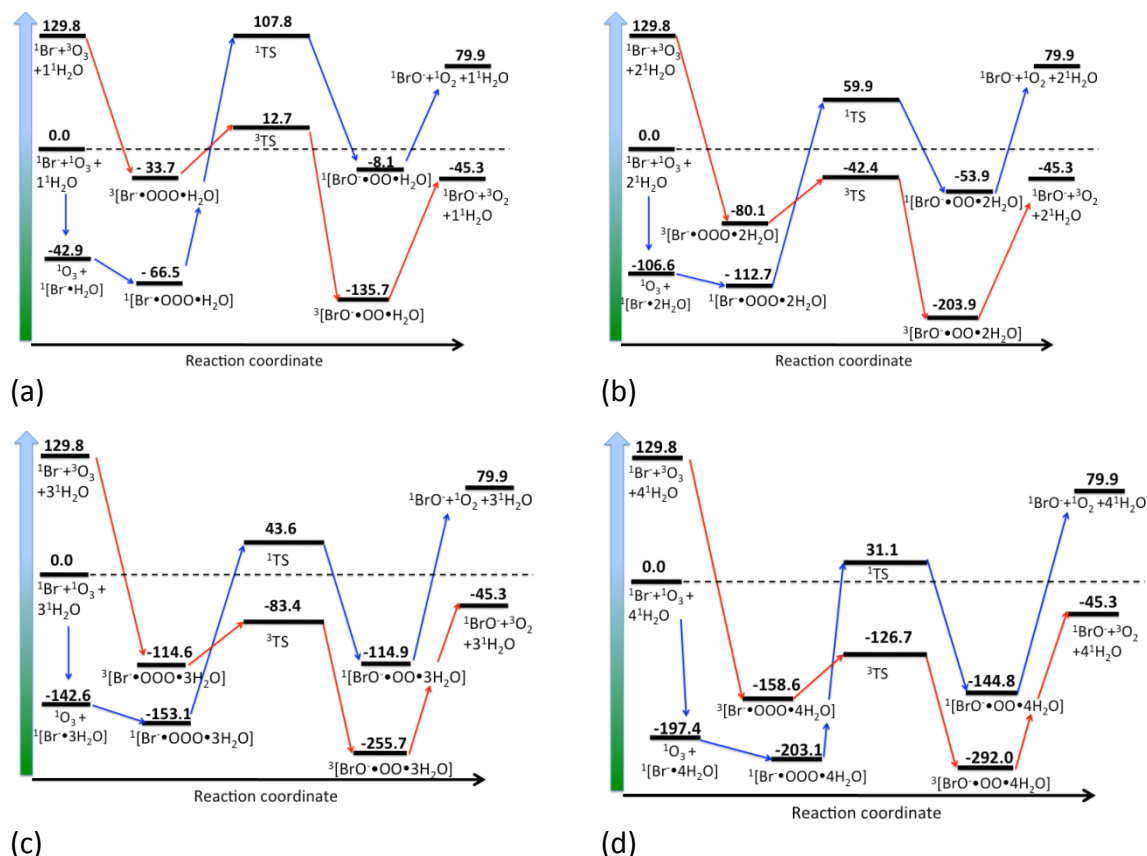


Supplementary Figure 3. $^1[\text{Br}\bullet\text{OOO}^-]$ optimized geometries at MP2/6-311++g(df,p) level with one, two, three and four water molecules in panels a), b), c) and d), respectively. The figure also show the distance between the bromine atom and the closest $^1[\text{Br}\bullet\text{OOO}^-]$ oxygen.



Supplementary Figure 4. Reaction profile for the gas-phase reaction of bromide with ozone along the singlet (blue) and triplet (red) surface obtained at CCSD(T)//MP2 level using 6-311++g(df,p) basis set. All energies are relative to the singlet reactants, corrected by adding the Zero Point Energy (ZPE) and expressed in kJ/mol.

Supplementary Figure 5 shows the reaction profile in 1, 2, 3, and 4 water clusters, indicating that the addition of water stabilizes the pre-complex compared the reaction level, while the barrier on the single and triplet transition states remains high.



Supplementary Figure 5. Reaction profile for the bromide–ozone reaction along the singlet (blue) and triplet (red) surface obtained at CCSD(T)/MP2 level with 6–311++g(df,p) basis set. Panels **a**, **b**, **c** and **d** show the energetic profiles for the different intermediates with one, two, three and four water molecules, respectively. All energies are relative to the singlet reactants and are reported in kJ/mol, including Zero Point Energy (ZPE) correction.

First Principle Molecular Dynamics Simulations

First Principle molecular dynamics simulations based on density functional theory were performed using the CP2K code to study the stability and dynamics of the $^1[\text{Br}\bullet\text{OOO}^-]$ on the surface of water (Hutter *et al.*, 2014). The $^1[\text{Br}\bullet\text{OOO}^-]$ structure obtained at electronic structure level (see above) was placed on the top of an equilibrated water slab of 216 water molecules on a simulation cell of $20 \text{ \AA} \times 20 \text{ \AA} \times 60 \text{ \AA}$ dimension. An optimization of the initial condition was then performed in order to avoid artificially large forces. Next, a molecular

Chapter 2 Probing the interfacial process of bromide oxidation by ozone in aqueous salt solutions

dynamics simulation was carried out in a constant volume and temperature ensemble, using BLYP functional (Becke, 1988; Lee *et al.*, 1988) with Grimme dispersion correction (Grimme *et al.*, 2010). Temperature was kept at 300 K by using a Nose–Hoover thermostat. While the valence electrons were explicitly taken into account, Goedecker–Teter–Hutter pseudopotentials were used to model core electrons (Goedecker *et al.*, 1996). The Gaussian–type orbital basis set DZVP was used in combination with plane wave representation, with an energy cutoff at 400 Ry. Similar set–up has been already adopted in literature for studies of liquid water interfaces with and without surfactants (Baer *et al.*, 2011; Baer *et al.*, 2014).

Core Electron Binding Energy Calculations

Core electron binding excitation (CEBE) energies were calculated on top of MP2/6–311++g(df,p) geometries. Additionally, it is assumed that the core–hole state geometries are identical to the corresponding ground states. The effect of relaxation was described by the Δ MP2 approach where the electron correlation was described using MP2/aug–cc–pVTZ level of theory (Holme *et al.*, 2011; Shim *et al.*, 2011). The CEBE is calculated as the difference between the ground state energy and the cation core–hole state formed by ejection of Br[–] 3d electron. Freezing the molecular orbitals during the SCF procedure prevented the collapse of the core–hole state to the more stable energetic state. All CEBE calculations were performed using GAMESS suite of codes (Schmidt *et al.*, 1993).

Supplementary Note 4. Liquid–jet x–ray photoelectron spectroscopy

Technical and experimental details

A gas dosing system, developed by Microliquids GmbH, was connected to the liquid jet assembly. A second nozzle, made of titanium, was screwed concentrically to the quartz nozzle delivering the liquid (see Figure 3a). The outer nozzle has a 500 μm orifice, which is placed 1.0 mm far from the aperture of the quartz nozzle. The gas (either pure oxygen or a mixture of 1% ozone in oxygen, generated in situ by means of a commercial ozone generator (502, Fischer Technology), whose flow was adjusted by means of a variable leak valve connected to the nozzle *via* a 1/16" PEEK tube, reached the nozzle and was interacting efficiently with the liquid wire in the area prior to injection into the experimental chamber. The efficiency of O₂ to O₃ conversion in the ozone generator was checked in separate experiments by means of the same ozone analyzer as described in the context of the kinetic experiments above. The purity of the gas was checked by means of a quadrupole mass spectrometer installed in the second differential pumping stage of the electron analyzer. During the experiment, we made use of two cold traps (liquid nitrogen) and a 27 m³ h^{–1} root pump. Before dosing the gas, the pressure in the experimental chamber was 3·10^{–2} mbar. While dosing the gas, we set the pressure to 0.25 mbar. The advantage of using a gas

delivery nozzle, is that we can expect a higher local pressure in the area between the orifice of the quartz nozzle and that of the titanium one. The diffusion of the gas into the liquid is fast enough that gas–liquid equilibrium over the probe depth of the XPS experiments is established within 1 μ s. Because the solubility of ozone is low, the net flux into the liquid is low, and no gradients will limit this flux in the gas phase. The residence time of the liquid filament within the dosing system is approx. 100 μ s and between the dosing system and the point at which it hits the X–ray is 100 μ s. Therefore, the gas – surface and gas – liquid equilibria follow the changing pressure in the gas phase. A preliminary experiment carried out without the gas dosing system showed a similar evolution of the Br 3d spectrum while dosing ozone (0.1–0.2 mbar background pressure). However, the effect was less pronounced than after employing the gas dosing system, indicating that loss of ozone to the chamber walls has a significant effect on the gas exposure on the liquid.

Concerning the diffusion of bromide ions in the solution, the evolution of the surface concentration of an initially free surface by diffusion from the bulk with time is given by equation 12:

$$c_s = 2 \left(\frac{D}{\pi} \right)^{1/2} c t^{1/2} \quad (12)$$

where c is the bulk concentration of the bromide solution ($7.53 \cdot 10^{19}$ molecules cm^{-3}), c_s is the surface concentration of $[\text{Br} \bullet \text{OOO}^-]$ (estimated as $2 \cdot 10^{12}$ molecules cm^{-2}), and D is the diffusion coefficient ($2.41 \cdot 10^{-10}$ $\text{cm}^2 \text{s}^{-1}$), evaluated through the Stokes–Einstein equation. The time needed to re–establish the equilibrium concentration is approx. 2 μ s, much lower than the time between the injection of the liquid filament and the detection point (100 μ s).

The Swiss light source synchrotron operates in top–up mode, thus the photon flux did not change during measurements. It is well known from the literature that X–rays can induce the radiolysis of water, leading to the formation of highly reactive hydroxyl radicals (reference (George *et al.*, 2012) and references therein), which could affect the measurements. Thanks to the high speed of the injected liquid filament, the liquid microjet technique limits the beam damage, and the concentration of radicals does not reach $1 \cdot 10^{-6}$ mol/L under the experimental conditions adopted in this study.

The 0.125 mol L^{-1} solutions of bromide and bromate were prepared by adding sodium bromide (NaBr, $\geq 99.0\%$, Sigma–Aldrich) and sodium bromate (NaBrO₃, $\geq 99.5\%$, Sigma–Aldrich), respectively, to Milli–Q water (Millipore, $18.2 \text{ M}\Omega \text{ cm}^{-1}$ at 25 °C). The 0.08 mol L^{-1} hypobromite solution was prepared by disproportionation of Br₂ in a 0.5 mol L^{-1} solution of NaOH (Polak *et al.*, 1966). Hypobromite and bromide were generated based on the reaction:

Chapter 2 Probing the interfacial process of bromide oxidation by ozone in aqueous salt solutions

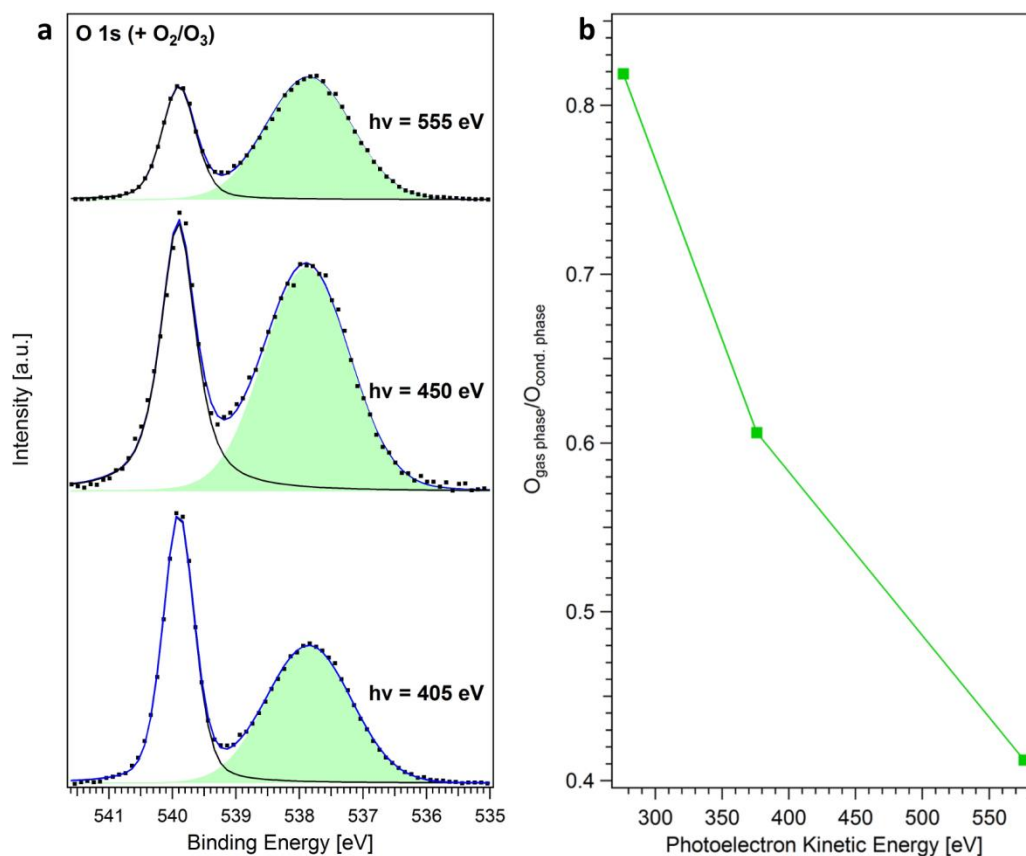


Hypobromite is thermodynamically unstable and disproportionates to bromide and bromate. To slower this reaction, we cooled the solution to 0 °C both during the preparation and the experiment. According to our spectra (Figure 3c), bromate was not formed for the whole duration of the experiment.

The photoemission spectra were fitted using Shirley background subtraction and Gaussian line shapes (Lee *et al.*, 2015). For Br 3d, the spin-orbit split was fixed at 1.03 eV. The Full width at half maximum (FWHM) of the peaks was constrained for the whole set of processed data (1.05 eV). A single doublet allowed getting a good deconvolution of the Br 3d signals acquired without dosing and while dosing oxygen. In the presence of ozone, a second doublet had to be added to reach the same correlation. The second doublet is made of Gaussian peaks having a spin-orbit split fixed at 1.09 eV and FWHM of 1.10 eV. The best correlation was obtained applying a chemical shift of +0.7 eV to the binding energy of the second doublet.

Evolution of the O 1s spectrum as a function of the excitation energy

The spectra reported in the Supplementary Figure 6a show the O 1s spectra (excited by second order photon light) acquired at increasing excitation energy, which corresponds to increasing kinetic energy of the photoelectrons. The three kinetic energies are the same as those of the Br 3d spectra plotted in Figure 4c (manuscript). The spectra were separated into two components: one at high binding energy (centered at 539.9 eV), associated to the gas phase of water, and another, centered at 537.9 eV, associated to the condensed phase of water. The latter was used to normalize the area of the Br 3d signal of the [Br•OOO⁻] complex (Figure 4d). Water being the solvent, it can be considered as a reference during the measurements. The Supplementary Figure 6b shows the ratio between the area of the peak of the oxygen gas phase and that of the condensed phase. The ratio decreases as the kinetic energy of the photoelectrons increases. Indeed, an increase of the kinetic energy of the photoelectrons corresponds to an increase of the probed depth. As long as the energy is increased, a larger thickness of the liquid wire is probed, while the contribution of the gas phase remains constant, apart from changes due to changes in photon flux and cross section (the pressure in the experimental chamber was constant during the whole duration of the experiment).



Supplementary Figure 6. Signal of the O 1s acquired at different excitation energies, $h\nu=405$, 450, and 555 eV (corresponding to the second order excitation energies $h\nu=810$, 900, and 1110 eV), corresponding to the kinetic energies (peak centroid) of 276, 376 and 575 eV, respectively.

Evaluation of the [Br•OOO⁻] surface coverage

Supplementary Figure 7 shows a rough estimate of the surface coverage of [Br•OOO⁻] complex based on the XPS data acquired at increasing photoelectron kinetic energy (276, 376, and 576 eV). We employed two models to fit the behavior of the ratio between the intensity of the peaks related to the complex (I_{BrOOO^-}) and that of the peaks related to the bulk 0.125 mol L⁻¹ solution of Br⁻ (I_{Br^-}) (see Figure 4c). Passing from 276 to 376 eV there is not a significant decrease of the $I_{\text{BrOOO}^-}/I_{\text{Br}^-}$ ratio, and this reflects on the quality of the fitting (the experimental point corresponding to 376 eV is out of the confidence interval). A possible reason is that the difference in the excitation energy (100 eV) is not enough to vary considerably the information depth.

The first model (Supplementary Figure 7a and b) does not take into account the attenuation of the photoemission signal from the bulk by the overlayer ([Br•OOO⁻] complex). The formula adopted is the following:

Chapter 2 Probing the interfacial process of bromide oxidation by ozone in aqueous salt solutions

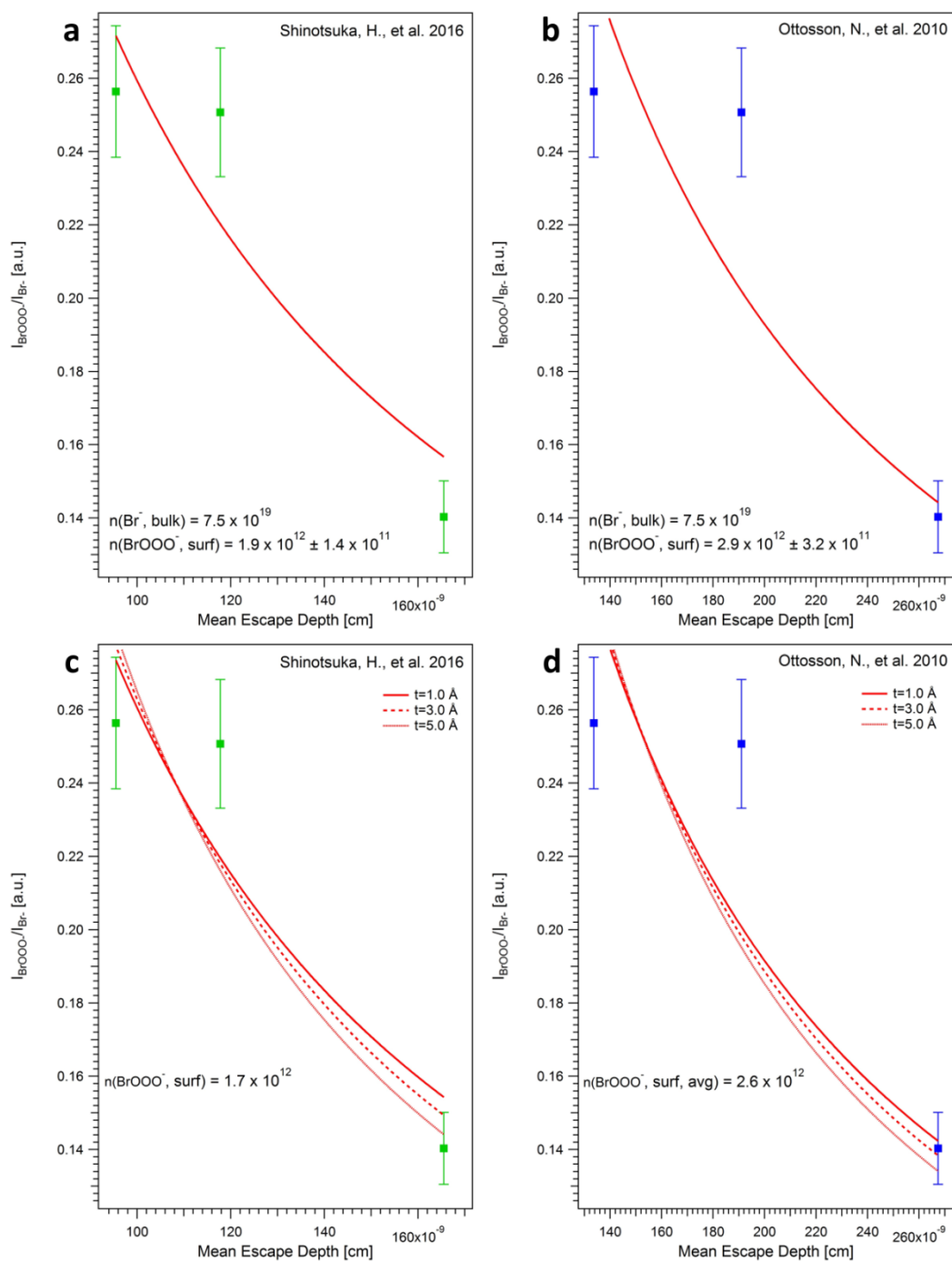
$$\frac{I_{[\text{Br}\cdot\text{OOO}^-]}}{I_{\text{Br}^-}} = \frac{n([\text{Br}\cdot\text{OOO}^-]_{\text{surface}})}{n(\text{Br}^-, \text{bulk}) \cdot \text{MED}} \quad (13)$$

where $n([\text{Br}\cdot\text{OOO}^-]_{\text{surface}})$ is the surface coverage of the $[\text{Br}\cdot\text{OOO}^-]$ complex (complexes/cm²), $n(\text{Br}^-, \text{bulk})$ is the ion density of bromide ions in the solution (ions/cm³), and MED is the mean escape depth of the photoelectrons emitted from the ions (defined as $\langle \text{MED} \rangle_{\text{avg}} = 2/\pi \cdot \text{IMFP}$, where IMFP is the inelastic mean free path of the photoelectrons at each kinetic energy) (Winter and Faubel, 2006). We estimated the surface coverage employing two sets of IMFPs. In 2010, Ottosson *et al.* obtained an experimental curve of the electron attenuation length (EAL) in the 70–900 eV range for water (Ottosson *et al.*, 2010). Recently, Shinotsuka *et al.* calculated the electron inelastic mean free path for liquid water from its optical energy–loss function (Shinotsuka *et al.*, 2016). The values are different from each other, thus we calculated the surface coverage using Shinotsuka’s IMFPs in Supplementary Figure 7a, and Ottosson’s EALs in Supplementary Figure 7b. The surface coverages are 1.9 and $2.9 \cdot 10^{12}$ complexes cm⁻², respectively.

We adopted a second model to fit the experimental data available, which takes into account the attenuation of the signal from the bulk aqueous solution by a thin surface layer of $[\text{Br}\cdot\text{OOO}^-]$ complex. The simplified equation, inspired by the literature (Fadley, 1978; Cimino *et al.*, 1999), is the following:

$$\frac{I_{[\text{Br}\cdot\text{OOO}^-]}}{I_{\text{Br}^-}} = \frac{\rho_{[\text{Br}\cdot\text{OOO}^-]}}{n(\text{Br}^-, \text{bulk})} \cdot \left[1 - \exp\left(-\frac{t}{\text{MED}}\right) \right] \cdot \exp\left(\frac{t}{\text{MED}}\right) \quad (14)$$

where $\rho_{[\text{Br}\cdot\text{OOO}^-]}$ is the ion density of the $[\text{Br}\cdot\text{OOO}^-]$ complex (complexes cm⁻³), and t is the thickness of the surface layer ($[\text{Br}\cdot\text{OOO}^-]$ complex). Supplementary Figure 7 c and d show the results attained using the MED from Shinotsuka and Ottosson, respectively. Three fitting functions, obtained employing three pre-set values of t (in the 1.0 to 5.0 Å range) are showed. The best correlation is found using the lower values, i.e. 1.0 and 3.0 Å, proving that the complex does not diffuse toward the bulk. The surface coverages (average value between the three thicknesses, obtained multiplying $\rho_{[\text{Br}\cdot\text{OOO}^-]}$ by t) are in good agreement with the results shown in Supplementary Figure 7a and b. The values, 1.7 and $2.6 \cdot 10^{12}$ complexes cm⁻², decrease by ca. 10% as compared to those obtained with the first model, because of the attenuation.



Supplementary Figure 7. Evaluation of the surface coverage of the $[\text{Br}\bullet\text{OOO}^-]$ complex (a)–(b) Simple approximation, without considering the surface attenuation due to the $[\text{Br}\bullet\text{OOO}^-]$ complex; (c)–(d) considering the attenuation of the signal from the bulk (0.125 mol L^{-1} aqueous solution of Br^-) by a surface layer containing the $[\text{Br}\bullet\text{OOO}^-]$ complex. The error bars were calculated propagating the errors associated to the peak areas of three different measurements.

Bibliography

Abbatt, J., Oldridge, N., Symington, A., Chukalovskiy, V., McWhinney, R. D., Sjostedt, S., and Cox, R. A.: Release of Gas-Phase Halogens by Photolytic Generation of OH in Frozen Halide-Nitrate Solutions: An Active Halogen Formation Mechanism?, *J Phys Chem A*, 114, 6527–6533, 10.1021/jp102072t, 2010.

Ammann, M., Poschl, U., and Rudich, Y.: Effects of reversible adsorption and Langmuir-Hinshelwood surface reactions on gas uptake by atmospheric particles, *Phys Chem Chem Phys*, 5, 351–356, 10.1039/b208708a, 2003.

Baer, M. D., Mundy, C. J., McGrath, M. J., Kuo, I. F. W., Siepmann, J. I., and Tobias, D. J.: Re-examining the properties of the aqueous vapor-liquid interface using dispersion corrected density functional theory, *The Journal of Chemical Physics*, 135, 124712, 10.1063/1.3633239, 2011.

Baer, M. D., Tobias, D. J., and Mundy, C. J.: Investigation of Interfacial and Bulk Dissociation of HBr, HCl, and HNO₃ Using Density Functional Theory-Based Molecular Dynamics Simulations, *The Journal of Physical Chemistry C*, 118, 29412–29420, 10.1021/jp5062896, 2014.

Battino, R., Rettich, T. R., and Tominaga, T.: The Solubility of Oxygen and Ozone in Liquids, *J Phys Chem Ref Data*, 12, 163–178, 1983.

Becke, A. D.: Density-functional exchange-energy approximation with correct asymptotic behavior, *Physical Review A*, 38, 3098–3100, 10.1103/PhysRevA.38.3098, 1988.

Berkemeier, T., Huisman, A. J., Ammann, M., Shiraiwa, M., Koop, T., and Pöschl, U.: Kinetic regimes and limiting cases of gas uptake and heterogeneous reactions in atmospheric aerosols and clouds: a general classification scheme, *Atmospheric Chemistry and Physics*, 13, 6663–6686, 10.5194/acp-13-6663-2013, 2013.

Bibliography

Berkemeier, T., Steimer, S. S., Krieger, U. K., Peter, T., Poschl, U., Ammann, M., and Shiraiwa, M.: Ozone uptake on glassy, semi-solid and liquid organic matter and the role of reactive oxygen intermediates in atmospheric aerosol chemistry, *Phys Chem Chem Phys*, 18, 12662–12674, 10.1039/c6cp00634e, 2016.

Bertram, T. H., Thornton, J. A., Riedel, T. P., Middlebrook, A. M., Bahreini, R., Bates, T. S., Quinn, P. K., and Coffman, D. J.: Direct observations of N₂O₅ reactivity on ambient aerosol particles, *Geophys Res Lett*, 36, Artn L19803

10.1029/2009gl040248, 2009.

Bin, A. K.: Ozone solubility in liquids, *Ozone–Sci Eng*, 28, 67–75, 10.1080/01919510600558635, 2006.

Brown, M. A., Redondo, A. B., Jordan, I., Duyckaerts, N., Lee, M. T., Ammann, M., Nolting, F., Kleibert, A., Huthwelker, T., Machler, J. P., Birrer, M., Honegger, J., Wetter, R., Worner, H. J., and van Bokhoven, J. A.: A new endstation at the Swiss Light Source for ultraviolet photoelectron spectroscopy, X-ray photoelectron spectroscopy, and X-ray absorption spectroscopy measurements of liquid solutions, *Rev Sci Instrum*, 84, Artn 073904

10.1063/1.4812786, 2013.

Cao, L., Wang, C. G., Mao, M., Grosshans, H., and Cao, N. W.: Derivation of the reduced reaction mechanisms of ozone depletion events in the Arctic spring by using concentration sensitivity analysis and principal component analysis, *Atmos Chem Phys*, 16, 14853–14873, 10.5194/acp-16-14853-2016, 2016.

Chameides, W. L., and Davis, D. D.: The Free-Radical Chemistry of Cloud Droplets and Its Impact Upon the Composition of Rain, *J Geophys Res–Oc Atm*, 87, 4863–4877, DOI 10.1029/JC087iC07p04863, 1982.

Chameides, W. L.: Possible Role of NO₃ in the Nighttime Chemistry of a Cloud, *J Geophys Res–Atmos*, 91, 5331–5337, DOI 10.1029/JD091iD05p05331, 1986.

Cimino, A., Gazzoli, D., and Valigi, M.: XPS quantitative analysis and models of supported oxide catalysts, *J Electron Spectrosc*, 104, 1–29, Doi 10.1016/S0368-2048(98)00300-4, 1999.

Bibliography

Clifford, D., and Donaldson, D. J.: Direct experimental evidence for a heterogeneous reaction of ozone with bromide at the air–aqueous interface, *J Phys Chem A*, 111, 9809–9814, 10.1021/jp074315d, 2007.

De Haan, D. O., Brauers, T., Oum, K., Stutz, J., Nordmeyer, T., and Finlayson–Pitts, B. J.: Heterogeneous chemistry in the troposphere: experimental approaches and applications to the chemistry of sea salt particles, *Int Rev Phys Chem*, 18, 343–385, Doi 10.1080/014423599229910, 1999.

Fadley, C. S., Brundle, C. R., Baker, A. D.: *Electron Spectroscopy: Theory, Techniques and Applications*, Academic Press, New York, 1978.

Frisch, M. J., Trucks, G. W., Schlegel, H. B., Scuseria, G. E., Robb, M. A., Cheeseman, J. R., Scalmani, G., Barone, V., Mennucci, B., Petersson, G. A., Nakatsuji, H., Caricato, M., Li, X., Hratchian, H. P., and Izmaylov, A. F.: *Gaussian, Inc. Rev. E01*, Wallingford CT, 2009.

George, G. N., Pickering, I. J., Pushie, M. J., Nienaber, K., Hackett, M. J., Ascone, I., Hedman, B., Hodgson, K. O., Aitken, J. B., Levina, A., Glover, C., and Lay, P. A.: X–ray–induced photo–chemistry and X–ray absorption spectroscopy of biological samples, *J Synchrotron Radiat*, 19, 875–886, 10.1107/S090904951203943x, 2012.

Gerber, R. B., Varner, M. E., Hammerich, A. D., Riikonen, S., Murdachaew, G., Shemesh, D., and Finlayson–Pitts, B. J.: Computational Studies of Atmospherically–Relevant Chemical Reactions in Water Clusters and on Liquid Water and Ice Surfaces, *Accounts Chem Res*, 48, 399–406, 10.1021/ar500431g, 2015.

Ghosal, S., Shbeeb, A., and Hemminger, J. C.: Surface segregation of bromine in bromide doped NaCl: Implications for the seasonal variations in Arctic ozone, *Geophys Res Lett*, 27, 1879–1882, Doi 10.1029/2000gl011381, 2000.

Gladich, I., Francisco, J. S., Buszek, R. J., Vazdar, M., Carignano, M. A., and Shepson, P. B.: Ab Initio Study of the Reaction of Ozone with Bromide Ion, *J Phys Chem A*, 119, 4482–4488, 10.1021/jp5101279, 2015.

Goedecker, S., Teter, M., and Hutter, J.: Separable dual–space Gaussian pseudopotentials, *Physical Review B*, 54, 1703–1710, 10.1103/PhysRevB.54.1703, 1996.

Bibliography

Grimme, S., Antony, J., Ehrlich, S., and Krieg, H.: A consistent and accurate ab initio parametrization of density functional dispersion correction (DFT–D) for the 94 elements H–Pu, *Journal of Chemical Physics*, 132, 154104, 10.1063/1.3382344, 2010.

Gunten, U. v.: Ozonation of drinking water: Part II. Disinfection and by–product formation in presence of bromide, iodide or chlorine, *Water Res*, 37, 2003.

Haag, W. R., and Hoigne, J.: Ozonation of Bromide–Containing Waters – Kinetics of Formation of Hypobromous Acid and Bromate, *Environ Sci Technol*, 17, 261–267, DOI 10.1021/es00111a004, 1983.

Haag, W. R., Hoigne, J., and Bader, H.: Improved Ammonia Oxidation by Ozone in the Presence of Bromide Ion during Water–Treatment, *Water Res*, 18, 1125–1128, Doi 10.1016/0043–1354(84)90227–6, 1984.

Hammerich, A. D., and Buch, V.: An alternative near–neighbor definition of hydrogen bonding in water, *J Chem Phys*, 128, Artn 111101
10.1063/1.2889949, 2008.

Hanson, D. R., Ravishankara, A. R., and Solomon, S.: Heterogeneous Reactions in Sulfuric–Acid Aerosols – a Framework for Model–Calculations, *J Geophys Res–Atmos*, 99, 3615–3629, Doi 10.1029/93jd02932, 1994.

Haruta, K., and Takeyama, T.: Kinetics of Oxidation of Aqueous Bromide Ion by Ozone, *J Phys Chem–Us*, 85, 2383–2388, DOI 10.1021/j150616a018, 1981.

Heeb, M. B., Criquet, J., Zimmermann–Steffens, S. G., and von Gunten, U.: Oxidative treatment of bromide–containing waters: Formation of bromine and its reactions with inorganic and organic compounds – A critical review, *Water Res*, 48, 15–42, 10.1016/j.watres.2013.08.030, 2014.

Hofft, O., Borodin, A., Kahnert, U., Kemper, V., Dang, L. X., and Jungwirth, P.: Surface segregation of dissolved salt ions, *J Phys Chem B*, 110, 11971–11976, 10.1021/jp061437h, 2006.

Bibliography

Holme, A., Børve, K. J., Sæthre, L. J., and Thomas, T. D.: Accuracy of Calculated Chemical Shifts in Carbon 1s Ionization Energies from Single-Reference ab Initio Methods and Density Functional Theory, *J Chem Theory Comput*, 7, 4104–4114, 10.1021/ct200662e, 2011.

Hunt, S. W., Roeselova, M., Wang, W., Wingen, L. M., Knipping, E. M., Tobias, D. J., Dabdub, D., and Finlayson-Pitts, B. J.: Formation of molecular bromine from the reaction of ozone with deliquesced NaBr aerosol: Evidence for interface chemistry, *J Phys Chem A*, 108, 11559–11572, 10.1021/jp0467346, 2004.

Hutter, J., Iannuzzi, M., Schiffmann, F., and VandeVondele, J.: cp2k: atomistic simulations of condensed matter systems, *Wiley Interdisciplinary Reviews: Computational Molecular Science*, 4, 15–25, 10.1002/wcms.1159, 2014.

Inaba, S.: Theoretical Study of Water Cluster Catalyzed Decomposition of Formic Acid, *J Phys Chem A*, 118, 3026–3038, 10.1021/jp5021406, 2014.

Inaba, S., and Sameera, W. M. C.: Dehydration of Methanediol in Aqueous Solution: An ONIOM(QM/MM) Study, *J Phys Chem A*, 120, 6670–6676, 10.1021/acs.jpca.6b06575, 2016.

Jungwirth, P., and Tobias, D. J.: Molecular structure of salt solutions: A new view of the interface with implications for heterogeneous atmospheric chemistry, *J Phys Chem B*, 105, 10468–10472, DOI 10.1021/jp012750g, 2001.

Kolb, C. E., Cox, R. A., Abbatt, J. P. D., Ammann, M., Davis, E. J., Donaldson, D. J., Garrett, B. C., George, C., Griffiths, P. T., Hanson, D. R., Kulmala, M., McFiggans, G., Poschl, U., Riipinen, I., Rossi, M. J., Rudich, Y., Wagner, P. E., Winkler, P. M., Worsnop, D. R., and O'Dowd, C. D.: An overview of current issues in the uptake of atmospheric trace gases by aerosols and clouds, *Atmos Chem Phys*, 10, 10561–10605, 10.5194/acp-10-10561-2010, 2010.

Krepelova, A., Newberg, J. T., Huthwelker, T., Bluhm, H., and Ammann, M.: The nature of nitrate at the ice surface studied by XPS and NEXAFS, *Phys Chem Chem Phys*, 12, 8870–8880, 10.1039/c0cp00359j, 2010.

Kurahashi, N., Karashima, S., Tang, Y., Horio, T., Abulimiti, B., Suzuki, Y. I., Ogi, Y., Oura, M., and Suzuki, T.: Photoelectron spectroscopy of aqueous solutions: Streaming potentials of

Bibliography

NaX (X = Cl, Br, and I) solutions and electron binding energies of liquid water and X⁻, *J Chem Phys*, 140, Artn 174506

10.1063/1.4871877, 2014.

Lakey, P. S. J., Berkemeier, T., Tong, H. J., Arangio, A. M., Lucas, K., Poschl, U., and Shiraiwa, M.: Chemical exposure–response relationship between air pollutants and reactive oxygen species in the human respiratory tract, *Sci Rep–Uk*, 6, ARTN 32916

10.1038/srep32916, 2016.

Lampimaki, M., Zelenay, V., Krepelova, A., Liu, Z., Chang, R., Bluhm, H., and Ammann, M.: Ozone–Induced Band Bending on Metal–Oxide Surfaces Studied under Environmental Conditions, *Chemphyschem*, 14, 2419–2425, 10.1002/cphc.201300418, 2013.

Lee, C., Yang, W., and Parr, R. G.: Development of the Colle–Salvetti correlation–energy formula into a functional of the electron density, *Physical Review B*, 37, 785–789, 10.1103/PhysRevB.37.785, 1988.

Lee, M. T., Brown, M. A., Kato, S., Kleibert, A., Turler, A., and Ammann, M.: Competition between Organics and Bromide at the Aqueous Solution–Air Interface as Seen from Ozone Uptake Kinetics and X–ray Photoelectron Spectroscopy, *J Phys Chem A*, 119, 4600–4608, 10.1021/jp510707s, 2015.

Li, L., Kumar, M., Zhu, C. Q., Zhong, J., Francisco, J. S., and Zeng, X. C.: Near–Barrierless Ammonium Bisulfate Formation *via* a Loop–Structure Promoted Proton–Transfer Mechanism on the Surface of Water, *J Am Chem Soc*, 138, 1816–1819, 10.1021/jacs.5b13048, 2016.

Liu, Q., Schurter, L. M., Muller, C. E., Aloisio, S., Francisco, J. S., and Margerum, D. W.: Kinetics and mechanisms of aqueous ozone reactions with bromide, sulfite, hydrogen sulfite, iodide, and nitrite ions, *Inorg Chem*, 40, 4436–4442, 10.1021/ic000919j, 2001.

Marx, D., and Hutter, J.: *Ab initio molecular dynamics*, in, Cambridge University Press, 2009.

Bibliography

McCabe, J., and Abbatt, J. P. D.: Heterogeneous Loss of Gas–Phase Ozone on n–Hexane Soot Surfaces: Similar Kinetics to Loss on Other Chemically Unsaturated Solid Surfaces, *J Phys Chem C*, 113, 2120–2127, 10.1021/jp806771q, 2009.

Miller, Y., Thomas, J. L., Kemp, D. D., Finlayson–Pitts, B. J., Gordon, M. S., Tobias, D. J., and Gerber, R. B.: Structure of Large Nitrate–Water Clusters at Ambient Temperatures: Simulations with Effective Fragment Potentials and Force Fields with Implications for Atmospheric Chemistry, *J Phys Chem A*, 113, 12805–12814, 10.1021/jp9070339, 2009.

Moller, C., and Plesset, M. S.: Note on an approximation treatment for many–electron systems, *Phys Rev*, 46, 0618–0622, DOI 10.1103/PhysRev.46.618, 1934.

Nishikata, E., Ishii, T., and Ohta, T.: Viscosities of Aqueous Hydrochloric–Acid Solutions, and Densities and Viscosities of Aqueous Hydroiodic Acid–Solutions, *J Chem Eng Data*, 26, 254–256, DOI 10.1021/je00025a008, 1981.

Nissenson, P., Wingen, L. M., Hunt, S. W., Finlayson–Pitts, B. J., and Dabdub, D.: Rapid formation of molecular bromine from deliquesced NaBr aerosol in the presence of ozone and UV light, *Atmospheric Environment*, 89, 491–506, 10.1016/j.atmosenv.2014.02.056, 2014.

Oldridge, N. W., and Abbatt, J. P. D.: Formation of Gas–Phase Bromine from Interaction of Ozone with Frozen and Liquid NaCl/NaBr Solutions: Quantitative Separation of Surficial Chemistry from Bulk–Phase Reaction, *J Phys Chem A*, 115, 2590–2598, 10.1021/jp200074u, 2011.

Olivieri, G., Parry, K. M., Powell, C. J., Tobias, D. J., and Brown, M. A.: Quantitative interpretation of molecular dynamics simulations for X–ray photoelectron spectroscopy of aqueous solutions, *J Chem Phys*, 144, Artn 154704

10.1063/1.4947027, 2016.

Ottosson, N., Faubel, M., Bradforth, S. E., Jungwirth, P., and Winter, B.: Photoelectron spectroscopy of liquid water and aqueous solution: Electron effective attenuation lengths and emission–angle anisotropy, *J Electron Spectrosc*, 177, 60–70, 10.1016/j.elspec.2009.08.007, 2010.

Bibliography

Oum, K. W., Lakin, M. J., and Finlayson-Pitts, B. J.: Bromine activation in the troposphere by the dark reaction of O₃ with seawater ice, *Geophys Res Lett*, 25, 3923–3926, Doi 10.1029/1998gl900078, 1998.

Parrella, J. P., Jacob, D. J., Liang, Q., Zhang, Y., Mickley, L. J., Miller, B., Evans, M. J., Yang, X., Pyle, J. A., Theys, N., and Van Roozendaal, M.: Tropospheric bromine chemistry: implications for present and pre-industrial ozone and mercury, *Atmos Chem Phys*, 12, 6723–6740, 10.5194/acp-12-6723-2012, 2012.

Polak, H. L., Fennstra, G., and Slagman, J.: Stability of Hypobromite Solutions, *Talanta*, 13, 715–&, Doi 10.1016/0039-9140(66)80006-1, 1966.

Poschl, U., Rudich, Y., and Ammann, M.: Kinetic model framework for aerosol and cloud surface chemistry and gas-particle interactions – Part 1: General equations, parameters, and terminology, *Atmos Chem Phys*, 7, 5989–6023, 2007.

Raghavachari, K., Trucks, G. W., Pople, J. A., and Replogle, E.: Highly correlated systems: Structure, binding energy and harmonic vibrational frequencies of ozone, *Chemical Physics Letters*, 158, 207–212, 10.1016/0009-2614(89)87322-1, 1989.

Ramabhadran, R. O., and Raghavachari, K.: Extrapolation to the gold-standard in quantum chemistry: computationally efficient and accurate CCSD(T) energies for large molecules using an automated thermochemical hierarchy, *J Chem Theory Comput*, 9, 3986–3994, 10.1021/ct400465q, 2013.

Raso, A. R. W., Custard, K. D., May, N. W., Tanner, D. J., Newburn, M. K., Walker, L., Moore, R., Huey, L. G., Alexander, M. L., Shepson, P. B., and Pratt, K. A.: Active Molecular Iodine Snowpack Photochemistry in the Arctic, *Proceedings of the National Academy of Science*, 114, 10053–10058, 2017.

Rischbieter, E., Stein, H., and Schumpe, A.: Ozone solubilities in water and aqueous salt solutions, *J Chem Eng Data*, 45, 338–340, DOI 10.1021/je990263c, 2000.

Sander, R., Keene, W. C., Pszenny, A. A. P., Arimoto, R., Ayers, G. P., Baboukas, E., Cainey, J. M., Crutzen, P. J., Duce, R. A., Honninger, G., Huebert, B. J., Maenhaut, W., Mihalopoulos,

Bibliography

N., Turekian, V. C., and Van Dingenen, R.: Inorganic bromine in the marine boundary layer: a critical review, *Atmos Chem Phys*, 3, 1301–1336, 2003.

Schmidt, J. A., Jacob, D. J., Horowitz, H. M., Hu, L., Sherwen, T., Evans, M. J., Liang, Q., Suleiman, R. M., Oram, D. E., Le Breton, M., Percival, C. J., Wang, S., Dix, B., and Volkamer, R.: Modeling the observed tropospheric BrO background: Importance of multiphase chemistry and implications for ozone, OH, and mercury, *J Geophys Res–Atmos*, 121, 11819–11835, 10.1002/2015jd024229, 2016.

Schmidt, M. W., Baldrige, K. K., Boatz, J. A., Elbert, S. T., Gordon, M. S., Jensen, J. H., Koseki, S., Matsunaga, N., Nguyen, K. A., Su, S., Windus, T. L., Dupuis, M., and Montgomery, J. A.: General atomic and molecular electronic structure system, *Journal of Computational Chemistry*, 14, 1347–1363, 10.1002/jcc.540141112, 1993.

Setschenow, J. Z.: Uber Die Konstitution Der Salzlosungen auf Grund Ihres Verhaltens Zu Kohlensaure, *Z. Physik. Chem.*, 4, 117–125, 1889.

Shim, J., Klobukowski, M., Barysz, M., and Leszczynski, J.: Calibration and applications of the Δ MP2 method for calculating core electron binding energies, *Phys Chem Chem Phys*, 13, 5703, 10.1039/c0cp01591a, 2011.

Shinotsuka, H., Da, B., Tanuma, S., Yoshikawa, H., Powell, C. J., and Penn, D. R.: Calculations of electron inelastic mean free paths. XI. Data for liquid water for energies from 50eV to 30keV, *Surface and Interface Analysis*, 10.1002/sia.6123, 2016.

Shiraiwa, M., Sosedova, Y., Rouviere, A., Yang, H., Zhang, Y. Y., Abbatt, J. P. D., Ammann, M., and Poschl, U.: The role of long-lived reactive oxygen intermediates in the reaction of ozone with aerosol particles, *Nat Chem*, 3, 291–295, 10.1038/Nchem.988, 2011.

Slavicek, P., Kryzhevoi, N. V., Aziz, E. F., and Winter, B.: Relaxation Processes in Aqueous Systems upon X-ray Ionization: Entanglement of Electronic and Nuclear Dynamics, *J Phys Chem Lett*, 7, 234–243, 10.1021/acs.jpcclett.5b02665, 2016.

Tamamushi, R., and Isono, T.: A Quasithermodynamic Approach to the Viscous-Flow of Aqueous-Electrolyte Solutions at Moderate and High-Concentrations, *J Chem Soc Farad T* 1, 80, 2751–2758, DOI 10.1039/f19848002751, 1984.

Bibliography

Thurmer, S., Oncak, M., Ottosson, N., Seidel, R., Hergenahm, U., Bradforth, S. E., Slavicek, P., and Winter, B.: On the nature and origin of dicationic, charge-separated species formed in liquid water on X-ray irradiation, *Nat Chem*, 5, 590–596, 10.1038/Nchem.1680, 2013.

Vaida, V.: Perspective: Water cluster mediated atmospheric chemistry, *J Chem Phys*, 135, Artn 020901

10.1063/1.3608919, 2011.

Weber, R., Winter, B., Schmidt, P. M., Widdra, W., Hertel, I. V., Dittmar, M., and Faubel, M.: Photoemission from aqueous alkali-metal-iodide salt solutions using EUV synchrotron radiation, *J Phys Chem B*, 108, 4729–4736, 10.1021/jp030776x, 2004.

Weisenberger, S., and Schumpe, A.: Estimation of gas solubilities in salt solutions at temperatures from 273 K to 363 K, *Aiche J*, 42, 298–300, DOI 10.1002/aic.690420130, 1996.

Winter, B., and Faubel, M.: Photoemission from liquid aqueous solutions, *Chem Rev*, 106, 1176–1211, 10.1021/cr040381p, 2006.

Winter, B., Aziz, E. F., Hergenahm, U., Faubel, M., and Hertel, I. V.: Hydrogen bonds in liquid water studied by photoelectron spectroscopy, *J Chem Phys*, 126, 124504, Artn 124504

10.1063/1.2710792, 2007.

Wren, S. N., Kahan, T. F., Jumaa, K. B., and Donaldson, D. J.: Spectroscopic studies of the heterogeneous reaction between O₃(g) and halides at the surface of frozen salt solutions, *J Geophys Res-Atmos*, 115, Artn D16309

10.1029/2010jd013929, 2010.

Xantheas, S. S., and Voth, G. A.: Aqueous Solutions and Their Interfaces, *J Phys Chem B*, 113, 3997–3999, 10.1021/jp900202a, 2009.

Bibliography

Zhu, C. Q., Kumar, M., Zhong, J., Li, L., Francisco, J. S., and Zeng, X. C.: New Mechanistic Pathways for Criegee–Water Chemistry at the Air/Water Interface, *J Am Chem Soc*, 138, 11164–11169, 10.1021/jacs.6b04338, 2016.

Zuend, A., Marcolli, C., Luo, B. P., and Peter, T.: A thermodynamic model of mixed organic–inorganic aerosols to predict activity coefficients, *Atmos Chem Phys*, 8, 4559–4593, 2008.

Zuend, A., Marcolli, C., Booth, A. M., Lienhard, D. M., Soonsin, V., Krieger, U. K., Topping, D. O., McFiggans, G., Peter, T., and Seinfeld, J. H.: New and extended parameterization of the thermodynamic model AIOMFAC: calculation of activity coefficients for organic–inorganic mixtures containing carboxyl, hydroxyl, carbonyl, ether, ester, alkenyl, alkyl, and aromatic functional groups, *Atmos Chem Phys*, 11, 9155–9206, 10.5194/acp-11-9155-2011, 2011.

Interplay of microphysics and kinetics in bromide oxidation by ozone

Published as: Edebeli, J., M. Ammann, T. Bartels–Rausch. Microphysics of the aqueous bulk counter water activity driven rate acceleration in bromide oxidation by ozone from 289 – 245 K. *RSC Environmental Processes*. 2018

3.1 Microphysics of the aqueous bulk counter water activity driven rate acceleration in bromide oxidation by ozone from 289 – 245 K

3.1.1 Abstract

The reaction of ozone with bromide is an initiation processes in bromine activation resulting in the formation of reactive bromine species with impacts on the fate of compounds in the lower atmosphere. Environmental halides sources often contain organics, which are known to influence aqueous bulk reactivity. Here, we present work investigating the temperature dependence of bromide oxidation by ozone using a coated wall flow tube reactor coated with an aqueous mixture of citric acid, as a proxy for oxidized secondary organic matter, and sodium bromide. Using the resistor model formulation, we quantify changes in the properties of the aqueous bulk relevant for the observed reactivity. The reactive uptake

Chapter 3 Interplay of microphysics and kinetics in bromide oxidation by ozone

coefficient decreased from 2×10^{-6} at 289 K to 0.5×10^{-6} at 245 K. Our analysis indicates that the humidity-driven increased concentration with corresponding increase in the *pseudo*-first order reaction rate was countered by the colligative change in ozone solubility and the effect of the organic fraction *via* increased viscosity and decreased diffusivity of ozone as temperature decreased. From our parameterization, we provide an extension of the temperature dependence of the reaction rate coefficients driving the oxidation of bromide, and assess the temperature-dependent *salting* effects of citric acid on ozone solubility. This study shows effects of the organic species at relatively mild temperatures, between the freezing point and eutectic temperature of sea salt as typical for Earth's cryosphere. Thus, this study may be relevant for atmospheric models at different scales describing halogen activation in the marine boundary layer or free troposphere including matrices such as sea-spray aerosol and brine on sea ice, snow, and around of mid-latitude salt lakes.

3.1.2 Introduction

The reaction of ozone (O_3) with halides producing reactive halogen species (RHS) in the troposphere is an important chemical process with implications for the oxidation capacity of the atmosphere and the fate of compounds in the atmosphere (Simpson *et al.*, 2007; Abbatt *et al.*, 2012; Simpson *et al.*, 2015). Of importance is reaction between RHS and gas phase elemental mercury resulting in increased mercury deposition and bioavailability, which has ecosystem and human health implications (Simpson *et al.*, 2007; Simpson *et al.*, 2015; Nerentorp Mastromonaco *et al.*, 2016). While all halides may be involved, with respect to sea ice and sea spray aerosols, bromide may dominate due to its relative abundance and reactivity compared to other halides (Simpson *et al.*, 2007; Abbatt *et al.*, 2012; Bartels-Rausch *et al.*, 2014).

Studies show that aerosols containing halides such as sea spray aerosol significantly contribute to global halogen chemistry *via* multiphase chemistry on and within aerosol particles (Long *et al.*, 2014; Wang *et al.*, 2015; Schmidt *et al.*, 2016; Peterson *et al.*, 2017). Sea-spray aerosol is also partly responsible for the salinity of surface snow (Dominé *et al.*, 2004; Abbatt *et al.*, 2012) resulting from scavenging and deposition along with snow fall onto polar and alpine snow packs. Field and satellite measurements have identified local, regional, and global scale effects of atmospheric halogen chemistry on O_3 and on the mercury cycle (Wang *et al.*, 2015; Peterson *et al.*, 2017). However, there are still uncertainties in the mechanism of halide oxidation by ozone especially in less understood complex sources such as aerosols or snow containing mixtures of organics and salts (Long *et al.*, 2014; Schmidt *et al.*, 2016).

While the microphysics of aqueous aerosol particles is reasonably well understood, in the complex environment such as snow and sea-ice, the structural arrangement of the non-frozen aqueous phase is less obvious. It may be expected that the water activity is controlled by the presence of ice (Koop *et al.*, 2000; Abbatt *et al.*, 2012; Bartels-Rausch *et al.*, 2014). The concentration of aqueous solutes in equilibrium with ice depends on temperature and follows the phase diagram of the aqueous mixtures (Cho *et al.*, 2002; Bartels-Rausch *et al.*, 2014). Below the freezing point of ice, as temperature decreases, the water activity in solution decreases until the eutectic point is reached (Figure 3.1). The activity of the solutes increase similarly to the so-called “freeze concentration effect” described by Takenaka and Watson (1992). When concentration of the solutes in the unfrozen aqueous phase exceeds the solubility limit of a solute, precipitation of that solute may occur (Abbatt *et al.*, 2012). In sea-ice formation, sodium chloride (NaCl) precipitates out at a warmer temperature than bromide leading to an enrichment of bromide relative to NaCl (Abbatt *et al.*, 2012). Figure 3.1 gives an example and shows how the equilibrium mass fraction of sodium bromide (NaBr) in aqueous solution increases during freezing (Rumble, 2018). The environmental impact of this increase in concentration of solutes with decreasing temperature has been discussed (Bartels-Rausch *et al.*, 2014), and may include the formation of products not typically formed at lower concentrations (O'Concubhair and Sodeau, 2012).

Investigations of the composition of sea-spray aerosol show a significant organic component, which may be up to 50% of the aerosol mass (O'Dowd *et al.*, 2004). The organic fraction plays a role in the properties of the aerosol such as hygroscopic properties and viscosity (Reid *et al.*, 2011; Lienhard *et al.*, 2012; Reid *et al.*, 2018). Indeed, investigations of halide oxidation on organic acid-halide mixtures indicate effects of the organic fraction on the uptake of O₃ (Hayase *et al.*, 2011). These studies show that in addition to providing acidity (which catalyses the reaction), the acids may affect the prevalence of the surface reaction (Hayase *et al.*, 2011), and the propensity of halide ions for the interface (Lee *et al.*, 2015; Werner *et al.*, 2016). On the physical properties of organic containing solutions, studies show that the viscosity of organic solutions may reduce bulk reactivity by decreasing diffusivity of the reactive solute (in this case, O₃; (Renbaum-Wolff *et al.*, 2013; Steimer *et al.*, 2014; Marshall *et al.*, 2016)).

Thus, the organic fraction of sea-spray aerosols, though not considered in atmospheric chemistry models, may impact the observed multiphase halogen activation, both during long range transport of sea spray aerosol in the troposphere or in snow and on sea-ice after deposition. Environmental ice compartments, such as sea ice and snow also contain halides and can partake in halide oxidation (Mitchell and Lamb, 1989; Toom-Sauntry and Barrie, 2002; Grannas *et al.*, 2006; McNeill *et al.*, 2012). Just like inorganic salts, organics may also be excluded to the brine pockets during freezing and may similarly affect the properties of the unfrozen aqueous phase on snow and environmental ice (Grannas *et al.*, 2007). These effects, in particular the influence of viscosity on reactivity usually requires rather low

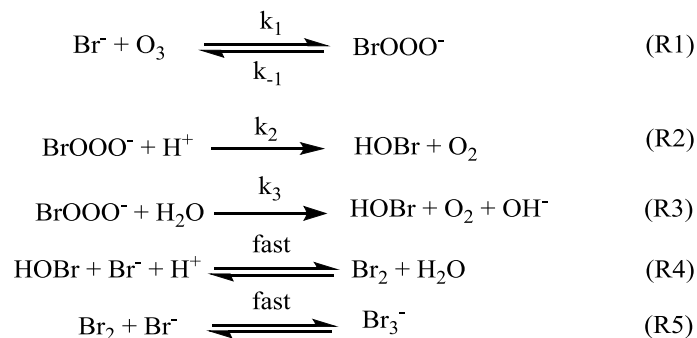
Chapter 3 Interplay of microphysics and kinetics in bromide oxidation by ozone

relative humidity as typically found in the free troposphere. Here we focus on these effects of an organic acid on the chemical reactivity at moderate humidity as typical for the snow covered boundary layer and the interstitial air in snow.

The reaction between O_3 in the gas phase and bromide in the condensed phase of aerosols, sea ice, and snow is one initiation process for the formation of reactive bromine species. This is a multiphase reaction, which can occur in the dark, leading to the production of photo-labile bromine (Br_2 ; R1–R5) with R2 and R3 as the rate limiting steps (Haruta and Takeyama, 1981; Oum *et al.*, 1998; Liu *et al.*, 2001; Sakamoto *et al.*, 2018). Br_2 produced during night time or during the polar winter may serve as a reservoir for daytime or polar spring photolytic halogen activation (Liao *et al.*, 2012; Nerentorp Mastromonaco *et al.*, 2016). Reactions R4 and R5 may also involve chloride and/or iodide leading to the production of reactive inter-halogen species (e.g. IBr, BrCl; (Abbatt, 1994; Fickert *et al.*, 1999)). Production of inter-halogen species, especially BrCl, may also depend on the relative abundance of the respective halides (Frinak and Abbatt, 2006).

Here, we focus on the reaction of bromide with ozone in the dark. Kinetic studies on bromide (Br^-) oxidation by O_3 indicate a multiphase process with a significant interfacial component (Hunt *et al.*, 2004; Oldridge and Abbatt, 2011; Artiglia *et al.*, 2017). Aqueous bulk bromide oxidation by ozone is relatively slow with a rate coefficient of $\sim 258 \text{ M}^{-1}\text{s}^{-1}$ at 298 K (Liu *et al.*, 2001). Hunt *et al.* (2004) showed that observed Br_2 production resulting from this reaction system exceeded that expected from bulk aqueous production alone, and suggested a contribution from interfacial processes. Other studies probing possibilities of additional interfacial processes corroborate this suggestion by Hunt *et al.* (e.g., Clifford and Donaldson, 2007; Wren *et al.*, 2010; Oldridge and Abbatt, 2011; Artiglia *et al.*, 2017). Oldridge and Abbatt (2011), while monitoring Br_2 production, showed that the interfacial processes become significant at atmospherically relevant low ozone concentrations.

Studies on the interfacial process indicate that this process proceeds *via* the formation of an adsorbed intermediate species on the surface of the observed system (Hunt *et al.*, 2004). Artiglia *et al.* (2017) recently observed this intermediate, the bromide ozonide, $BrOOO^-$, and showed that it is surface active and stabilized by water molecules on the surface. The mechanism of formation and the role of this intermediate has also been studied by theoretical calculation (Gladich *et al.*, 2015). Gladich *et al.* (2015), in their theoretical study of this reaction, showed that *via* intersystem crossing of $BrOOO^-$ from the singlet state to triplet state, this Br^- oxidation process can proceed successfully in the dark.



Often, studies investigate halide oxidation on salt solutions only. In addition, though research has concentrated mostly on halogen chemistry with O₃ in polar regions, similar halogen activation has been observed in warmer environments (Hebestreit *et al.*, 1999; Oldridge and Abbatt, 2011). Temperature influences properties such as solubility, viscosity, and reaction rates with implications on the observed reactive loss of O₃.

Therefore, there are two objectives for the study presented herein. The first objective was to measure the uptake of O₃ *via* reaction with bromide in a mixture containing citric acid (CA) and NaBr in water, over a wide temperature (T) range (−25 °C to 16 °C). CA was chosen as a proxy for oxidised organic material representative of aged primary or secondary organic material abundant in marine environments. Experiments were conducted using thin films (equilibrated to experimental conditions) of the mixture in a temperature–regulated coated wall flow tube setup. An essential part of the experimental design was to avoid freezing while staying close to the ice–*liquidus* line in the NaBr–water–organic ternary solution at temperatures below 0 °C (Figure 3.1). This was achieved by maintaining a relative humidity of about 96% with respect to water vapour pressure over ice (RH_{ice}) in the setup at temperatures below 0 °C and a relative humidity of 96% above 0 °C (RH_{water}) (Marti and Mauersberger, 1993; Murphy and Koop, 2005). This means that the relative humidity with respect to liquid water (RH_{water}) ranged from 96% at 16 °C to 75% at −25 °C (Marti and Mauersberger, 1993; Murphy and Koop, 2005). Thus, the RH_{water} – T space covered in this study is directly relevant for atmospheric aerosol trajectories, but also remains close, in terms of water activity, to the conditions of liquid phases in equilibrium with ice, such as within snow or sea ice. As such, it allows for covering a significant temperature range without the complications related to ice formation.

The second objective is to extensively assess the influence of temperature–induced changes in the system on the observed uptake coefficients of O₃ *via* temperature–dependent variables controlling the microphysics and kinetics (Takenaka and Bandow, 2007; Bartels-Rausch *et al.*, 2014; Steimer *et al.*, 2014). Using the resistor model formulation (Finlayson-Pitts and Pitts, 2000; Ammann *et al.*, 2013), we attempt to describe the changes in reactant concentration, diffusivity, and pH to provide information on how these potentially opposing effects influence the observed temperature–dependent O₃ uptake. Development of the

Chapter 3 Interplay of microphysics and kinetics in bromide oxidation by ozone

parameterization used in this study focused on the properties and reactivity in the aqueous bulk.

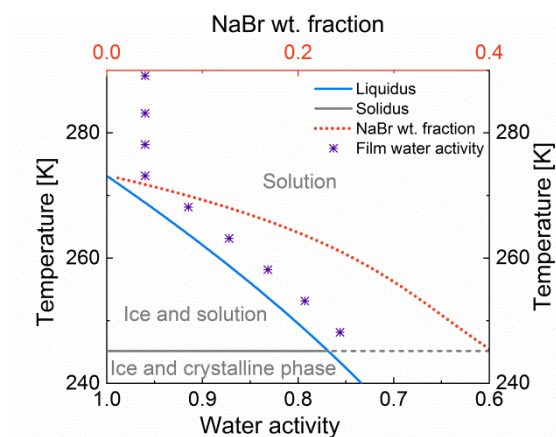


Figure 3.1: Representation of the phase diagram of NaBr–water binary solution (lines) and of the water activity in the film of study (Purple ‘*’) as a function of water activity and temperature. The blue line denotes the solid–liquid equilibrium curve of ice; the red dot line is the weight fraction of NaBr in solution in equilibrium with ice; the grey line indicates the eutectic temperature, where NaBr crystallises (Rumble, 2018). Water activity = relative humidity with respect to liquid water (%) / 100.

3.1.3 Experimental

Materials and methods

The experimental work in this study was conducted using a temperature–regulated coated wall flow tube setup at atmospheric pressure (SI. Figure S3.1). The setup is fitted with a temperature–regulated injector for dosing humidified O₃ (and other gases) to the coated flow tube. This study was conducted using sodium bromide (NaBr, Sigma Aldrich, > 99.0%), citric acid monohydrate (CA, Sigma Aldrich > 99.0%), and ultrapure water (18 MΩ cm).

Tube preparation. A 50 cm long flow tube with an internal diameter of 1.2 cm was coated with a NaBr (0.34 M) and citric acid (0.31 M) mixture in 400 μL water (pH = 1.60 ± 0.02). Before coating, the tube was etched with 5% hydrofluoric acid (HF) and rinsed thoroughly with deionized water until the pH of the water on the tube was near neutral. The tube was then dried and coated with the solution under a N₂ flow at 55% relative humidity (RH_{water}) and room temperature. No crystal formation was observed during this process. The coated tube was conditioned at the experimental temperature and RH_{water} (see Figure 3.1) with a flow of a humidified synthetic air for an hour before exposure to O₃. Gases were delivered to the flow tube *via* the injector.

Ozone exposure. O₃ was generated from oxygen (at a flow rate of 200 ml min⁻¹ at standard temperature and pressure (STP)) over a Hg penray UV lamp. The generated O₃ stream was humidified by adding a flow of humidified N₂ (780 ml min⁻¹). The coated flow tube was exposed to the humidified O₃ in O₂/N₂ in 15 minute cycles between the flow tube and a bypass (to measure the maximum O₃ and check for fluctuations in the O₃ delivered to the flow tube). The O₃ concentration in parts per billion by volume (ppb) was measured using a commercial O₃ analyser (Teledyne, model 400E).

Experiments were conducted from -25 °C to 16 °C. At each temperature, a cycle between the bypass and the flow tube was repeated at least three times at an exposure length of 25 cm (exposed surface area of 94.3 cm²). O₃ concentrations were also measured at 0 cm (just outside the tube) to account for losses that were not from the coated part of the flow tube (<1%). The ozone concentration was also measured as a function of injector position and thus length of the coated flow tube exposed at 5 °C and -5 °C to confirm the first order kinetics for our analyses (SI. Figure S3.2). At least one independent repeat was conducted on a different day for each temperature. O₃ loss was also measured at different O₃ concentrations at some temperatures (0 °C, -10 °C, -20 °C, and -25 °C).

Viscosity measurement. The equilibrium concentration in the film at each temperature was calculated using AIOMFAC model version 2.18 (Zuend *et al.*, 2008). We measured the viscosity of the equilibrium compositions using the Thermo-Scientific Haake Viscotester iQ Air. Viscosity was measured at the experimental temperature and relative humidity using plate geometry. The relative humidity in the viscometer measurement cell was controlled with a flow humidified N₂ (200 ml min⁻¹). The samples were allowed to equilibrate at the set temperature and relative humidity for 10 to 15 minutes before measurement.

Data analyses

Uptake coefficients: Observed uptake coefficients (γ_{obs}).

We determined the uptake coefficient of O₃ in the system from observing the change in O₃ concentration due to the exposure to the coated flow tube. Figure 3.2 shows a sample of the raw data obtained from the O₃ analyser at 5 °C during ozone exposure to a coated flow tube. Uptake coefficients (γ_{obs}) were calculated with the average O₃ concentration through the bypass ($[\text{O}_3]_{\text{bypass}}$) before and after the flow tube exposure, and through the flow tube ($[\text{O}_3]_{\text{flow tube}}$) in ppb for each cycle using equation (3.1) below. The uptake coefficient is defined as the probability that a collision of an O₃ molecule with the coated wall will result in O₃ loss (Finlayson-Pitts and Pitts, 2000; Oldridge and Abbatt, 2011; Ammann *et al.*, 2013). These coefficients provide the “normalized sum of” losses, which is a combination of all processes involved in the removal of ozone. The average O₃ uptake coefficient of the three cycles between the bypass and the flow tube per repeat is taken as the mean uptake

Chapter 3 Interplay of microphysics and kinetics in bromide oxidation by ozone

coefficient for that experiment. γ_{obs} was corrected for gas phase diffusion limitation following the Cooney, Kim, Davis CKD–method (Poschl *et al.*, 2007; see SI for details).

$$\gamma_{\text{obs}} = \frac{4\varphi \times \left[\ln \left(\frac{[\text{O}_3]_{\text{bypass}}}{[\text{O}_3]_{\text{flow tube}}} \right) \right]}{\omega_{\text{O}_3} \times \text{SA}} \times C_{\text{gd}} \quad (3.1)$$

$$\omega_{\text{O}_3} = \sqrt{\frac{8RT}{\pi M_{\text{wO}_3}}} \quad (3.2)$$

Where φ is the flow rate of O_3 through the flow tube (980 ml min^{-1}); ω is the mean thermal velocity of O_3 in the gaseous phase, cms^{-1} (Shiraiwa *et al.*, 2012); SA is the exposed internal surface area of the tube, 94.3 cm^2 ; M_{wO_3} is the molecular weight of O_3 , C_{gd} is the diffusion correction factor.

Uptake coefficients: Parameterization of uptake coefficients.

The uptake coefficient is a combination of surface and bulk uptake processes, which is often evaluated using a resistance model method (Finlayson-Pitts and Pitts, 2000; Ammann *et al.*, 2013). This method describes the uptake coefficient as convolution of serial and parallel processes (expressed as resistances) under steady state conditions. Uptake starts with accommodation of O_3 on the surface by collision from the gas phase, from where it may undergo a reaction with other species on the surface, desorb back to the gas phase, or enter into the bulk of the solution, diffuse, and react there. The resistance model is a representation of the complete solutions to the coupled differential equations describing these processes under steady state conditions analogous to electrical resistances of parallel or serial processes.

In this study, we assume that accommodation on the surface (preceding the surface reaction described by Γ_{surf} and preceding as well surface to bulk transfer) is not rate limiting. We also assume that surface to bulk transfer of O_3 is not rate limiting, as justified further below. Thus, within these assumptions, the surface reaction operates independently of and parallel to diffusion and reaction in the bulk. Hence, the total uptake can be represented by the sum of the inverse resistances for diffusion and reaction in the bulk (Γ_{bulk}) and for the surface reaction (Γ_{surf}) (equation (3.3)). By themselves, Γ_{bulk} and Γ_{surf} are reaction rates normalized to the gas kinetic collision if they would be the only limiting processes.

$$\gamma_{\text{calc}} = \Gamma_{\text{surf}} + \Gamma_{\text{bulk}}, \quad (3.3)$$

where

$$\Gamma_{\text{surf}} = \frac{4 k_s K N_{\text{max}}}{\omega_{\text{O}_3} (1 + K [\text{O}_3]_{\text{g}})} \quad (3.4)$$

and

$$\Gamma_{\text{bulk}} = \frac{4 H R T \times \sqrt{D_{\text{O}_3} \times k_{\text{b}}^{\text{I}}}}{\omega_{\text{O}_3}} \quad (3.5)$$

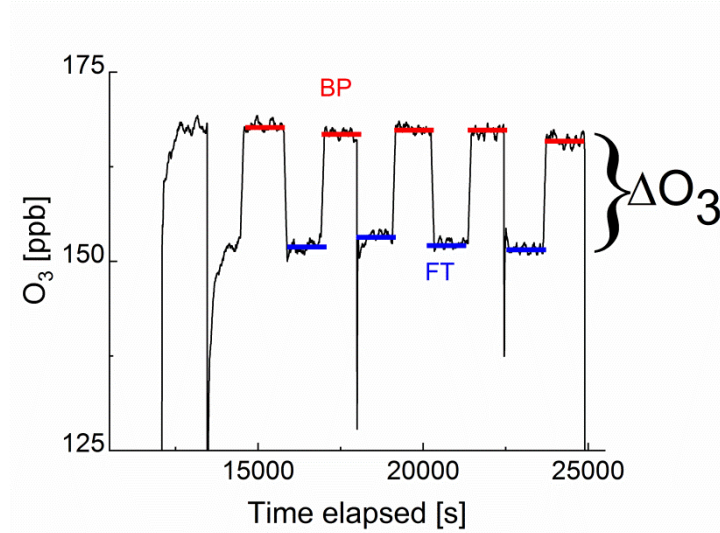


Figure 3.2: An example of O_3 mixing ratio measured downstream of the flow tube in response to switching the gas flow from the bypass (BP, red lines) to the injector and thus, through the coated wall flow tube (FT, blue lines). Experiments were done at 5 °C and with an activity of Br^- of 0.58 M and of citric acid of 0.08 M

The reactive surface uptake (Γ_{surf}) calculated using equation (3.4) (Ammann *et al.*, 2013) represents “Langmuir–Hinshelwood–type” surface reaction mechanism (Oldridge and Abbatt, 2011), in which “Langmuir–type” adsorption precedes reaction. Partitioning of the reactive gas to the surface from the gas phase is described by the equilibrium constant, K , such that $K \times [\text{O}_3]_{\text{g}} / (1 + K \times [\text{O}_3]_{\text{g}})$ is the surface coverage in molecule per cm^2 (Oldridge and Abbatt, 2011). Artiglia *et al.* (2017) have recently shown that the Langmuir equilibrium constant, K , and the maximum surface coverage, N_{max} , in equation (3.4), are linked to the equilibrium and maximum coverage of the reaction intermediate, a bromide ozonide, at the surface, when describing the oxidation of bromide. Here, we used the same approach and set N_{max} to 10^{12} molecule per cm^2 , the saturation surface concentration of the bromide ozonide intermediate as reported by Artiglia *et al.* (2017). The apparent equilibrium partitioning coefficient K represents a lumped parameter describing the equilibrium between gas–phase ozone and the surface concentration of the ozonide and was set to $(K = 6 \times 10^{-13} \cdot \exp(686/T)) \text{ cm}^3$ per molecule. The surface reaction rate coefficient is denoted k_s and was set to $2.1 \times 10^{12} \cdot \exp\left(\frac{-76400}{RT}\right) \text{ s}^{-1}$ (Artiglia *et al.*, 2017). We note that transfer of O_3 into the bulk aqueous phase also first involves adsorption of O_3 to the surface,

Chapter 3 Interplay of microphysics and kinetics in bromide oxidation by ozone

in parallel to and independently of the formation of the bromide ozonide. Given the fairly low bromide concentrations, the surface is still largely dominated by water molecules. The adsorption equilibrium constant and the value of N_{\max} for this process (presumably driven by the dimensions of the molecule and thus likely in the range of 10^{14} molecules per cm^2) are both not known. As obvious from the present data set and also others discussed below, there are no indications so far that adsorption saturation of O_3 on water affects surface to bulk transfer.

The parameterization for Γ_{bulk} (equation (3.5)) contains temperature-dependent parameters (Henry's law constant (H), Diffusivity (D_{O_3}), the mean thermal velocity of O_3 (ω_{O_3}), and the *pseudo*-first order bulk aqueous phase rate coefficient ($k_b^I = k_b^{II} \times a_{[\text{Br}^-]}$ ($a_{[\text{Br}^-]}$ is bromide activity)). R is the ideal gas constant. There is limited information on the aforementioned parameters and their temperature dependences. In cases where there are measurement data, these are often conducted for single solute solutions and not below 0°C . Therefore, we have parameterized these factors to ternary mixtures and lower temperatures as described below.

3.1.4 Results and discussion

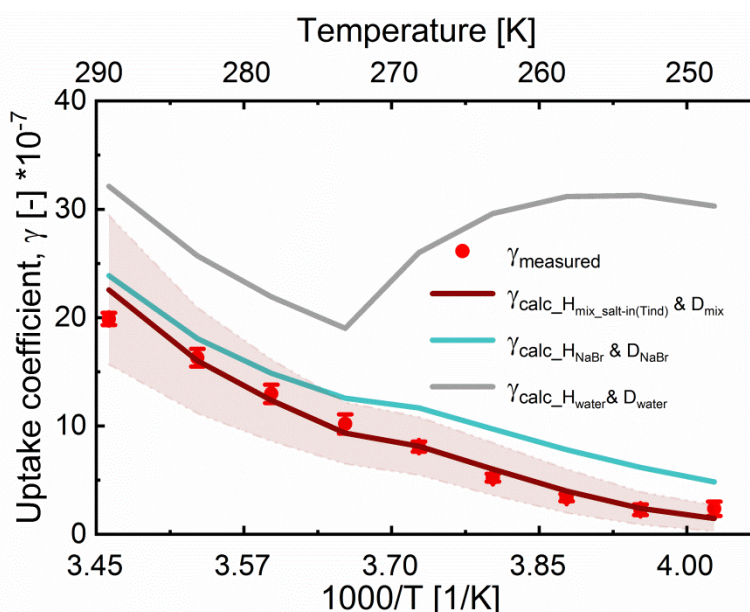


Figure 3.3: Measured (dots) and parameterized (lines) uptake coefficients as a function of temperature at 5×10^{12} molecules per cm^3 ozone concentration. The grey line parameterization uses solubility and diffusivity of ozone in water. The cyan line uses the diffusivity and solubility in a solution containing the film's concentration of NaBr, but not citric acid. The red line uses the diffusivity and solubility of ozone as estimated for both NaBr and citric acid. The reaction rate coefficients are the same for all three runs. The red shaded area denotes the standard deviation (s.d.) of multiple repeats.

In Figure 3.3, we present the measured uptake coefficients corrected for gas phase diffusion limitation (γ_{obs}) of O_3 in the mixed citric acid/NaBr solutions as a function of temperature from $-25\text{ }^\circ\text{C}$ to $16\text{ }^\circ\text{C}$. The observed temperature dependence shows that uptake coefficients of ozone decrease with decreasing temperature. This decrease slows down and plateaus below $-10\text{ }^\circ\text{C}$. The observed uptake coefficients at $-20\text{ }^\circ\text{C}$ and $-25\text{ }^\circ\text{C}$ are invariant. The uptake coefficients observed in our study were about 1×10^{-7} at $-20\text{ }^\circ\text{C}$ with 3×10^{13} molecules per cm^3 ozone concentration which compares well with that of Oldridge and Abbatt's (2011) study on acidic ternary mixtures of NaCl, NaBr, and water. The concentration of the condensed phase reactant in both studies is determined by the freezing point depression at temperatures below $0\text{ }^\circ\text{C}$ (Figure 3.1). Thus, the agreement of the observed uptake coefficients for this particular run with similar experimental conditions supports the finding of the earlier study. The comparison is, however, hampered by the presence of citric acid in our study. In this study, we have extended the temperature range and, in particular, increased the sampling interval to investigate the multiphase reactivity in more detail. As described below, there are distinct differences in the observed uptake coefficient as function of ozone concentration between the studies.

In Figure 3.3, we also present three predictions of the uptake coefficients (γ_{calc} , lines) as a function of temperature. The runs differ in the parameterization of the diffusivity of ozone and the ozone solubility in the film. The grey line denotes a run where the diffusivity and the solubility of ozone in the reactive medium are parameterized without considering the effect of solutes on either. Such parameterization based on the diffusivity of ozone (Johnson and Davis, 1996) and ozone solubility in water (Chaimedes and Stelson, 1992) does not capture the observations. In particular, the marked increase in the uptake coefficient at 273 K , when water activity decreases leading to an increase in bromide activity (Figure 3.1), is not evident in the experimental data. The agreement between the parameterization output and the observations is drastically improved, when accounting for the impact of bromide on the solution's properties. Finally, incorporating the effect of the organic solute as well further optimizes the parameterization result showing the importance of accurately describing the physical properties of organic–inorganic mixtures. The relevant film properties and parameters such as the viscosity and diffusivity of ozone, solubility of ozone in the film, pH of the film, and the rate of the reaction in the aqueous bulk are developed further below and summarized in Table 3.1 and SI Tables S3.1–S3.3.

Aqueous bulk reaction rate coefficients

One parameter of r_{bulk} is the pseudo–first order rate coefficient for the reaction of ozone with bromide (k_{b}^{I} , equation (3.5)) which is the product of the activity of bromide (a_{Br^-}) and the second–order rate coefficient (k_{b}^{II}). The activities and concentrations of the bromide and citric acid solutes were calculated using the AIOMFAC model, web version 2.18 (Zuend *et al.*, 2008). The mass fractions calculated using the AIOMFAC model for the binary water–bromide and water–citric acid systems, respectively, compare well with that obtained using

Chapter 3 Interplay of microphysics and kinetics in bromide oxidation by ozone

freezing point depression data for NaBr (Rumble, 2018) and growth factors for citric acid (Zardini *et al.*, 2008). To convert the AIOMFAC output to activities based on molarity as required for the kinetic description, the density of the film was estimated using a mass fraction (of dry solute) mixing rule of the individual solutes and their solutions. The density of the citric acid solution was determined using Lienhard *et al.*'s parameterization (2012). The density of the NaBr solution was estimated by extrapolating measurements by Isono (Isono, 1984).

The second order rate coefficients for the reaction of Br^- with O_3 (equation (3.6)) is based on the mechanism presented in R1–R5, and is pH dependent (Liu *et al.*, 2001).

$$k_b^{II} = \frac{k_1 \left(\frac{k_2}{k_{-1}} [\text{H}^+] + \frac{k_3}{k_{-1}} \right)}{1 + \frac{k_2}{k_{-1}} [\text{H}^+] + \frac{k_3}{k_{-1}}} \quad (3.6)$$

Estimation of the pH of the film was based on citric acid dissociation constants and activity in the film (Hastings and Slyke, 1922). The estimated pH ranged from ~ 2 at 16 °C to ~ 1.7 at –25 °C (Table 3.1). The temperature dependence of k_b^{II} was a free tuning parameter benchmarked against the pH independent rate coefficient involving R3 but not R2 ($k_{\text{H}_2\text{O}} = k_1 / ((k_{-1}/k_3) + 1)$) proposed by Liu *et al.* (2001), $258 \text{ M}^{-1}\text{s}^{-1}$ at 25 °C. This study's parameterized k_b^{II} at 16 °C was $388 \text{ M}^{-1}\text{s}^{-1}$. The calculated k_b^{II} with our own fit at 25 °C and 1 M H^+ is $1.7 \times 10^3 \text{ M}^{-1}\text{s}^{-1}$, which is much smaller than that calculated by Liu *et al.* (2001) at 25 °C, $3.64 \times 10^3 \text{ M}^{-1}\text{s}^{-1}$. The pH independent rate coefficient, which was used as a benchmark, from our parameterization is $257 \text{ M}^{-1}\text{s}^{-1}$ at 25 °C, and like that of Liu *et al.* (2001), is larger than that of Haruta and Takeyama's pH independent rate ($211 \text{ M}^{-1}\text{s}^{-1}$ at 27 °C; (1981)) and Haag and Hoigné ($206 \text{ M}^{-1}\text{s}^{-1}$ at 25 °C at pH 2; (1983)).

This comparison illustrates the uncertainty in the present second order rate coefficients and their temperature dependence, which is directly reflected in the uncertainty of k_b^I . Further uncertainty in the *pseudo*–first order rate coefficients arises from the uncertainties in the activity coefficients as derived by the AIOMFAC model, the density estimates for the film, and the pH of the film (SI Table S3.4). We have assigned about 20% (35%) uncertainty to this parameter at temperatures above 0 °C (at –20 °C) taking the aforementioned sources of errors into consideration. A 22% change in the *pseudo*–first order rate coefficient at 0 °C results in a 9% change in the γ_{calc} and 34% change in rate coefficient at –20 °C results in a 16% change in the γ_{calc} (Table 3.2).

Overall, the increase in $\gamma_{\text{calc_Hwater_Dwater}}$ following the trend in bromide activity with temperature is in line with a concentration driven acceleration of apparent reaction rates observed in other bimolecular (or higher–order) reactions (Bartels-Rausch *et al.*, 2014).

Figure 3.3 shows that other factors reduce the apparent reactivity in this multiphase system, which we will discuss in the following.

Ozone solubility in the aqueous bulk

Figure 3.3 shows the profound influence of composition driven equilibrium partitioning of ozone between the gas phase and the aqueous bulk on Γ_{bulk} (equation (3.5)). This is a well-known effect (Battino, 1981b; Biń, 2006); however, there are no data quantifying these effects at high molarities and at low temperatures typical for atmospheric chemistry. Here, we present and test approaches to overcome this limitation.

The effect of solutes on solubility is referred to as “*Salting*,” which may be *salting-out* or *salting-in* and are described with the so-called “Sechenov relationship” (equation (3.7));(Sechenov, 1889; Battino, 1981b; Schumpe, 1993; Rischbieter *et al.*, 2000a; Biń, 2006)).

$$\log(H_{\text{solution}}/H_{\text{water}}) = K_s a_s \quad (3.7)$$

H_{solution} (mol/ (L atm)) is the Henry’s law constant of ozone in the solution and K_s is the Sechenov constant. H_{water} is the Henry’s law constant of ozone in water (mol/(L atm); equation (3.8))(Chaimedes and Stelson, 1992)). This explicit treatment of the high ionic strength of bromide and the high concentration of citric acid expands the use of the term, Henry’s law constant that strictly refers only to the limiting case of gas – aqueous bulk partitioning for low ionic strength and solute concentrations.

$$H_{\text{water}} = 0.0115 \times \exp\left(2560 \times \left(\frac{1}{T} - \frac{1}{298}\right)\right) \quad (3.8)$$

where T denotes the temperature.

In the presence of NaBr, the ozone gas–aqueous bulk partitioning coefficient decreases significantly by ~30% above 0 °C with a stronger *salting-out* as NaBr concentrations increase with decreasing temperatures below 0 °C (Figure 3.3). This is in agreement with the general trend for gases less polar than water, where inorganic salts tend to decrease gas solubility (a *salting-out* effect; (Schumpe, 1993; Weisenberger and Schumpe, 1996)). The solubility was derived using parameterizations of the Sechenov constants for NaBr solutions as described by Weisenberger and Schumpe (Weisenberger and Schumpe, 1996). These parameterizations were done using data obtained above 0 °C (Weisenberger and Schumpe, 1996; Rischbieter *et al.*, 2000b). Due to low confidence on the temperature dependence as expressed by the authors (Weisenberger and Schumpe, 1996), we fixed it to that at 25 °C (Rischbieter *et al.*, 2000a).

Additional incorporation of the effect of the organic co-solute on Γ_{bulk} leads to a perfect agreement with the experimental data (Figure 3.3). To achieve this, two scenarios estimating the solubility of O₃ in the aqueous citric acid solution were developed as part of this study. On the one hand, we described the *salting* effect of citric acid as that typical for

Chapter 3 Interplay of microphysics and kinetics in bromide oxidation by ozone

organic species, for which a *salting-in* effect with increasing concentration of the organic species is generally observed (Biń, 2006). For this, we used measurements of O₃ solubility in propionic acid–water mixtures at room temperature between 0 weight percent and 100 weight percent propionic acid (Battino, 1981b). On the other hand, measurements of oxygen solubility in citric acid solutions at 25 °C indicate a *salting-out* effect with increasing citric acid concentrations (between 0.13 and 1.04 M citric acid; (Popovic *et al.*, 1979; Battino, 1981a)). Since O₃ solubility often follows similar dependences as that of O₂ (Biń, 2006), we consider this *salting-out* scenario as likely as the *salting-in*.

Figure 3.4 presents the solubility for the aforementioned two scenarios. The *salting-in* scenario, $H_{O_3_CA_{salt-in}}$, shows a strong increase of ozone solubility with decreasing temperature. This trend is driven by the temperature dependence of $H_{solution}$ that we set to that of H_{water} . Since we are uncertain about the temperature dependence of ozone solubility in this solution, we considered a second alternative to this *salting-in* scenario, where the solubility has no temperature dependence and the small trend in Figure 3.4 is only caused by the change in citric acid concentration.

The *salting-out* scenario, $H_{O_3_CA_{salt-out}}$, shows a similar temperature dependence to H_{O_3NaBr} with an increase in solubility with decreasing temperature, a decrease at 0 °C as concentrations increase and a further increase as the temperature effect dominates again. $H_{O_3CA_salt-out}$ is significantly lower than H_{water} . The solubility of O₃ in the film mixture (H_{O_3Mix}) was calculated by applying a volume mixing rule to the three scenarios for the citric acid fraction and the solubility in the NaBr fraction, H_{O_3NaBr} (equation (3.9)).

In summary, the solubility in the different fractions shows an increase with decreasing temperature up to 0 °C. Below 0 °C, there is a discontinuity (except in $H_{O_3_CA_{salt-in}}$ and $H_{O_3_CA_{salt-in}(T-ind)}$) due to the effect of increasing solute concentrations with decreasing water activity as temperatures decrease. All mixture scenarios (H_{O_3Mix}) show an overall *salting-out* effect; that is, H_{O_3Mix} is less than H_{water} . The discontinuity at 0 °C in the fractions is also reflected in the H_{O_3Mix} .

$$H_{O_3Mix} = Volfrac_{NaBr} \cdot H_{O_3NaBr} + Volfrac_{CA} \cdot H_{O_3CA} \quad (3.9)$$

Figure 3.5 shows an assessment of the impact of the different solubility scenarios on the uptake coefficients, all other factors remaining the same. The γ_{calc} for the *salting-in* scenario with $H_{O_3_CA_{salt-in}}$, $\gamma_{HO_3Mix_salt-in}$, does not concur with the observed uptake coefficients below 0 °C. This indicates that the rather strong temperature dependence described by the temperature dependence of H_{O_3water} poorly represents the temperature dependence of O₃ solubility with the *salting-in* effect. This observation is in agreement with the small general temperature dependence found in the *salting effect* of organic co-solutes (Eley, 1939).

Decoupling the temperature dependence of this solubility effect of the organic fraction from that of water gives better results ($\gamma_{\text{HO3Mix_CA salt-in}(T\text{-ind})}$ and $\gamma_{\text{HO3Mix_CA salt-out}}$).

The difference between these two scenarios calls for further studies on gas solubility in organic mixtures at low temperatures. In general, due to the absence of measurements of ozone solubility in organic–inorganic mixtures and at temperatures below 0 °C, there are large uncertainties. We have estimated this uncertainty based on the difference between the different scenarios (SI Table S3.4). A 20% change in the solubility parameter at 0 °C resulted in 12% change in the γ_{calc} and a 35% change in the solubility parameter resulted in 32% change in γ_{calc} at –20 °C (Table 3.2).

In summary, both $H_{\text{O3Mix_CA salt-in}(T\text{ind})}$ and $H_{\text{O3Mix_CA salt-out}}$ give good results and can be used to assess ozone solubility in mixed systems at temperatures below the freezing point of water.

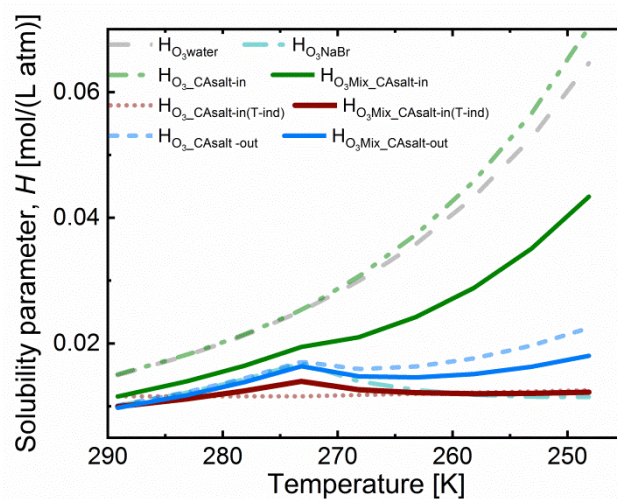


Figure 3.4: Calculated ozone solubility in solution fractions and in the mixture (by volume mixing rule). H_{O3i} is Henry's law O_3 solubility in solution i ; Grey dash line: H_{O3water} ; Cyan dash-dot line: H_{O3NaBr} ; Green-dash-dot-dot line: $H_{\text{O3_CA salt-in}}$, *salting-in* effect with T dependence of H_{O3water} ; Red-dot line: $H_{\text{O3_CA salt-in}(T\text{-ind})}$, *salting-in* effect without a T-dependence; blue-dash line: $H_{\text{O3_CA salt-out}}$, *salting-out* effect with T dependence of H_{O3water} ; solid green line: $H_{\text{O3Mix_CA salt-in}}$ with $H_{\text{O3_CA salt-in}}$; solid red line: $H_{\text{O3Mix_CA salt-in}(T\text{-ind})}$ with $H_{\text{O3_CA salt-in}(T\text{-ind})}$; solid blue line: $H_{\text{O3Mix_CA salt-out}}$ with $H_{\text{O3_CA salt-out}}$; all H_{O3Mix} contain volume ratio combinations of the $H_{\text{O3_CA}}$ scenarios and H_{O3NaBr} -Surface reaction

Viscosity and aqueous bulk diffusivity of ozone

The excellent agreement between γ_{calc} and γ_{obs} in Figure 3.3 was also achieved by parameterizing the diffusivity in the film. The viscosity of the film influences the diffusivity of ozone and products within the film. The diffusivity of ozone in the film was estimated using the Stokes–Einstein relationship (equation (3.10)), in which diffusivity is inversely related to

Chapter 3 Interplay of microphysics and kinetics in bromide oxidation by ozone

viscosity. The Stokes–Einstein relationship is valid for small molecules and viscosities lower than 10 Pa s (Power *et al.*, 2013). The viscosity of the film was obtained by measuring the viscosity of the solutions containing the equilibrium concentrations, as calculated by AIOMFAC, at each experimental temperature. The viscosity of the film increased from 1.4 mPa s at 16 °C to 43.9 mPa s at –24 °C, which leads to an almost 40 times decrease in diffusivity. The measured viscosity of the mixture is similar to that measured in citric acid solutions (Lienhard *et al.*, 2014). Therefore, this increase in viscosity with decreasing T and increasing concentration is predominantly driven by citric acid (SI Figure S3.3; (Apelblat, 2014; 2018)).

$$D_{O_3l} = \frac{k_B T}{6\pi\eta(T)r_{O_3}} \quad (3.10)$$

Γ_{bulk} as presented in equation (3.5) above is applicable if the reacto–diffusive length (l_{rd}) is smaller than the thickness of the film (t_{film}). In this case, the uptake in the aqueous bulk is limited by both reaction and diffusion in the aqueous bulk. The l_{rd} is defined as the characteristic distance over which the reactant (O_3) is lost due to reaction in the film (equation (3.11); (Finlayson-Pitts and Pitts, 2000)).

$$l_{rd} = \sqrt{\frac{D_{O_3l}}{k_b^I}} \quad (3.11)$$

If the l_{rd} is almost equal or larger than t_{film} , reaction occurs almost throughout the depth or thickness of the film; Γ_{bulk} will be proportional to the volume of the film (or thickness). The thickness of the film was obtained by dividing the estimated volume of the film by the internal surface area of the tube (188.5 cm²). The film thickness ranged from ~2 μm at –25 °C to ~13 μm at 16 °C while the l_{rd} ranged from 0.7 μm at –25 °C to 2.3 μm at 16 °C. Hence, we assumed that equation (3.5) is a good representation of Γ_{bulk} .

We have assigned a low uncertainty to the diffusivity parameter due to the viscosity measurements for the equilibrium concentrations of solutes in the film, which were conducted as part of this study. The equilibrium concentrations calculated using the AIOMFAC model may also be a source of uncertainty for this parameter. A 5% change in the diffusivity parameter at 0 °C results in 2% change in γ_{calc} and a 10% change in the diffusivity at –20 °C results in the 4% change in γ_{calc} (Table 3.2).

Table 3.1 Film composition and properties at 16 °C, 0 °C and –20 °C ^a

| T [°C] | $a_{[\text{Br}^-]}$ M | $a_{[\text{CA}]}$ M | pH | k_b^{II} [M ⁻¹ s ⁻¹] | $D_{O_3l, \text{mix}}$ [cm ² /s] | $H_{\text{mix, salt-in}(T\text{-ind})}$ [mol/(L atm)] | O_3 [#/cm ⁻³] | k_s^I [s ⁻¹] | K [cm ³] |
|------------|--------------------------|------------------------|-----|---|--|--|--------------------------------|-------------------------------|---------------------------|
| 16 | 0.6 | 0.09 | 2.1 | 388 | 1.20E–05 | 9.94E–03 | 4.31E+12 | 3.31E–02 | 6.43E–12 |
| 0 | 0.6 | 0.08 | 2.1 | 123 | 6.80E–06 | 1.40E–02 | 4.57E+12 | 5.15E–03 | 7.38E–12 |
| –20 | 3.8 | 0.5 | 1.7 | 25 | 5.70E–07 | 1.20E–02 | 4.93E+12 | 3.61E–04 | 9.00E–12 |

^a T is temperature; $a_{[\text{Br}^-]}$ is Bromide activity and $a_{[\text{CA}]}$ is citric acid activity (AIOMFAC calculations); k_b^{II} is second order bulk rate coefficient; D_{O_3l} is O_3 diffusivity; H_{mix} is ozone solubility, k_s^I is the surface rate coefficient, K is the surface adsorption coefficient

Uncertainty in aqueous bulk properties and impact on γ_{calc}

Although we are able to predict the measured uptake coefficients in this system, there are uncertainties in the parameters. The uncertainties arise from the lack of measurements of the parameters for the organic component and mixtures, in particular, below 0 °C. Therefore, extrapolation to lower temperatures comes with large uncertainties. Figure 3.5 shows the γ_{calc} with error bands (thinner lines). The error bands were determined *via* error propagation with increasing percentage error as temperatures decreased below 0 °C for all surface and bulk parameters.

Table 3.2 presents a summary of uncertainties in the bulk parameters and their implications on the bulk uptake coefficients and total uptake coefficients at 16 °C, 0 °C, and –20 °C. Uncertainties in all parameters increase as temperatures decrease below 0 °C due to the absence of measurements and parameterizations at colder temperatures and high concentrations. SI Table S3.4 contains information on uncertainties assigned to each parameter and at the different temperatures. In summary, the bulk uptake coefficients and the total uptake coefficients are most sensitive to the solubility parameter. The solubility parameter is also the largest source of uncertainty.

Table 3.2 : Uncertainty and sensitivity of Γ_{bulk} and γ_{calc} to solubility ($H_{\text{O}_3\text{Mix}}$), diffusivity of ozone ($D_{\text{O}_3\text{I}_{\text{mix}}}$), and the rate of reaction in the aqueous bulk (k_{b}^{I})

| T [°C] | $H_{\text{O}_3\text{Mix}}$ | | | $D_{\text{O}_3\text{I}_{\text{mix}}}$ | | | k_{b}^{I} | | |
|------------------------------------|----------------------------|----|-----|---------------------------------------|---|-----|---------------------------|----|-----|
| | 16 | 0 | –20 | 16 | 0 | –20 | 16 | 0 | –20 |
| % uncertainty applied | 20 | 20 | 35 | 5 | 5 | 9 | 22 | 22 | 34 |
| % Change in Γ_{bulk} | 19 | 20 | 34 | 3 | 2 | 4 | 11 | 11 | 17 |
| % Change in γ_{calc} | 12 | 17 | 32 | 2 | 2 | 4 | 7 | 9 | 16 |

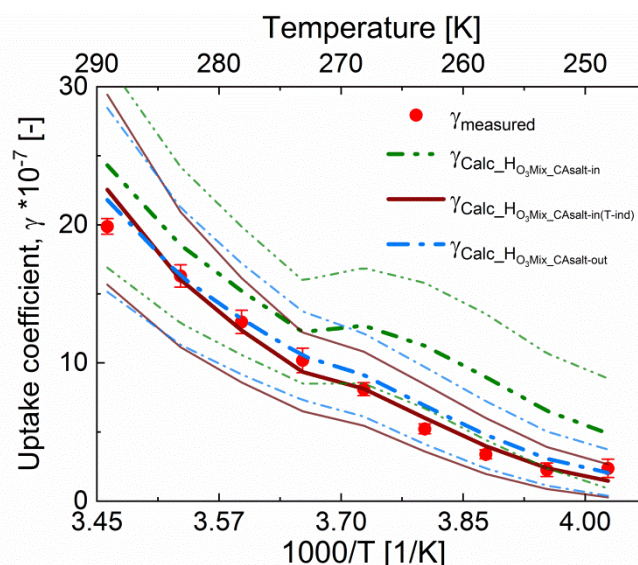


Figure 3.5: Measured (dots) and parameterized (lines) uptake coefficients as a function of temperature at 5×10^{12} molecules per cm^3 ozone concentration. The parameterizations differ in the ozone solubility in presence of citric acid: The dash-dot-dot green line is the parameterization with the salting-in effect of the organic with a temperature dependence of O_3 solubility in water + salting-out effect of NaBr; the solid red line is the parameterization with the salting-in effect of the organic without a temperature dependence of O_3 solubility in water + salting-out effect of NaBr; the dash-dot blue is the parameterization with the salting-out effect of the organic with the temperature dependence of O_3 solubility in water + salting-out effect of NaBr. The thin lines are error bands to the output.

Figure 3.6 presents the measured uptake coefficients as a function of ozone concentration at 0 °C, -10 °C, -20 °C and -25 °C, also corrected for gas phase diffusion limitation. The uptake coefficients were independent of ozone concentration at 0 and -10 °C. At temperatures below -10 °C, this independence occurs only at high ozone concentrations. That the uptake coefficient is invariant with increasing ozone concentration shows that Γ_{bulk} is not limited by the uptake of ozone from the gas phase. Only at higher ozone concentration, the surface to bulk transfer rate may be limited by saturation in surface coverage (Poschl *et al.*; Oldridge and Abbatt).

There is some evidence of negative O_3 concentration dependence at -20 °C and -25 °C, but not at higher temperatures. At -20 and -25 °C, the uptake coefficients decrease with increasing ozone concentration and then plateau to a constant value at high O_3 concentrations. This negative O_3 concentration dependence of the uptake coefficient is the result of the saturation of the surface coverage of the bromide ozonide occurring at ozone concentrations below those employed here. This observation is different from that of Oldridge and Abbatt with 8.6 mM NaBr concentration at 0 °C (2011), and Artiglia *et al.* with 0.12 M and 0.24 M NaBr concentration at 1 °C (2017) where a negative O_3 concentration dependence was observed. Considering that bromide was 0.7 M at 0 °C in the study

presented here, the absence of the O₃ concentration dependence is not linked to the bromide concentration.

The uptake coefficients at –20 °C and –25 °C are essentially the same. This observation is similar to the levelling off with temperature observed by Oldridge and Abbatt below –30 °C in their system without organics (2011). This plateauing in temperature dependence at a warmer temperature in our study may be due to the presence of the organic component. Due to increase in viscosity with temperature (and concentration of the organic species), the decrease in the diffusivity may lower the contribution of the aqueous bulk to the total O₃ uptake; hence similar total uptake coefficients are observed. These conditions may also increase the potential for surface uptake.

The parameterization output, also presented in Figure 3.6, was able to predict the O₃ concentration dependence of the uptake coefficients reasonably well. At –20 °C, the parameterization is not able to capture the observed similarity in uptake coefficients between –20 °C and –25 °C. This may be due to uncertainties in the solubility parameter at the low temperatures and higher viscosity as well as uncertainties in the surface uptake parameters.

The surface uptake parameterization used in this study was that developed by Artiglia *et al.* for a system without organics (2017). This may not be ideal for the mixed matrix in this study, where the partitioning of the solutes to the surface may not be the same as in a single solute solution (Hayase *et al.*, 2011; Lee *et al.*, 2015; Werner *et al.*, 2016). In particular, recent X-ray photoelectron spectroscopy data by Lee *et al.* (2015) have demonstrated that the presence of citric acid led to a reduction of the bromide abundance at the solution – air interface. In addition, the temperature dependence of the surface rate coefficient, k_s , may be different in this study due to the presence of organics. The k_s from Artiglia *et al.* (2017) applied in this study was based on the energy difference between the water stabilized surface intermediate, BrOOO⁻·4H₂O and the transition state species after intersystem crossing in the reaction scheme on the surface. The organics present on the surface may influence the stabilization of this intermediate, as citric acid is a good ligand, with impacts on the k_s .

The γ_{calc} is quite sensitive to the magnitude of N_{max} and k_s in equation (3.4). An increase in k_s by a factor of 10 increases γ_{calc} by a factor of 4.3 at 16 °C and 1.25 at –25 °C. An increase in N_{max} by a factor of 10 increases γ_{calc} by a factor of 2.2 at 16 °C and 1.1 at –25 °C. γ_{calc} is partly sensitive to K with a maximum of about 2% increase with an increase by a factor of 10. Increasing K increases surface coverage of the intermediate ozonide. Since the parameterization of the surface uptake coefficients is already close to maximum surface coverage, there is no significant change with an increase in K . A decrease in K by a factor of 10 decreases γ_{calc} at warmer temperatures by about 8% due to significant decrease in surface coverage at the warmer temperatures. At temperatures below 0 °C, the change

Chapter 3 Interplay of microphysics and kinetics in bromide oxidation by ozone

(increase) is about 1% due to much weaker effect on surface coverage. This is due to the temperature dependence of the K .

In summary, the data indicate a surface process at low temperatures (-20 °C and -25 °C) and low ozone concentrations. The lower surface adsorption equilibrium constant and lower coverage at warmer temperatures result in lower contributions from the surface reaction. At the colder temperatures, the coverage is higher, but the surface reaction rate coefficients are lower. The parameterization indicates a significant surface process at ozone concentrations lower than the experimental range. We attribute this difference to uncertainties in k_s , K , and their temperature dependence.

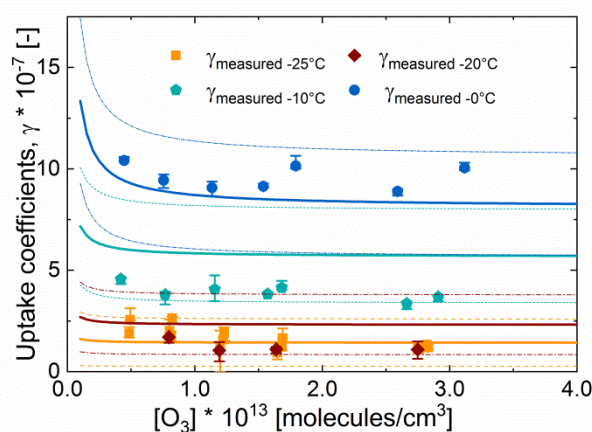


Figure 3.6: Measured and parameterized uptake coefficients ($H_{O_3\text{Mix_CA}\text{salt-in}(T\text{-ind})}$) with error bands at different temperatures as a function of gas phase ozone concentration. The dots are the measured uptake coefficients; the solid lines are the model lines; the thin dash lines are the error bands for the parameterization output. The parameterization output and error bands have the same colour as the temperature in question: *blue circles* • for 0 °C , *cyan pentagons* • for -10 °C , *red diamond* ♦ for -20 °C , and *orange squares* ■ for -25 °C .

3.1.5 Conclusions and implication

In this study, we measured the temperature dependence of the dark reaction of O_3 with bromide in a proxy for sea-spray aerosols and brine on sea-ice and in snow. This proxy contained a mixture of an organic species and an inorganic salt (citric acid and sodium bromide). A decrease in temperature resulted in a significant increase in the concentration of solutes below 0 °C as the water vapour pressure decreased. This further resulted in an increase in the *pseudo*-first order rate coefficients.

For this mixed system with organics, a combination of increased viscosity and a strong decrease in the solubility of ozone due to increase in concentrations of the solutes countered the reaction acceleration. Increased viscosity due to increased concentration of citric acid with decreasing temperature led to a significant decrease in diffusivity. Sea-spray

aerosols and brine on environmental ice surfaces such as snow and sea ice contain a significant organic component, which may strongly influence their viscosity (O'Dowd *et al.*, 2004; Reid *et al.*, 2018). This effect of citric acid on the viscosity and on the uptake of O₃ in this study is in agreement with that of other studies, which have shown similar reduced reactivity due to the impact of high viscosity on heterogeneous reactions (Steimer *et al.*, 2014; Marshall *et al.*, 2016). We note, though, that the viscosity effect seen here becomes relevant even at high relative humidity, as it is common for environmental compartments where brine is in equilibrium with ice. This effect has implications for the reaction of halides with O₃ in snow covered Arctic sea-ice where a significant source of salinity on surface snow is from sea-spray aerosols (Abbatt *et al.*, 2012), and where aged organic species (represented by citric acid in this study) are likely co-located with the halide ions (Grannas *et al.*, 2007; Abbatt *et al.*, 2012).

There is limited information on the solubility of O₃ and other oxidants in organic solutions and in organic/inorganic mixtures although O₃ is one of the important oxidants in the atmosphere. The heterogeneous reaction of O₃ in aerosols or brine pockets, which contain complex mixtures of solutes, may not be properly assessed without properly accounting for the concentration of O₃ in the condensed phase. From our solubility calculations, the composition of the mixture resulted in a significant *salting-out* effect on O₃ relative to O₃ solubility in water; using the solubility of O₃ in water overestimates the uptake coefficients. Based on our results, atmospheric models may simply be able to use a general representation of the *salting* effect of solutes on the solubility of the reacting gas.

Halogen activation *via* reaction between O₃ and halides in sea-spray aerosols have recently been updated in global atmospheric chemistry models (Schmidt *et al.*, 2016). The addition of the multiphase chemistry contribution from sea-spray aerosols has been shown to improve model predictions. These models may be further improved by including some information about the average viscosity of sea-spray aerosols and the composition effect on solubility. This implies that there is need for measurements of solubility of O₃ in mixtures which is presently lacking. Recently, there have been more studies measuring the viscosity of sea-spray aerosol (Reid *et al.*, 2018).

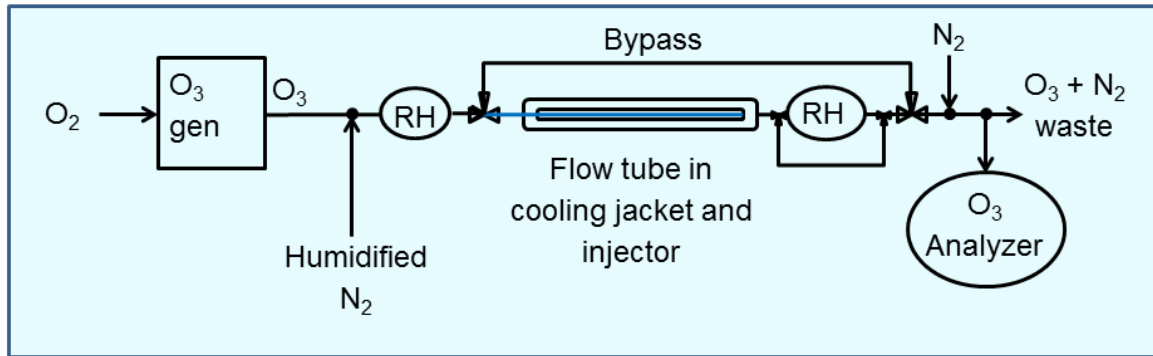
In addition, we did not focus on the surface uptake of ozone in the mixture as part of this study. There is increasing knowledge of significant surface contributions to the uptake of O₃ in aerosols at lower, atmospherically relevant O₃ concentrations. Organics have been shown to influence the partitioning of the halides to the surface (Lee *et al.*, 2015; Werner *et al.*, 2016) and the reactivity on the surface (Hayase *et al.*, 2011). Further studies at low ozone concentration on the influence of organics and mixtures on the surface uptake of ozone is needed for information on the surface uptake parameters such as the surface rate coefficients, the surface adsorption coefficients, and the maximum coverage of the reactants on the surface (N_{\max}). The total uptake coefficients are particularly sensitive to the N_{\max} and the surface rate coefficients.

3.1.6 Acknowledgements

This work was funded by the Swiss National Foundation grant number 155999. We acknowledge M. Birrer assistance with the technical parts of the experimental set up.

3.2 Supplementary information

Experimental setup



SI Figure S3.1 : Schematic of the coated wall flow tube experimental setup. RH = relative humidity sensors

Gas diffusion correction factor (Ammann and Pöschl, 2007; Poschl *et al.*, 2007)

$$C_{gd} = \frac{1}{1 + \gamma_{obs} \times \frac{0.75 + 0.28Kn}{Kn(1+Kn)}} \quad \text{SI1}$$

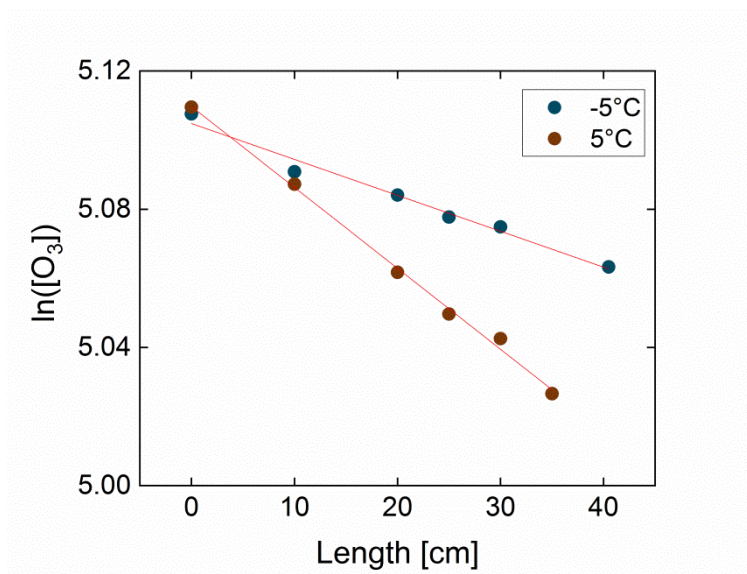
Where Kn is the knudsen number (descriptor for the flow regime) and C_{gd} is the gad diffusion correction factor

$$Kn = \frac{6D_{gO_3}}{w_{O_3} \cdot h} \quad \text{SI2}$$

Where D_{gO_3} is the gas phase diffusion coefficient of ozone,^{3,4} w_{O_3} is the mean thermal velocity of ozone, and h is the characteristic length, in this case the diameter of the flow tube.

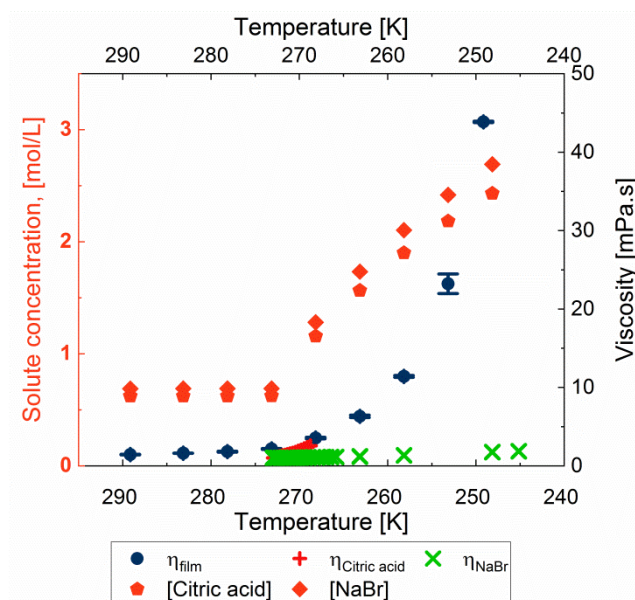
Chapter 3 Interplay of microphysics and kinetics in bromide oxidation by ozone

Test of first order kinetics



SI Figure S3.2: Plot of $\ln([O_3])$ exiting the flow tube as a function of length of the coated wall flow tube exposed at $-5\text{ }^\circ\text{C}$ and $5\text{ }^\circ\text{C}$. The observed linear trend indicates that reactive loss of ozone follows first order kinetics with respect to Br^-

Temperature dependence of viscosity



SI Figure S3.3: Comparison between measured viscosity in the mixture in the film (blue circles $\bullet \pm \text{s.d.}$) and viscosity data for NaBr (+) and citric acid solutions (x) (Rumble, 2018). \blacklozenge is the equilibrium concentration of NaBr in the film as calculated using the AIOMFAC model; \blacktriangleleft is the equilibrium concentration of citric acid in the film as calculated using the AIOMFAC model (Zuend *et al.*, 2008).

Parameterization of the second order bulk reaction rate coefficients

The bulk uptake coefficient was parameterized using Liu *et al.*'s measurements at different temperatures and pHs (Liu *et al.*, 2001). Below we present the Arrhenius representation of the rate coefficients for the reactions presented in the paper (R1–R5).

$$k_b^{II} = \frac{k_1 \left(\frac{k_2}{k_{-1}} [H^+] + \frac{k_3}{k_{-1}} \right)}{1 + \frac{k_2}{k_{-1}} [H^+] + \frac{k_3}{k_{-1}}} \quad (1)$$

Where,

$$k_1 = 2.05 \times 10^{13} \exp(-6916/T);$$

$$k_2 = 1.50 \times 10^{39} \exp(-23863/T);$$

$$k_3 = 1.60 \times 10^{36} \exp(-23515/T);$$

$$k_{-1} = 4.20 \times 10^{41} \exp(-26714/T);$$

Summary tables of parameters and uncertainty analysis

SI Table S3.1: Estimated solubility parameters at temperatures of study

| T [K] | H _{water} [mol/Latm] | H _{NaBr} [mol/Latm] | H _{salt in} [mol/Latm] | H _{salt-in(T-ind)} [mol/Latm] | H _{salt-out} [mol/Latm] | H _{mix_salt out} [mol/Latm] | H _{mix_salt-in(T-ind)} [mol/Latm] | H _{mix_salt-in} [mol/Latm] |
|----------|----------------------------------|---------------------------------|------------------------------------|---|-------------------------------------|---|---|--|
| 289.15 | 1.50E-02 | 1.01E-02 | 1.51E-02 | 1.16E-02 | 1.01E-02 | 9.75E-03 | 9.94E-03 | 1.16E-02 |
| 283.15 | 1.81E-02 | 1.21E-02 | 1.82E-02 | 1.16E-02 | 1.22E-02 | 1.18E-02 | 1.12E-02 | 1.39E-02 |
| 278.15 | 2.12E-02 | 1.43E-02 | 2.14E-02 | 1.16E-02 | 1.44E-02 | 1.38E-02 | 1.24E-02 | 1.64E-02 |
| 273.15 | 2.51E-02 | 1.68E-02 | 2.53E-02 | 1.16E-02 | 1.71E-02 | 1.64E-02 | 1.40E-02 | 1.94E-02 |
| 268.15 | 2.99E-02 | 1.40E-02 | 3.07E-02 | 1.18E-02 | 1.59E-02 | 1.48E-02 | 1.26E-02 | 2.10E-02 |
| 263.15 | 3.59E-02 | 1.26E-02 | 3.74E-02 | 1.20E-02 | 1.63E-02 | 1.46E-02 | 1.22E-02 | 2.42E-02 |
| 258.15 | 4.33E-02 | 1.18E-02 | 4.58E-02 | 1.22E-02 | 1.76E-02 | 1.51E-02 | 1.20E-02 | 2.88E-02 |
| 253.15 | 5.27E-02 | 1.15E-02 | 5.65E-02 | 1.23E-02 | 1.96E-02 | 1.63E-02 | 1.20E-02 | 3.51E-02 |
| 248.15 | 6.46E-02 | 1.15E-02 | 7.03E-02 | 1.25E-02 | 2.25E-02 | 1.80E-02 | 1.22E-02 | 4.34E-02 |

SI Table S3.2: Estimated diffusivities (D) applied to Figure 3

| T [K] | D _{water} cm ² /s | D _{NaBr} cm ² /s | D _{mix} cm ² /s |
|----------|--|---|--|
| 289.15 | 1.56E-05 | 1.47E-05 | 1.18E-05 |
| 283.15 | 1.36E-05 | 1.25E-05 | 1.01E-05 |
| 278.15 | 1.21E-05 | 1.10E-05 | 8.74E-06 |
| 273.15 | 1.06E-05 | 9.60E-06 | 6.82E-06 |
| 268.15 | 9.35E-06 | 8.09E-06 | 4.28E-06 |
| 263.15 | 8.17E-06 | 6.83E-06 | 2.49E-06 |
| 258.15 | 7.11E-06 | 5.79E-06 | 1.30E-06 |
| 253.15 | 6.15E-06 | 4.92E-06 | 5.94E-07 |
| 248.15 | 5.29E-06 | 4.21E-06 | 3.02E-07 |

Chapter 3 Interplay of microphysics and kinetics in bromide oxidation by ozone

SI Table S3. 3: Values of other parameters used in the study models

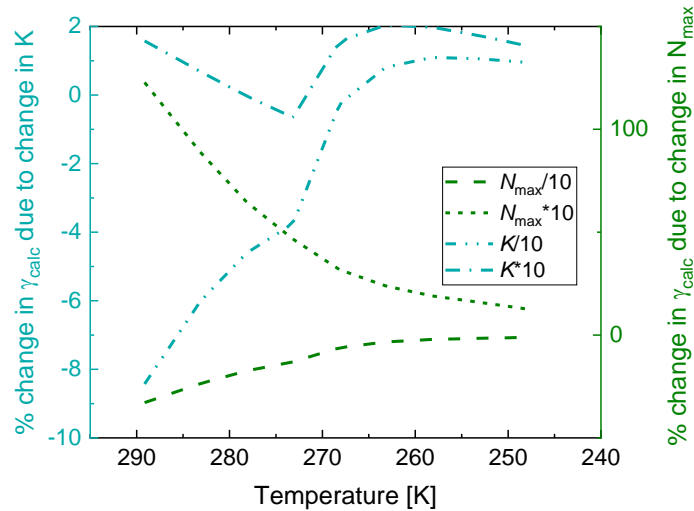
a is the activity of bromide (Br⁻) and citric acid (CA) in the film; k_b^{II} is the 2nd order rate coefficient; l_{rd} is the reacto diffusive length; t_{film} is the calculated film thickness; k_s^I is the *pseudo*-first order surface reaction rate coefficient; K is the surface adsorption coefficients.

| T [K] | $a_{[Br^-]}$ M | $a_{[CA]}$ M | pH | k_b^{II} [M ⁻¹ s ⁻¹] | l_{rd} [μm] | t_{film} [μm] | O ₃ [#/cm ⁻³] | k_s^I [s ⁻¹] | K [cm ³] |
|----------|-------------------|-----------------|-----|--|------------------|--------------------|---|-------------------------------|---------------------------|
| 289.15 | 0.59 | 0.09 | 2.0 | 388 | 2.3 | 13 | 4.31E+12 | 3.31E-02 | 6.43E-12 |
| 283.15 | 0.59 | 0.09 | 2.1 | 258 | 2.6 | 13 | 4.41E+12 | 1.69E-02 | 6.76E-12 |
| 278.15 | 0.58 | 0.08 | 2.1 | 180 | 2.9 | 13 | 4.49E+12 | 9.43E-03 | 7.06E-12 |
| 273.15 | 0.57 | 0.08 | 2.1 | 123 | 3.1 | 13 | 4.57E+12 | 5.15E-03 | 7.38E-12 |
| 268.15 | 1.27 | 0.19 | 1.9 | 92 | 1.9 | 6 | 4.65E+12 | 2.75E-03 | 7.74E-12 |
| 263.15 | 2.04 | 0.30 | 1.8 | 62 | 1.4 | 4 | 4.74E+12 | 1.43E-03 | 8.12E-12 |
| 258.15 | 2.87 | 0.42 | 1.7 | 40 | 1.1 | 3 | 4.83E+12 | 7.29E-04 | 8.54E-12 |
| 253.15 | 3.76 | 0.52 | 1.7 | 25 | 0.8 | 2 | 4.93E+12 | 3.61E-04 | 9.00E-12 |
| 248.15 | 4.69 | 0.62 | 1.6 | 15 | 0.7 | 2 | 5.03E+12 | 1.74E-04 | 9.51E-12 |

SI Table S3. 4: Uncertainty analysis and sensitivity of the bulk (Γ_{bulk}) and total (γ_{calc}) uptake coefficients to the bulk uptake parameters

| T [K] | Diffusivity (D) | | | Aqueous bulk rate coefficient (k_b^I) | | | Solubility (H) | | |
|--------|-----------------|-----------------------------|-----------------------------|---|-----------------------------|-----------------------------|----------------|-----------------------------|-----------------------------|
| | % error | % Change in Γ_{bulk} | % Change in γ_{calc} | % error | % Change in Γ_{bulk} | % Change in γ_{calc} | % error | % Change in Γ_{bulk} | % Change in γ_{calc} |
| 289.15 | 5 | 3 | 2 | 22 | 11 | 7 | 20 | 19 | 12 |
| 283.15 | 5 | 3 | 2 | 22 | 11 | 8 | 20 | 19 | 14 |
| 278.15 | 5 | 3 | 2 | 22 | 11 | 9 | 20 | 19 | 16 |
| 273.15 | 5 | 2 | 2 | 22 | 11 | 9 | 20 | 20 | 17 |
| 268.15 | 6 | 3 | 3 | 25 | 12 | 11 | 21 | 20 | 19 |
| 263.15 | 7 | 4 | 3 | 27 | 13 | 13 | 23 | 22 | 21 |
| 258.15 | 8 | 4 | 4 | 31 | 15 | 14 | 27 | 26 | 25 |
| 253.15 | 9 | 4 | 4 | 34 | 17 | 16 | 35 | 34 | 32 |
| 248.15 | 10 | 5 | 5 | 39 | 19 | 19 | 51 | 49 | 47 |

Sensitivity of γ_{calc} to surface parameters



SI Figure S3.4 Sensitivity of γ_{calc} to N_{max} and K presented as % change in γ_{calc} as a function of temperature. The *green dash* lines represent changes to γ_{calc} due to change in N_{max} . The *cyan dash-dot* lines represent changes with change in K . ($K = 6 \times 10^{13} \cdot \exp(\frac{686}{T})$)

Increase in K leads to increase in surface coverage. Since the model is already close to maximum coverage, 10 times increase in K does not significantly increase surface coverage. However, decrease in K by a factor of 10 significantly decreases surface coverage and more strongly at the warmer temperatures than at the lower temperatures. As a result, there is a much stronger effect on the γ_{calc} .

Uncertainty consideration and error propagation

- Bulk uptake coefficients

$$\Gamma_{\text{bulk}} = \frac{4HRT}{\omega_{\text{O}_3}} \times \sqrt{D_{\text{O}_3\text{l}} \times k_{\text{b}}^{\text{I}}} = \frac{4HRT}{\omega_{\text{O}_3}} \times \sqrt{D_{\text{O}_3\text{l}} \times k_{\text{b}}^{\text{II}} \times \alpha_{\text{Br}^-}}$$

$$\text{Let } a = \sqrt{D_{\text{O}_3\text{l}}}; \quad b = \sqrt{k_{\text{b}}^{\text{II}}}; \quad c = \sqrt{\alpha_{\text{Br}^-}}; \quad A = \frac{4RT}{\omega_{\text{O}_3}};$$

$$\text{Let } P = H \times a \times b \times c;$$

Then, $\Gamma_{\text{bulk}} = AP$; where A is a considered as a constant at each T ,

By error propagation,

$$\frac{\delta a}{|a|} = \frac{1}{2} \frac{\delta D_{\text{O}_3\text{l}}}{|D_{\text{O}_3\text{l}}|}, \quad \frac{\delta b}{|b|} = \frac{1}{2} \frac{\delta k_{\text{b}}^{\text{II}}}{|k_{\text{b}}^{\text{II}}|}, \quad \frac{\delta c}{|c|} = \frac{1}{2} \frac{\delta \alpha_{\text{Br}^-}}{|\alpha_{\text{Br}^-}|};$$

Chapter 3 Interplay of microphysics and kinetics in bromide oxidation by ozone

$$\frac{\delta P}{|P|} = \frac{\delta \Gamma_{\text{bulk}}}{|\Gamma_{\text{bulk}}|} = \sqrt{\left(\frac{\delta H}{|H|}\right)^2 + \left(\frac{\delta a}{|a|}\right)^2 + \left(\frac{\delta b}{|b|}\right)^2 + \left(\frac{\delta c}{|c|}\right)^2};$$

- Surface uptake coefficients

$$\Gamma_{\text{surf}} = \frac{4 \cdot k_s \cdot K \cdot N_{\text{max}}}{\omega_{\text{O}_3} \cdot (1 + K \cdot [\text{O}_3]_{\text{g}})}$$

$$\frac{\delta \Gamma_{\text{surf}}}{|\Gamma_{\text{surf}}|} = \sqrt{\left(\frac{\delta k_s}{|k_s|}\right)^2 + \left(\frac{\delta N_{\text{max}}}{|N_{\text{max}}|}\right)^2 + \left(\frac{\delta K}{|K|}\right)^2 + \left(-1 \frac{\delta K}{|K|}\right)^2};$$

- Total calculated uptake coefficients

$$\frac{\delta \gamma_{\text{calc}}}{|\gamma_{\text{calc}}|} = \sqrt{\left(\frac{\delta \Gamma_{\text{surf}}}{|\Gamma_{\text{surf}}|}\right)^2 + \left(\frac{\delta \Gamma_{\text{bulk}}}{|\Gamma_{\text{bulk}}|}\right)^2};$$

$$\gamma_{\text{calc_upper}} = \gamma_{\text{calc}} \left(1 + \frac{\delta \gamma_{\text{calc}}}{|\gamma_{\text{calc}}|}\right);$$

$$\gamma_{\text{calc_lower}} = \gamma_{\text{calc}} \left(1 - \frac{\delta \gamma_{\text{calc}}}{|\gamma_{\text{calc}}|}\right);$$

Bibliography

Abbatt, J. P.: Heterogeneous reaction of HOBr with HBr and HCl on ice surfaces at 228 K, *Geophys Res Lett*, 21, 665 - 668, 1994.

Abbatt, J. P. D., Thomas, J. L., Abrahamsson, K., Boxe, C., Granfors, A., Jones, A. E., King, M. D., Saiz-Lopez, A., Shepson, P. B., Sodeau, J., Toohey, D. W., Toubin, C., von Glasow, R., Wren, S. N., and Yang, X.: Halogen activation *via* interactions with environmental ice and snow in the polar lower troposphere and other regions, *Atmos Chem Phys*, 12, 6237-6271, 10.5194/acp-12-6237-2012, 2012.

Ammann, M., and Pöschl, U.: Kinetic model framework for aerosol and cloud surface chemistry and gas-particle interactions - Part 2: Exemplary practical applications and numerical simulations, *Atmos. Chem. Phys*, 7, 6025 -6045, 2007.

Ammann, M., Cox, R. A., Crowley, J. N., Jenkin, M. E., Mellouki, A., Rossi, M. J., Troe, J., and Wallington, T. J.: Evaluated kinetic and photochemical data for atmospheric chemistry: Volume VI – heterogeneous reactions with liquid substrates, *Atmos Chem Phys*, 13, 8045-8228, 10.5194/acp-13-8045-2013, 2013.

Apelblat, A.: Properties of Citric Acid and Its Solutions, in: *Citric acid*, 13-141, 2014.

Artiglia, L., Edebeli, J., Orlando, F., Chen, S., Lee, M.-T., Corral Arroyo, P., Gilgen, A., Bartels-Rausch, T., Kleibert, A., Vazdar, M., Andres Carignano, M., Francisco, J. S., Shepson, P. B., Gladich, I., and Ammann, M.: A surface-stabilized ozonide triggers bromide oxidation at the aqueous solution-vapour interface, *Nat Comm*, 8, 700, 10.1038/s41467-017-00823-x, 2017.

Bartels-Rausch, T., Jacobi, H. W., Kahan, T. F., Thomas, J. L., Thomson, E. S., Abbatt, J. P. D., Ammann, M., Blackford, J. R., Bluhm, H., Boxe, C., Domine, F., Frey, M. M., Gladich, I., Guzmán, M. I., Heger, D., Huthwelker, T., Klán, P., Kuhs, W. F., Kuo, M. H., Maus, S., Moussa, S. G., McNeill, V. F., Newberg, J. T., Pettersson, J. B. C., Roeselová, M., and Sodeau, J. R.: A review of air–ice chemical and physical interactions (AICI): liquids, quasi-liquids, and solids in snow, *Atmos Chem Phys*, 14, 1587-1633, 10.5194/acp-14-1587-2014, 2014.

Bibliography

Battino, R.: Ozone Solubilities, in: Solubility data series, Pergamon Press Ltd, Oxford UK, 1981a.

Battino, R.: Oxygen and Ozone - Solubility data series, International Union of Pure and Applied Chemistry, 1981b.

Biń, A. K.: Ozone Solubility in Liquids, *Ozone: Science & Engineering*, 28, 67-75, 10.1080/01919510600558635, 2006.

Chaimedes, W. L., and Stelson, A. W.: Aqueous-phase chemical processes in deliquescent sea-salt aerosols: A mechanism that couples the atmospheric cycles of S and sea salt, *J. Geophys Res.*, 97, 20565-20580, 1992.

Cho, H., Shepson, P. B., Barrie, L. A., Cowin, J. P., and Zaveri, R.: NMR investigation of the quasi-brine layer in ice/brine mixtures, *J. Phys. Chem. B*, 106, 11226-11232, 10.1021/jp020449+, 2002.

Clifford, A., and Donaldson, D. J.: Direct experimental evidence for a heterogeneous reaction of ozone with bromide at the air-aqueous interface, *J. Phys. Chem. A*, 111, 9809-9814, 2007.

Dominé, F., Sparapni, R., Ianniello, A., and Beine, H. J.: The origin of sea salt in snow on Arctic sea ice and in coastal regions, *Atmos. Chem. Phys*, 4, 2259 - 2271, 2004.

Eley, D. D.: On the solubility of gases. Part II.—A comparison of organic solvents with water, *Transactions of the Faraday Society*, 35, 1421-1432, 10.1039/TF9393501421, 1939.

Fickert, S., Adams, J. W., and Crowley, J. N.: Activation of Br₂ and BrCl *via* uptake of HOBr onto aqueous salt solutions, *Journal of Geophysical Research*, 104, 23719, 10.1029/1999jd900359, 1999.

Finlayson-Pitts, B. J., and Pitts, J. N. J.: Chemistry of the upper and lower atmosphere, Academic Press, San Diego California, USA, 969 pp., 2000.

Frinak, E. K., and Abbatt, J. P.: Br₂ production from the heterogeneous reaction of gas-phase OH with aqueous salt solutions: Impacts of acidity, halide concentration, and organic surfactants, *J. Phys. Chem.*, 110, 10456 - 10464, 2006.

Bibliography

Gladich, I., Francisco, J. S., Buszek, R. J., Vazdar, M., Carignano, M. A., and Shepson, P. B.: Ab initio study of the reaction of ozone with bromide ion, *J Phys Chem A*, 119, 4482-4488, 10.1021/jp5101279, 2015.

Grannas, A. M., Hockaday, W. C., Hatcher, P. G., Thompson, L. G., and Mosley-Thompson, E.: New revelations on the nature of organic matter in ice cores, *Journal of Geophysical Research*, 111, 10.1029/2005jd006251, 2006.

Grannas, A. M., Bausch, A. R., and Mahanna, K. M.: Enhanced aqueous photochemical reaction rates after freezing, *J. Phys. Chem. A*, 111, 11043-11049, 2007.

Haag, R. W., and Hoigné, J.: Ozonation of bromide-containing waters: Kinetics of the formation of hypobromous acid and bromate, *Environ Sci Technol*, 17, 261-267, 1983.

Haruta, K., and Takeyama, T.: Kinetics of oxidation of aqueous bromide ion by ozone, *J Phys Chem*, 85, 2383- 2388, 1981.

Hastings, A. B., and Slyke, D. D. V.: The determination of the three dissociation constants of citric acid, *J. Biol. Chem.*, 53, 269-276, 1922.

Hayase, S., Yabushita, A., Kawasaki, M., Enami, S., Hoffmann, M. R., and Colussi, A. J.: Weak acids enhance halogen activation on atmospheric water's surfaces, *J Phys Chem A*, 115, 4935-4940, 10.1021/jp2021775, 2011.

Hebestreit, K., Stutz, J., Rosen, D., Matveiv, V., Peleg, M., Luria, M., and Platt, U.: DOAS measurements of tropospheric bromine oxide in mid-latitudes, *Science*, 283, 55-57, 1999.

Hunt, S. W., Roeselová, M., Wang, W., Wingen, L. M., Knipping, E. M., Tobias, D. J., Dabdub, D., and Finlayson-Pitts, B. J.: Formation of molecular bromine from the reaction of ozone with deliquesced NaBr Aerosol: Evidence of interface chemistry, *J. Phys. Chem. A*, 108, 11559 - 11572, 2004.

Isono, T.: Density, viscosity, and electrolytic conductivity of concentrated aqueous electrolyte solutions at several temperatures. Alkaline-earth chlorides, LaCl_3 , Na_2SO_4 , NaNO_3 , NaBr , KNO_3 , KBr , and $\text{Cd}(\text{NO}_3)_2$, *J. Chem Eng Data*, 29, 45-52, 1984.

Ivanov, A. V., Trakhtenberg, S., Bertram, A. K., Gershenson, Y. M., and Molina, M. J.: OH, HO_2 , and ozone gaseous diffusion coefficients, *J. Phys. Chem. A*, 111, 1632 - 1637, 2007.

Bibliography

Johnson, P. N., and Davis, R. A.: Diffusivity of ozone in water, *J. Chem Eng Data*, 41, 1485-1487, 1996.

Koop, T., Kapilashrami, A., Molina, L. T., and Molina, M. J.: Phase transitions of sea-salt/water mixtures at low temperatures: Implications for ozone chemistry in polar marine boundary layer, *Journal of Geophysical Research*, 105, 26393 - 26402, 10.1029/2000JD900413, 2000.

Lee, M. T., Brown, M. A., Kato, S., Kleibert, A., Turler, A., and Ammann, M.: Competition between organics and bromide at the aqueous solution-air interface as seen from ozone uptake kinetics and X-ray photoelectron spectroscopy, *J Phys Chem A*, 119, 4600-4608, 10.1021/jp510707s, 2015.

Liao, J., Huey, L. G., Tanner, D. J., Flocke, F. M., Orlando, J. J., Neuman, J. A., Nowak, J. B., Weinheimer, A. J., Hall, S. R., Smith, J. N., Fried, A., Staebler, R. M., Wang, Y., Koo, J. H., Cantrell, C. A., Weibring, P., Walega, J., Knapp, D. J., Shepson, P. B., and Stephens, C. R.: Observations of inorganic bromine (HOBr, BrO, and Br₂) speciation at Barrow, Alaska, in spring 2009, *Journal of Geophysical Research: Atmospheres*, 117, 1 - 11, 10.1029/2011jd016641, 2012.

Lienhard, D. M., Bones, D. L., Zuend, A., Krieger, U. K., Reid, J. P., and Peter, T.: Measurements of thermodynamic and optical properties of selected aqueous organic and organic-inorganic mixtures of atmospheric relevance, *J Phys Chem A*, 116, 9954-9968, 10.1021/jp3055872, 2012.

Lienhard, D. M., Huisman, A. J., Bones, D. L., Te, Y. F., Luo, B. P., Krieger, U. K., and Reid, J. P.: Retrieving the translational diffusion coefficient of water from experiments on single levitated aerosol droplets, *Phys Chem Chem Phys*, 16, 16677-16683, 10.1039/c4cp01939c, 2014.

Liu, Q., Schurter, L. M., Muller, C. E., Aloiso, S., Francisco, J. S., and Margerum, D. W.: Kinetics and mechanisms of aqueous ozone reactions with bromide, sulfite, hydrogen sulfite, and nitrite ions, *Inorg. Chem*, 40, 4436-4442, 2001.

Long, M. S., Keene, W. C., Easter, R. C., Sander, R., Liu, X., Kerkweg, A., and Erickson, D.: Sensitivity of tropospheric chemical composition to halogen-radical chemistry using a fully coupled size-resolved multiphase chemistry–global climate system: halogen distributions, aerosol composition, and sensitivity of climate-relevant gases, *Atmos Chem Phys*, 14, 3397-3425, 10.5194/acp-14-3397-2014, 2014.

Bibliography

Marshall, F. H., Miles, R. E. H., Song, Y. C., Ohm, P. B., Power, R. M., Reid, J. P., and Dutcher, C. S.: Diffusion and reactivity in ultraviscous aerosol and the correlation with particle viscosity, *Chem Sci*, 7, 1298-1308, 10.1039/c5sc03223g, 2016.

Marti, J., and Mauersberger, K.: A survey and new measurements of ice vapor pressure at temperatures between 170 and 250K, *Geophys Res Lett*, 20, 363 - 366, 1993.

McNeill, V. F., Grannas, A. M., Abbatt, J. P. D., Ammann, M., Ariya, P., Bartels-Rausch, T., Domine, F., Donaldson, D. J., Guzman, M. I., Heger, D., Kahan, T. F., Klán, P., Masclin, S., Toubin, C., and Voisin, D.: Organics in environmental ices: sources, chemistry, and impacts, *Atmos Chem Phys*, 12, 9653-9678, 10.5194/acp-12-9653-2012, 2012.

Mitchell, D. L., and Lamb, D.: Influence of riming on the chemical composition of snow in winter orographic storms, *Journal of Geophysical Research*, 94, 14831-14840, 1989.

Murphy, D. M., and Koop, T.: Review of the vapour pressures of ice and supercooled water for atmospheric applications, *Quarterly Journal of the Royal Meteorological Society*, 131, 1539-1565, 10.1256/qj.04.94, 2005.

Nerentorp Mastromonaco, M., Gårdfeldt, K., Jourdain, B., Abrahamsson, K., Granfors, A., Ahnoff, M., Dommergue, A., Méjean, G., and Jacobi, H. W.: Antarctic winter mercury and ozone depletion events over sea ice, *Atmospheric Environment*, 129, 125-132, 10.1016/j.atmosenv.2016.01.023, 2016.

O'Concubhair, R., and Sodeau, J. R.: Freeze-induced formation of bromine/chlorine interhalogen species from aqueous halide ion solutions, *Environ Sci Technol*, 46, 10589-10596, 10.1021/es301988s, 2012.

O'Dowd, C. D., Facchini, M. C., Cavalli, F., Cebrunis, D., Mircea, M., Decesari, S., Fuzzi, S., Yoon, Y. J., and Putaud, J.-P.: Biogenically driven organic contribution to marine aerosol, *Nature*, 431, 672-676, 10.1038/nature02970, 2004.

Oldridge, N. W., and Abbatt, J. P.: Formation of gas-phase bromine from interaction of ozone with frozen and liquid NaCl/NaBr solutions: quantitative separation of surficial chemistry from bulk-phase reaction, *J Phys Chem A*, 115, 2590-2598, 10.1021/jp200074u, 2011.

Oum, K. W., Lakin, M. J., and Finlayson-Pitts, B. J.: Bromine activation in the troposphere by the dark reaction of O₃ with seawater ice, *Geophys Res Lett*, 25, 3923-3926, 10.1029/1998gl900078, 1998.

Bibliography

Peterson, P. K., Pöhler, D., Sihler, H., Zielcke, J., General, S., Frieß, U., Platt, U., Simpson, W. R., Nghiem, S. V., Shepson, P. B., Stirm, B. H., Dhaniyala, S., Wagner, T., Caulton, D. R., Fuentes, J. D., and Pratt, K. A.: Observations of bromine monoxide transport in the Arctic sustained on aerosol particles, *Atmos Chem Phys*, 17, 7567-7579, 10.5194/acp-17-7567-2017, 2017.

Popovic, M., Niebelschuetz, H., and Reuss, M.: Oxygen solubilities in fermentation fluids, *European J. Appl. Microbiol. Biotechnol*, 8, 1-15, 1979.

Poschl, U., Rudich, Y., and Ammann, M.: Kinetic model framework for aerosol and cloud surface chemistry and gas particle interactions - Part 1: General equations, parameters, and terminology, *Atmos. Chem. Phys*, 7, 5989 -6023, 2007.

Power, R. M., Simpson, S. H., Reid, J. P., and Hudson, A. J.: The transition from liquid to solid-like behaviour in ultrahigh viscosity aerosol particles, *Chemical Science*, 4, 2597, 10.1039/c3sc50682g, 2013.

Reid, J. P., Dennis-Smith, B. J., Kwamena, N. O., Miles, R. E., Hanford, K. L., and Homer, C. J.: The morphology of aerosol particles consisting of hydrophobic and hydrophilic phases: hydrocarbons, alcohols and fatty acids as the hydrophobic component, *Phys Chem Chem Phys*, 13, 15559-15572, 10.1039/c1cp21510h, 2011.

Reid, J. P., Bertram, A. K., Topping, D. O., Laskin, A., Martin, S. T., Petters, M. D., Pope, F. D., and Rovelli, G.: The viscosity of atmospherically relevant organic particles, *Nat Commun*, 9, 956, 10.1038/s41467-018-03027-z, 2018.

Renbaum-Wolff, L., Grayson, J. W., Bateman, A. P., Kuwata, M., Sellier, M., Murray, B. J., Shilling, J. E., Martin, S. T., and Bertram, A. K.: Viscosity of α -pinene secondary organic material and implications for particle growth and reactivity, *PNAS*, 110, 8014-8019, doi/10.1073/pnas.1219548110, 2013.

Rischbieter, E., Stein, H., and Schumpe, A.: Ozone Solubilities in Water and Aqueous Salt Solutions, *Journal of Chemical & Engineering Data*, 45, 338-340, 10.1021/je990263c, 2000a.

Rischbieter, E., Stein, H., and Schumpe, A.: Ozone solubilities in water and aqueous salt solutions, *J Chem Eng Data*, 45, 338-340, DOI 10.1021/je990263c, 2000b.

Rumble, J. R.: "Concentrative properties of aqueous solutions: density, refractive index, freezing point depression, and viscosity" in *CRC Handbook of Chemistry and Physics*, in, 99th Edition (Internet Version 2018) ed., CRC Press/Taylor & Francis, Boca Raton, FL, 2018.

Bibliography

Sakamoto, Y., Goda, M., and Hirokawa, J.: Kinetics Study of Heterogeneous Bromine Release from the Reaction between Gaseous Ozone and Aqueous Bromide Solution, *J Phys Chem A*, 122, 2723-2731, 10.1021/acs.jpca.7b12819, 2018.

Schmidt, J. A., Jacob, D. J., Horowitz, H. M., Hu, L., Sherwen, T., Evans, M. J., Liang, Q., Suleiman, R. M., Oram, D. E., Le Breton, M., Percival, C. J., Wang, S., Dix, B., and Volkamer, R.: Modeling the observed tropospheric BrO background: Importance of multiphase chemistry and implications for ozone, OH, and mercury, *Journal of Geophysical Research: Atmospheres*, 121, 11,819-811,835, 10.1002/2015jd024229, 2016.

Schumpe, A.: The estimation of gas solubilities in salt solutions, *Chemical Engineering Science*, 48, 153-1158, 1993.

Sechenov, M.: Über die Konstitution der Salzlösungen auf Grund ihres Verhaltens zu Kohlensäure, *Z. phys Chem.*, 4, 117 - 125, 1889.

Shiraiwa, M., Pfrang, C., Koop, T., and Pöschl, U.: Kinetic multi-layer model of gas-particle interactions in aerosols and clouds (KM-GAP): linking condensation, evaporation and chemical reactions of organics, oxidants and water, *Atmos Chem Phys*, 12, 2777-2794, 10.5194/acp-12-2777-2012, 2012.

Simpson, W. R., von Glasow, R., Riedel, K., Anderson, P., Ariya, P., Bottenheim, J., Burrows, J., Carpenter, L. J., Friess, U., Goodsite, M. E., Heard, D., Hutterli, M., Jacobi, H. W., Kaleschke, L., Neff, B., Plane, J., Platt, U., Richter, A., Roscoe, H., Sander, R., Shepson, P. B., Sodeau, J., Steffen, A., Wanger, T., and Wollf, E.: Halogens and their role in polar boundary-layer ozone depletion, *Atmos Chem Phys*, 7, 4375 - 4418, 2007.

Simpson, W. R., Brown, S. S., Saiz-Lopez, A., Thornton, J. A., and Glasow, R.: Tropospheric halogen chemistry: sources, cycling, and impacts, *Chem Rev*, 115, 4035-4062, 10.1021/cr5006638, 2015.

Steimer, S. S., Lampimäki, M., Coz, E., Grzanic, G., and Ammann, M.: The influence of physical state on shikimic acid ozonolysis: a case for in situ microspectroscopy, *Atmos Chem Phys*, 14, 10761-10772, 10.5194/acp-14-10761-2014, 2014.

Takenaka, N., Akihiro, U., and Yasuaki, M.: Acceleration of the rate of nitrite oxidation by freezing in aqueous solution, *Nature*, 358, 736 - 738, 1992.

Takenaka, N., and Bandow, H.: Chemical kinetics of reactions in the unfrozen solutions of ice, *J Phys Chem A*, 111, 8780-8786, 2007.

Bibliography

Tang, M. J., Cox, R. A., and Kalberer, M.: Compilation and evaluation of gas phase diffusion coefficients of reactive trace gases in the atmosphere: volume 1. Inorganic compounds, *Atmospheric Chemistry and Physics*, 14, 9233-9247, 10.5194/acp-14-9233-2014, 2014.

Toom-Sauntry, D., and Barrie, L. A.: Chemical composition of snowfall in the high Arctic, *Atmospheric Environment*, 36, 2683-2693, 2002.

Wang, S., Schmidt, J. A., Baidar, S., Coburn, S., Dix, B., Koenig, T. K., Apel, E., Bowdalo, D., Campos, T. L., Eloranta, E., Evans, M. J., DiGangi, J. P., Zondlo, M. A., Gao, R. S., Haggerty, J. A., Hall, S. R., Hornbrook, R. S., Jacob, D., Morley, B., Pierce, B., Reeves, M., Romashkin, P., Ter Schure, A., and Volkamer, R.: Active and widespread halogen chemistry in the tropical and subtropical free troposphere, *Proc Natl Acad Sci U S A*, 112, 9281-9286, 10.1073/pnas.1505142112, 2015.

Weisenberger, S., and Schumpe, A.: Estimation of gas solubilities in salt solutions at temperature from 273 K to 363 K, *Aiche J*, 42, 298 - 300, 1996.

Werner, J., Dalirian, M., Walz, M. M., Ekholm, V., Wideqvist, U., Lowe, S. J., Ohrwall, G., Persson, I., Riipinen, I., and Bjorneholm, O.: Surface Partitioning in Organic-Inorganic Mixtures Contributes to the Size-Dependence of the Phase-State of Atmospheric Nanoparticles, *Environ Sci Technol*, 50, 7434-7442, 10.1021/acs.est.6b00789, 2016.

Wren, S. N., Kahan, T. F., Jumaa, K. B., and Donaldson, D. J.: Spectroscopic studies of the heterogeneous reaction between O₃(g) and halides at the surface of frozen salt solutions, *Journal of Geophysical Research*, 115, 10.1029/2010jd013929, 2010.

Zardini, A. A., Sjogren, S., Marcolli, C., Krieger, U. K., Weingartner, E., Baltensperger, U., and Peter, T.: A combined particle trap/HTDMA hygroscopicity study of mixed inorganic /organic aerosol particles, *Atmos. Chem. Phys*, 8, 5589-5601, 2008.

Zuend, A., Marcolli, C., Luo, B. P., and Peter, T.: A thermodynamic model of mixed organic-inorganic aerosols to predict activity coefficients, *Atmos. Chem. Phys*, 8, 4559-4593, 2008.

Urban wintertime atmospheric composition: gas phase – PM_{2.5} partitioning, snow cover, and meteorology

4.1.1 Abstract

Urban wintertime ambient concentrations of nitric acid/nitrate ($\text{HNO}_3/\text{NO}_3^-$), ammonia/ammonium ($\text{NH}_3/\text{NH}_4^+$), and sulfur dioxide/sulfate ($\text{SO}_2/\text{SO}_4^{2-}$) in the gas and particulate (PM_{2.5}) phases were monitored from January to February, 2018 at Kalamazoo, Michigan, United States. NO_3^- dominated the PM_{2.5} mass with an average mass concentration of $0.90 \mu\text{g}/\text{m}^3$. Average NH_4^+ mass concentration was $0.52 \mu\text{g}/\text{m}^3$ and SO_4^{2-} was $0.26 \mu\text{g}/\text{m}^3$. Calculated PM_{2.5} pH using ISORROPIA ranged from 1.8 to 4.4 with an average of 3.4. Episodes of high PM_{2.5} concentrations were more frequent on days with snow cover. There was always excess NH_3 in the gas phase with an average mixing ratio of 1.74 ppb, which showed significant temperature dependence. The enthalpy of volatilization derived from the measured NH_3 concentration was $50 \pm 6 \text{ kJ}/\text{mol}$ for the entire period, which is similar to the enthalpy of aqueous dissociation of $\text{NH}_4^+_{(\text{aq})}$. SO_2 and HNO_3 concentrations were low with average concentrations of 0.07 ppb and 0.04 ppb, respectively. Average surface snow concentrations of NH_4^+ , SO_4^{2-} , and NO_3^- were 46 μM , 4.5 μM , and 27 μM , respectively. The measured surface snow pH was 6.3, which may be due to the high ammonium concentration.

4.1.2 Introduction

Interactions exist between environmental ice compartments (snow (snowpack or snow grains), sea-ice, glaciers) and the atmosphere (Domine and Shepson, 2002). Field investigations of these interactions often focus on polar regions with just a few investigating wintertime urban atmospheric composition and interactions with snow. Interactions between snow and atmospheric chemistry already begin during cloud formation as particles serve as cloud condensation nuclei or ice nuclei in the atmosphere (Barrie, 1985; Mitchell and Lamb, 1989; Grannas *et al.*, 2013). Riming, the freezing of super-cooled water on growing ice, may also lead to incorporation of atmospheric contaminants in ice (Grannas *et al.*, 2013). Trace gases may be adsorbed on the surface of ice crystals with scavenging of particles during precipitation (Grannas *et al.*, 2013). Compounds in these ice crystals/snow grains are transported and deposited on the ground with snowfall.

One of the main pathways of deposition of atmospheric contaminants to the ground surface during wintertime and in cold regions is *via* snow deposition (Mitchell and Lamb, 1989; Bergin *et al.*, 1995; Wolff *et al.*, 1998). Other transportation pathways include deposition with fog, or dry deposition (Barrie, 1985; Bergin *et al.*, 1995; Wolff *et al.*, 1998). The efficiency of these depositional processes depend on the solubility and diffusivity of gases, the hygroscopicity and size of particles, meteorological conditions, and the concentration of the contaminants in the atmosphere (Bergin *et al.*, 1995). Laboratory studies have investigated the adsorptive uptake of atmospheric trace gases by ice with links to atmospheric ice growth (scavenging and riming) (Bartels–Rausch *et al.*, 2002; Hoog *et al.*, 2007; Krepelova *et al.*, 2013), as well as uptake in snow through diffusion (Bartels–Rausch *et al.*, 2013).

Snow and ice on the ground may also serve as reactive media with products remaining in the snow or released to the atmosphere (Domine and Shepson, 2002; Abbatt, 2003; Grannas *et al.*, 2007; Simpson *et al.*, 2007; Bartels–Rausch *et al.*, 2014). The high surface area of snow facilitates the exchange between the snow and the atmosphere, as well as provides multiple avenues for reactions of contaminants on the surface of the snow grains, in liquid pockets on snow grains, or in grain boundaries (Domine and Shepson, 2002; Bartels–Rausch *et al.*, 2014). Contaminants trapped in snow may also be released as ice sublimates, may diffuse into the snowpack, or get transported to the soil below or removed with melt water (Domine and Shepson, 2002; Galitskaya and Rumyantseva, 2017). There is also the possibility of diffusion within the pore space and to the atmosphere and active transport *via* wind pumping from the snowpack back to the atmosphere (Colbeck, 1989; Albert and Hawley, 2002; Domine and Shepson, 2002). Therefore, snow can be a sink and/or a source of atmospheric trace gases and contaminants (Domine and Shepson, 2002).

Urban regions generally have more atmospheric contaminants than polar regions. Therefore, there are likely higher contaminant loadings in and on urban snow (Baysal *et al.*, 2017). Studies of snow composition in urban areas have primarily focused on trace element

Chapter 4 Urban wintertime atmospheric composition

composition and contributions to the quality of meltwater runoff (Baysal *et al.*, 2017; Galitskaya and Rumyantseva, 2017). In polar regions, there are a few studies relating snow composition to sources of contaminants highlighting the importance of air–snow exchange (Krnavek *et al.*, 2012; Macdonald *et al.*, 2017). Snow composition studies are also often conducted to aid interpretation of ice core records especially to understand the transfer of atmospheric tracers from the atmosphere to ice sheets (Davidson *et al.*, 1993; Bergin *et al.*, 1995). Some other studies investigate individual reaction processes in snow *via* observations of products of those reactions, for example, halogen activation in polar regions (e.g., Pratt *et al.*, 2013; Nerentorp Mastromonaco *et al.*, 2016).

The influence of meteorology and snow cover on atmospheric composition in polar regions also applies to urban areas. Atmospheric composition during the winter in the mid–latitudes, as in polar regions, is strongly influenced by the low temperature and low and stable boundary layer height (BL) with stagnant air (Stanier *et al.*, 2012). Such conditions often result in the buildup of contaminants in the atmosphere, which may also be deposited on the ground surface (Stanier *et al.*, 2012). In urban areas, accumulation of atmospheric contaminants may be a cause for concern as contaminant levels may exceed air quality standards (Chen *et al.*, 2012).

In addition to meteorology, snow cover may impact atmospheric chemistry. Studies have linked episodes of high concentrations of precursor trace gases (such as ammonia (NH₃), sulfur dioxide (SO₂), and nitric acid (HNO₃)) and high concentrations of PM_{2.5} (particulate matter less than 2.5 μm in diameter) to the presence of snow cover in addition to meteorology. Depending on the location, particulate composition during wintertime PM_{2.5} episodes may be dominated by ammonium nitrate (NH₄NO₃), and to a lesser extent, by ammonium sulfate ((NH₄)₂SO₄) (Katzman *et al.*, 2010; Stanier *et al.*, 2012; Kundu and Stone, 2014). Wintertime episodes have been marked by slightly warmer and stagnant air mass leading to the accumulation of atmospheric traces gases, acids, and produced (NH₄)₂SO₄ and NH₄NO₃ (Katzman *et al.*, 2010; Stanier *et al.*, 2012). Green *et al.* (2015) also observed higher concentrations of NH₄NO₃ on snow covered days than on days without snow cover (Green *et al.*, 2015). The presence of snow cover and slightly warmer air allows for an increase in ambient moisture promoting particle formation and growth (Stanier *et al.*, 2012).

NH₃, SO₂, and HNO₃ are important trace gases in the atmosphere. NH₃ and HNO₃ are important because of their potential for nitrification, and SO₂ and HNO₃ are important for acidification of soils, aerosol, and water bodies (Cadle *et al.*, 1982; Bouwman *et al.*, 1997; Battye, 2003; Pleim *et al.*, 2013). These gases are also important for particle formation and growth with potential climate and health impacts (Battye, 2003; Pleim *et al.*, 2013). NH₃, the dominant alkaline gas in the atmosphere, neutralizes the acidity of sulfate and nitrate in the atmosphere forming ammonium nitrate (NH₄NO₃) and ammonium sulfate ((NH₄)₂SO₄) (Cadle *et al.*, 1982; Ianniello *et al.*, 2010). Ammonia may also contribute to the alkalinity or neutralization of snow due to significant uptake and deposition with snow (Bergin *et al.*,

1995; Hoog *et al.*, 2007). Nitric acid, HNO_3 , is also efficiently scavenged by snow (Bergin *et al.*, 1995), with implications for snow pH and nitrate photochemistry (Domine and Shepson, 2002).

Due to the temperature dependence of NH_3 emissions, low concentrations are often expected in the winter. In addition, agricultural applications of fertilizers and other agricultural practices are much lower in the winter (Chen *et al.*, 2012). These sources are temperature dependent emitting higher concentrations of NH_3 at warmer temperatures due to evaporation (Bouwman *et al.*, 1997; Chen *et al.*, 2012). In the winter, however, there are other sources of NH_3 emissions that may dominate, one of which is traffic (Sutton *et al.*, 2000; Chen *et al.*, 2012). Cars with catalytic converters tend to release more NH_3 (Sutton *et al.*, 2000), and may contribute to NH_3 loading in the winter. Prevalence of NH_3 from automobile emissions may be identified by the diurnal pattern of NH_3 concentrations with peaks around rush hours (Sutton *et al.*, 2000; Chen *et al.*, 2012). The major sinks for NH_3 in the winter are partitioning onto particles and deposition.

Despite observations demonstrating relationships between atmospheric chemistry, meteorology, and snow cover, urban wintertime atmospheric composition data are scarce. There are only a few studies relating the concentrations in urban snow to the atmospheric composition.

Therefore, the goals for this study are:

- i. to investigate wintertime urban atmospheric chemistry with particular attention to $\text{PM}_{2.5}$ ammonium, sulfate, and nitrate and associated gas-phase species,
- ii. to assess the impact of meteorology on atmospheric composition, and
- iii. to investigate snow cover and composition and potential links to atmospheric composition.

4.1.3 Method:

A wintertime field atmospheric composition monitoring campaign was conducted between the 5th of January and the 23rd of February, 2018. This study was conducted in Kalamazoo, Michigan, United States (SI Figure S1). The measurement site (42.278406°N, 85.610516W) was located on the Western Michigan University (WMU) campus and close to Kalamazoo College. The mobile laboratory was on a low traffic residential road/parking lot (Gar Ln). To the southwest (SW) were a residential block and an open field. This field had a small inactive student garden and electrical boxes. To the west (W) and northwest (NW) was a major road (Stadium Dr.; perpendicular (NW) distance from the mobile laboratory was 55 m). To the north (N), there was a small stretch of forest (30 m from the laboratory), and behind the forest in the NE direction, was a power plant (300 m from the lab). To the east (E) and southeast (SE) were a forest beyond Gar Ln, and a smaller length of the open field than in the SW direction. The dominant wind direction was W/SW (Figure 1b). Therefore, the wind

Chapter 4 Urban wintertime atmospheric composition

from the dominant wind direction blew over a long stretch of the open field after residential buildings and the west end of Stadium Dr.

Meteorology

A Campbell Scientific CSAT3 3-D sonic anemometer was mounted 60 m SE from the mobile laboratory and 1.4 m above the ground on the open field from January 20th. This anemometer measured temperature and wind vectors, which were converted to wind speed and direction. For the period before 20th of January and on February 20 and 21st, air temperatures were obtained from the weather station at the Battle Creek International Airport, Kalamazoo (KZ station), which is about 7 km SE from the mobile laboratory (weatherunderground.com). There was less than 1 °C difference between the KZ station and the anemometer during overlapping periods. Relative humidity (RH), and weather event data were also obtained from the KZ station. Hourly modeled boundary layer height (BL height) was obtained from the National Oceanic and Atmospheric Administration real-time environmental applications and display system (NOAA-READY) High-Resolution Rapid Refresh (HRRR) model with a 3 km horizontal resolution (<https://rapidrefresh.noaa.gov/hrrr/>).

Atmospheric composition measurement

Ambient concentrations of NH_3 , SO_2 , and $\text{PM}_{2.5}$ concentrations of NH_4^+ , SO_4^{2-} , and NO_3^- were measured in solution using an ambient ion monitor coupled to anion (Thermo Dionex ICS 2100) and cation (Thermo Dionex ICS 1100) ion chromatographs (AIM-IC; URG Corp., Chapel Hill, NC). The AIM-IC semi-continuously measures the composition of the gas and particulate phases in solution. For this study, a sampling duration of 3 hours was primarily used. The description, operation, and optimization of this instrument have been described in detail by Markovic *et al.* (2012).

The AIM-IC as used for this study had three main parts: the sampling box, the AIM tower containing the valves and sample syringes, and the ICs (Anion and cation IC). Air was sampled at 3 L/min through a $\text{PM}_{2.5}$ sharp-cut cyclone mounted on the sampling box, located outdoors. The inlet to the cyclone was about 1.8 m above the ground. In the sampling box, the cyclone was directly connected to a parallel plate wet denuder (PPWD) with Teflon membranes wetted with 5.5 mM hydrogen peroxide solution (H_2O_2 ; to enhance solubility of SO_2 (Markovic *et al.*, 2012)) flowing upwards at 10 mL/h. This way, the sampled air composition is directly transferred into solution, avoiding losses due to transport in an otherwise long sampling line. Soluble gases were extracted from the sampled air by dissolution in the PPWD. Insoluble gases and particles passed through the denuder. The particles were grown in a particle super-saturation chamber fed with steam, and were pooled in an inertial particle separator. The sampling box stayed outside the mobile laboratory. The sampling box was insulated and fitted with a heater to keep solutions from freezing on cold days.

The sampled gas and particles in solution were delivered to sampling syringes at a flow rate of 5 mL/h through a 20 m-long heated sampling line (heated to 25 °C). Samples collected in the syringes within one hour were transferred to concentrator columns within the last 5 minutes of the hour. For the 3 h sampling period, the concentrator columns were loaded three times. During the fourth hour of sampling, the samples on the concentrator column were analyzed by the ICs.

All solutions and standards used during this study were obtained from Dionex and Thermo Fisher. The anion IC had a potassium hydroxide (KOH) ion exchange eluent generator cartridge. The cation IC had a methanesulfonic acid ion eluent generator. The conductivity with residence time (in $\mu\text{S}\cdot\text{min}$) measured by the ICs were obtained *via* Chromeleon 7.2 software (Dionex Inc., Sunnyvale, CA and URG AIM). These were converted to concentration in $\mu\text{g}/\text{m}^3_{\text{air}}$ using calibration curves (5 point calibration from 0 to $3.0 \mu\text{g}/\text{m}^3$ for $\text{NH}_3/\text{NH}_4^+$, 0 to $2.8 \mu\text{g}/\text{m}^3$ for $\text{SO}_2/\text{SO}_4^{2-}$ and 0 to $3.7 \mu\text{g}/\text{m}^3$ for NO_3^- for 3 h sampling duration). Offline calibrations were done using Dionex™ combined anion/cation calibration standards by Thermo Fisher Scientific *via* direct injection into the ICs.

Blanks were run using the same water used for preparing the analytical solutions (18 MΩ ultrapure water). Blank samples were injected into the concentrator columns. The limits of detection (LOD) were calculated as 3σ of the blank peak areas and converted to concentrations using the calibration curves. The LODs corresponding to 3 h average measurement were $29 \text{ ng}/\text{m}^3$ for particulate sulfate (SO_4^{2-}), $1 \text{ ng}/\text{m}^3$ for particulate Nitrate (NO_3^-), $12 \text{ ng}/\text{m}^3$ for particulate ammonium (NH_4^+), $10 \text{ ng}/\text{m}^3$ (2.3 ppt at 273.15 K) for gas phase sulfate (SO_2 is measured as SO_4^{2-} in solution through the gas samples lines), and $14 \text{ ng}/\text{m}^3$ (17 ppt at 273.15 K) for gas phase ammonia (NH_3 is measured as NH_4^+ in solution). Rinses of the sampling syringes and the sampling lines were also analyzed to identify potential sources of contamination along the line. Due to the possibility of N_2O_5 interference in the measurements of gas phase nitric acid, HNO_3 , using the AIM-IC, gas phase HNO_3 concentration was measured using a chemical ionization mass spectrometer (CIMS) for the duration of the study.

Chemical Ionization Mass Spectrometer for HNO_3 measurement

The operating principle of the CIMS has been described in detail by Liao et al (2011). For this study, the CIMS inlet was a 30 cm long, 4.6 cm internal diameter (i.d.) aluminum pipe fitted with a stainless steel ring torus on the outside side of the mobile laboratory. This inlet was mounted about 1.5 m above the ground. Air was drawn at 300 L/min, from which 6.4 L/min was sampled from the center line into a 20 cm long, 0.95 cm i.d. FEP tube. This FEP tube was fitted with a 30°C heated 3-way valve for calibration and background measurements. The CIMS sampled 0.9 L/min of this flow into the ion-molecule reaction region, which was kept at a pressure of 15.5 torr.

Chapter 4 Urban wintertime atmospheric composition

The reagent ion for this study was $\text{I}(\text{H}_2\text{O})^-$, which was produced by passing 3 – 4 L/min methyl iodide (CH_3I) through a polonium ionizer (^{210}Po). The reagent ion was humidified with a stream of humidified N_2 at 0.25 L/min. This humidification was done to avoid effects of changing ambient relative humidity on the CIMS sensitivity during measurements. HNO_3 was measured at m/z 190 (IHNO_3^-), with a dwell time of 500 ms. The CIMS monitored a total of 25 masses. All signals were normalized to $\text{I}(\text{H}^{18}\text{O})$ at m/z 147.

Background measurements on the CIMS were carried out every 15 minutes. Air flow was directed through a glass wool scrubber to remove analytes of interest before being sent to the CIMS. HNO_3 calibrations were done offline using its relative sensitivity to Cl_2 (m/z 199). This sensitivity was determined to be 3.8 ± 0.9 (m/z 190 / m/z 199). Calibration of HNO_3 in the laboratory was conducted using HNO_3 in N_2 from a 50 ng/min permeation source (VICI). The HNO_3 permeation rate was confirmed by directing the gas stream from the source into 4 mL of H_2O for 40 minutes. The concentration of nitrate in the solution was quantified using ion chromatography. Corresponding to 1-minute average data, the 3σ LOD was 59 ppt; since counting statistics dominate this value, the 10 minute LOD can be estimated as 19 ppt. The 60 minute LOD was 10 ppt. 1-minute averaging measurement uncertainties for HNO_3 were estimated to be 30%.

Field snow samples

Snow samples were obtained from three locations on the field next to the mobile laboratory on most of the days with snow cover in Whirl-pak bags. Samples were collected using polypropylene scoops, which were cleaned before and after use with ultrapure water. The depth of the snow cover was also measured during sampling. Surface samples were obtained from the top 2 to 3 cm of the snow. When the snow depth was below 5cm, the entire snow column was sampled as one. The samples were stored in a -20°C freezer during the campaign and transferred to a -30°C freezer after the campaign until analyzed. The samples were analyzed using the aforementioned anion and cation ion chromatographs after the field study. The LODs (3σ) were 0.2 μM for sulfate, 0.07 μM for nitrate, and 0.01 μM for ammonium.

Modeled aerosol pH and thermodynamic partitioning

Thermodynamic partitioning and aerosol pH were modeled using the ISORROPIA-II model (Fountoukis and Nenes, 2007). The ISORROPIA-II model was run in forward mode, that is, including both particulate and gas phase concentrations of ammonia, nitrate, and sulfate species. ISORROPIA was run assuming metastable state, that is, with no particulate formation. The thermodynamic partitioning of nitrate, sulfate, and ammonia was also modeled using the E-AIM model II in batch mode, also assuming no solid formation (Clegg *et al.*, 1998; Murphy *et al.*, 2017). Aerosol pH was also estimated using the E-AIM model output based on the method prescribed by Murphy *et al.* (2017), which includes gas phase NH_3 (Clegg *et al.*, 1998).

4.1.4 Results and discussion

Meteorology

Weather conditions during this winter study were variable with very warm periods (resulting in loss of snow cover e.g. from January 24th to January 31st) occurring between periods of cold days with heavy snowfall especially in February (Figure 4.1a). Temperatures during the study ranged from 255 K to 290 K with high relative humidity (RH) for most of the period (75% average RH). The modeled boundary layer height varied from 50 m and 1500 m (Figure 4.1b). Wind speed was generally low ranging from 0 to 4 m/s for most of the period (Figure 4.1b). The dominant wind direction was W/SW.

General observations – Atmospheric composition

Average PM_{2.5} NO₃⁻ concentration was 0.90 µg/m³ (range: <1 ng/m³ – 3.94 µg/m³), NH₄⁺ was 0.52 µg/m³ (range: 0.02 – 3.94 µg/m³), and SO₄²⁻ was, 0.26 µg/m³ (range: 0.03 – 3.94 µg/m³), throughout the campaign (Table 4.1). Positive correlations were observed between NH₄⁺ and NO₃⁻ (R² = 0.89) and between NH₄⁺ and SO₄²⁻ (R² = 0.5), which suggests that NO₃⁻ and SO₄²⁻ were primarily in the form of NH₄NO₃ and (NH₄)₂SO₄ in ambient aerosol <2.5 µm (PM_{2.5}). Episodes of elevated NO₃⁻ and NH₄⁺ were observed typically during periods with shallow boundary layer height and high relative humidity (e.g., January 25–26 and February 9–12). This suggests a relationship between boundary layer height, relative humidity, and the particulate concentrations as have been observed in other studies (Katzman *et al.*, 2010; Chen *et al.*, 2012; Stanier *et al.*, 2012; Green *et al.*, 2015).

There were generally high concentrations of NH₃ in the gas phase, compared to SO₂ and HNO₃, with a range from 0.22 to 5.75 ppb and an average of 1.74 ppb. Significant decreases in NH₃ were driven primarily by precipitation (for example, between February 2 and 15). NH₃ concentrations were associated with temperature, with higher concentrations at warmer temperatures. For example, NH₃ concentrations increased significantly as temperatures increased on February 13 after the winter storms (February 2–12; Figure 4.1). Periods of high concentrations of NH₃ in the gas phase often coincided with low concentrations of NH₄⁺ in the particulate phase and vice versa, likely driven by the partitioning of NH₃ between the gas phase and the particulate phase (January 27 to 28, Figure 4.1).

There were also episodes of high concentrations of SO₂ and HNO₃ in the gas phase, though at much lower concentrations than NH₃ (Figure 4.1d). SO₂ concentrations ranged from 2.8 ppt to 0.55 ppb with an average of 70 ppt. SO₂ peaks in the gas phase often coincided with periods of higher concentrations in particulate SO₄²⁻ (e.g. February 9–11, SI Figure S4.2) The Henry's law constant of SO₂ is quite low in water and the acid dissociation constant of sulfuric acid is large; the high pH in the aerosol phase may, therefore, also increase the effective solubility of SO₂ (Cheng *et al.*, 2016). In addition, oxidation in the condensed phase,

Chapter 4 Urban wintertime atmospheric composition

aerosols and clouds, and in the gas phase by oxidants such as OH in gas phase photochemistry, $\text{H}_2\text{O}_2/\text{O}_3$, and NO_2 , can lead to the formation of $\text{H}_2\text{SO}_4/\text{SO}_4^{2-}$ in the gas and particulate phases (Cheng *et al.*, 2016).

HNO_3 concentrations ranged from <10.6 ppt to 0.53 ppb, with an average of 37 ppt. Generally, episodes of high HNO_3 occurred before NO_3^- episodes in the particulate phase, with the partitioning of HNO_3 to the particulate phase (e.g., January 25–26, Figure 4.1 and SI Figure S4.2). The partitioning of HNO_3 is dependent on the interplay of the particle pH, neutralization ratio ($\text{NH}_x/\text{SO}_4^{2-}$), temperature, and RH (Murphy *et al.*, 2017). High concentrations of HNO_3 often coincided with low concentrations of total ammonia and lower $\text{NH}_x/\text{SO}_4^{2-}$ ratio (which was always greater than 2; e.g., January 26, SI Figure S4.3). With $\text{NH}_x/\text{SO}_4^{2-}$ always greater 2, there is always excess NH_3 in the gas phase (Murphy *et al.*, 2017). High RH, high pH, and low T drive HNO_3 into the particulate phase (Murphy *et al.*, 2017). Consistent with this, higher NO_3^- in the particulate phase coincided with periods of high RH (e.g. February 15, Figure 4.1; (Cheng *et al.*, 2016).

Table 4.2: Mean, standard deviation, minimum and maximum values of gas phase concentrations (in ppb) and particulate concentrations ($\text{PM}_{2.5}$; in $\mu\text{g}/\text{m}^3$) at Kalamazoo, Michigan from January 12 to February 23, 2018, including periods with precipitation

| | Mean | Std. Dev | Minimum | Maximum |
|--|------|----------|---------|---------|
| SO_2 (ppb) | 0.07 | 0.09 | 0.003 | 0.55 |
| HNO_3 (ppb) | 0.04 | 0.06 | <0.01 | 0.53 |
| NH_3 (ppb) | 1.74 | 0.99 | 0.22 | 5.75 |
| SO_4^{2-} ($\mu\text{g}/\text{m}^3$) | 0.26 | 0.15 | 0.03 | 0.91 |
| NO_3^- ($\mu\text{g}/\text{m}^3$) | 0.90 | 0.81 | 0.01 | 3.94 |
| NH_4^+ ($\mu\text{g}/\text{m}^3$) | 0.52 | 0.54 | 0.02 | 2.69 |

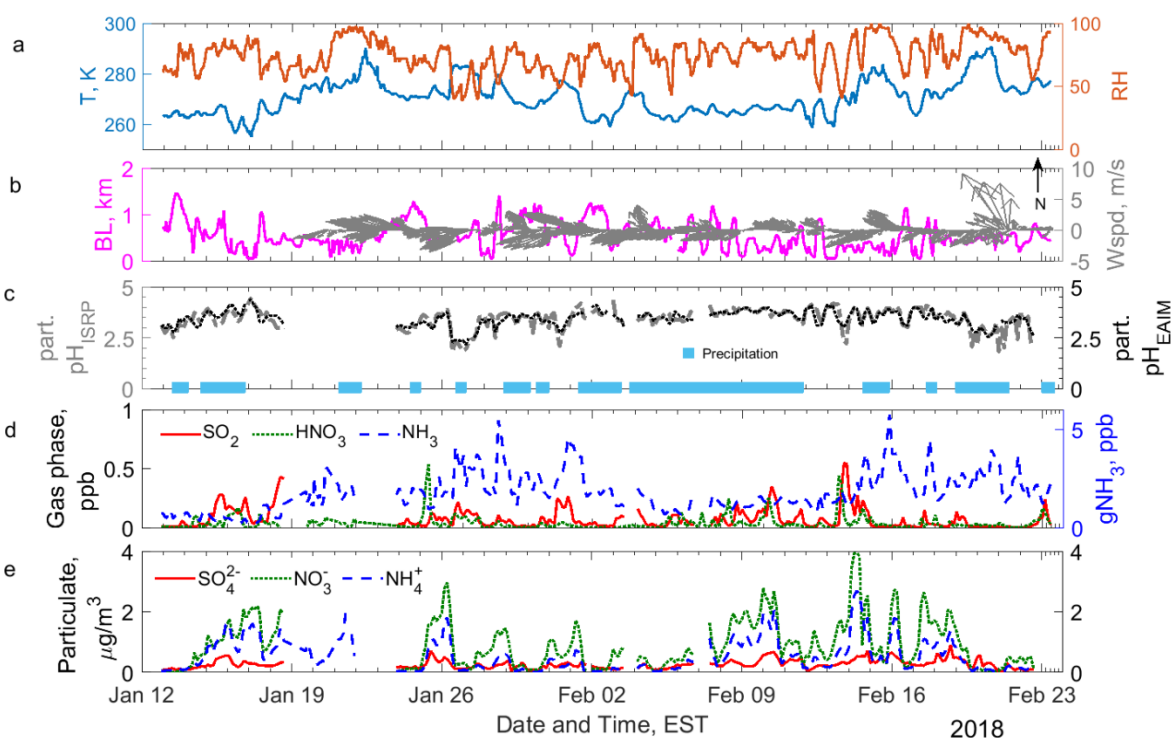


Figure 4.1 Observations of temperature and relative humidity (a), modeled boundary layer height, measured wind speed and direction (b), modeled aerosol pH from ISORROPIA (grey line) and EAIM (black-dotted line); occurrence of active precipitation including fog (blue boxes) (c), observed gas phase concentrations in ppb (d), observed $PM_{2.5}$ mass concentrations (e) at Kalamazoo, MI. T is temperature. RH is relative humidity. BL is boundary layer height in km; Wspd is wind speed in m/s; part. refers to $PM_{2.5}$.

Diurnal patterns

No strong diurnal patterns were observed during this study for the species of focus, both in the particulate and gas phases (Figure 4.2a and b). There were, however, some slight increases in concentrations in the gas phase with temperature; NH_3 showed the strongest increase with temperature (Figure 4.2). Modeled BL height and measured temperatures were correlated; the small increase in temperature during the day (peaking at 15:00) was generally accompanied by a slight increase in the boundary layer height. Similar observations of the absence of strong diurnal patterns in $PM_{2.5}$ composition have been observed during the winter in the Great Lakes Region (Stanier *et al.*, 2012). In addition, the absence of a strong diurnal pattern in NH_3 concentrations indicates that traffic was not a significant source of NH_3 emissions during this campaign.

Although the overall period did not have general diurnal patterns, there were individual days which had some patterns. These diurnal patterns were more pronounced in the $PM_{2.5}$ concentrations and NH_3 than in the gas phase concentrations on HNO_3 and SO_2 . Below, we look into some case study days to assess the drivers of diurnal patterns, as well as the absence thereof.

Chapter 4 Urban wintertime atmospheric composition

January 24th was a day with no patterns in all compounds, except NH₃ which also had the highest concentration (Figure 4.3a–c). The boundary layer was high (> 720 to 1160 m) and increased through the day. There was also very low temperature variability (269 – 272 K), and winds were from the NW coming in from the roads and WMU. All other compounds were very low in concentration. NH₃ followed the small variability in temperature. There was no snow on the ground on January 24th.

On January 25th, NH₃ concentrations showed similar patterns as on January 24th (Figure 4.3d–f). However, concentrations in the particulate phase increased as the day progressed. This increase in particulate concentration followed the decrease in BL height as the day progressed. The temperature range was also low (270 – 275K), at slightly higher temperatures than the 24th. There was no clear maximum or minimum concentrations in both particulate and gas phase concentrations, except in NH₃. There was also no snow cover on this day and winds were from the SW to SE, over the wide field.

January 26 and February 14 had similar concentrations and meteorological patterns with clear diurnal patterns in the particulate phase and NH₃ (Figure 4.4a–f). NO₃⁻ dominated the particulate phase, while SO₄²⁻ had the lowest concentration and the smallest indication of a diurnal pattern. Nitrate and ammonium showed a wide peak maximizing around 09:00, decreasing in the early afternoon, with a minimum around 15:00. NH₃ concentrations followed the temperature profile very closely, increasing after noon. The ground was bare on January 26 and snow covered on February 14. Both days were marked by low and stable BL height (450 to 600 m on January 26; 220 to 330 m on February 14). The temperature profile was similar on both days with a relatively large diurnal range (270 K to 285K on January 26; 270 K to 280 K on February 14). Both days also had similar relative humidity patterns with a wide diurnal range (> 80% before noon and decreasing to below 50% on January 26 and just above 60% on Feb 14). Relative humidity was anti-correlated with temperature. The wind direction on both days was SE to SW. Measurements on both days after 18:00 were not considered here due to precipitation.

In summary, on average, there was no diurnal pattern in gas phase and PM_{2.5} concentrations in for the entire period of study due to little average diurnal variations in meteorological conditions. This is evident from the case by case analysis, which showed that variability in the diurnal profiles of the BL height, temperature, relative humidity, and wind direction influenced changes in the observed concentrations. The NH₃ profile was mostly driven by temperature with less influence from the BL height. Particulate concentrations changed with BL height, RH, and wind direction. At high BL height, PM_{2.5} concentrations were generally low. PM_{2.5} concentrations were higher at high RH, potentially due to particle growth at high RH (Stanier *et al.*, 2012). It appears that air from the south (going over the field) had higher particulate concentrations than from the north. The particulate concentrations were higher on the day with snow cover (February 14). In addition, the

decrease in PM_{2.5} concentrations with snow cover present was not as strong as with the bare field (January 26) potentially due to higher RH on the snow covered day.

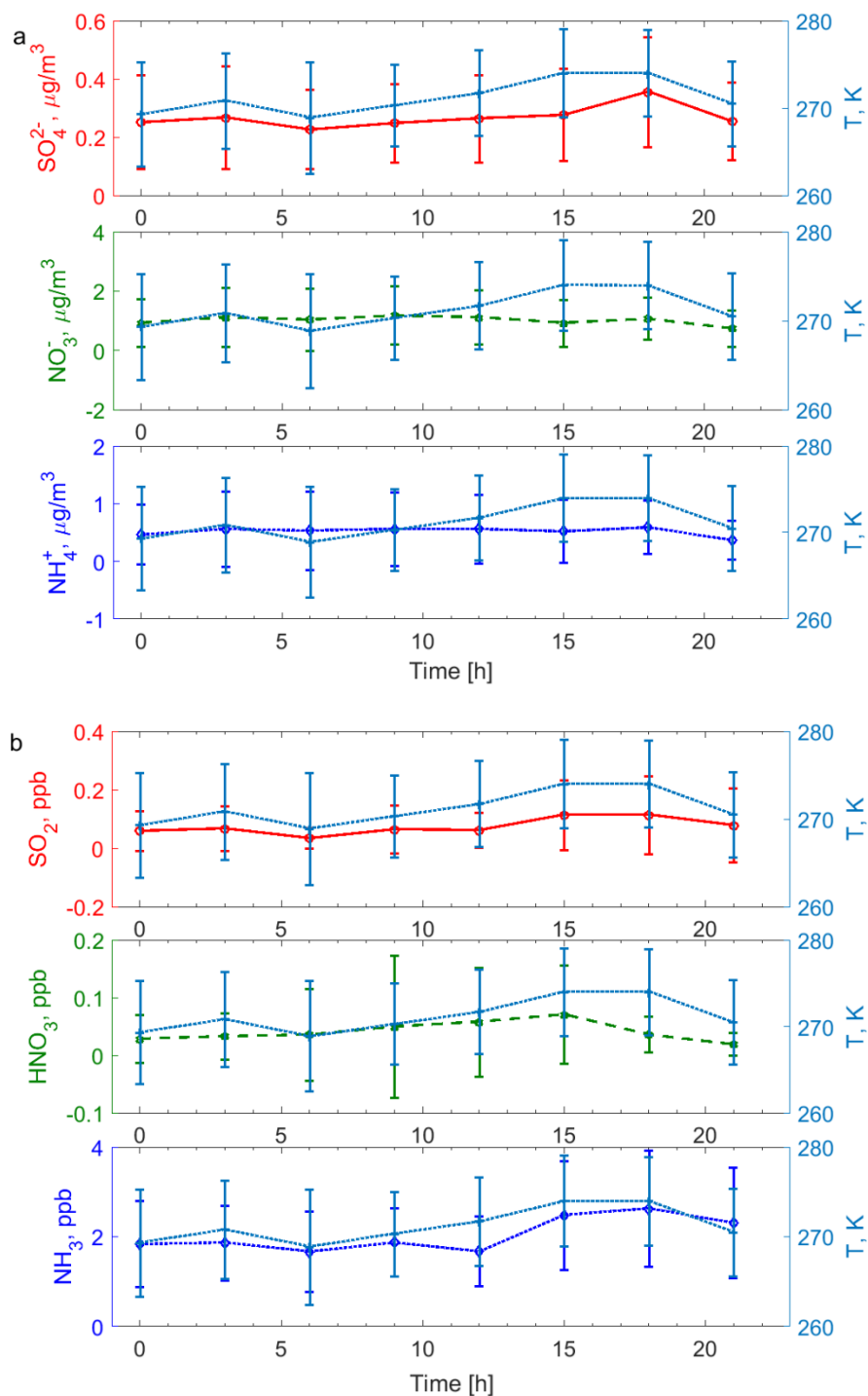


Figure 4.2 Average diurnal profiles of gas phase and PM_{2.5} observations, as well as temperature, for the study period, January 12 to February 23, 2018. Error bars are 1 σ of observations (a) PM_{2.5} concentrations of SO₄²⁻, NO₃⁻, and NH₄⁺ and temperature; (b) Gas phase concentrations of SO₂, HNO₃, and NH₃.

Chapter 4 Urban wintertime atmospheric composition

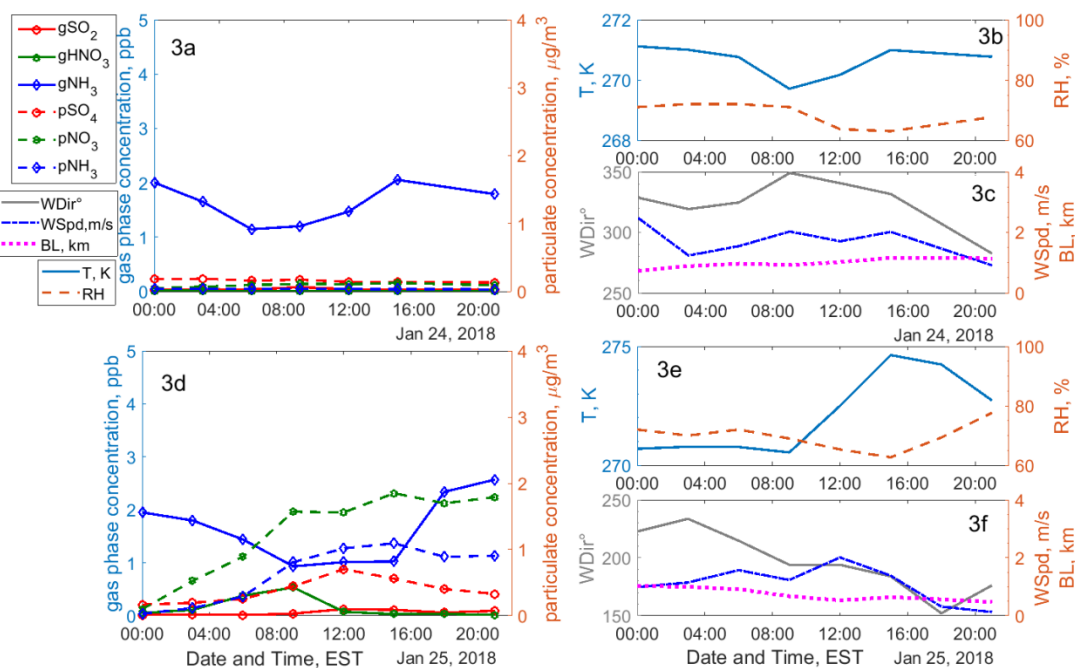


Figure 4.3 PM_{2.5} and gas phase concentrations of ammonia, nitrate, and sulfate species (left); wind speed (Wspd in m/s), wind direction (WDir, in degrees), temperature (T, in K) and relative humidity (RH) observations and modeled boundary layer height (BL in km; right) on January 24th and 25th.

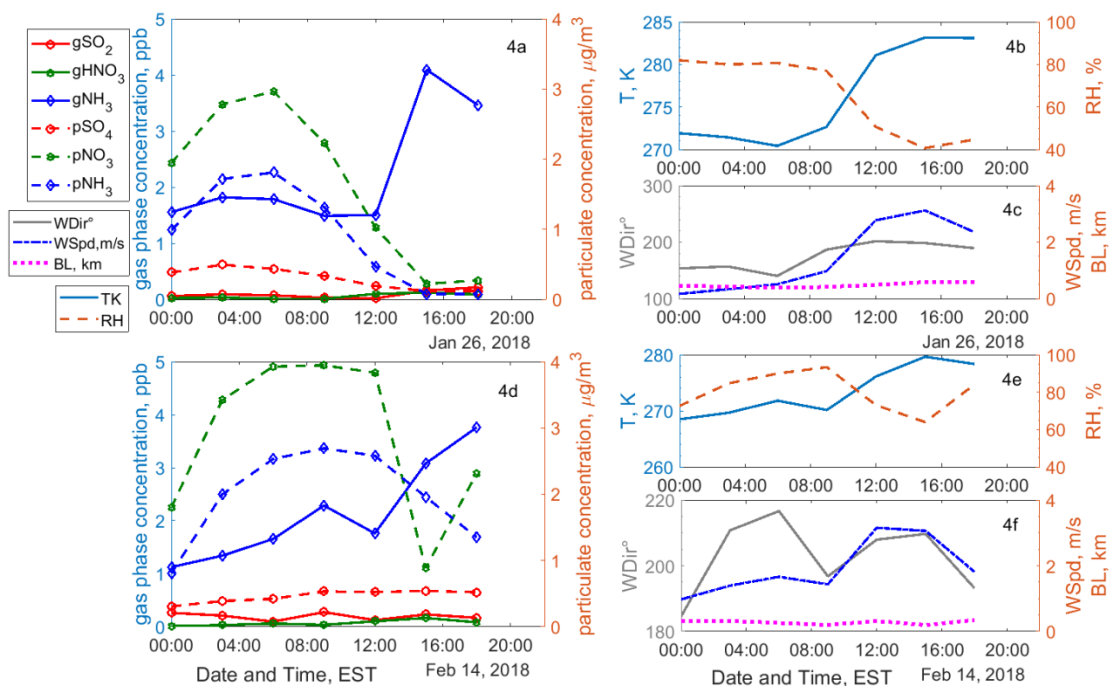


Figure 4.4 PM_{2.5} and gas phase concentrations of ammonia, nitrate, and sulfate species (left); wind speed (Wspd, in m/s), wind direction (WDir, in degrees), temperature (T, in K) and relative humidity (RH) observations and modeled boundary layer height (BL in km; right) on January 26 and February 14.

Aerosol pH

A major factor affecting the partitioning between the particulate and the gas phases is particle pH (Markovic *et al.*, 2014; Cheng *et al.*, 2016; Guo *et al.*, 2016). At low pH (< 2.5 at 0 °C, for example) a large fraction of NO_3^- in the particulate phase is expected to be present in its protonated form, which is more volatile (Guo *et al.*, 2016). Due to the high acid dissociation constant of sulfuric acid, the effective solubility of SO_2 increases at higher pH in the aerosol aqueous phase. HNO_3 and SO_2 partitioning into the aerosol phase may increase acidity in the aerosol, but due to high hygroscopicity of both ions, water uptake increases, which may also increase pH, promoting further partitioning to the condensed phase (Guo *et al.*, 2016).

Modeled $\text{PM}_{2.5}$ pH from ISORROPIA (ISRP) and E-AIM (EAIM) were in close agreement with each other (Figure 4.1c; Figure 4.5a), as has been previously noted (Hennigan *et al.*, 2015). The calculated $\text{PM}_{2.5}$ pH ranged from 1.8 to 4.4, with an average of 3.4. Lower pH was estimated during periods of low NH_4^+ concentrations in the particle phase (high NH_3/NH_x ; Figure 4.5). The average pH, being greater than 3, was not so low as to strongly shift nitrate (as HNO_3) and sulfate (as SO_2) to the gas phase for most of the period (Cheng *et al.*, 2016; Guo *et al.*, 2016). NO_3^- mass concentration dominated over NH_4^+ and SO_4^{2-} in the particulate phase.

Predicted HNO_3 from both models were in good agreement with each other. The models were, however, not able to capture the frequency and, especially, the magnitude of most of the observed HNO_3 episodes observed (Figure 4.5c). The NH_3 fraction (NH_3/NH_x) was generally well captured by the models, but there were periods with significantly higher NH_3 estimates from the models (Figure 4.5b). These deviations from observations may have been due to precipitation during those periods where the models fail due to particle-phase scavenging (for example, between January 14 and 17, and February 4 and February 15, which had snowfall).

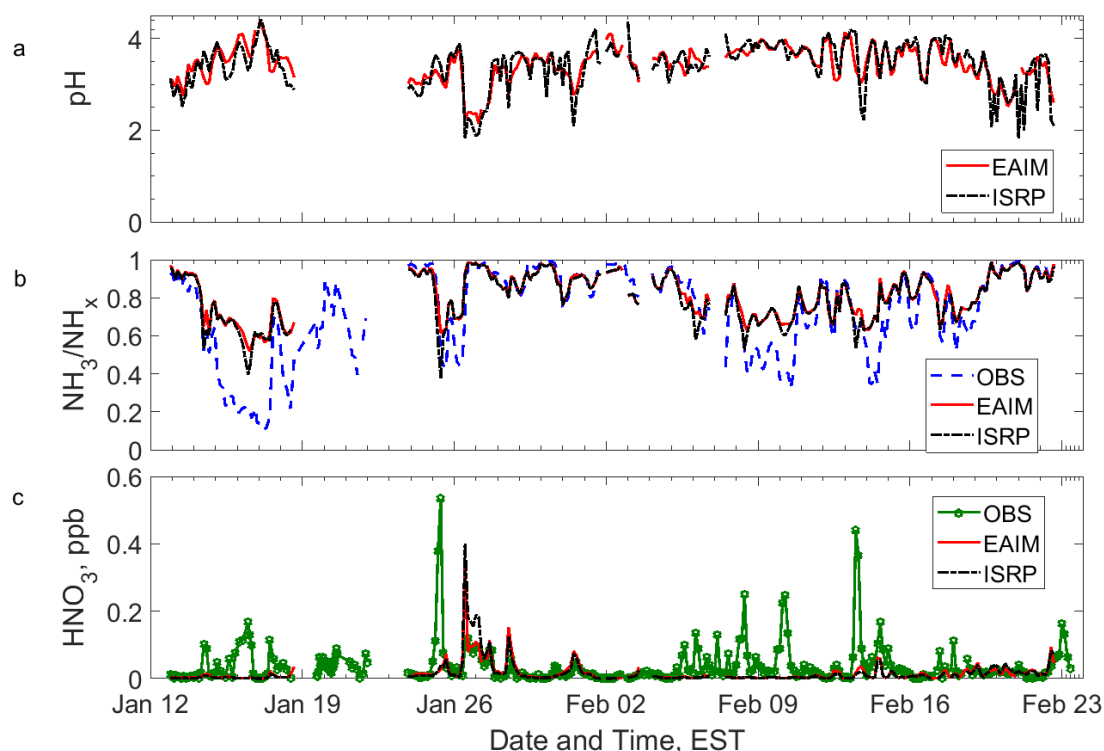


Figure 4.5 (a) Modeled aerosol pH using E-AIM model II (EAIM) and ISORROPIA-II (ISRP) in forward mode; (b) Comparison between observed (OBS) NH_3/NH_x and that predicted by the E-AIM model II (EAIM) and ISORROPIA-II (ISRP); (c) Comparison between observed HNO_3 (CIMS; OBS), and HNO_3 simulated by the E-AIM model II (EAIM) and ISORROPIA-II (ISRP) models.

Temperature dependence of NH_3 partitioning

NH_3 emissions from agricultural sources (including vegetation, animal waste, and fertilizer), waste water treatment plants, and soils are temperature dependent (Bouwman *et al.*, 1997; Ianniello *et al.*, 2010; Markovic *et al.*, 2014). At higher temperatures, volatilization of NH_3 is higher, hence, an increase in the gas phase concentration of NH_3 with increasing temperature (Bouwman *et al.*, 1997; Markovic *et al.*, 2014). In the winter, NH_3 emissions from agricultural sources and soils are much reduced because of lower activity in terms of fertilization and also lower temperatures (Bouwman *et al.*, 1997; Battye, 2003; Ianniello *et al.*, 2010). At the Kalamazoo site, potential local temperature-dependent sources of NH_3 were a student garden, which was not active, the open field, snow cover, the neighboring forest, and partitioning from regionally transported aerosol. In addition, on some days during the study, the site was visited by a family of deer, which may also be local sources of NH_3 from their waste (Bouwman *et al.*, 1997; Sutton *et al.*, 2013). NH_3 may also have been transported from non-local sources as the residence time of NH_3 in the atmosphere could be up to a few days (Tsunogai and Ikeuchi, 1968).

A major sink for atmospheric gases and particles is snow deposition (Baltensperger *et al.*, 1993; Bergin *et al.*, 1995). Field studies have observed significant scavenging of NH_3 by falling snow (Baltensperger *et al.*, 1993; Bergin *et al.*, 1995). Laboratory studies investigating

the uptake of NH₃ in snow and ice indicate that there is higher uptake in growing ice and wet ice than in non-growing ice; in the presence of SO₄²⁻, this uptake is enhanced (Hoog *et al.*, 2007). These studies suggest that there could be significant deposition of NH₃ on snow, with snow serving as a sink. Due to the temperature dependence of NH₃ emissions, there could be potential temperature dependent release from snow. NH₃ taken up or deposited on snow may also be released with sublimation of snow. To the best of our knowledge, the temperature dependent release of NH₃ from snow or the role of snow in NH₃ emission is yet to be investigated.

The temperature dependence of NH₃ concentration represented as equation (4.1), a Van't Hoff expression, provides an enthalpy of volatilization (ΔH_{vol}) for NH₃ from surrounding sources (Markovic *et al.*, 2014). Figure 4.6a shows this temperature dependence of the observed NH₃ during periods without precipitation. ΔH_{vol} calculated from the observed concentrations was 50 ± 6 kJ/mol, which implies about 125% increase in NH₃ emissions from 268 to 278 K. This ΔH_{vol} is very similar to that calculated for the enthalpy of dissociation of NH₄⁺_(aq); equation (4.2) (Bates and Pinching, 1949; Markovic *et al.*, 2014) at 270 K ($\Delta H_{dis} = 51.6$ kJ/mol (Olofsson, 1975)). Particulate NH₄⁺ is not negligible compared to NH₃ in our study (average NH₄⁺/average NH₃ = 0.37), but the NH₃-temperature correlation still exists, which suggests a temperature-dependent NH₃ source or/and that NH₃ follows temperature-dependent thermodynamic equilibrium with the surrounding environment (ground and particles).

$$\ln(NH_3(g)) + \ln(c) = \left(-\frac{\Delta H_{vol}}{R}\right) \left[\left(\frac{1}{T}\right) - \left(\frac{1}{298.15}K\right)\right] \quad (1)$$



where R is the ideal gas constant and T is temperature.

Since there were warm periods during this study, there were days with no snow cover. Figure 4.7 shows similar temperature dependence assessment of NH₃ observed when there was no snow cover compared to periods with snow cover. ΔH_{vol} observed during the periods without snow cover was 28 ± 15 kJ/mol, which is similar to that observed by Markovic *et al.*, and attributed to local sources such as agricultural practices (Markovic *et al.*, 2014). ΔH_{vol} observed for the entire period with snow cover was similar to that for the entire study period (51 ± 8 kJ/mol). Considering only snow-cover observations within the same temperature range as periods with no snow cover, the calculated ΔH_{vol} was 40 ± 17 kJ/mol, suggesting stronger temperature dependence on snow cover periods than periods without snow cover (Bates and Pinching, 1949).

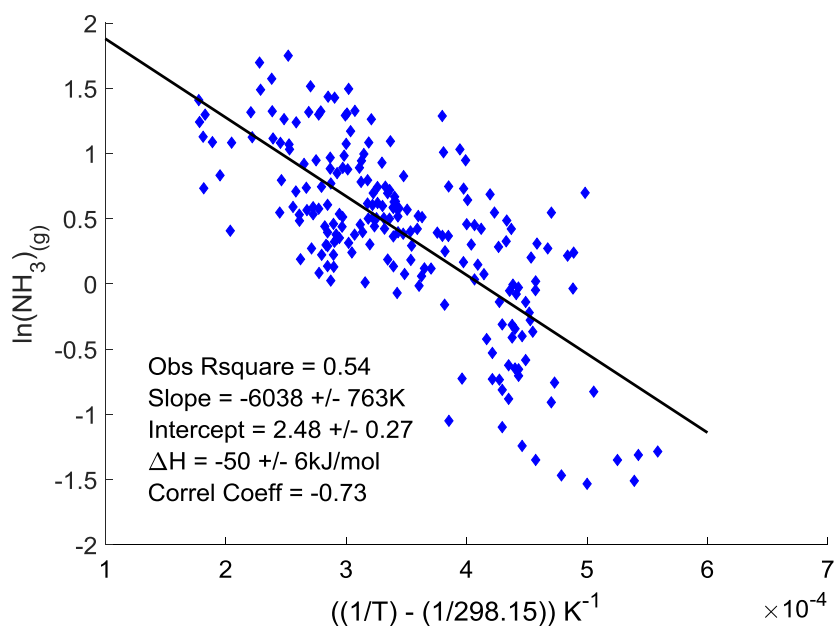


Figure 4.6: Temperature dependence of measured gas phase ammonia concentrations for observations (plotted as the natural log of NH_3 against inverse of temperature); intercept is the natural log of NH_3 concentration at 298.15 K. ΔH is the enthalpy of volatilization of ammonia.

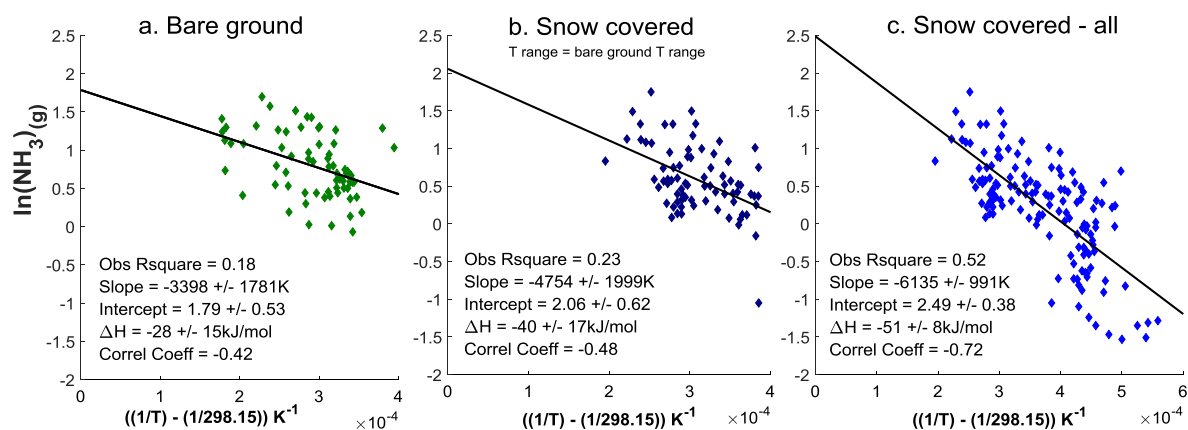


Figure 4.7: Temperature dependence of measured gas phase ammonia plotted as the natural log of ammonia against inverse temperature; divided by ground cover to assess (a) no snow on the ground, bare ground; (b) snow cover on the ground, but the same temperature range as the period without snow cover on the ground; (c) all observations during periods with snow cover on the ground.

Snow chemical composition and atmospheric concentrations

Surface snow samples collected during the study (from the field in the dominant wind direction) had relatively high pH, from 5.2 to 7.2. The average pH of all surface samples was 6.3 ± 0.6 (1σ). This high pH may be due to very high concentration of NH_4^+ observed in the snow samples (Figure 4.8). The snow samples also contained significant concentrations of nitrate and sulfate. Average concentrations ($\pm 1\sigma$ of all samples) were $46 \pm 55 \mu\text{M}$ for NH_4^+ , $27 \pm 19 \mu\text{M}$ for NO_3^- , and $5 \pm 3 \mu\text{M}$ for SO_4^{2-} . These concentrations are much higher than that observed in alpine snow: $2.4 \mu\text{M}$ NH_4^+ , $8.5 \mu\text{M}$ NO_3^- , and $2.6 \mu\text{M}$ SO_4^{2-} (Baltensperger *et al.*, 1993), and similar to those observed in other urban areas: $3.1 - 48 \mu\text{M}$ for nitrate, and $7.8 - 51 \mu\text{M}$ for sulfate (Baysal *et al.*, 2017).

During the snow storm from Feb 2nd to Feb 12th, there was a strong washout of NH_3 and particles from the atmosphere (Figure 4.9). This occurrence coincides with high concentrations of NH_4^+ , SO_4^{2-} , and NO_3^- in the snow. Such observation is common as snow deposition is a dominant transport for materials in the atmosphere to the ground in cold regions (Mitchell and Lamb, 1989; Baltensperger *et al.*, 1993; Bergin *et al.*, 1995; Wolff *et al.*, 1998). Towards the end of that winter storm, the particulate concentrations increased significantly. This may be due to very low boundary layer height (~ 300 m) and increasing temperature (Figure 4.1b). On Feb 15 to 16, there was also a strong increase in NH_3 concentration as temperatures increased to about 280 K during the day. This increased NH_3 concentration, which coincides with decrease in snow ammonium concentrations (Figure 4.9), may be related to a temperature dependent release from the snow in addition to other local sources such the neighboring forest soils.

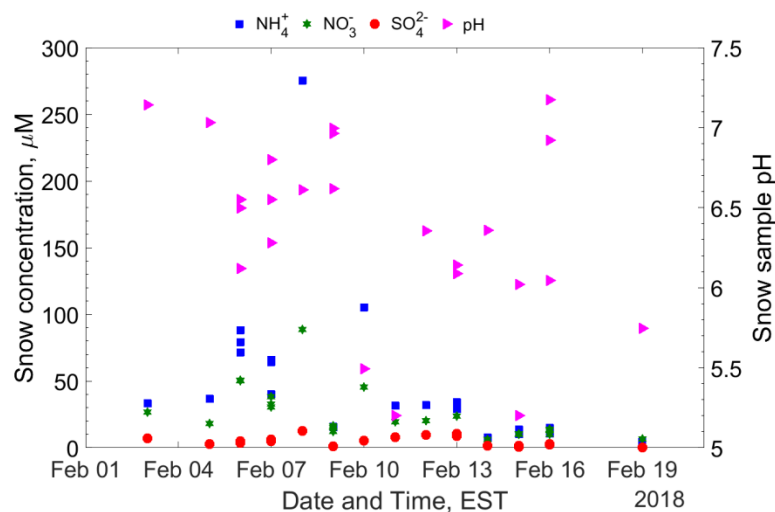


Figure 4.8: pH and concentrations of NH_4^+ , SO_4^{2-} , and NO_3^- in surface snow sampled from the field adjacent to the mobile laboratory at Kalamazoo, MI (on Jan 17, surface snow pH was 5.2, and concentrations were $43.9 \mu\text{M}$, $3.6 \mu\text{M}$, and $42.5 \mu\text{M}$ for NH_4^+ , SO_4^{2-} , and NO_3^- , respectively).

Chapter 4 Urban wintertime atmospheric composition

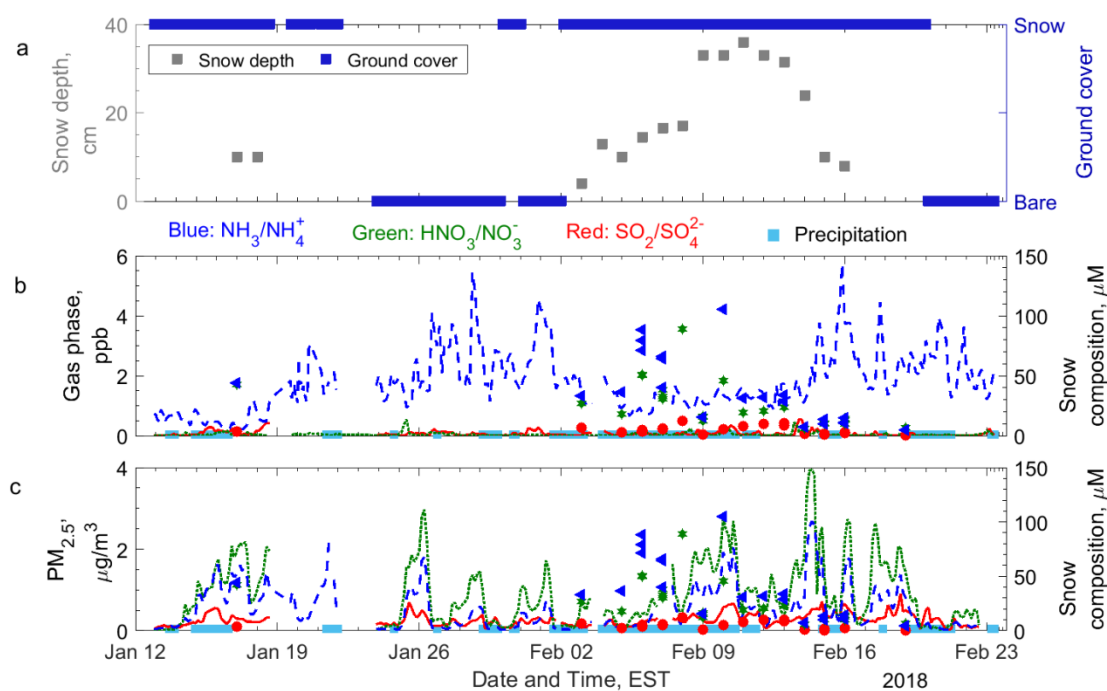


Figure 4.9: (a) Snow depth and ground cover condition (snow covered vs bare ground); (b) snow concentrations of ammonium, sulfate, and nitrate, and gas phase concentrations of NH_3 , SO_2 , and HNO_3 ; (c) Snow and $\text{PM}_{2.5}$ concentrations of NH_4^+ , SO_4^{2-} , and NO_3^- .

4.1.5 Conclusions

Observations of wintertime gas phase NH_3 , HNO_3 , and SO_2 and $\text{PM}_{2.5}$ NH_4^+ , SO_4^{2-} , and NO_3^- were made at Kalamazoo, MI, United States in January and February, 2018. NH_3 dominated the gas phase concentrations, while NO_3^- dominated in the particulate phase. No diurnal patterns dominated the entire study period, but there were days with diurnal patterns mostly driven by boundary layer height and temperature. Our observations indicate a strong influence of boundary layer height and snow cover on $\text{PM}_{2.5}$ concentrations. $\text{PM}_{2.5}$ episodes coincided with low boundary layer height and were more frequent during periods with snow cover. These $\text{PM}_{2.5}$ episodes were similar to observations of particulate episodes during wintertime observed in other urban studies (Chen *et al.*, 2012; Stanier *et al.*, 2012).

NH_3 concentrations were strongly correlated with temperature. This temperature dependence was stronger for periods with snow cover than for periods without snow cover. This is an indication that, although snow deposition is one of the major sinks for NH_3 , snow may also serve as a temperature dependent source of NH_3 in the winter. This becomes important for air quality especially during winters with warm spells like those observed during this study. It may be necessary for climate models to consider snow as potential sources of atmospheric trace gases. Quantification of ammonia deposition with snowfall and uptake in snow cover, and the release of ammonia from snow is needed to clearly differentiate between the emission of ammonia from snow and other surrounding sources.

To our knowledge, there have not been studies, field and laboratory, investigating the temperature dependent release of NH_3 from snow and ice. Few studies have investigated the uptake of NH_3 on ice (e.g., Hoog *et al.*, 2007). Laboratory studies of ammonia uptake on and release from ice films or packed snow columns at different temperatures may provide information on the kinetics and mechanism of this uptake process and potential for release. NH_3 is an important trace gas for particle formation with implications on both human and ecosystem health. Information from these studies could help improve predictions of air quality models especially in wintertime, which often have high particulate concentrations.

4.1.6 Acknowledgements

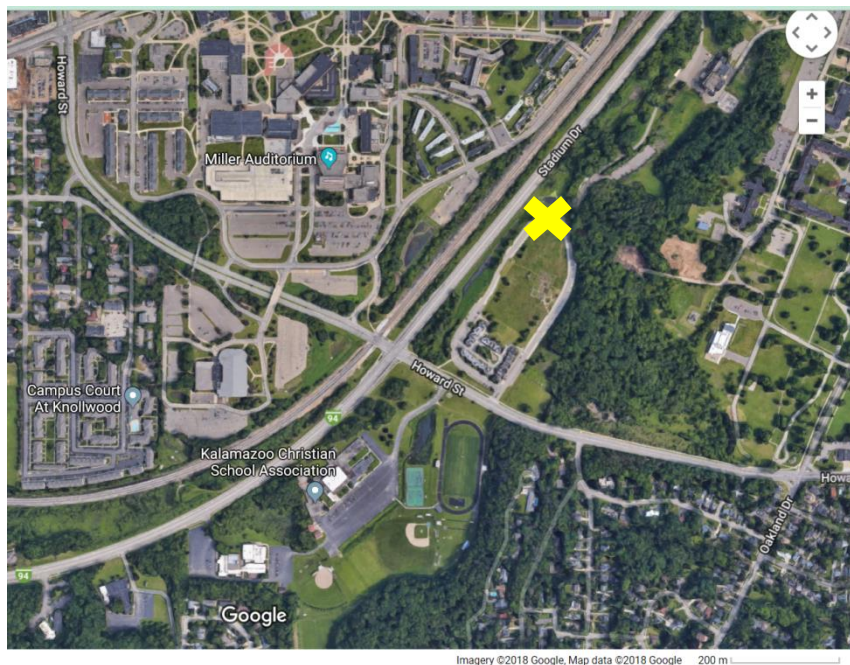
The field study was conducted as part of a US National Science Foundation grant (Pratt Laboratory, University of Michigan, Michigan, United States, grant AGS-1738588). My participation in this study was funded through Swiss National Science Foundation (SNF), grant 155999.

CIMS measurements were conducted by Stephen McNamara from the Pratt Laboratory, University of Michigan, United States. Snow cover was determined based on pictures from the site by Qianjie Chen at the Pratt Laboratory, University of Michigan. Snow samples were analyzed by Kathryn Kulju and Jasmine Mumpfield at the Pratt Laboratory, University of Michigan, United States.

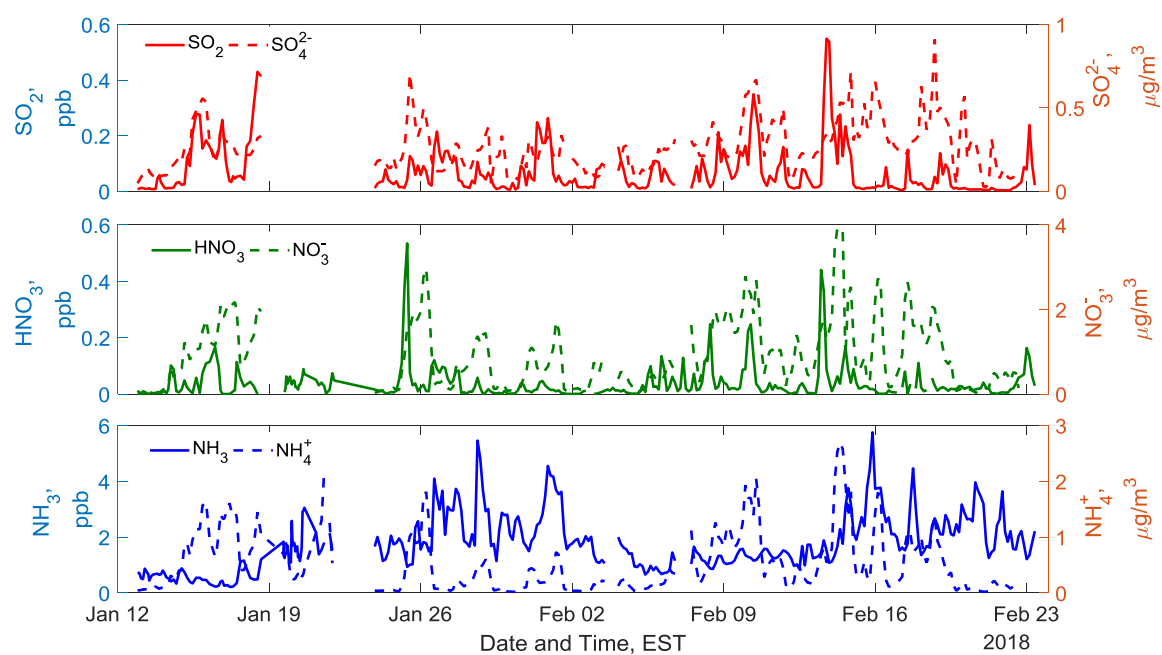
Co-authors: Stephen McNamara, Nate May, Kathryn Kulju, Jasmine Mumpfield, Qianjie Chen, Steve Bertman, and Kerri Pratt.

We are grateful to Havala Pye for insightful discussions on partitioning between the gas and particulate phases.

4.2 Supplementary Information



SI Figure S4.1: Map showing the location of the study site (yellow x). Map was obtained from Google maps (maps.google.com on 10 May, 2018).



SI Figure S4.2: Observed PM_{2.5} concentrations (dashed lines) of SO₄²⁻, NO₃⁻, and NH₄⁺ in µg/m³ and gas phase concentrations (solid lines) of SO₂, HNO₃, and NH₃ in ppb.

Bibliography

Abbatt, J. P.: Interaction of Atmospheric trace gases with ice surfaces: Adsorption and reaction, *Chemical Review*, 103, 4783 – 4800, 2003.

Albert, M., and Hawley, R. L.: Seasonal changes in snow surface roughness characteristics at summit, Greenland: implications for snow and firn ventilation, *Journal of Glaciology*, 35, 510–514, 2002.

Baltensperger, U., Schwikowski, M., Gäggeler, H. W., Jost, D. T., Beer, J., Siegenthaler, U., Wagenbach, D., Hofmann, H. J., and Synal, A.: Transfer of atmospheric constituents into an alpine snow field, *Atmospheric Environment*, 27A, 1881–1890, 1993.

Barrie, L. A.: Scavenging ratios, wet deposition, and in-cloud oxidation: An application to the oxides of sulphur and nitrogen, *Journal of Geophysical Research*, 90, 5789–5799, 1985.

Bartels–Rausch, T., Eichler, B., Zimmermann, P., Gäggeler, H. W., and Ammann, M.: The adsorption enthalpy of nitrogen oxides on crystalline ice, 2002.

Bartels–Rausch, T., Wren, S. N., Schreiber, S., Riche, F., Schneebeli, M., and Ammann, M.: Diffusion of volatile organics through porous snow: impact of surface adsorption and grain boundaries, *Atmospheric Chemistry and Physics*, 13, 6727–6739, 10.5194/acp–13–6727–2013, 2013.

Bartels–Rausch, T., Jacobi, H. W., Kahan, T. F., Thomas, J. L., Thomson, E. S., Abbatt, J. P. D., Ammann, M., Blackford, J. R., Bluhm, H., Boxe, C., Domine, F., Frey, M. M., Gladich, I., Guzmán, M. I., Heger, D., Huthwelker, T., Klán, P., Kuhs, W. F., Kuo, M. H., Maus, S., Moussa, S. G., McNeill, V. F., Newberg, J. T., Pettersson, J. B. C., Roeselová, M., and Sodeau, J. R.: A review of air–ice chemical and physical interactions (AICI): liquids, quasi–liquids, and solids in snow, *Atmospheric Chemistry and Physics*, 14, 1587–1633, 10.5194/acp–14–1587–2014, 2014.

Bates, R. G., and Pinching, G. D.: Acidic dissociation constant of ammonium ion at 0° to 50°C, and the base strength of ammonia, *Journal of Research of the National Bureau of Standards*, 42, 419–430, 1949.

Battye, W.: Evaluation and improvement of ammonia emissions inventories, *Atmospheric Environment*, 37, 3873–3883, 10.1016/s1352-2310(03)00343-1, 2003.

Baysal, A., Baltaci, H., Ozbek, N., Destanoglu, O., Ustabasi, G. S., and Gumus, G.: Chemical characterization of surface snow in Istanbul (NW Turkey) and their association with atmospheric circulations, *Environ Monit Assess*, 189, 275, 10.1007/s10661-017-5982-7, 2017.

Bergin, M. H., Jaffrezo, J. L., Davidson, C. I., Dibb, J. E., Pandis, S. N., Hillamo, R., Maenhaut, W., Kuhns, H. D., and Makela, T.: The contributions of snow, fog, and dry deposition to the summer flux of anions and cations at Summit, Greenland, *Journal of Geophysical Research*, 100, 16,275–216,288, 1995.

Bouwman, A. F., Lee, D. S., Asman, W. A. H., Dentener, F. J., Van Der Hoek, K. W., and Olivier, J. G. J.: A global high-resolution emission inventory for ammonia, *Global Biogeochemical Cycles*, 11, 561–587, 10.1029/97gb02266, 1997.

Cadle, S. H., Countess, R. J., and Kelly, N. A.: Nitric acid and ammonia in urban and rural locations, *Atmospheric Environment*, 16, 2501–2506, 1982.

Chen, L. W. A., Watson, J. G., Chow, J. C., Green, M. C., Inouye, D., and Dick, K.: Wintertime particulate pollution episodes in an urban valley of the Western US: a case study, *Atmospheric Chemistry and Physics*, 12, 10051–10064, 10.5194/acp-12-10051-2012, 2012.

Cheng, Y., Zheng, G., Wei, C., Mu, Q., Zheng, B., Wang, Z., Gao, M., Zhang, Q., He, K., Carmichael, G., Pöschl, U., and Su, H.: Reactive nitrogen chemistry in aerosol water as a source of sulfate during haze events in China, *Sci. Adv*, 2, 1–11, 2016.

Clegg, S. L., Brimblecombe, P., and Wexler, A. S.: Thermodynamic model of the system $\text{H}^+ - \text{NH}_4^+ - \text{SO}_4^{2-} - \text{NO}_3^- - \text{H}_2\text{O}$ at tropospheric temperatures, *J. Phys. Chem. A*, 102, 2137 – 2154, 1998.

Colbeck, S. C.: Air movement in snow due to windpumping, *Journal of Glaciology*, 35, 209–213, 1989.

Bibliography

Davidson, C. I., Jaffrezo, J. L., Mosher, B. W., Dibb, J. E., Borys, R. D., Bodhaine, B. A., Rasmussen, R. A., Boutron, C. F., Gurlach, U., Cachier, H., Ducret, J., Colin, J. L., Heidman, N. Z., Kemp, K., and Hillamo, R.: Chemical constituents in the air and snow at Dye 3, Greenland – I. Seasonal variation, *Atmospheric Environment*, 27A, 2709–2722, 1993.

Domine, F., and Shepson, P. B.: Air–snow interactions and atmospheric chemistry, *Science*, 297, 1506–1510, 10.1126/science.1074610, 2002.

Fountoukis, C., and Nenes, A.: ISORROPIA II: a computationally efficient thermodynamic equilibrium model for K^+ – Ca^{2+} – Mg^{2+} – NH_4^+ – SO_4^{2-} – NO_3^- – Cl^- – H_2O aerosols, *Atmos Chem Phys*, 7, 4639–4659, 2007.

Galitskaya, I. V., and Rumyantseva, N. A.: Snow–cover contamination in urban territories (Lefortovo district, Moscow), *Annals of Glaciology*, 53, 23–26, 10.3189/2012AoG61A009, 2017.

Grannas, A. M., Jones, A. E., Dibb, J., Ammann, M., Anastasio, C., Beine, H. J., Bergin, M., Bottenheim, J., Boxe, C., Carver, G., Chen, G., Crawford, J. H., Domine, F., Frey, M. M., Guzman, M. I., Heard, D., Helmig, D., Hoffmann, M. R., Honrath, R. E., Huey, L. G., Hutterli, M., Jacobi, H. W., Klan, P., Lefer, B., McConnell, J., Plane, J., Sander, R., Savarino, J., Shepson, P. B., Simpson, W. R., Sodeau, J., von Glasow, R., Weller, R., Wolff, E., and Zhu, T.: An overview of snow photochemistry, evidence, mechanisms, and impacts, *Atmos. Chem. Phys*, 7, 4329 – 4373, 2007.

Grannas, A. M., Bogdal, C., Hageman, K. J., Halsall, C., Harner, T., Hung, H., Kallenborn, R., Klán, P., Klánová, J., Macdonald, R. W., Meyer, T., and Wania, F.: The role of the global cryosphere in the fate of organic contaminants, *Atmospheric Chemistry and Physics*, 13, 3271–3305, 10.5194/acp–13–3271–2013, 2013.

Green, M. C., Chow, J. C., Watson, J. G., Dick, K., and Inouye, D.: Effects of Snow Cover and Atmospheric Stability on Winter PM_{2.5} Concentrations in Western U.S. Valleys, *Journal of Applied Meteorology and Climatology*, 54, 1191–1201, 10.1175/jamc–d–14–0191.1, 2015.

Guo, H., Sullivan, A. P., Campuzano–Jost, P., Schroder, J. C., Lopez–Hilfiker, F. D., Dibb, J. E., L, J. J., Thornton, J. A., Brown, S. S., Nenes, A., and Weber, R. J.: Fine particle pH and the partitioning of nitric acid during winter in the northeastern United States, *J. Geophys Res. Atmos*, 121, 10,355 – 310,376, 10.1002/2016JD025311, 2016.

Hennigan, C. J., Izumi, J., Sullivan, A. P., Weber, R. J., and Nenes, A.: A critical evaluation of proxy methods used to estimate the acidity of atmospheric particles, *Atmospheric Chemistry and Physics*, 15, 2775–2790, 10.5194/acp–15–2775–2015, 2015.

Hoog, I., Mitra, S. K., Diehl, K., and Borrmann, S.: Laboratory studies about the interaction of ammonia with ice crystals at temperatures between 0 and -20°C , *Journal of Atmospheric Chemistry*, 57, 73–84, 10.1007/s10874-007-9063-0, 2007.

Ianniello, A., Spataro, F., Esposito, G., Allegrini, I., Rantica, E., Ancora, M. P., Hu, M., and Zhu, T.: Occurrence of gas phase ammonia in the area of Beijing (China), *Atmospheric Chemistry and Physics*, 10, 9487–9503, 10.5194/acp-10-9487-2010, 2010.

Katzman, T. L., Rutter, A. P., Schauer, J. J., Lough, G. C., Kolb, C. J., and Klooster, S. V.: PM_{2.5} and PM_{10-2.5} Compositions during Wintertime Episodes of Elevated PM Concentrations across the Midwestern USA, *Aerosol and Air Quality Research*, 10, 140–153, 10.4209/aaqr.2009.10.0063, 2010.

Krepelova, A., Bartels-Rausch, T., Brown, M. A., Bluhm, H., and Ammann, M.: Adsorption of acetic acid on ice studied by ambient-pressure XPS and partial-electron-yield NEXAFS spectroscopy at 230–240 K, *J Phys Chem A*, 117, 401–409, 10.1021/jp3102332, 2013.

Krnavek, L., Simpson, W. R., Carlson, D., Domine, F., Douglas, T. A., and Sturm, M.: The chemical composition of surface snow in the Arctic: Examining marine, terrestrial, and atmospheric influences, *Atmospheric Environment*, 50, 349–359, 10.1016/j.atmosenv.2011.11.033, 2012.

Kundu, S., and Stone, E. A.: Composition and sources of fine particulate matter across urban and rural sites in the Midwestern United States, *Environ Sci Process Impacts*, 16, 1360–1370, 10.1039/c3em00719g, 2014.

Liao, J., Sihler, H., Huey, L. G., Neuman, J. A., Tanner, D. J., Friess, U., Platt, U., Flocke, F. M., Orlando, J. J., Shepson, P. B., Beine, H. J., Weinheimer, A. J., Sjostedt, S. J., Nowak, J. B., Knapp, D. J., Staebler, R. M., Zheng, W., Sander, R., Hall, S. R., and Ullmann, K.: A comparison of Arctic BrO measurements by chemical ionization mass spectrometry and long path-differential optical absorption spectroscopy, *Journal of Geophysical Research*, 116, 10.1029/2010jd014788, 2011.

Macdonald, K. M., Sharma, S., Toom, D., Chivulescu, A., Hanna, S., Bertram, A. K., Platt, A., Elsassner, M., Huang, L., Tarasick, D., Chellman, N., McConnell, J. R., Bozem, H., Kunkel, D., Lei, Y. D., Evans, G. J., and Abbatt, J. P. D.: Observations of atmospheric chemical deposition to high Arctic snow, *Atmos Chem Phys*, 17, 5775–5788, 10.5194/acp-17-5775-2017, 2017.

Markovic, M. Z., VandenBoer, T. C., and Murphy, J. G.: Characterization and optimization of an online system for the simultaneous measurement of atmospheric water-soluble

Bibliography

constituents in the gas and particle phases, *J Environ Monit*, 14, 1872–1884, 10.1039/c2em00004k, 2012.

Markovic, M. Z., VandenBoer, T. C., Baker, K. R., Kelly, J. T., and Murphy, J. G.: Measurements and modeling of the inorganic chemical composition of fine particulate matter and associated precursor gases in California's San Joaquin Valley during CalNex 2010, *Journal of Geophysical Research: Atmospheres*, 119, 6853–6866, 10.1002/2013jd021408, 2014.

Mitchell, D. L., and Lamb, D.: Influence of riming on the chemical composition of snow in winter orographic storms, *Journal of Geophysical Research*, 94, 14831–14840, 1989.

Murphy, J. G., Gregoire, P. K., Tevlin, A. G., Wentworth, G. R., Ellis, R. A., Markovic, M. Z., and VandenBoer, T. C.: Observational constraints on particle acidity using measurements and modelling of particles and gases, *Faraday Discuss*, 200, 379–395, 10.1039/c7fd00086c, 2017.

Nerentorp Mastromonaco, M., Gårdfeldt, K., Jourdain, B., Abrahamsson, K., Granfors, A., Ahnoff, M., Dommergue, A., Méjean, G., and Jacobi, H. W.: Antarctic winter mercury and ozone depletion events over sea ice, *Atmospheric Environment*, 129, 125–132, 10.1016/j.atmosenv.2016.01.023, 2016.

Olofsson, G.: Thermodynamic quantities for the dissociation of the ammonium ion and for the ionization of aqueous ammonia over a wide temperature range, *J. Chem. Thermodynamics*, 7, 507–514, 1975.

Pleim, J. E., Bash, J. O., Walker, J. T., and Cooter, E. J.: Development and evaluation of an ammonia bidirectional flux parameterization for air quality models, *Journal of Geophysical Research: Atmospheres*, 118, 3794–3806, 10.1002/jgrd.50262, 2013.

Pratt, K. A., Custard, K. D., Shepson, P. B., Douglas, T. A., Pöhler, D., General, S., Zielcke, J., Simpson, W. R., Platt, U., Tanner, D. J., Gregory Huey, L., Carlsen, M., and Stirm, B. H.: Photochemical production of molecular bromine in Arctic surface snowpacks, *Nature Geoscience*, 6, 351–356, 10.1038/ngeo1779, 2013.

Simpson, W. R., von Glasow, R., Riedel, K., Anderson, P., Ariya, P., Bottenheim, J., Burrows, J., Carpenter, L. J., Friess, U., Goodsite, M. E., Heard, D., Hutterli, M., Jacobi, H. W., Kaleschke, L., Neff, B., Plane, J., Platt, U., Richter, A., Roscoe, H., Sander, R., Shepson, P. B., Sodeau, J., Steffen, A., Wanger, T., and Wolf, E.: Halogens and their role in polar boundary-layer ozone depletion, *Atmospheric Chemistry and Physics*, 7, 4375 – 4418, 2007.

Stanier, C., Singh, A., Adamski, W., Baek, J., Caughey, M., Carmichael, G., Edgerton, E., Kenski, D., Koerber, M., Oleson, J., Rohlf, T., Lee, S. R., Riemer, N., Shaw, S., Sousan, S., and Spak, S. N.: Overview of the LADCO winter nitrate study: hourly ammonia, nitric acid and PM_{2.5}; composition at an urban and rural site pair during PM_{2.5} episodes in the US Great Lakes region, *Atmospheric Chemistry and Physics*, 12, 11037–11056, 10.5194/acp-12-11037-2012, 2012.

Sutton, M. A., Dragosits, U., Tang, Y. S., and Fowler, D.: Ammonia emissions from non-agricultural sources in the UK, *Atmospheric Environment*, 34, 855–869, 2000.

Sutton, M. A., Reis, S., Riddick, S. N., Dragosits, U., Nemitz, E., Theobald, M. R., Tang, Y. S., Braban, C. F., Vieno, M., Dore, A. J., Mitchell, R. F., Wanless, S., Daunt, F., Fowler, D., Blackall, T. D., Milford, C., Flechard, C. R., Loubet, B., Massad, R., Cellier, P., Personne, E., Coheur, P. F., Clarisse, L., Van Damme, M., Ngadi, Y., Clerbaux, C., Skjoth, C. A., Geels, C., Hertel, O., Wichink Kruit, R. J., Pinder, R. W., Bash, J. O., Walker, J. T., Simpson, D., Horvath, L., Misselbrook, T. H., Bleeker, A., Dentener, F., and de Vries, W.: Towards a climate-dependent paradigm of ammonia emission and deposition, *Philos Trans R Soc Lond B Biol Sci*, 368, 20130166, 10.1098/rstb.2013.0166, 2013.

Tsunogai, S., and Ikeuchi, K.: Ammonia in the atmosphere, *Geochemical Journal*, 2, 157–166, 1968.

Wolff, E. W., Hall, J. S., Mulvaney, R., Pasteur, E. C., Wagenbach, D., and Legrand, M.: Relationship between chemistry of air, fresh snow and firn cores for aerosol species in coastal Antarctica, *Journal of Geophysical Research: Atmospheres*, 103, 11057–11070, 10.1029/97jd02613, 1998.

Snow metamorphism and chemistry in snow: reactive assessment of ion redistribution in snow grains

5.1.1 Abstract

Changes in the structure of snow with time, also known as metamorphism, occur with and without temperature induced gradient (TGM) in a snowpack. Metamorphism, which involves the movement of water vapor in the direction of the temperature gradient from high to low temperature, may result in the partitioning of ions in the snow grains between the surface and the bulk with the movement of water vapor. Reactive ions that are buried with metamorphism will not be available for reaction. In this study, we present preliminary assessment of results from experiments investigating the effects of TGM on doped (6 μM bromide) snow after 12 days under TGM. Change in the structure of snow with TGM was assessed using snow X-ray tomography. Structural changes with TGM were small between 0 and 12 days of TGM. The redistribution of bromide ions with TGM was assessed *via* a reactive method at $-15\text{ }^{\circ}\text{C}$ by exposing the bromide-doped samples to ozone and monitoring ozone loss. This method probes only the bromide ions available for reaction (that is, on the surface). Results showed that bromide was buried after 12 days under TGM. With respect to halogen activation, such burial may reduce the potential release photo-labile Br_2 , thereby decelerating photocatalytic bromide oxidation. Future work will assess TGM changes at different time steps between 0 and 12 days and characterize the actual surface area exposed to ozone using a chemical adsorption method.

5.1.2 Introduction

Field observations of atmospheric composition in snow covered regions have identified significant relationships between the concentration of compounds in the air and snow cover (Wang *et al.*, 2011; Chen *et al.*, 2012; Krnavek *et al.*, 2012; Stanier *et al.*, 2012; Michoud *et al.*, 2015). These studies indicate that snow actively influences atmospheric composition through chemical processing, the release of products to the atmosphere, and other related processes. Exchange between the atmosphere and snow is an interplay of scavenging and deposition with snowfall, dry deposition on the snowpack, post-depositional (photo)chemical and physical processes, diffusion in and out of the snowpack, wind pumping through the snowpack, and sublimation with snow (Domine and Shepson, 2002; Krnavek *et al.*, 2012).

The uptake of compounds, chemical processing (reactivity), and the release of products depend on the concentrations of the contaminants in the snow, the location of the contaminants in or on the snow grains as well as the physical properties of the snowpack (Domine and Shepson, 2002). Snowpack properties relevant for chemical reactivity and exchange with the atmosphere include the specific surface area, the porosity and permeability, and the density (Domine *et al.*, 2008). The dynamic nature of snow, which involves continuous change in the properties, is referred to as metamorphism (Sommerfeld and LaChapelle, 1970; Colbeck, 1983). Metamorphism in snow is due to the movement of water vapor from warmer to colder regions of the snow, where the vapor recrystallizes, due to water vapor pressure gradients (Colbeck, 1983).

The impact of snow metamorphism on the physical properties of snow is well known. Metamorphism could be dry, that is, without liquid water or wet, with liquid water. The work described here is focused on dry metamorphism, which is the most common form of metamorphism observed in snow in the field (Pinzer *et al.*, 2012). Dry metamorphism could be isothermal, that is, without an external temperature gradient, which results in the formation of rounded, uniform grains (Colbeck, 1983; Pinzer *et al.*, 2012). Vapor flux in isothermal metamorphism is induced by small gradients due to the curvature of the grains (Colbeck, 1983; Pinzer *et al.*, 2012). The second form of dry metamorphism is temperature gradient induced metamorphism (TGM) which involves an external temperature gradient and leads to the formation of faceted, more coarse grains on the colder side in the direction of the gradient from high to low temperature (Colbeck, 1983; Pinzer *et al.*, 2012). Temperature gradients can vary from <10 K/m to 100 K/m in the field (Birkeland *et al.*, 1998).

Metamorphism leads to changes in snow properties to varying degrees depending on the age of the snow. Some of the properties affected by metamorphism include the specific surface area (SSA), and permeability (K), and density; effects on these properties may affect reactivity in snow and the release of compounds from snow (Sommerfeld and LaChapelle, 1970; Colbeck, 1983; Domine *et al.*, 2002; Schneebeli and Sokratov, 2004; Pinzer and

Chapter 5 Snow metamorphism, ion redistribution, and chemistry

Schneebeli, 2009; Pinzer *et al.*, 2012). In aged snow, although the changes may be small, there could still be large turnover of water vapor; calculated turnover rates of snow grains range from 121 to 190 kg m⁻³d⁻¹ (Pinzer *et al.*, 2012).

Water vapor flux and recrystallization during metamorphism may be likened to growing ice. Studies investigating the adsorption and uptake of trace gases like nitric acid and hydrochloric acid on growing ice and have observed higher uptake than on ice at equilibrium (Dominé and Thibert, 1996; Ullerstam and Abbatt, 2005). Others have looked at fresh and aged snow, and the effect of snow properties at those ages on the processes such as diffusion and adsorption of trace gases and volatile organics (Domine *et al.*, 2007; McNeill *et al.*, 2007; Kerbrat *et al.*, 2010; Pinzer *et al.*, 2010; Bartels–Rausch *et al.*, 2013). Having higher SSA, fresh snow or vapor deposited ice was observed to have higher equilibrium adsorption or uptake of trace gases than aged snow (Domine *et al.*, 2007; McNeill *et al.*, 2007).

With turnover of snow grains and the movement of water vapor, contaminants deposited on the snow grains or with the snowfall may be redistributed between the surface and bulk of the snow grains. Redistribution may also involve incorporation in grain boundaries or in triple junctions in the snow grains (Bartels–Rausch *et al.*, 2014; Hullar and Anastasio, 2016). Laboratory studies investigating TGM effects on the location of ions in natural (containing millimolar concentrations of ions) and artificial snow (containing nanomolar concentrations of ions) by elution have observed preferential elution of ions (Hewitt *et al.*, 1989, 1991; Cragin *et al.*, 1996). The preferential elution was attributed to the relocation of the ions during metamorphism (Hewitt *et al.*, 1989, 1991; Cragin *et al.*, 1996). These studies also affirmed that the preferential elution was not due to chromatographic property of the snow, that is, the affinity of the snow to the different ions (Hewitt *et al.*, 1989, 1991; Cragin *et al.*, 1996). Relocation of ions was attributed to the solubility limit of the ions in ice, and partitioning similar to the rejection of ions during slow freezing of an ionic solution (Hewitt *et al.*, 1989, 1991; Cragin *et al.*, 1996). Elution sequence observed from these laboratory studies were similar to those observed in samples that had undergone natural metamorphism in the field (Brimblecombe *et al.*, 1985; Brimblecombe *et al.*, 1988 ; Eichler *et al.*, 2001). Studies show that sulfate is preferentially excluded to the surface and was easily eluted while chloride, a more soluble ion than sulfate, was retained in the bulk of the ice (Brimblecombe *et al.*, 1985; Davis *et al.*, 1995).

While elution studies have been applied extensively for investigating the distribution of ions in snow grains in a snowpack, these methods involve the use of an eluent. The eluent is the liquid used to rinse out the ions exposed in grain boundaries, on the surface of snow grains, and in the pore spaces in the snowpack. The type of eluent used for elution also affects the results for elution experiments (Cragin *et al.*, 1996). With the introduction of an eluent, there is also the possibility of changing the structure of the snow under study as well as dilution of the ion concentrations (Cragin *et al.*, 1996), which complicates interpretation of elution experiments.

More recent studies have investigated the effects of ions on the crystallization of ice, the size of grains in polycrystalline ice, and the inclusion of ions in grain boundaries and micropockets in the ice (Eichler *et al.*, 2017; Wu *et al.*, 2017; Nagashima *et al.*, 2018). The study by Wu *et al.* (2017) showed ion effects on the grain size, which correlates well with observed elution sequences (Wu *et al.*, 2017). For instance, sulfate, which is eluted early (due to low solubility in ice), resulted in smaller grain size than chloride, which tends to remain in the bulk (Brimblecombe *et al.*, 1985; Davis *et al.*, 1995; Wu *et al.*, 2017). The smaller grain size occurs because these poorly soluble ions hinder the recrystallization of ice, thereby forcing water molecules to rearrange around these ions and creating disruptions in the ice structure (Wu *et al.*, 2017). Wu *et al.* (2017) also observed that the grain size increased with concentration due to incorporation in the ice crystals up to a critical concentration (10^{-4} M for bromide) after which the size decreased as higher concentrations start to suppress crystal growth (Wu *et al.*, 2017). Nagashima *et al.* (2018) have also observed the formation of brine inclusions in ice (HCl) with recrystallization, which may increase the apparent Henry's law solubility of HCl in ice. These studies demonstrate that ions could be on the surface of snow grains as well as in grain boundaries, in the ice structure, and in liquid micro-pockets in the ice.

As has been previously mentioned, metamorphism involves continuous loss, recrystallization, and growth of ice crystals in the snowpack. The physics and structural changes with metamorphism are well known. Considering the aforementioned studies on the locations of ions in ice, one can hypothesize that at low concentrations of bromide, bromide ions may partition into the bulk of the ice with recrystallization, which occurs during metamorphism. This may also be expected based on elution studies, which have shown that bromide may be preserved in the ice crystal (Davis *et al.*, 1995). However, there is still the complication of the eluent and the effects of the eluent on the samples probed (wet metamorphism during the experiment) and dilution of ions, and the question of the depth probed by the eluent.

Therefore, the objective of this study is to use observed reactivity (bromide oxidation by ozone) to assess the partitioning of bromide between the bulk and the surface of snow grains with TGM on artificial snow as well as assess the structural changes in the snow due to TGM. We observed the loss of ozone through a packed column of artificial snow, clean and doped with bromide. We also assessed the relationship between ozone loss in the system and changes in the SSA and permeability of the snow column after exposure to a temperature gradient. By this method, we avoid the complications of eluents as in elution studies. We also only probe the accessible surfaces of the snow grains as ions on these surfaces would be the ions available for reaction.

This study is a reactive method of investigating the distribution of ions in a snowpack with TGM. The present study makes use of low concentrations of bromide which can be found in the natural environment (6 μ M; (Krnavek *et al.*, 2012)). Although in the field, the presence

of other ions and compounds may affect the recrystallization and the redistribution of ions, this study investigated the first level in complexity for a reactive approach to investigating chemistry in snow.

This is an ongoing study. In this chapter, we present the assessment of two time points in the TGM experiments 0–day (no exposure to TGM) and 12–day (after 12 days of TGM). With the full series including TGM time steps at 1 day, and 6 days, the study may provide relevant information on changing distribution of bromide in the snow crystals during the metamorphism process. This study provides a way of linking the physics of snow metamorphism with reactivity as may be observed in the environment.

5.1.3 Methods

Sample preparation

Artificial snow was produced from ultrapure water (18 M Ω ; clean) and a solution containing ~600 ppb sodium bromide (NaBr) in water (doped). The snow was produced by shock freezing droplets of the solution in liquid nitrogen. The samples were left overnight at -45 °C and then, exposed to isothermal metamorphism at -5 °C for 7 days to anneal, which should lead to increased uniformity and decreased grain boundaries (Pinzer and Schneebeli, 2009). The samples were returned to -45 °C after this isothermal treatment to slow down further metamorphism. The produced snow was sieved using pre-cleaned stainless steel sieves in a -20 °C cold laboratory at the Swiss Snow and Avalanche research Institute (SLF, Davos, Switzerland). Snow grains in the size range 300 – 600 μm were packed into the 12.0 ± 0.1 cm long glass reactor tubes with 2.4 ± 0.1 cm internal diameter. The tubes had a thickness of 2.25 ± 0.25 mm. The packed clean samples had a density of 0.36 ± 0.02 g/cm³ while the doped samples had a density of 0.43 ± 0.02 g/cm³. The difference in density is due to the variability in the packing of the samples. The bromide (Br⁻) concentration in the sieved doped snow samples was 498 ± 3 ppbv (~6 μM) measured by ion chromatography.

Temperature gradient metamorphism

Samples were exposed to a gradient, ∇T , of 33 K/m for 12 days (12–day; samples were also exposed to TGM for 1, and 6 days, but not discussed here) in a snow metamorphism box mounted in a cold room at -8 °C (at SLF, Davos, Switzerland). For control, a set of samples was not exposed to TGM (but had undergone the isothermal metamorphism in the sample preparation steps; 0–day). Figure 5.1a presents a schematic of the assembly of the metamorphism box. The metamorphism box was a heavily insulated box with a heating plate set to -4 °C at the bottom. Over this plate, there was a ~2–3 cm thick layer of ice from ultrapure water. The sample holders were mounted on a disk with a 0.5 cm layer of ice made with ultrapure water in contact with the snow grains to increase thermal contact (Pinzer and Schneebeli, 2009). The disk was mounted and fused with the ice layer in the box with water. The spaces between the sample tubes were filled by sieving in snow. The box

was then covered with a thin plastic film in contact with the filled-in snow and caps of the samples to avoid losses due to sublimation. After the TGM treatment, the samples were stored at $-45\text{ }^{\circ}\text{C}$ till they were tested for reactivity with O_3 and other analyses. The 0-day samples were also stored at $-45\text{ }^{\circ}\text{C}$ before reactivity tests.

Structural changes in the samples were measured using an X-ray computer micro-tomography scanner (CT; Scanco micro-CT 40) with a resolution of $10\text{ }\mu\text{m}$. This micro-CT was operated at $-20\text{ }^{\circ}\text{C}$. Details of operations of the CT scans have been described by Pinzer *et al.* (2009). 3 cm segments from the top third, middle layer, and bottom third of the samples were analyzed. The outer parts of the samples in contact with the sample holders were shaved off before inserting them into the CT sample holders. Output from the micro-CT scans were used to calculate the porosity, SSA, and permeability.

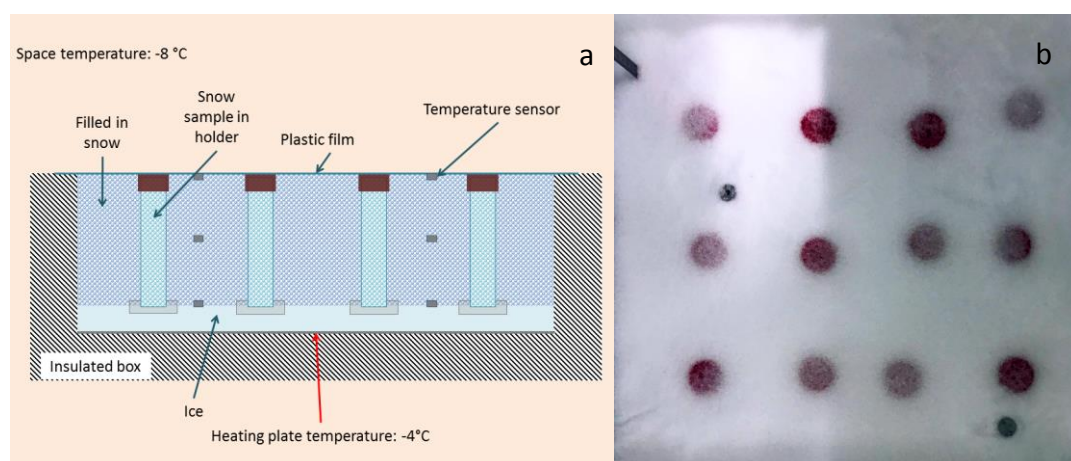


Figure 5.1 a. Cross-section of the metamorphism box assembly (not to scale); b. Samples in the metamorphism box without the plastic film (top view).

Ozone exposure:

Samples were exposed to ozone at $-15\text{ }^{\circ}\text{C}$. Before exposure, about 2 cm of the samples were scraped off from the top and bottom of the samples to avoid potential contamination from contact with the ice layer on the disk in the metamorphism box or the caps for the sample holder/reactor tubes. 3 cm was shaved from both ends from one of the 0-day doped samples. The samples tubes were placed in the reactor cell, an insulated cooling jacket, at $-15\text{ }^{\circ}\text{C}$ (following similar setup arrangement as in Chapters 2 and 3). The sample was allowed to temperature equilibrate for an hour before exposure to gases. Humidified airflow of about 200 ml/min O_2 and about 200 ml/min N_2 was delivered through the sample for 30 minutes to condition the sample (total flow rate through the sample was $395\text{ ml/min} \pm 5\text{ ml/min}$). This airflow was humidified to a water vapor pressure of $-15.0 \pm 0.3\text{ }^{\circ}\text{C}$.

Ozone (O_3) was generated by passing the N_2/O_2 airflow through a penray Hg UV lamp ozone generator. O_3 flow was also humidified before delivery to the sample. When O_3 production

was stable (after 1 to 1.5 hours), the flow was delivered through the sample for an hour. After the first hour, the flow was alternated between a bypass and the sample to control for drifts in O₃ concentration. O₃ concentration was monitored using a commercial Teledyne API O₃ analyzer. The average O₃ concentration for each experiment was slightly different due to the day to day variability in the efficiency of the ozone generator. For all experiments ozone concentrations varied from 163 to 190 ppb. The maximum variability during any one experiment was less than 5 ppb after attaining initial stability at the start of the experiment.

5.1.4 Results and discussion (Preliminary analysis)

Table 5.1: Morphology of the snow samples; TGM age is number of days in the metamorphism box. SSA is specific surface area ($\pm 6\%$ error; Kerbrat *et al.*, 2008). ϵ is porosity. K is permeability.

| TGM age | Sample | SSA cm ² /g | ϵ | K m ² |
|---------|------------------|------------------------|------------------|----------------------------------|
| 0 | Clean (<10 ppbv) | 176 \pm 11 | 0.45 \pm 0.005 | 1.6 \pm 0.43 $\times 10^{-10}$ |
| 12 | Clean (<10 ppbv) | 167 \pm 10 | 0.56 \pm 0.01 | 6.0 \pm 1.45 $\times 10^{-10}$ |
| 0 | Doped (498 ppbv) | 183 \pm 11 | 0.47 \pm 0.01 | 1.8 \pm 0.49 $\times 10^{-10}$ |
| 12 | Doped (498 ppbv) | 162 \pm 10 | 0.47 \pm 0.001 | 2.3 \pm 0.57 $\times 10^{-10}$ |

Table 5.1 presents a summary of the snow morphology based on the micro-CT measurements. The TGM induced structural changes in the doped samples were not as pronounced as in the clean samples. There was a very slight decrease in SSA between 0 day and 12 days under TGM for both the clean and doped samples: from 176 \pm 11 cm²/g to 167 \pm 10 cm²/g for the clean sample and 183 \pm 11 cm²/g to 162 \pm 10 cm²/g in the doped sample. These measurements indicate that the decrease in SSA was not significant.

The porosity (ϵ ; fraction of pores in the column, (1 – ice fraction)) increased between the 0-day and 12-day clean samples from 0.45 (± 0.005) to 0.56 (± 0.01), while that of the doped samples remained the same, 0.47 (± 0.01) for the 0-day and 0.47 (± 0.001) for the 12-day samples. The estimated permeability (K) using the parameterization by Calonne *et al.* (2012; equation (5.1)) was higher in the 12-day samples (6.0 \pm 1.45 $\times 10^{-10}$ m² for clean and 2.3 \pm 0.57 $\times 10^{-10}$ m² for doped) than in the 0-day samples (1.6 \pm 0.43 $\times 10^{-10}$ m² for clean and 1.8 \pm 0.49 $\times 10^{-10}$ m² for doped). K is smaller in the doped sample than in the clean sample.

$$K = (3.0 \pm 0.3)r_{es}^2 \exp((-0.0130 \pm 0.0003)\rho_s) \quad (5.1)$$

Where r_{es} is the equivalent sphere radius of the snow ($r_{es} = 3/(SSA \times \rho_i)$); ρ_i is the density of ice (917 kg/m³) and SSA is the specific surface area of the snow in m²/kg) and ρ_s is the density of the snow ($\rho_s = \rho_i(1 - \epsilon)$ in kg/m³) (Calonne *et al.*, 2012). The permeability gives an indication of the connectivity of the pores and the ease of fluid flow through the snow column. Higher permeability means easier air flow through the snow.

The observed quantities of the structural properties are within the range observed for hard wind-packed snow, depth hoar and wet snow in the field (Domine *et al.*, 2002; Zermatten *et*

al., 2011; Calonne *et al.*, 2012). Therefore, these values agree with observations of slower changes in snow properties as snow ages (Cabanes *et al.*, 2003; Domine *et al.*, 2008).

Figure 5.2 presents O₃ loss as a function of O₃ exposure time for samples exposed to TGM for 12 days and samples not exposed to TGM, clean and doped. Percent O₃ loss was calculated using equation (5.2). All samples reached similar percent O₃ loss at the end of the each experiment. Samples did not reach 0% O₃ loss (including the clean samples) indicating that there is a small loss of O₃ which may be due to its self-reaction on the ice surface, slow diffusion into pores, contamination and/or experimental uncertainty.

$$\% O_3 \text{ loss} = \frac{O_{3_Bypass(avg)} - O_{3_flowtube}}{O_{3_Bypass(avg)}} \times 100 \quad (5.2)$$

There is no difference in the losses between the clean samples (0-day and 12-day). This is expected because the clean samples should not have a reactive loss more than the background. In addition, there is no significant difference in the SSA between 0 and 12 days, which may have affected adsorptive losses (if the SSAs were significantly different). However, there should be no adsorptive loss of ozone on the ice at -15 °C as other studies have observed no adsorptive loss of ozone to ice at temperatures below -70 °C (Dlugokencky and Ravishankara, 1992; Borget *et al.*, 2001).

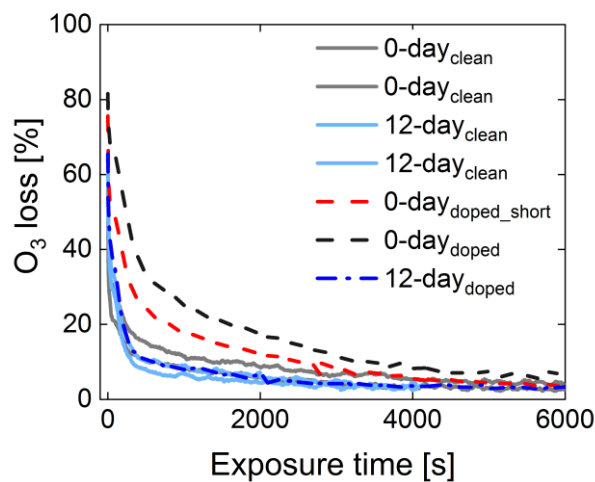


Figure 5.2 Percent ozone loss with duration of exposure from clean samples (0 ppb Br⁻) and doped samples (498 ± 3 ppb Br⁻) that have been exposed to temperature gradient metamorphism (TGM) for 12 days or not (0 days). Average [O₃] for all samples was ~180 ppb. Experimental temperature was -15 °C.

The only difference in the clean samples is the recovery rate of the ozone concentration through the sample after switching ozone flow to the sample. This may be indicated by the slope of the O₃ concentration through the reactor plotted against exposure time (Figure 5.3). The recovery rate of the 12-day clean samples was 2 times faster than the 0-day clean sample (0.2 ± 0.003 ppb/s for the 12-day sample, and 0.1 ± 0.002 ppb/s for the 0-day

sample). This may be an indication of better permeability in the 12-day samples than in the samples not exposed to TGM. This is corroborated by the TGM induced permeability changes between the 0 and 12-day samples where K for the 12-day sample is 3.75 times larger than for the 0-day sample (Table 5.1). Nitric oxide (NO) breakthrough curves may give a better indication of the residence time of the gas in the system. This experiment would be conducted in continuation of this study.

The recovery rate as described for the clean samples may not be appropriate for the doped samples due to reactive losses especially in the 0-day sample. There is also very small difference in permeability between the 0-day and the 12-day doped samples (Table 5.1). The 0-day doped sample (0-day_{doped} and 0-day_{doped_short}) had a much higher initial loss of ozone than the 12-day doped sample (Figure 5.3). The 0-day_{doped_short} sample had about 6 grams less snow than the 0-day_{doped}.

The loss profile for the 12-day doped sample is similar to that of the clean samples (Figure 5.2). The difference in SSA and ϵ between the 0-day and the 12-day doped samples is relatively small (Table 5.1). This implies that the reduction in loss of ozone after 12 days under TGM may be due to the unavailability of bromide in the 12-day sample. Uptake coefficients of ozone in the system may be a better parameter for comparing ozone loss in the system. The uptake coefficients normalize the loss rate to the collision rate of ozone with the surfaces (equation (5.3)). Therefore, there is an intrinsic normalization to the total surface area (TSA; $TSA = SSA \text{ (cm}^2\text{/g)} \times \text{mass of sample (g)}$) of the samples. For this analysis, we have used the SSA measured in the micro-CT. The true SSA that ozone sees during the experiment may be better quantified using adsorption experiments. Studies however show very good agreement between the micro-CT calculated SSA and SSA measured by adsorption (Kerbrat *et al.*, 2008).

$$\gamma_{\text{obs}} = \frac{4\varphi \times \left[\ln\left(\frac{[O_3]_{\text{bypass}}}{[O_3]_{\text{flow tube}}}\right) \right]}{\omega_{O_3} \times TSA} \quad (5.3)$$

Where φ is the gas flow rate at -15°C and atmospheric pressure ($7 \text{ cm}^3\text{/s}$); ω_{O_3} is the mean thermal velocity of ozone (at $-15^\circ\text{C} = 33743.5 \text{ cm/s}$), γ_{obs} is the uptake coefficients. TSA in $\text{cm}^2 = SSA \text{ (cm}^2\text{/g}_{\text{snow}}) * \text{mass of snow (g)}$.

The uptake coefficients calculated for both 0-day doped samples are the same and are larger than that of the 12-day doped sample (Figure 5.4). The 12-day doped samples had the same uptake coefficients as the 12-day clean samples. The 0-day clean samples are also similar to the 12-day clean samples. At the end of each experiment, all samples arrived at similar uptake coefficients including the 0-day doped samples. For the 0-day doped sample, this may be an indication of depletion of bromide on the surface due to oxidation by ozone. The difference between the 0-day and the 12-day doped samples may be due to significant burial of the bromide with TGM as was hypothesized. The question still unanswered is why

the 0-day doped sample after the isothermal treatment at $-5\text{ }^{\circ}\text{C}$ for 7 days during the sample preparation still has exposed bromide.

In response to the above question, one can think about the rate of structural change with TGM as presented on Table 5.1. Based on the information on Table 1, we may infer that changes in the doped samples occur at a slower rate than in the clean samples. This may be attributed to the effect of ions present on the recrystallization of the ice; ions disrupt ice crystallization (He *et al.*, 2016; Wu *et al.*, 2017). We also know that changes due to isothermal metamorphism occur more slowly than in TGM (Domine *et al.*, 2008). The isothermal treatment was done at $-5\text{ }^{\circ}\text{C}$ and the TGM gradient was between $-4\text{ }^{\circ}\text{C}$ and $-8\text{ }^{\circ}\text{C}$. Therefore, the rate of change for TGM should be stronger than in the isothermal. Hence, we can infer that although some burial of the bromide may have occurred during the isothermal treatment, there may be significantly larger concentration of bromide still on the surface of snow grains in the 0-day sample than in the 12-day sample.

Burial in the 12-day sample may be due to ice growth covering brine on the surface of the grains (Nagashima *et al.*, 2018) or incorporation in the crystal (Wu *et al.*, 2017). Sublimation and deposition are largely responsible for the turnover of ice grains during metamorphism (Pinzer *et al.*, 2012). Deposition on the colder side of small and large gradients may also lead to burial of exposed brine (Nagashima *et al.*, 2018). These hypotheses may be better verified by looking at the reactive uptake on samples at intervals between 0 and 12 days as well as samples that remained under isothermal metamorphism for 12 days. Also, tomographic mapping of bromide coverage on the surface of the snow crystals with different durations in TGM may clearly show how much of the surface is covered by bromide and how that changes with time in TGM. Tomography during metamorphism (Pinzer *et al.*, 2012) may allow visualization and quantification of water vapor flux and the relationship to the movement of bromide with metamorphism (Hullar and Anastasio, 2016).

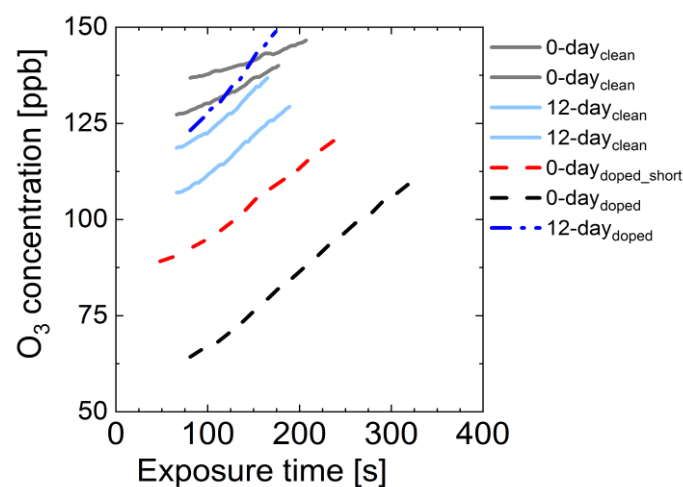


Figure 5.3 Initial ozone concentration through the reactor column plotted against exposure time showing the initial rate of recovery after switching to the reactor.

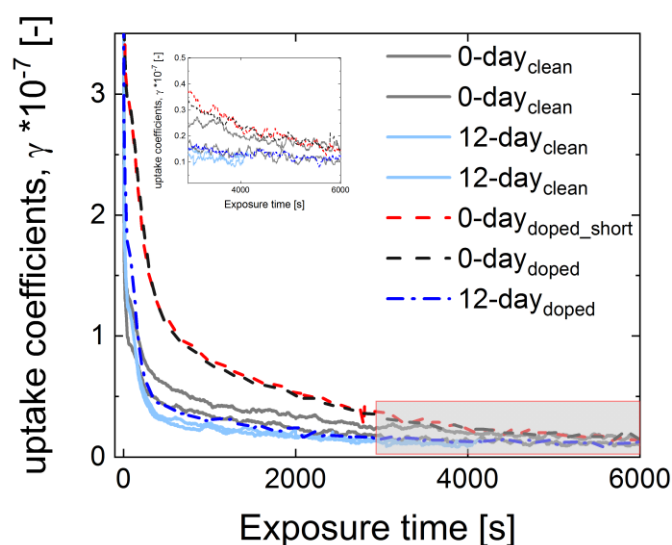


Figure 5.4 Uptake coefficients of ozone plotted against exposure time.
 $T = -15\text{ }^{\circ}\text{C}$; ozone flow rate was $7\text{ cm}^3/\text{s}$ with average ozone concentration of $\sim 180\text{ ppb}$.

5.1.5 Conclusions and outlook

We have presented an assessment of the effects of metamorphism on the reactivity of ozone with bromide in bromide doped and clean artificial snow. Samples, doped with NaBr ($498 \pm 3\text{ ppb}$, $6\text{ }\mu\text{M Br}^-$) and clean (pure water) were either exposed to TGM for 12 days (12-day) or not (0-day). Micro-CT scans assessing structural changes in the sample due to TGM show that there was a coarsening of the snow structure with time inducing a small increase in the porosity and permeability. There was an insignificant decrease in the specific surface area between 0 and 12 days under TGM for both clean and doped samples as has been observed in other studies for this type of aged snow (Domine *et al.*, 2002; Pinzer and Schneebeli, 2009). The doped samples showed slightly smaller changes in structural properties than the clean sample. This may be due to effects of the bromide ions on the recrystallization process of ice as observed by He *et al.* (2016) and Wu *et al.* (2017). This, however, needs further investigation.

Observation of ozone loss by reaction with bromide in the 12-day doped snow samples showed less ozone consumed than in the 0-day doped sample. We attributed this observation to bromide burial driven by large ice turnover during the 12 days under TGM. This observation agrees with elution studies on samples containing a mixture of four salts (containing 8 mM NaBr), which showed that bromide has a tendency to be incorporated in the ice with metamorphism (wet; (Davis *et al.*, 1995)). A recent study by Wu *et al.* (2017) also showed that bromide is likely to be incorporated in the ice with recrystallization especially at low concentration. Wu *et al.*'s molecular dynamics simulations showed that the charge density around a Br^- does not result in very large disruptions of the "local ice structure" as one would observe for SO_4^{2-} or F^- , for example, which are expelled to the

surface of snow grains (Brimblecombe *et al.*, 1985; Cragin *et al.*, 1996). Therefore, bromide may be incorporated into the ice structure or in micropockets buried in the ice.

Percent O₃ loss and uptake coefficients on the 0-day doped sample eventually reduce to the loss observed in the clean samples with exposure time. This indicates that the concentration of bromide available for reaction is very low and may get depleted with longer exposure to O₃. This work used low concentrations of bromide, ~6 μM, which is on the lower end of observations in environmental ice (Krnavek *et al.*, 2012), but slightly higher than that observed in snow in the Arctic (Dibb *et al.*, 2010). This concentration is also lower than the critical concentration for grain size increase in Wu *et al.*'s study (2017). Although this concentration is representative of concentrations in the field, low concentrations may pose difficulty in quantifying reactivity. Future experiments may consider higher experimental concentrations in the upper range of field observations (~93 μM; (Krnavek *et al.*, 2012)) or a bromide concentration dependence study. One should however note that higher concentrations also might influence the changes and rate of change with TGM due to impacts (hindrance) on recrystallization (Wu *et al.*, 2017).

Losses on the clean samples did not get to 0% during this experiment indicating that there are some losses to ice in the system. Studies indicate that O₃ uptake by adsorption on ice is very low (Dlugokencky and Ravishankara, 1992; Borget *et al.*, 2001). Taking that there were no leaks in the system, the sustained loss of O₃ from the system may be due to this low uptake and/or the ozone self-reaction (and destruction) on the surface of ice (Berkemeier *et al.*, 2016). Continuation on this work may investigate this further by comparing the estimated loss due to self-reaction against the uptake coefficients in the clean system as well as on ice flow tubes.

In summary, we have conducted a reactive assessment of the effect of TGM on the redistribution bromide ions in snow grains. With this method, we probed only the ions present on the surface and available for reaction. We also avoid complications of wet metamorphism that may occur during elution studies. In our case study with bromide, TGM resulted in burial of Br⁻, which is in agreement with molecular based studies on the effect of ions on recrystallization of ice.

With relevance to bromide oxidation, which has significant environmental implications on the atmosphere's oxidation capacity, burial due to TGM may reduce the availability to reactive gases such as O₃. This burial of halides with TGM ageing may reduce the renewal of photo-labile di-halogenes in the atmosphere and may contribute to the deceleration of the process in the environment while buried. One should however note that burial leads to enrichment in the snow, which may contribute to later meltwater pollution. Studies have found such enrichment of bromide in snow pits which were larger than in aerosols (Dibb *et al.*, 2010). In addition, with relevance to ice core research, burial of bromide with metamorphism may increase the preservation of bromide as snow gets transformed to firn and ice. This study investigated a bromide-water system. In the environment, there are

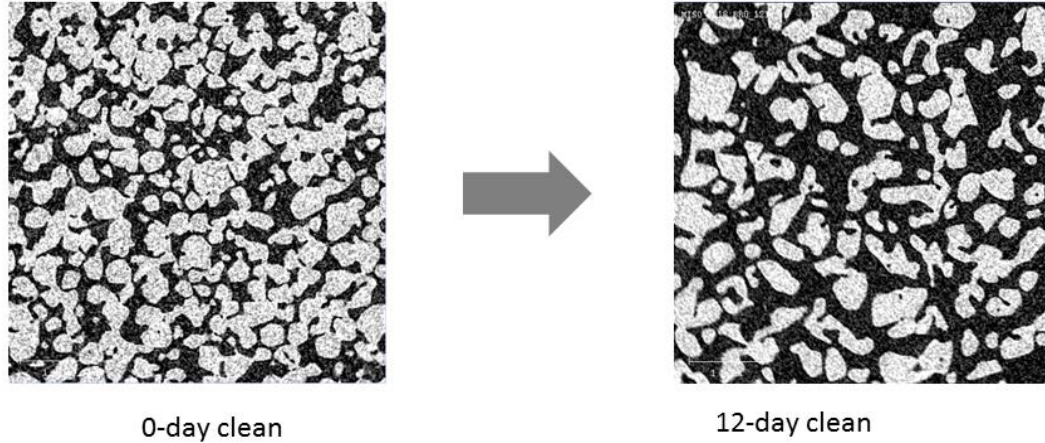
other ions and compounds present which may also affect the recrystallization of ice. Therefore, this study is the first complexity level for assessing environmental systems.

5.1.6 Acknowledgements

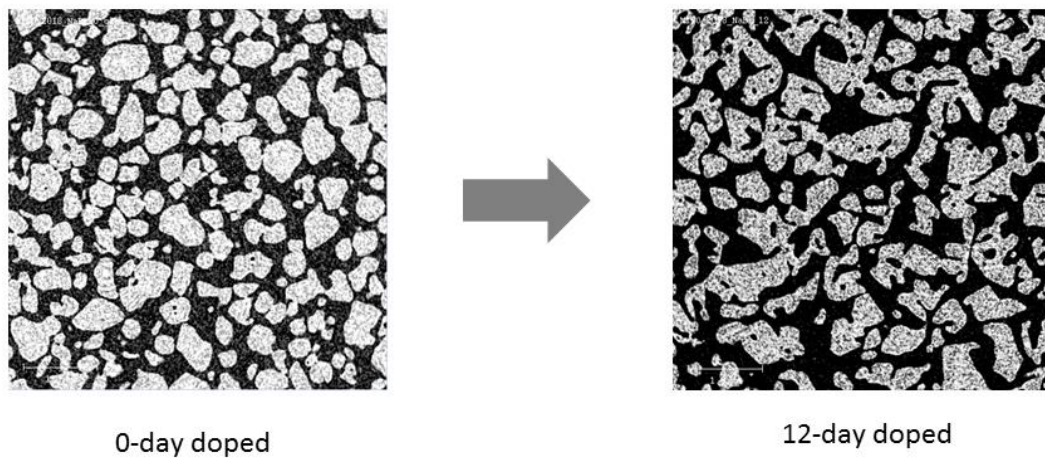
This work was funded by the Swiss National Science Foundation grant number 155999. Metamorphism and micro-CT based work were conducted at the Swiss Avalanche Research Institute, SLF, Davos in collaboration with Jürg Trachsel from the Schneeeli, Snow and Permafrost, research group. We are grateful to Mario Birrer and Andrés Laso for technical support with the kinetics setup.

5.2 Supplementary information

Micro-CT images



SI Fig S5. 1 Micro-CT images of the clean samples after 0 and 12 days exposure to TGM. The 0 day samples (after 7 days at -5°C) have smaller grains and lower porosity than the 12 day samples which shows much higher porosity and larger snow grains.



SI Fig S5. 2 Micro-CT images of the doped samples after 0 and 12 days exposure to TGM. The 0 day samples (after 7 days at -5°C) have smaller grains and lower porosity than the 12 day samples which shows much larger and more connected snow grains.

Bibliography

Bartels–Rausch, T., Wren, S. N., Schreiber, S., Riche, F., Schneebeli, M., and Ammann, M.: Diffusion of volatile organics through porous snow: impact of surface adsorption and grain boundaries, *Atmospheric Chemistry and Physics*, 13, 6727–6739, 10.5194/acp–13–6727–2013, 2013.

Bartels–Rausch, T., Jacobi, H. W., Kahan, T. F., Thomas, J. L., Thomson, E. S., Abbatt, J. P. D., Ammann, M., Blackford, J. R., Bluhm, H., Boxe, C., Domine, F., Frey, M. M., Gladich, I., Guzmán, M. I., Heger, D., Huthwelker, T., Klán, P., Kuhs, W. F., Kuo, M. H., Maus, S., Moussa, S. G., McNeill, V. F., Newberg, J. T., Pettersson, J. B. C., Roeselová, M., and Sodeau, J. R.: A review of air–ice chemical and physical interactions (AICI): liquids, quasi–liquids, and solids in snow, *Atmos Chem Phys*, 14, 1587–1633, 10.5194/acp–14–1587–2014, 2014.

Berkemeier, T., Steimer, S. S., Krieger, U. K., Peter, T., Poschl, U., Ammann, M., and Shiraiwa, M.: Ozone uptake on glassy, semi–solid and liquid organic matter and the role of reactive oxygen intermediates in atmospheric aerosol chemistry, *Phys Chem Chem Phys*, 18, 12662–12674, 10.1039/c6cp00634e, 2016.

Birkeland, K. W., Johnson, R. F., and Schmidt, S. D.: Near–surface faceted crystals formed by diurnal recrystallization: A case study of weak layer formation in the mountain snowpack and its contribution to snow avalanches, *Arctic and Alpine research*, 30, 200 – 204, 1998.

Borget, F., Chiavassa, T., Allouche, A., and Aycard, J. P.: Experimental and quantum study of adsorption of ozone (O₃) on amorphous water ice film, *J. Phys. Chem.*, 105, 499 – 454, 2001.

Brimblecombe, P., Tranter, M., Abrahams, P. W., Blackwood, I., Davies, T. D., and Vincent, C. E.: Relocation and preferential elution of acidic solute through the snowpack of a small, remote, high–altitude Scottish catchment, *Annals of Glaciology*, 7, 141–147, 1985.

Brimblecombe, P., Clegg, S. L., Davies, T. D., Shooter, D., and Tranter, M.: The loss of halide and sulphate ions from melting ice, *Water Resources*, 22, 693–700, 1988.

Cabanes, A., Legagneux, L., and Domine, F.: Rate of evolution of specific surface area of surface snow layers, *Environ. Sci. Technol.*, 37, 661–666, 10.1021/es025880r, 2003.

Calonne, N., Geindreau, C., Flin, F., Morin, S., Lesaffre, B., Rolland du Roscoat, S., and Charrier, P.: 3-D image-based numerical computations of snow permeability: links to specific surface area, density, and microstructural anisotropy, *The Cryosphere*, 6, 939–951, 10.5194/tc-6-939-2012, 2012.

Chen, L. W. A., Watson, J. G., Chow, J. C., Green, M. C., Inouye, D., and Dick, K.: Wintertime particulate pollution episodes in an urban valley of the Western US: a case study, *Atmospheric Chemistry and Physics*, 12, 10051–10064, 10.5194/acp-12-10051-2012, 2012.

Colbeck, S. C.: Theory of metamorphism of dry snow, *Journal of Geophysical Research*, 88, 5475 – 5482, 10.1029/JC088iC09p05475, 1983.

Cragin, J. H., Hewitt, A. D., and Colbeck, S. C.: Grain-scale mechanisms influencing the elution of ions from snow, *Atmos. Environ.*, 30, 171 – 208, 1996.

Davis, E. R., Petersen, C. E., and Bales, R. C.: Ion flux through a shallow snowpack: effects of initial conditions and melt sequences, *Biogeochemistry of seasonally snow-covered catchments (proceedings of a Boulder Symposium)*, 228, 115–126, 1995.

Dibb, J. E., Ziemba, L. D., Luxford, J., and Beckman, P.: Bromide and other ions in the snow, firn air, and atmospheric boundary layer at Summit during GSHOX, *Atmospheric Chemistry and Physics*, 10, 9931–9942, 10.5194/acp-10-9931-2010, 2010.

Dlugokencky, E. J., and Ravishankara, A. R.: Laboratory measurements of direct ozone loss on ice and doped-ice surfaces, *Geophysical Research Letters*, 19, 41 – 44, 1992.

Domine, F., Cabanes, A., and Legagneux, L.: Structure, microphysics and surface area of the Arctic snowpack near Alert during ALERT 2000 campaign, *Atmospheric Environment*, 36, 2753–2765, 2002.

Domine, F., and Shepson, P. B.: Air-snow interactions and atmospheric chemistry, *Science*, 297, 1506–1510, 10.1126/science.1074610, 2002.

Domine, F., Cincinelli, A., Bonnaud, E., Martellini, T., and Picaud, S.: Adsorption of phenanthrene on natural snow, *Environ. Sci. Technol.*, 41, 6033 – 6038, 2007.

Bibliography

Domine, F., Albert, M., Huthwelker, T., Jacobi, H. W., Kokhanovsky, A. A., Lehning, M., Picard, G., and Simpson, W. R.: Snow physics as relevant to snow photochemistry, *Atmos Chem Phys*, 8, 171–208, 2008.

Dominé, F., and Thibert, E.: Mechanism of incorporation of trace gases in ice grown from the gas phase, *Geophysical Research Letters*, 23, 3627–3630, 10.1029/96gl03290, 1996.

Eichler, A., Schwikowski, M., and Gäggeler, H. W.: Meltwater–induced relocation of chemical species in Alpine firn, *Tellus*, 53B, 191–203, 2001.

Eichler, J., Kleitz, I., Bayer–Giraldi, M., Jansen, D., Kipfstuhl, S., Shigeyama, W., Weikusat, C., and Weikusat, I.: Location and distribution of micro–inclusions in the EDML and NEEM ice cores using optical microscopy and in situ Raman spectroscopy, *The Cryosphere*, 11, 1075–1090, 10.5194/tc–11–1075–2017, 2017.

He, Z., Xie, W. J., Liu, Z., Liu, G., Wang, Z., Gao, Y. Q., and Wang, J.: Tuning ice nucleation with counterions on polyelectrolyte brush surfaces, *Sci. Adv*, 2, 1–7, DOI: 10.1126/sciadv.1600345, 2016.

Hewitt, A. D., Cragin, J. H., and Colbeck, S. C.: Does snow have ion chromatographic properties?, 46th Ann. Eastern Snow Conference, Quebec City, Quebec, Canada, 1989, 165–171.

Hewitt, A. D., Cragin, J. H., and Colbeck, S. C.: Effects of crystal metamorphosis on the elution from chemical species from snow, 48th Ann. Eastern Snow Conference, Guelph, Ontario, Canada, 1991, 1–10.

Hullar, T., and Anastasio, C.: Direct visualization of solute locations in laboratory ice samples, *The Cryosphere*, 10, 2057–2068, 10.5194/tc–10–2057–2016, 2016.

Kerbrat, M., Pinzer, B. R., Huthwelker, T., Gäggeler, H. W., Ammann, M., and Schneebeli, M.: Measuring the specific surface area of snow with X–ray tomography and gas adsorption: comparison and implications for surface smoothness, *Atmos Chem Phys*, 8, 1261–1275, 2008.

Kerbrat, M., Huthwelker, T., Gäggeler, H. W., and Ammann, M.: Interaction of nitrous acid with polycrystalline ice: adsorption on the surface and diffusion into the bulk, *J. Phys. Chem. C*, 114, 2208 – 2219, 2010.

Krnavek, L., Simpson, W. R., Carlson, D., Domine, F., Douglas, T. A., and Sturm, M.: The chemical composition of surface snow in the Arctic: Examining marine, terrestrial, and atmospheric influences, *Atmospheric Environment*, 50, 349–359, 10.1016/j.atmosenv.2011.11.033, 2012.

McNeill, V. F., Geiger, F. M., Loerting, T., Trout, B. L., Molina, L. T., and Molina, M. J.: Interaction of hydrogen chloride with ice surfaces: the effects of grain size, surface roughness and surface disorder, *J. Phys. Chem. A*, 111, 6274–6284, 2007.

Michoud, V., Doussin, J.-F., Colomb, A., Afif, C., Borbon, A., Camredon, M., Aumont, B., Legrand, M., and Beekmann, M.: Strong HONO formation in a suburban site during snowy days, *Atmospheric Environment*, 116, 155–158, 10.1016/j.atmosenv.2015.06.040, 2015.

Nagashima, K., Sazaki, G., Hama, T., Murata, K.-i., and Furukawa, Y.: Uptake Mechanism of Atmospheric Hydrogen Chloride Gas in Ice Crystals *via* Hydrochloric Acid Droplets, *Crystal Growth & Design*, 18, 4117–4122, 10.1021/acs.cgd.8b00531, 2018.

Pinzer, B. R., and Schneebeli, M.: Snow metamorphism under alternating temperature gradients: Morphology and recrystallization in surface snow, *Geophysical Research Letters*, 36, 10.1029/2009gl039618, 2009.

Pinzer, B. R., Kerbrat, M., Huthwelker, T., Gäggeler, H. W., Schneebeli, M., and Ammann, M.: Diffusion of NO_x and HONO in snow: A laboratory study, *Journal of Geophysical Research*, 115, 10.1029/2009jd012459, 2010.

Pinzer, B. R., Schneebeli, M., and Kaempfer, T. U.: Vapor flux and recrystallization during dry snow metamorphism under a steady temperature gradient as observed by time-lapse micro-tomography, *The Cryosphere*, 6, 1141–1155, 10.5194/tc-6-1141-2012, 2012.

Schneebeli, M., and Sokratov, S. A.: Tomography of temperature gradient metamorphism of snow and associated changes in heat conductivity, *Hydrological Processes*, 18, 3655–3665, 10.1002/hyp.5800, 2004.

Sommerfeld, R. A., and LaChapelle, E.: The classification of snow metamorphism, *Journal of Glaciology*, 9, 1–17, 1970.

Stanier, C., Singh, A., Adamski, W., Baek, J., Caughey, M., Carmichael, G., Edgerton, E., Kenski, D., Koerber, M., Oleson, J., Rohlf, T., Lee, S. R., Riemer, N., Shaw, S., Sousan, S., and Spak, S. N.: Overview of the LADCO winter nitrate study: hourly ammonia, nitric acid and PM_{2.5} composition at an urban and rural site pair during

Bibliography

PM_{2.5}; episodes in the US Great Lakes region, *Atmospheric Chemistry and Physics*, 12, 11037–11056, 10.5194/acp-12-11037-2012, 2012.

Ullerstam, M., and Abbatt, J. P.: Burial of gas-phase HNO₃ by growing ice surfaces under tropospheric conditions, *Phys Chem Chem Phys*, 7, 3596–3600, 10.1039/b507797d, 2005.

Wang, F., Lin, W., Wang, J., and Zhu, T.: NO_x Release from Snow and Ice Covered Surface in Polar Regions and the Tibetan Plateau, *Advances in Climate Change Research*, 2, 141–148, 10.3724/sp.j.1248.2011.00141, 2011.

Wu, S., Zhu, C., He, Z., Xue, H., Fan, Q., Song, Y., Francisco, J. S., Zeng, X. C., and Wang, J.: Ion-specific ice recrystallization provides a facile approach for the fabrication of porous materials, *Nat Commun*, 8, 15154, 10.1038/ncomms15154, 2017.

Zermatten, E., Haussener, S., Schneebeli, M., and Steinfeld, A.: Tomography-based determination of permeability and Dupit–Forchheimer coefficient of characteristic snow samples, *Journal of Glaciology*, 57, 811–816, 2011.

Summary and Outlook

The theme of my thesis is chemical reactivity in the cold regions of the world including reactivity in snow and ice. Of the chemical processes occurring in these regions, I have focused on halide (bromide) oxidation by ozone. This thesis has described the kinetics of the dark oxidation of bromide and for the first time, at temperatures from 0 °C to –25 °C. We now have a parameterization which may improve predictions of halogen chemistry in atmospheric chemistry models that couple processes in snow, sea ice, and sea spray aerosol.

Halogen activation in environmental condensed phases is a multiphase process. The interfacial process was kinetically described in Chapter 2 where we reported on the first direct identification of the interfacial species (BrOOO^-) driving the dark reaction of bromide with ozone in a single solute reactive medium. We also confirmed the importance of this interfacial process for high surface area compartments like sea spray aerosol. We showed that this interfacial process is a major contributor to the bromide oxidation and may be more important than reaction in the aqueous bulk especially in sea spray aerosols and at environmentally relevant ozone concentrations.

Motivated by the ubiquitous presence of organics in almost every environmental compartment, I increased the complexity of the reactive medium in the laboratory studies described in Chapter 3. With particular attention to the aqueous bulk processes, Chapter 3 presented a temperature dependent kinetic description of bromide oxidation in a mixture containing an organic species (citric acid) and an inorganic species (sodium bromide). This study not only accounted for the temperature dependence of the reaction rate, but also for the effects of temperature on the physical properties of the reactive medium. The key

finding here was that the rate acceleration that may have occurred with decreasing water activity as temperature decreased at a fixed relative humidity (also with respect to ice) was significantly countered by increased viscosity (especially due to the organic species) and decreased solubility of the reactive gas (ozone) as the activity of the solutes increased with decreasing temperature. This will be important for sea spray aerosols, which also contain a significant organic fraction (O'Dowd *et al.*, 2004).

In particular, I parameterized the Henry's law solubility of ozone (H) in the reactive medium studied. This parameterization has a large uncertainty due to lack of data on Henry's law solubility of ozone although ozone is one of the main oxidants in the environment. Data and parameterizations available on the effects of solutes on this H of ozone do not go below 0 °C (Rischbieter *et al.*, 2000; Bin, 2006) and do not consider mixtures of organic and inorganic species. Therefore, I recommend that just as there are increasingly available viscosity measurements in different reactive compartments (Reid *et al.*, 2018), there should be a parallel increase in the measurements of Henry's law solubility of ozone and other environmentally relevant trace gases.

Further, the effect of the organic species on the stability of the interfacial intermediate, BrOOO^- , is presently not known. Future experiments should investigate the interfacial process applying a combination of detailed kinetic studies at low ozone concentration, liquid jet X-ray photoelectron spectroscopy to probe the surface coverage and stability of the interfacial species in the presence of organic species, and computational work to investigate the energetics of the complex stabilization. It may be necessary to investigate the effect of the organic species on the partitioning of bromide to the surface (Lee *et al.*, 2015; Werner *et al.*, 2016), the stability of the interfacial species, and the relative importance of this stability by complexing with water versus complexing with the organic species.

Next to aerosol, snow has received much attention as a reactive medium where impurities can be located at the interface or in the bulk of the ice matrix. Preliminary assessment of bromide oxidation by ozone in a packed snow column and the effects of metamorphism are presented in Chapter 5. Present results indicate that bromide may be incorporated from the interface into the ice matrix after 12 days under temperature gradient induced metamorphism at a gradient of 33 K/m. From an atmospheric chemistry perspective, this process is of importance as only solutes or products at the surface can be released to the overlying air within short time scales. Special care was taken to work at low, environmentally relevant solute concentration that may be low enough to form solid solution with the ice or to be incorporated into micropockets within the ice matrix (Bartels-Rausch *et al.*, 2014; Eichler *et al.*, 2017; Wu *et al.*, 2017). This method of applying reactivity in investigating the partitioning of ions between the surface and the bulk of snow grains with metamorphism is new. Generally, the ice matrix as host for impurities in snow has gotten little attention in the past for ions of atmospheric relevance.

Chapter 6 Summary and outlook

Future work on this ion redistribution study in snow due to temperature–gradient–metamorphism would conduct similar reactivity experiments at different time points between 0 and 12 days as well as on a sample, which remained under only isothermal treatment for the 12 days. Future work could also better characterize the location of bromide on the snow grains using X–ray computed tomography (Hullar and Anastasio, 2016). This tomographic method may be able to map the distribution of the bromide ions on the snow grains. If sensitivity is high enough, low concentrations of bromide may be used. Coupled to a metamorphism cell, the tomographic method may be able to monitor the evolution of the snow grains as well as the changing distribution of the bromide between the surface and the bulk of the snow grains with TGM. The redistribution of other less soluble contaminants with metamorphism may also be studied using this method with a gas that reacts with those contaminants.

In addition to the distribution of the reactive ion on the surface of the snow grain, for this reactive method, the actual area probed by the reactive gas is important. This may not be the same as that measured by snow computed micro–tomography (micro–CT). An adsorptive method, as has been described in studies like Bartels–Rausch *et al.* (2005) and Kerbrat *et al.* (2008), may be a complementary approach to the micro–CT.

The study in Chapter 5 is the lowest level complexity with only one reactive species present. In the natural environment, there are often mixtures present and sometimes higher concentrations. Solutes have been shown to influence the crystallization of ice during freezing; higher concentrations lead to smaller grain sizes (Wu *et al.*, 2017). In addition, the type of solute also affects crystallization and grain size (Wu *et al.*, 2017). The presence of multiple solutes may influence the partitioning of the ions between the bulk and the surface. High concentrations may lead to formation of brine, which may be on the surface of the snow grain or included in micropockets in the snow (Eichler *et al.*, 2017). Therefore, future work with increased composition complexity may provide relevant information on the effects of solute mixtures on structural changes during metamorphism, ion partitioning to the different compartments in the ice and implications for reactivity, and effects of snow in atmospheric composition and ice core research.

Chapter 5 focused on dry metamorphism and the effects on ion redistribution. However, with warming during the day on a warmer winter day, melt–freeze cycles occur, which can lead to wet metamorphism especially during the warmer periods (Davis *et al.*, 1995). This often occurs in the natural environment with implications on the distribution of ions. Melt increases the fraction of liquid water in the snowpack. Ions can partition into this liquid volume, brine can also be diluted and/or be transported with this liquid water. There are few studies investigating wet metamorphism and its impacts on the distribution of ions in the snow pack using an elution method (Davis *et al.*, 1995). A laboratory method with controlled wet metamorphism, melt–freeze sequences (Davis *et al.*, 1995), combined with a reactive method for assessing redistribution of ions and/or X–ray tomography may be better

able to tell what occurs in the field, which is often a combination of wet and dry metamorphism. Information on this will be especially important for the ice core community as melting smears ice core information with impacts on the interpretation of ice core data.

The natural environment is made up of multiple compartments simultaneously contributing to atmospheric composition. With respect to polar regions, some of these compartments include the snow, sea ice, sea spray aerosols, brine and frost flowers in brine pools. Understanding the relative contributions of each of these compartments under the same conditions may be able to provide a wholesome picture which links research in individual compartments to the larger environment. Therefore, I recommend a study simulating this environment using a setup similar to the Roland Von Glasow air–sea–ice chamber (<https://www.uea.ac.uk/environmental-sciences/sea-ice-chamber>). In such a setup, one could simulate each compartment in one. This would include diurnal cycles in temperature and sunlight, wind and sea spray aerosol generation, brine and frost flower production, and sea ice formation. One would be able to define and characterize the composition of the different compartments including the gas phase. A model, which includes all compartments and their interactions, will be ideal for upscaling to the larger scale environment.

To really bring all laboratory work to the natural environment, it would be ideal to conduct a halogen activation field campaign over a sea ice region. During such a campaign, atmospheric compositions especially of reactive halogen species should be measured as well as aerosol concentrations and composition (e.g. Nerentorp Mastromonaco *et al.*, 2016; Peterson *et al.*, 2017). For snow and ice in the field, the concentrations of ions in snow, sea ice and brine pools should be measured (e.g. Pratt *et al.*, 2013). The snow structural properties such as density, porosity, water equivalent, and light penetration depth should be measured (Domine *et al.*, 2002). Models could also be developed which incorporate the relevant compartments. A model developed from the sea ice chamber study could be validated and improved based on measurements in the field.

Interpretation of field study data can however be complicated as there are many facets contributing to observations. Such difficulties in piecing out contributions of snow to atmospheric composition from other factors are demonstrated in Chapter 4, which is based a wintertime urban field campaign in Kalamazoo, Michigan, United States. Looking at ammonia concentrations during the campaign, for instance, we observed some indication of higher temperature dependent emission of ammonia on snow covered days than on days without snow cover. This temperature dependence may not be explicitly confirmed based on the field observations only; laboratory studies on the temperature dependent emission of ammonia from ice are needed. Future campaigns should better characterize the snow properties to be able to properly determine the influence of snow on observations of wintertime atmospheric composition.

Observations show that atmospheric interactions with snow are not well understood. The transfer of atmospheric composition to ice archives is not straight forward. This may have

Chapter 6 Summary and outlook

implications on our ability to understand past atmospheric composition and ability to predict future conditions. Collaborative studies involving field researchers, who identify questions arising from field campaigns, laboratory researchers, who simplify the field cases to answer the questions from field studies, and modelers, who link the results of laboratory studies to field observations, will improve our ability to understand past observations and predict future environmental conditions.

Bibliography

Bartels–Rausch, T., Jacobi, H. W., Kahan, T. F., Thomas, J. L., Thomson, E. S., Abbatt, J. P. D., Ammann, M., Blackford, J. R., Bluhm, H., Boxe, C., Domine, F., Frey, M. M., Gladich, I., Guzmán, M. I., Heger, D., Huthwelker, T., Klán, P., Kuhs, W. F., Kuo, M. H., Maus, S., Moussa, S. G., McNeill, V. F., Newberg, J. T., Pettersson, J. B. C., Roeselová, M., and Sodeau, J. R.: A review of air–ice chemical and physical interactions (AICI): liquids, quasi–liquids, and solids in snow, *Atmos Chem Phys*, **14**, 1587–1633, 10.5194/acp–14–1587–2014, 2014.

Bin, A. K.: Ozone solubility in liquids, *Ozone–Sci Eng*, **28**, 67–75, 10.1080/01919510600558635, 2006.

Davis, E. R., Petersen, C. E., and Bales, R. C.: Ion flux through a shallow snowpack: effects of initial conditions and melt sequences, *Biogeochemistry of seasonally snow–covered catchments (proceedings of a Boulder Symposium)*, **228**, 115–126, 1995.

Domine, F., Cabanes, A., and Legagneux, L.: Structure, microphysics and surface area of the Arctic snowpack near Alert during ALERT 2000 campaign, *Atmospheric Environment*, **36**, 2753–2765, 2002.

Eichler, J., Kleitz, I., Bayer–Giraldi, M., Jansen, D., Kipfstuhl, S., Shigeyama, W., Weikusat, C., and Weikusat, I.: Location and distribution of micro–inclusions in the EDML and NEEM ice cores using optical microscopy and in situ Raman spectroscopy, *The Cryosphere*, **11**, 1075–1090, 10.5194/tc–11–1075–2017, 2017.

Hullar, T., and Anastasio, C.: Direct visualization of solute locations in laboratory ice samples, *The Cryosphere*, **10**, 2057–2068, 10.5194/tc–10–2057–2016, 2016.

Lee, M. T., Brown, M. A., Kato, S., Kleibert, A., Turler, A., and Ammann, M.: Competition between Organics and Bromide at the Aqueous Solution–Air Interface as Seen from Ozone Uptake Kinetics and X–ray Photoelectron Spectroscopy, *J Phys Chem A*, **119**, 4600–4608, 10.1021/jp510707s, 2015.

Nerentorp Mastromonaco, M., Gårdfeldt, K., Jourdain, B., Abrahamsson, K., Granfors, A., Ahnoff, M., Dommergue, A., Méjean, G., and Jacobi, H. W.: Antarctic winter mercury and ozone depletion events over sea ice, *Atmospheric Environment*, **129**, 125–132, 10.1016/j.atmosenv.2016.01.023, 2016.

O'Dowd, C. D., Facchini, M. C., Cavalli, F., Cebrunis, D., Mircea, M., Decesari, S., Fuzzi, S., Yoon, Y. J., and Putaud, J.–P.: Biogenically driven organic contribution to marine aerosol, *Nature*, **431**, 672–676, 10.1038/nature02970, 2004.

Peterson, P. K., Pöhler, D., Sihler, H., Zielcke, J., General, S., Frieß, U., Platt, U., Simpson, W. R., Nghiem, S. V., Shepson, P. B., Stirm, B. H., Dhaniyala, S., Wagner, T., Caulton, D. R., Fuentes, J. D., and Pratt, K. A.: Observations of bromine monoxide transport in the Arctic sustained on aerosol particles, *Atmos Chem Phys*, **17**, 7567–7579, 10.5194/acp–17–7567–2017, 2017.

Chapter 6 Summary and outlook

Pratt, K. A., Custard, K. D., Shepson, P. B., Douglas, T. A., Pöhler, D., General, S., Zielcke, J., Simpson, W. R., Platt, U., Tanner, D. J., Gregory Huey, L., Carlsen, M., and Stirm, B. H.: Photochemical production of molecular bromine in Arctic surface snowpacks, *Nature Geoscience*, 6, 351–356, 10.1038/ngeo1779, 2013.

Reid, J. P., Bertram, A. K., Topping, D. O., Laskin, A., Martin, S. T., Petters, M. D., Pope, F. D., and Rovelli, G.: The viscosity of atmospherically relevant organic particles, *Nat Commun*, 9, 956, 10.1038/s41467-018-03027-z, 2018.

Rischbieter, E., Stein, H., and Schumpe, A.: Ozone solubilities in water and aqueous salt solutions, *J Chem Eng Data*, 45, 338–340, DOI 10.1021/je990263c, 2000.

Werner, J., Dalirian, M., Walz, M. M., Ekholm, V., Wideqvist, U., Lowe, S. J., Ohrwall, G., Persson, I., Riipinen, I., and Bjorneholm, O.: Surface Partitioning in Organic–Inorganic Mixtures Contributes to the Size–Dependence of the Phase–State of Atmospheric Nanoparticles, *Environ Sci Technol*, 50, 7434–7442, 10.1021/acs.est.6b00789, 2016.

Wu, S., Zhu, C., He, Z., Xue, H., Fan, Q., Song, Y., Francisco, J. S., Zeng, X. C., and Wang, J.: Ion–specific ice recrystallization provides a facile approach for the fabrication of porous materials, *Nat Commun*, 8, 15154, 10.1038/ncomms15154, 2017.

Acknowledgements

This thesis could not be conducted without contributions from a lot of people, both in the actual work and thereabout. A non–exhaustive list of these people and or groups of people is presented below:

- I am grateful to Kris McNeill at ETH Zurich for his motivation and support, which led to my applying for this project.
- I am grateful to Thorsten Bartels–Rausch for the opportunity to participate in this project, the freedom to be creative in achieving the goals of the project, the assistance in experiments and experimental design, for the huge effort in developing the models for this thesis, for assisting in struggling with the MS, for exchanging ideas, for help in putting the thesis together, for seeking out an opportunity for me to be part of a field campaign and supporting me through it, the list goes on
- I am grateful to Markus Ammann for his great ideas in planning and executing experiments, in interpreting data, for reading all my writing and for prompt responses to emails and questions, for accepting the role of my doctor father. His list also goes on
- I am grateful to Mario Birrer for taking my small scale ideas on experimental setup and making them grand, for the awesome humidifier without which, my experimental results would be a mess, for fixing all of the instruments and equipment which (I) broke, for forgiving my misadventures with his instruments and software.
- I am grateful to Andrés Laso for picking up after Mario and allowing me to help him in solving my technical issues, for exchanging ideas on how to improve my experimental setup and solve lab issues.
- I am grateful to Sabina Brütsch–Suter for helping analyze all my ice and snow samples very quickly.
- I am grateful to the Surface Chemistry group members and the LUC for being there, and always asking me to join in for lunch and other activities, for the laughs and funny videos to help keep me sane when my experiments were hanging out at the eyewall of a tornado; for music lessons (Pablo Corral–Arroyo and Peter Alpert).
- I am grateful to Sven Avak and Jürg Trachsel, my MISO project teammates together with Anja Eichler and Martin Schneebeli, for the success of our team projects, which would

Chapter 6 Summary and outlook

not have been conducted if we were not a team, for the laughs, and support as our projects progressed, for being awesome members of our team.

- I am grateful to Martin Schneebeli for allowing us to work in the cold rooms at SLF Davos.
- I am grateful to the Kerri Pratt and the Pratt Laboratory for allowing me participate in their 2018 winter campaign, for help with data analysis, interpretation, and writing. I am especially grateful to Nate May for teaching me all I knew about the AIM-IC; and to Stephen McNamara for being an awesome teammate at the field campaign (It would have been difficult living with a new acquaintance at a winter field campaign for two whole months; Stephen's easy going attitude made it a piece of cake; 2 months flew by and we were still laughing amidst our tiredness), for teaching me all the wiring I know, for helping me find a place in Michigan, for making my stay in Michigan enjoyable.
- I am grateful to Angela Blattmann and Doris Bühler at the Paul Scherrer Institute, and Forney Petra and Eva Choffat at the Institute of Atmosphere and Climate, ETH Zurich for handling all my bureaucratic issues: they surely made my life easy.
- I am grateful to Xianguoi Kong, Ming Lee, Fabrizio Orlando, and Astrid Waldner, former surface chemistry group members for their support while they were here. I am grateful to Kong for teaching me to skate.
- I am grateful to Shuzehn Chen and Xing Wang, for giving me a roof over my head with awesome Chinese food when I did not have a place to stay.
- I am grateful to the Zurich Lacrosse team for giving me the opportunity to have a place to go to clear my head through physical activity.
- I am grateful to my UJ workout group, for also being my physical outlet and for the weekly dose of hugs.
- I am grateful to Biqing Zhu for being my friend, for walks, runs, talks and laughs, for tea and brunch with such good food, in essence, for giving me a chance to live while working.
- I am grateful to the McAlister family, and the Aquadro family for restful holidays, love, and a home.
- I am grateful to Bruce McAlister for all the time we spend in the valleys and on mountain tops, for road trips and train rides, for all letters and postcards and for reading my letters, for being my friend.
- I am grateful to my family, the Edebelis/Eramehs, for the encouragement and support and motivation to keep taking that next step.
- I am grateful to God, without whom I am nothing, but for his love, I am here; without whom, I can achieve nothing, but by His grace, I have come this far. His grace and love are enough for me.

THANK YOU; OBILO!

Jacinta Edebeli

Raesslerweg 2, 8057 Zuerich, Switzerland
+41 77 243 25 03; jacinta.edebeli@psi.ch; jacinta.edebeli@gmail.com

EDUCATION

- 11/2014 – 12/2018 **Swiss Federal Institute of Technology (ETHZ), Zurich, Switzerland**
Environmental Science
Doctoral thesis: Multi-phase chemical reactivity in cold regions
Supervisors: Prof. Dr. Markus Ammann; Dr. Thorsten Bartels-Rausch
- 9/2012 – 10/2014 **Swiss Federal Institute of Technology (ETHZ), Zurich, Switzerland**
MSc in Environmental Science, (final grade 5.51/6.0)
Major: Biogeochemistry and pollutant dynamics
Thesis: Bioanalytical assessment of water associated with coal seam gas mining
Advisors: Prof. Dr. Beate Escher, Prof. Dr. Martin Scheringer
- 09/2008 – 05/2012 **University of Massachusetts (UMass Amherst), Amherst, MA, USA**
BSc in Civil Engineering (GPA 3.97/4.0)
Senior project: Design of a drinking water booster pump station
- 01/2008 – 05/2011 **Mount Holyoke College (MHC), South Hadley, MA, USA**
BA in Environmental Studies (GPA 3.92/4.0)
Major: Conservation biology

PRACTICAL EXPERIENCES

- 05/2015 – 12/2018 **Doctoral Researcher – Environmental Chemistry**
Paul Scherrer Institute, Villigen PSI, Switzerland
- Managed laboratory and field research projects in snow and atmospheric chemistry
 - Developed methods for studying multiphase chemistry in aerosols, snow, and ice
 - Developed models for investigating multiphase bromide oxidation using Matlab
 - Presented results at local and international conferences, seminars, and meetings

Curriculum Vitae

- Wrote peer-reviewed publications and reports
- Mentored a junior PhD student and visiting students
- Assisted in managing laboratory supplies and instruments with technicians
- Teaching assistant, bachelor course in Atmospheric Chemistry

11/2017 – 03/2018 **Visiting scholar – Winter atmospheric composition in urban areas**

Pratt Laboratory, University of Michigan, Ann Arbor, MI, USA

- Deployed and managed an Ambient Ion Monitor Ion Chromatograph (AIM-IC) for a 2-month field study in a team at Kalamazoo, MI, USA
- Prepared an operations manual for the AIM-IC
- Maintained the AIM-IC including troubleshooting with technicians
- Assisted in experimental design and execution, data analysis and reporting

11/2014 – 04/2015 **Research Assistant – Synthesis of PBDEs for toxicity assessment**

McNeil Laboratory, Swiss Institute of Technology, ETH Zurich

- Synthesized Hydroxylated polybrominated diphenyl ethers (OH-PBDEs)
- Purified synthesized compounds using chromatography
- Ascertained the purity of synthesized compounds using NMR and LC-MS

04/2014 – 08/2014 **Master's Internship: Characterization of ceria-supported metal catalyst;**

Paul Scherrer Institute, Villigen PSI

- Characterized ceria-supported metal catalysts for fuel cell feed gas purification using GC-MS
- Assisted in planning and executing flow reactor experiments
- Assisted in super X-ray absorption spectroscopy (Super XAS) experiments
- Performed data analysis and report writing; results are presented in a scientific publication

05/2012 – 08/2012 **Field Floodplain Forest Intern – Connecticut River Project**

05/2009 – 08/2009 **The Nature Conservancy, Northampton, MA, USA**

- Surveyed floodplain vegetation and cross-section along the Connecticut River for a stream flow model in a team
- Developed a seedlings sampling method and seedling identification database for

Curriculum Vitae

the Connecticut River floodplain

05/2011 – 08/2011 **Summer Undergraduate Research Fellow**

Woods Hole Oceanographic Institute (WHOI), Woods Hole, MA, USA

- Developed and tested a prototype for measuring seawater pH and alkalinity during an ocean acidification research cruise to the North Atlantic Ocean

05/2010 – 08/2010 **Summer Undergraduate Research Fellow**

University of Massachusetts Amherst, MA, USA

- Developed stream flow models using Global Circulation Model data for a World Bank feasibility study on proposed dams on the Niger River
- Statistically evaluated the accuracy of spatial scales in climate analysis

LANGUAGES

| | |
|----------------|-------------------|
| Native | English |
| Conversational | German and French |

METHODS

| | |
|---|---------------------|
| Teledyne O ₃ and NO _x analysers | Very good knowledge |
| AIM-IC | Very good knowledge |
| Visco Air Viscometer | Good knowledge |
| CPC/SMPS | Basic knowledge |
| CIMS | Basic knowledge |

COMPUTER SKILLS

| | |
|----------------|---------------------|
| MS-Office | Very good knowledge |
| Matlab; Origin | Good knowledge |
| AutoCAD | Basic knowledge |
| ArcGIS (web) | Basic knowledge |
| LabView; Igor | Basic knowledge |

SELECTED PUBLICATIONS

- [Edebeli, J.](#), M. Ammann, T. Bartels-Rausch (2018). Microphysics of the

aqueous bulk counter water activity driven rate acceleration in bromide oxidation by ozone from 289 – 245 K. *Environ. Sci.: Process Impacts*. DOI: 10.1039/c8em00417j.

- Artiglia, L., J. Edebeli, F. Orlando, S. Chen, M.-T. Lee, P. C. Arroyo, A. Gilgen, T. Bartels-Rausch, A. Kleibert, M. Vazdar, M. A. Carignano, J. S. Francisco, P. B. Shepson, I. Gladich and M. Ammann (2017). A surface ozonide triggers bromide oxidation at the aqueous solution-vapor interface. *Nat Comms*, 8, 700. DOI:10.1038/s41467-017-00823-x
- Kopelent, R., van Bokhoven, J. A., Szlachetko, J., Edebeli, J., Paun, C., Nachtegaal, M., & Safonova, O. V. (2015). Catalytically Active and Spectator Ce(3+) in Ceria-Supported Metal Catalysts. *Angew Chem Int Ed Engl*, 54(30), 8728-8731. DOI:10.1002/anie.201503022

SELECTED PRESENTATIONS

- Oral Edebeli, J., L. Artiglia, T. Bartels-Rausch, M. Ammann. (2017). Halogen activation: Decomposing surface and bulk processes. ACS fall meeting, Washington DC, USA.
- Poster Edebeli, J. M. Ammann, & T. Bartels-Rausch. (2018). Viscosity and solubility counter water activity driven rate acceleration in bromide oxidation by ozone from 245 to 289 K. IGAC, Takamatsu, Japan

EXTRACURRICULAR ACTIVITIES

- Zurich Lions Lacrosse Academy, defence player
- Sunday volunteer at Limattalhospital

HOBBIES

- Lacrosse, hiking
- Reading fiction
- learning new skills, languages (Chinese, Norwegian, Dutch), and sports

SELECTED AWARDS

- Sports
- MVP, Switzerland, FIL Rathbones Women's Lacrosse world cup, 2017
 - All European Lacrosse Team, ELF Women's Championship, 2015
- ETHZ, 2012
- Excellence Scholarship and Opportunity Program, *ESOP*
- UMass, 2012
- Excellence Award, College of Engineering Diversity Programs Office
- MHC, 2011
- *Phi Beta Kappa Scholar*, Mount Holyoke College
 - Environmental Scholar Award

Curriculum Vitae

- Abbey Howe Turner Award for excellence in Biological Sciences
-